Regulation of Junction Configuration by Cell Tension

Kyasha Sri Ranjan

January 2016

A thesis submitted for the degree of

Doctor of Philosophy (PhD)

Department of Materials

Faculty of Engineering, Imperial College London,

Exhibition Road, London, SW7 2AZ

Declarations

Declaration of Originality

I hereby declare that the data presented in this thesis is my own work and written in my own words with due acknowledgement to those who have contributed.

Copyright declaration

Abstract

The maintenance of cell-cell contacts is essential for tissue cohesion and a variety of different physiological processes in morphogenesis and homeostasis. Adherens junctions are protein complexes that mediate cell-cell contacts in epithelial cells and E-cadherin receptors are their main component. During junction formation, thin bundles of actin localise towards cell-cell contacts in the characteristic cytoskeletal organization of epithelia. Tension at the underlying cortex and thin bundle compaction help form tight, straight junctions and maintain cadherin receptors in place. However, how these epithelia-specific structures are formed and remodelled lacks in-depth understanding.

In this study, I have addressed how contractile forces modulate junction configuration and molecular composition (adhesion receptors and actin cytoskeleton). Micropatterning was used to precisely confine the geometry of cells, control cortical forces and provide a permissive, simplistic way in which cells are allowed to interact. Three different shapes, namely squares, triangles and circles were patterned to study biophysical and junction properties. Although the average cell heights and volumes are similar between different geometries, cortical stiffness (i.e. Young's modulus) is two-fold higher in cells grown in geometries that impose higher contractility: squares and triangles. Doublets seeded on these shapes also position their nuclei further apart and exhibit preferences in junction orientation.

A majority of cells cultured on triangular and square geometries have shorter and straighter junctions with a clear presence of thin bundles parallel to the cell-cell interface. Localisation of phosphorylated myosin light chain to thin bundles reinforce the notion that these are the main contractile pool instead of the junctional actin at contacts. Counter-intuitively, E-cadherin and F-actin density are also reduced with increased contractility and tension. Taken together, higher levels of contractility and cortical tension imposed by the square and triangle geometric shapes, are necessary to properly generate the epithelial cellular architecture, configuration of junctions and their molecular makeup. This suggests that tensional constraints play an important role in regulating the stability of junctions and the organization of underlying actin filaments that support the characteristic epithelial cell shape.

Acknowledgments

I am immensely grateful to my supervisor, Dr Vania Braga, for her tireless supervision, encouragement, and guidance throughout my project. I truly admire her enthusiasm and dedication and thank her for always being there for me. Sincerest thanks to my co-supervisor, Prof. Molly Stevens, for being so caring, supportive of my work and providing me with great opportunities.

I deeply thank everyone in the Braga Lab for all their help, advice, the great friendships we have built and the chocolates we've shared over the years. My gratitude especially extends to Susann, Anna, and Fernanda for their kind words that motivated me to carry on. I am grateful to Jenni, Mat, Natalie, Faizah and Jess for their helpful advice all along. Thanks also to Irina and Mandy for all the things they do around the lab to keep it running smoothly. I also appreciate the support of all the members of Stevens's group who have never failed to give that warm and cheerful smile to lift me up and for caring about me. I am grateful for the helpful discussions I have had with Silvia and Thomas during the initial stages of my project. I would like to especially acknowledge, Ben and Sabrina, for all the letters they provided and forms they have filled besides everything else they do. Thank you all so much.

Heartfelt thanks to our collaborators, Steve and Debbie (FILM), Jose, Julia, Andrew, and Prof. Sean Sun. Thanks also to Georgina for opening the door to a fruitful collaboration with the Gorelik group. It was a great pleasure working with all of you. I am also grateful to the British Heart Foundation for their generous funding that allowed me to carry out this work.

Many thanks to my parents, Ammi and Thathi, you have always provided me with everything I need and I am truly fortunate to have the two of you beside me. I am also grateful to Mom and Mursal for always being so kind and generous to me. It is all your love, prayers and good wishes that kept me going.

Finally, I am grateful to Younis, without whom I could never have done it. You are truly the 'wind beneath my wings'. I thank you for inspiring me to shoot for the stars and holding my hand in sunshine and rain. I dedicate this thesis to you, with all my love.

Table of contents

List of figures

List of tables

Abbreviations

3D - Three dimensional

AFM - Atomic force microscopy

AJ - Adherens junctions

CCC - Cadherin catenin complex

EC - Extracellular cadherin

ECM - Extracellular matrix

FRAP - Fluorescence recovery after photobleaching

FRET - Förster resonance energy transfer

MDCK - Madine Darby canine kidney

RLC - Regulatory light chain

NM II - Non-muscle myosin II

NWASP - Neural Wiskott-Aldrich syndrome protein

PDMS - Polydimethylsiloxane

PMLC - Phosphorylated myosin light chain

ROCK - Rho-kinase

SEM - Scanning electron microscopy

SICM - Scanning ion conductance microscopy

CHAPTER ONE:

Introduction

1.1 Contractile networks in epithelial cells

Epithelial cells form epithelia (layers) that line cavities and surfaces throughout the body. The primary function of epithelia is to form a barrier against invasive pathogens, protect organs against physical and chemical trauma and regulate water and substances between compartments [1]. Epithelial cells play a central role in animal development and tissue regeneration. The development of cell shape and structure, culminating in the formation of tissues and organs in the body is termed morphogenesis [2]. Epithelial morphogenesis is a multi-step process, carefully coordinated through precise genetic programming and signal transduction [3]. The formation of functioning organs and body shape requires the conversion of simple two-dimensional epithelial sheets into complex three-dimensional (3D) configurations [4]. A number of cellular processes are regulated co-ordinately through contractile acto-myosinII networks to drive cell shape changes and epithelial sheet remodelling during organogenesis [5], [6].

1.1.1 Acto-myosinII cytoskeleton

In epithelial cells, nonmuscle myosin II (NMII) associates with actin producing contractile networks at distinct regions of the cortical cytoskeleton to maintain cell shape, cell motility ad tissue development. Such contractile networks are necessary to generate forces that propagate throughout the cells. At sites of cell-cell and cell-ECM adhesions these networks exist as thin bundles and stress fibres respectively. Thick contractile bundles that terminate at cell–extracellular matrix (ECM) adhesions, are known as stress fibres [17]. These are apparent at the base of epithelial cells in contact with the substratum and function to anchor and exert tension at focal adhesions through interaction with integrins [18].

Polarised epithelial cells with cell-cell contacts form a continuous circumferential acto-myosinII belt at the subapical region called the zonula adherens (ZA) to reinforce junctions [7], [8] while interactions exist between acto-myosinII and discrete adhesive clusters at the lateral region to maintain junction homeostasis [9]–[11]. In *Drosophila*, acto-myosinII meshworks (medial-apical network) also connect

cell-cell junctions at the apical region [12]. At the basal region where the cell anchors to the substrate, acto-myosinII stress fibres are formed [13]. The integrity of the cytoplasm depends on acto-myosinII contractility with the inhibition of myosinII leading to the loss of both stress fibres and circumferential actin bundles [14]. Transmission of contractile forces across the cytoskeleton takes place through lamellar networks [15] and nodular actin structures that are linked by myosin II [16].

1.1.2 F-actin cortex

Actin is the major cytoskeletal protein in most cells and form thin, flexible filaments through polymerization. Helical, polar actin filaments are constructed from globular actin (G-actin) monomers through self-assembly initiated by essential nucleation factors [26]. Nucleation drives linear actin filament polymerization [27]. Branched actin networks arise when nucleation complexes, characterized by the presence of actin-related protein (Arp2/3), binds to the sides of pre-existing filaments [28]. Elongation and shrinkage of filaments occur at either end, but polymerisation and depolymerisation are faster at the barbed end compared to the pointed. Formins are proteins that regulate actin dynamics by binding to the barbed ends and moving accordingly as elongation and shortening take place [27]. An equilibrium exists between actin monomers and filaments, as polymerisation is reversible and is dependent on the concentration of free monomers. Since G-actin monomers are present in excessive quantities within cells, filament growth is controlled through capping proteins that bind to filament ends and monomer-sequestering proteins that bind to G-actins [29]. Filament elongation occurs either through removal of the capping proteins and sequestering monomers or severing filaments into shorter fragments with free ends [26]. Repeated growth, branching and capping of actin filaments lead to branched network organisations found within the cytoskeleton [30].

The F-actin cortex exists in various structural forms bound by the plasma membrane to resist compressive forces and generate tensional forces maintaining cell shape [31]. Branched actin networks formed when the Arp2/3 complex binds to actin are typically formed at protrusions and

encounter compressive forces [32] as do bundled actin filaments linked by the bundling protein, fascin [33]. In contrast, non-aligned cortical networks involving crosslinking proteins such as filamin [34] generate tension as do bundled actin filaments associated with myosin motor proteins such as those found in stress fibres [35]. NMII, the key force generating protein, binds to F-actin enabling the stable generation of tension for dynamic cell shape changes in processes that require cellular reshaping such as adhesion, migration and division. The enhanced cross-bridging of NMII to actin filaments [36] resulting in force generation is termed contraction [37].

1.1.3 Nonmuscle myosinII

Nonmuscle myosinII (NMII) is comprised of a pair of globular head domains, a pair of heavy chains (MHCs, 200 kDa) and two pairs of light chains: essential light chains (ELCs, 17 kDa) and regulatory light chains (RLCs, 20 kDa) [38], [39] (Figure 1.1). The globular head domain contains binding sites for both adenosine triphosphate (ATP) and actin [40]. Tension arises when chemical energy of ATP is converted into mechanical movement along the actin filaments. There are three mammalian isoforms of myosin (myosin-IIA, myosin-IIB and myosin-IIC) determined by the MHC isoforms that are bound to the light chains to retain an active conformation [40]. The three isoforms are differentially expressed according to function and have differences in kinetics of ATP hydrolysis and time bound to actin [39], [41], [42]. Myosin IIa and IIb are both localised to stress fibres but the former is absent from the cell cortex [20]. Cell-cell contacts of epithelial cells contain myosin IIa and myosin IIb and their localization is dependent on the homophilic ligation of E-cadherin [21].

Regulation of NMII through ATP hydrolysis and filament formation mainly involves the reversible phosphorylation of RLCs on Ser19 or diphosphorylation at Ser19 and Thr18 [43], [44]. Phosphorylation of RLCs also unfolds inactive NMII toward an extended active conformation [45]. Diphosphorylated myosin regulatory light chains are restricted to stress fibres while monophosphorylated myosin light chain is found diffusely localised within the cytoplasm and scarcely at cell-cell contacts of epithelial cells [46]. In keratinocytes, monophosphorylated RLCs are found at thin bundles parallel to cell-cell

contacts indicating the contractile nature of this actin population [25]. The polarised epithelial cell shape with full elongation of the lateral domain is sustained through the stability and increased contractility of thin bundles [23]–[25]

RLC phosphorylation can occur through many kinases including myosin light chain kinase (MLCK), Rho-kinase (ROCK) and citron kinase to name but a few. MLCK is activate by calmodulin [47] while the small GTPase, RhoA, activates the later kinases. ROCK can either directly phosphorylate RLCs or indirectly phosphorylate it through the inhibition of myosin phosphatase, protein phosphatase 1 (PP1), which dephosphorylates NMII [48], [49]. ROCK also promotes inhibition of cofilin, an actin depolymerising protein and stabilises filaments via the phosphorylation of actin-binding kinases that bind and inactivate cofilin [50]. Additionally, Rho can bind to and activate the actin nucleation factor, mDia which is able to form stress fibres [51]. ROCK induces and maintains stress fibres via RLC phosphorylation in concert with mDia leading to increased contractility [52] and activation of LIM kinases, which inhibit cofilin and stabilize actin filaments [50].

1.1.4 Epithelial remodelling driven by contraction

Epithelial folding during morphogenesis is characterised by apical constriction, the shrinkage of cell apices, which is induced by the polarised contraction of the acto-myosinII belt in the ZA [53]. Neural plate bending in mammalian vertebrate embryos is driven by the ZA acto-myosinII contractions towards the mediolateral axis [54]. Shroom 3, a protein concentrated along the apical junctional complex in epithelial cells, is responsible for recruiting ROCK to the ZA and supporting contraction of the circumferential acto-myosinII belt [55].

In contrast, invertebrate *D. melanogaster* embryos undergo apical constriction during the developmental processes of gastrulation, dorsal closure and germband extension through pulsed acto-myosinII contractions at the apical cortex rather than directly at junctions [57], [58]. Similarly in *C. elegans*, cortical acto-myosinII contractions precede junction contraction and later coordinate in the two regions [59].

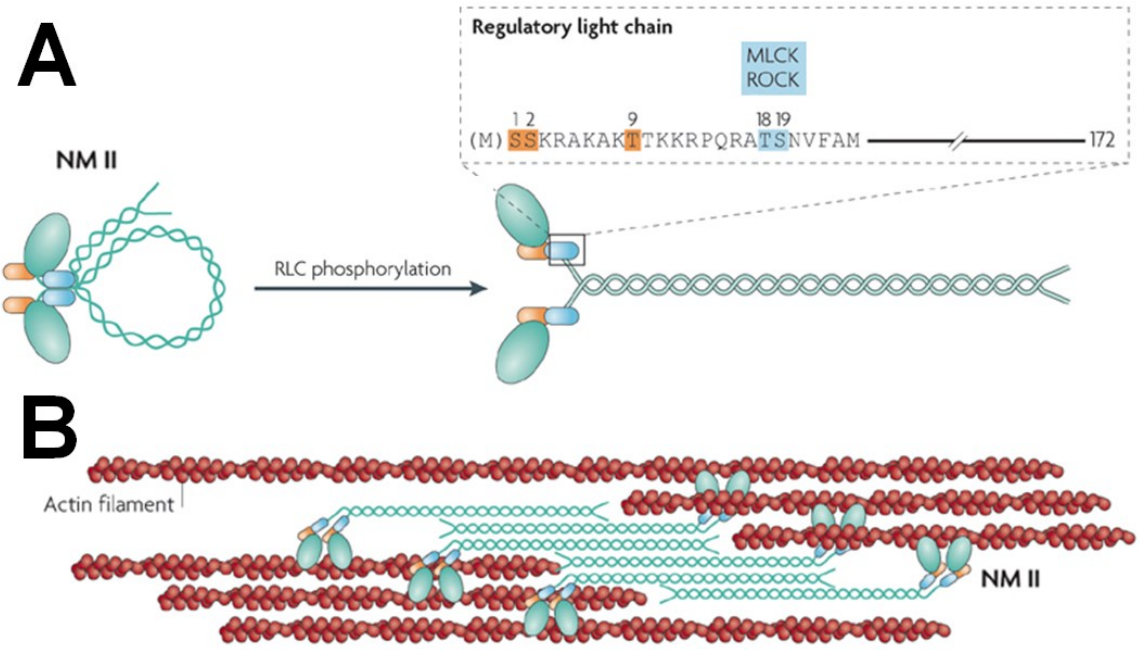

Figure 1.1: Non-muscle myosin II (NMII) and crosslinking with actin. (A) Incompetent NMII structure (left) unfolds upon phosphorylation of regulatory light chains (RLCs) to a linear competent form (right) showing site of action of kinases, MLCK and ROCK. (B) Crosslinking of actin filaments by attaching to the head domains of NMII to enable anti-parallel movements that generate acto-myosinII contractility. Images adapted from [56].

The radial acto-mysoinII fibers in the cell cortex join junctions through a supracellular tensile meshwork of acto-myosinII that are able to transmit forces to the tissue level [60]. The integration of contractile forces to maintain tension across tissues requires stabilization of apical myosinII through the transcription factor Twist. The underlying mechanism connecting cortical acto-myosin-II to that of the junctions involves Canoe, *D. melanogaster*'s homologue to mamallian afadin, a protein essential for adhesion and polarity establishment at junctions [61], [62]. Furthermore, recent evidence shows that Coronin mediates reorganisation of the actin architecture at the junctions into an aligned network that can generate force and sustain contractile events that necessitate morphogenesis [63], [64].

1.2 Cell-cell adhesions

Communication between neighbouring cells is a fundamental requirement for the formation of specialised tissues within the body [65]. During epithelial cell-cell contact formation, specific

membrane bound proteins localise to the intercellular regions, the cytoskeleton rearranges to dictate cellular architecture and cellular organelles re-distribute in order to create the polarised epithelial phenotype [66]. Four structurally and functionally unique types of intercellular contacts exist between epithelial cells, each with specific spatial locations on the apical-basolateral domain. Tight junctions are the most apical of the cell-cell contacts and claudins are their main transmembrane protein [67]. Tight junctions form a semi-permeable barrier system between neighbouring cells that can be modulated through signalling [68]. Adherens junctions (AJs) lie beneath tight junctions and both adhesive structures are connected to cytoskeletal actin filaments [69] (Figure 1.2). In contrast, desmosomes are connected to intermediate filaments through desmosomal cadherins and provide mechanical strength to junctions [70]. Desmosomes and Gap junctions are subsequently positioned close to the basal domain [71].

1.2.1 Adherens junctions: cadherins, catenins and actin filaments

Adherens junctions physically link neighbouring cells together and play a key role in morphogenesis and the maintenance of cell and tissue architecture [65], [72]–[74]. AJs are primarily composed of classical cadherins: transmembrane glycoproteins that interact with cadherins of neighbouring cells through calcium dependent homophilic interactions [75]. Classical cadherins exhibit a preserved cytoplasmic domain that can interact with catenins and elicit properties that are unique to AJs [76]. Epithelial cells contain two of the type I classical cadherins, E-cadherin (epithelial cadherin) and P-cadherin (placental cadherin) [77], [78]. Both cadherins are found at AJs of stratified epithelia but unlike E-cadherin that is expressed in all layers, expression of P-cadherin is limited to the basal layer and demonstrates weaker anchorage to the actin cytoskeleton [79]–[81]. In addition, other adhesive receptors such as nectins can localise to epithelial junctions during junction formation. Nectins are responsible for bringing neighbouring membranes together into close proximity and specifying basolateral adhesion sites such that cells can engage in the formation of adherens junctions [82], [83].

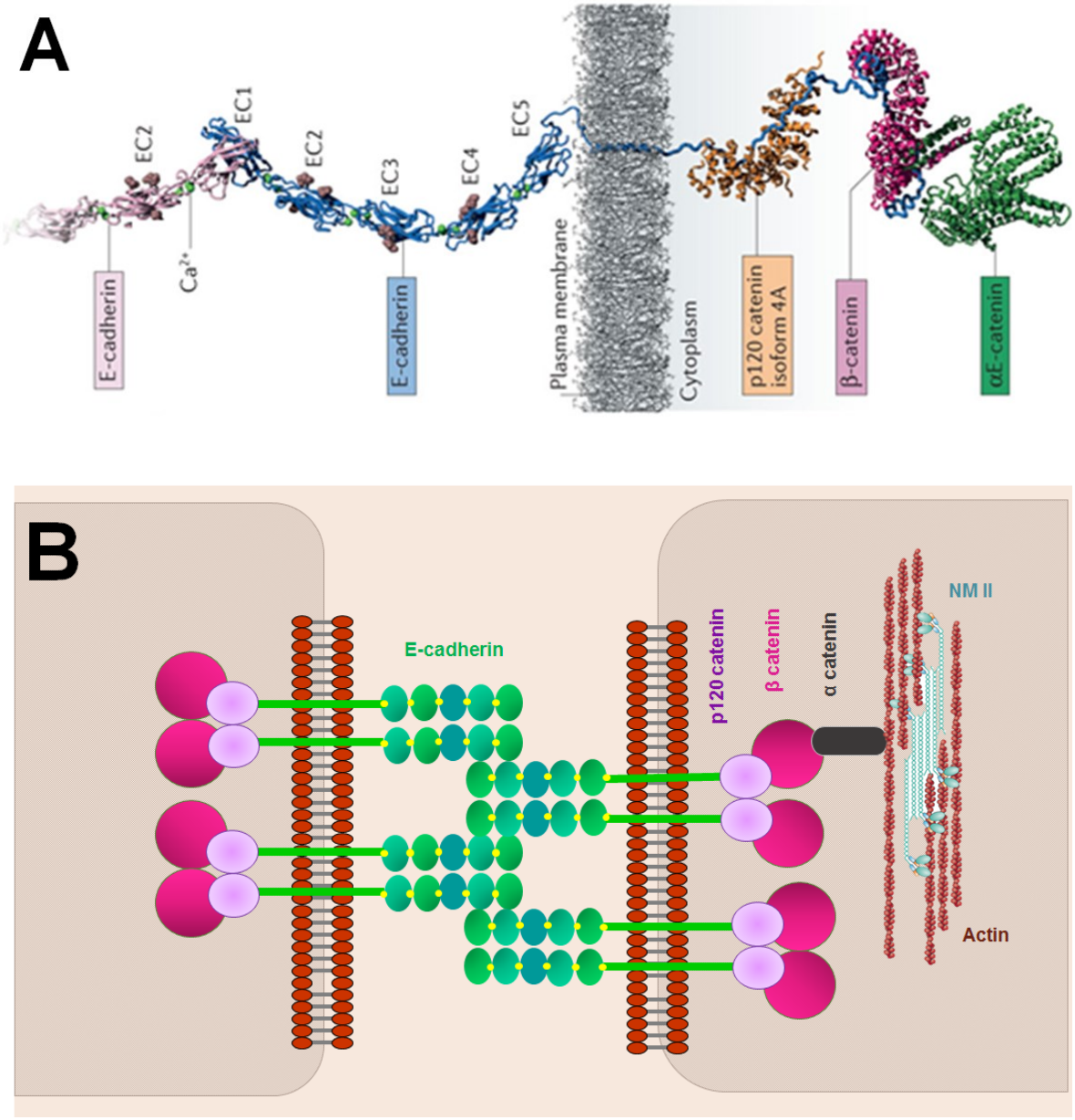

Figure 1.2: **Composition of adherence junctions in epithelia.** (A) Homophilic trans-binding of E-cadherin molecules [84] and (B) connection to the underlying acto-myosinII cytoskeleton through the catenins.

The ectodomains (extending in to the extracellular space) of classical cadherins contain repeats called 'extracellular cadherin' (EC) domains [85], [86]. The presence of calcium ions serves to rigidify and linearise cadherin homodimers (*cis*-dimers) [87] necessary to permit adhesiveness between neighbouring cells (*tran*-dimers) [88]. Cadherins have a conserved cytoplasmic tail with binding sites for catenins [89]. p120 catenin and β-catenin bind directly to E-cadherin at the juxtamembrane region

and C-terminus respectively of the cytoplasmic tail [90] followed by α-catenin to form the cadherin-catenin complex (CCC). The CCC mediates the attachment of cadherins with the actin cytoskeleton [91]. α-catenin is the main force involved in firmly 'zipping up' membranes [92], [93] but is unable to binds to F-actin directly through its carboxy-terminal domain when committed to the CCC [94]. α-catenin indirectly interacts with F-actin through Vinculin, an actin binding protein, through its M1 domain [95]. Binding to Vinculin is only permitted under tension which unmasks the M1 domain indicating the role of α-catenin in tension sensing [96].

Beyond its role in maintaining structural integrity, the CCC is a signalling hub that modulates intracellular processes in response to external cues [97]. Cadherins themselves are able to initiate cellular signalling events upon interaction with neighbours [98]. Regulation of cell-cell adhesion is mediated by the cadherin-catenin complex through localised phosphorylation events [99], recruitment of kinases [100] and signalling from GTPases [97], [101].

1.2.2 Adherens junction formation and the Zonula Adherens

Cell-cell contacts initiate when membrane protrusions of adjacent cells collide together [102], [103]. These protrusions contain surface cadherin receptors and can be either lamella (broad extensions of membrane enriched with branched filament networks) or filopodia (finger-like protrusions enriched in thick parallel F-actin bundles) [103]. These protrusions promote the interaction of E-cadherin and their clustering. Cadherin puncta form as *trans*-interaction occurs and accumulated α-catenin binds to F-actin [104]. F-actin recruitment to the vicinity of cell-cell adhesions is triggered by the homophilic ligation of cadherins in neighbouring cells [105]–[107]. Actin nucleation and polymerisation occur at adhesion sites where cadherins actively participate in F-actin remodelling [103], [108], [109]. Extension of newly formed contacts is mediated by α-catenin through actin cables via the inhibition of Arp2/3 mediated actin nucleation into branched networks [110]. This process could happen either directly through α-catenin binding of F-actin [111] or indirectly through proteins such as Formin-1 which promote actin cable assembly regulated by α-catenin [112].

In mature epithelial sheets, linear actin bundles run parallel to the cell borders forming a circumferential actin belt. These belts encircle individual cells that are engaged in cell-cell adhesion at their apical regions [113]. The region of cells where the adherens junctions contain these belts are termed the 'zonula adherens'.

1.2.3 F-actin at adherens junctions

F-actin provides structural integrity to the adherens junctions and are central to maintaining accurate junctional architecture. Two distinct pools of F-actin are associated with AJs: Junctional actin, which co-localises with clustered cadherin complexes, and circumferential thin bundles directly adjacent to the cadherin-complex [25], [114]. Junctional actin stabilises adhesive complexes but is non-contractile [25]. In contrast, thin bundles are contractile and participate in regulation of optimal lateral cell height [25]. The two populations have discrete dynamic properties as demonstrated by fluorescent recovery after photobleaching (FRAP) [109], [115] and fluorescence G-actin incorporation [116]. Recruitment of E-cadherin, their clustering and immobilization is modulated through mechanosensitive actin dynamics driven by myosin [117] and stabilization of E-cadherin emanates from the actin populations [118]. Actin additionally promotes strengthening of junctions through cadherin-dependent *cis*-interactions in the EC domain [119], [120]. Although actin at junctions have been implicated in many studies, the two distinct populations and their specific contributions to such events have not been differentiated.

Coupling of cadherins with the cytoskeleton enables mechanotransduction that drives morphogenetic processes such as apical constriction in gastrulating embryos [57] and cell intercalation during *Drosophila* germband extension [121] facilitated by actomyosin contraction. Transmission of tensional forces at cell-cell adhesions also relies on the cadherin-actin coupling enabling lengthening and strengthening of cell-cell contacts in response to increased forces [122]–[124]. The separation force of E-cadherin expressing paired cells, measured using a dual pipette assay, increases with the duration of contact and with cadherin levels to reach a maximum of 200 nanonewtons at 30 minutes [125].

Adhesion strengthening is heavily dependent on the actin cytoplasmic cadherin complex [125]. E-cadherin tension sensors that link the cytoskeleton through α-catenin have highlighted that E-cadherin is under actomyosin-generated tension [126] and is involved in direction sensing during essential cellular processes [127].

Recent insights suggest that α-catenin is a key elements of cadherin-based mechanotransduction [128], [129]. Increase in cell contractility, promotes vinculin recruitment to actin-anchored adhesions as displayed by E-cadherin-coated magnetic beads on confluent monolayers [122]. Vinculin binds to α-catenin upon force-induced release of the vinculin-binding site and promotes recruitment of filamentous actin to strengthen AJs as previously mentioned in section 1.2.2 [96], [130], [131]. Epithelial protein lost in neoplasma (EPLIN), a protein that can crosslink actin filaments, binds to α-catenin depending on actomyosin contractility [132], suggesting that mechanosensing is a key trigger for molecular interactions and cytoskeleton rearrangements.

Epithelial cytoskeleton remodelling events have been extensively studied with respect to actin dynamics that regulate actin polymerization and actomyosin contraction [84]. Much is known about F-actin recruitment to form junctional actin [102], [104], but how thin bundle compaction and regulation during junction formation is largely unknown.

1.2.4 Recycling of cadherins

Levels of cadherin at AJs are dependent on the fine balance between cadherin removal by endocytosis and degradation and cadherin replenishment by synthesis and recycling. The long metabolic half-life of cadherins means that transcriptional regulation alone cannot account for the rapid dynamic changes at cell adhesions [133], [134]. Therefore adhesion strength is mainly determined by endocytosis, degradation and recycling. Cadherin internalization occurs either through clathrin-mediated endocytosis [135], [136] or clathrin independent endocytic pathways which include caveolin-mediated [137], [138] and macropinocytosis-like pathways [139]. From the cadherin that

enter the endocytic pathways, some are recycled back to the plasma membrane through recycling pathways [136], [140], [141].

Catenins, the cytoplasmic binding partners of cadherins which secure them to the actin cytoskeleton have been implicated to play a major role in the regulation of cadherin junction dynamics. p120-catenin stabilises cell-cell adhesions upon E-cadherin ligation preventing cadherin endocytosis and subsequent degradation [142], [143]. Regulation of cadherin turnover through p120-catenin is facilitated by clathrin-dependent endocytosis [144], [145]. Interestingly, as an inhibitor of the RhoGTPase RhoA, p120-catenin could also regulate cadherin turnover through the local regulation of actin dynamics [146]. β-catenin, further along the CCC, is also associated with cadherin trafficking although its precise role is less well understood [147]–[149].

The involvement of catenins in cadherin turnover implicates that adherens junction architecture, more precisely the link to the actin cytoskeleton, plays a vital role in junction dynamics. In line with this, E-cadherin turnover is a mechanosensitive process and becomes faster as tension at the junction increases [150]. Actomyosin-II contractility regulates cadherin adhesions such that increased cortical tension results in a reduction of actin turnover to reduce the mobility of cadherin molecules and increase their junctional concentration [151].

1.2.5 Regulation of cell-cell adhesions by RhoGTPases

Rho GTPases are key regulators of cell-cell adhesions apart from their modulation of the F-actin cytoskeleton [17], [152]. At tight junctions, Rho modulates apical thin bundle organization of polarized intestinal epithelial cells [153]. Inhibition of Rho leads to the loss of the circumferential actin rings without perturbation of E-cadherin localisation at the junctions. However, other studies report contradictory findings that Rho inhibition leads to decreased levels of E-cadherin at junctions and perturbation of morphological features of MDCK cells [154], [155]. Particularly in keratinocytes, E-cadherin-mediated adhesions fail to form in the absence of endogenous Rho while inhibition of Rac

leads to loss of E-cadherin at newly-formed junctions [105]. Rho is essential for cell-cell adhesions and interference with Rho signalling leads to skin diseases such as blistering [156].

The formation of E-cadherin mediated intercellular junctions relies on the interplay between different Rho GTPases [157]. Rac but not Rho is needed for actin recruitment to E-cadherin clusters [105]. In *Droshophila*, Rac is necessary for actin recruitment to adherens junctions independent of E-cadherin and β-catenin localisation, while Cdc42 is a critical regulator of the actin cytoskeleton and maintenance of the polarised cell shape [158]. Active forms of both Rho and Rac have differential localisation at adherens junctions of mice epidermis *in vivo*. Rac co-localises with its effector Arp2/3 at lamellopodia during initiation of contacts [159], whereas Rho activity predominates at contact edges as it is involved in contact expansion [17] in MDCK cells. Activation of the Rho effector, ROCK and myosin-dependent contraction disrupts adherens junctions [160]. Apart from adhesion initiation, actin cytoskeletal remodelling during adhesion strengthening is facilitated by Rac and Cdc42 [125]. ROCK is equally important to the localisation of E-cadherin at intercellular surfaces as well as actin bundle organisations and establishment of the polarised cell shape [116], [161]. Evidence suggests that myosin II, a target of ROCK, is necessary for accumulation of E-cadherin receptors at intercellular regions to facilitate cell-cell cohesion [21]. ROCK facilitates actomyosin contraction by phosphorylation of myosin light chain (MLC) and MLC phosphatase which in turn phosphorylates MLC [49]. Although inhibition of ROCK with the Y27632 compound does not disrupt junctions, junctions lose their appearance and look rather jagged and discontinuous [162], [163]. Conversely, constitutive activation of ROCK disrupts junctions [164] by pulling peripheral actomyosin filaments perpendicularly thereby interrupting AJ formation [84].

The stability of actin filaments at AJs is highly modulated by Rho GTPases and their effectors [84]. The Rac effector complex, WAVE2-Arp2/3, mediates junctional actin nucleation necessary for junctional integrity and contractility by facilitating the recruitment of myosin IIa and IIb to junctions [165], [166]. However, Arp2/3 is also involved in the actin-mediated endocytosis of junctional components

downstream of Cdc42 [167]. The Cdc42 effector, Neural Wiskott-Aldrich syndrome protein (NWASP), facilitates the incorporation of actin filaments into apical rings and stabilises newly formed contacts [168]. The depletion of NWASP or Tuba, an activator of Cdc42, perturbs assembly of junctional actin leading to altered junctional configurations [169]. [170]. The perijunctional actin belt formed is decorated with the three isoforms of non-muscle myosin (IIa, IIb and IIc) and elicit the contractile behaviour necessary to maintain stable mature junctions as well as to dynamically remodel junctions [171].

Rho is particularly important in the modulation of actomyosin thin bundles and inhibition causes junction disruption [97], [172]. The Rho effector, diaphanous homologue 1 (Dia1), a member of the formin family, promotes actin polymerisation and accumulation at junctions [173]. Additionally, Dia1 coordinates adhesion and contractility of the actomyosin bundles through effects on myosin activity [174]. Formin1 is also critical to the formation of radial actin cables at cadherin puncta indicating that formins are key proteins in promoting junctional stability [175], [176]. Rho also plays a role in the suppression of cadherin internalization [177]. Thus, specific RhoGTPases should be well coordinated with precisely balanced activities of their effectors to ensure stability of AJs.

1.3 Cell-matrix adhesions

Attachment to the ECM functions as a signalling platform for epithelia to regulate migration, differentiation and proliferation [178]. Adhesion to the ECM additionally plays a pivotal role in maintaining the mechanical integrity of tissue by regulating the level of intra-cellular contraction [179] and transmitting long-range mechanical forces across cells through its linkage to the actin cytoskeleton [180].

Epithelial cells attach to the extracellular matrix through two types of cell-ECM adhesions at discrete locations on the basal surface: hemidesmosomes and focal adhesions [181]. Integrins are transmembrane proteins composed of distinct combinations of α and β subunits expressed according to the type of extracellular matrix ligand they bind to. Extracellular matrix proteins include fibronectin, laminin and collagens. Hemidesmosomes firmly anchor the cells to the extracellular matrix through the bullous pemphigoid antigen 180 (PB180), α6β4 integrins and tetraspanin CD151 binding mainly to laminin-332 [182]. The cytoplasmic side of the hemidesmosome is associated with intracellular proteins, BP230 and plectin, and attach the intermediate filament keratins and provides structural rigidity to cells [183]. Focal adhesions of basal keratinocytes comprise of different types of integrins of which α2β1 and α3β1 predominate and anchor to Collagen IV through interactions with laminin-332 [184]. Additionally, α5 integrins are expressed in the presence of fibronectin [185]. Integrins are regulated by a range of adapter proteins including actin-binding proteins, kinases and membrane-binding proteins [186].

1.3.1 Stress fibre formation and maturation

Stress fibres are composed of approximately 10-30 actin filaments forming overlapping bundles [187] that are held together by the actin crosslinking proteins, mainly α-actinin [188] but also others including fascin [189] and filamin [190]. Stress fibres exist in three different forms based on their attachment to adhesions and cellular localisation [191]. Ventral stress fibres are the most common type and attach to focal adhesions at each end, dorsal stress fibres also attach to focal adhesions but

only at one end and transverse arcs do not attached at all and lie away from the base toward the lamella of the cell unlike the former structures. Stress fibres assemble via distinct mechanisms; dorsal stress fibres form through actin polymerisation at focal adhesions driven by formins while transverse arcs are formed by combining myosin bundles and Arp2/3-nucleated actin bundles [192]. Both of these stress fibres can join to form the ventral stress fibres which are tethered at both ends to adhesions.

Binding of stress fibres to focal adhesions occur at the β1 and α5 subunits of integrins [193] through a variety of adapter proteins such as α-actinin, vinculin, talin, paxilin and focal adhesion kinase [194]. Maturation of nascent adhesions through growth and elongation occurs along an α-actinin-actin template and requires the activity of NMII [195], [196]. NMII may mediate adhesion maturation via two methods. First, its function as an actin bundling protein triggers integrin clustering that increases interactions with adhesion proteins in response to actomyosin-generated tension [194], [197]. Vinculin induces focal adhesion assembly by directly interacting with talin at its head and actomyosinII at its tail [198]. Second, NMII-generated mechanotransduction forces cause conformational changes that expose binding sites of adhesion molecules such as talin and lead to their activation upon tension sensing [199], [200].

1.3.2 Regulation of cell-matrix adhesion by Rho GTPases

The best-characterised Rho GTPases are RhoA, Rac1 and Cdc42. They exert their effects on different actin based structures and heavily regulate the actin cytoskeleton [201]–[204]. RhoA induces the formation of stress fibres and focal adhesions in fibroblasts [205], Rac1 drives lamellipodia [206] and membrane protrusions while Cdc42 is involved in filapodia formation [207] highlighting the distinct actin structures regulated by the activity of the three GTPases [208]. GTPase effectors such as Rho-kinase (ROCK), p21-activated kinase (PAK) and myotonin-related Cdc42-binding kinase (MRCK) among others are involved in regulation of cytoskeletal contraction [209]. Here, we will focus on ROCK, a downstream target of Rho, as the best understood regulator.

Stress fibre (SF) formation within the cytoplasm is activated by Rho through various pathways. First, formation is induced through the inherent cell tension upon Rho-dependent activation of myosin II and actomyosin contractility [210] (Figure 1.4). When activated Rho binds and activates its effector protein, ROCK, actomyosin contraction can occur in one of two ways. ROCK can either directly phosphorylate the light chain of myosin II or indirectly phosphorylate it through myosin light chain phosphatase [48], [49]. Secondly, ROCK promotes inhibition of cofilin, an actin depolymerising protein. ROCK stabilises filaments via the phosphorylation of actin-binding kinases that bind and inactivate cofilin [50]. Thirdly, Rho can bind to and activate the actin nucleation factor, mDia which is able to form stress fibres [51]. ROCK induces and maintains stress fibres via MLC phosphorylation in concert with mDia leading to increased contractility [52] and activation of LIM kinases, which inhibit cofilin and stabilize actin filaments [50].

ROCK exists as two distinct genes: ROCK1 and ROCK2 [211]. ROCKs mediate a plethora of cellular functions including contraction, polarity, morphology, cell division and gene expression [212]. Both ROCKs are critical regulators of contractility and contribute to cell elongation during polarization and maintenance of geometric shape in epithelia [116]. ROCK1 has been implicated in the control of epithelial polarity by directing basement membrane positioning through interactions with the PAR complex [213], [214]. ROCK2 is involved in the reorganization of the cytoskeleton during motility, cytokinesis and adhesion formation [201], [215]. ROCK2 is essential to the formation of focal adhesions and stress fibres through contractility-dependent activation of integrin clustering [216].

ROCK1 and ROCK2 regulate distinct aspects of contraction but are equally important for SF formation. Knockdown of ROCK1 results in the loss of SFs and focal adhesions. ROCK2 regulates microfilament bundles and focal adhesion sites [217]. ROCK2 deficient mice exhibit retarded intrauterine growth with 90% of foetal deaths, although, the labyrinth layer of their placenta displayed intact actin filaments and SFs, indicating that ROCK1 cannot compensate for ROCK2 [218]. SF disruption though RhoE mediated inhibition of ROCK1 could also not be rescued through ROCK2 [219].

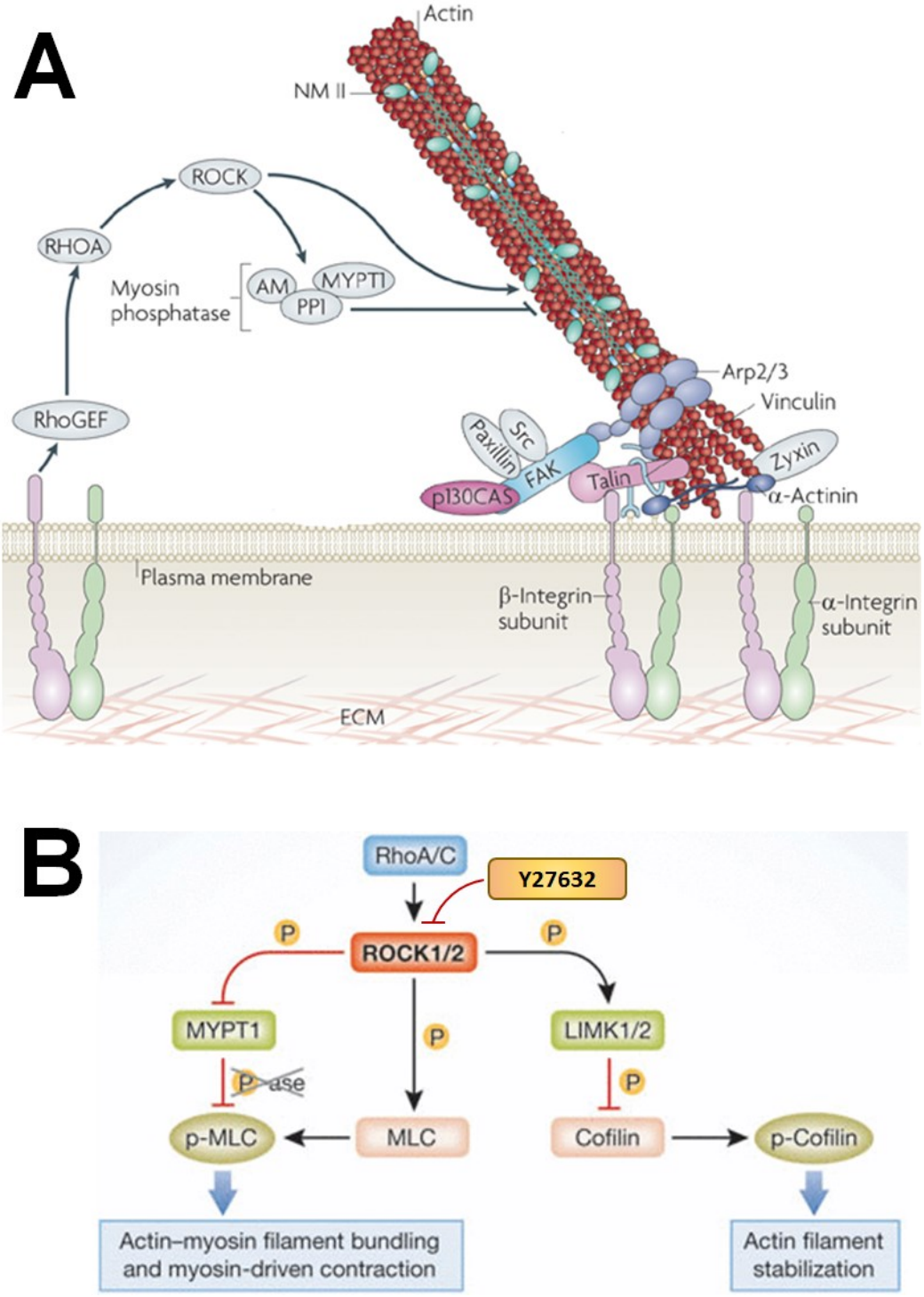

Figure 1.3: **Focal adhesion and stress fibre formation through ROCK.** (A) Integrin mediated attachment to stress fibres via the activation of Rho and its effecter ROCK that phosphorylates myosin II (NMII) directly or through myosin phosphatase. Image adapted from [56]. Summary of effects of ROCK1/2 on actin dynamics and point of inhibition by Y27632 treatment. Image modified from [220].

1.4 Interplay between cell-cell and cell-matrix adhesions

Cell adhesion is fundamental to tissue architecture: cell-cell and cell-ECM adhesions determine the cytoskeletal organisation and shape of individual cells constituting tissues and thereby define their distinct functions [65]. Cellular function is governed by the structure of cells and its intricate link with extracellular matrix mechanics and cytoskeletal tension [221]. Each cell has unique viscoelastic properties determined largely by the cytoskeleton, cell membrane and the extracellular matrix [222]. Among other processes, the ECM regulates cell and tissue morphogenesis by rearranging and coordinating mechanical stresses through alterations to the intracellular cytoskeletal organization [223]. Attachment to the ECM guides the assembly of actomyosin networks upon cell adhesion to extracellular ligands [224]. The localised cytoskeletal orientation at the base of cells escorts the construction of cell internal architecture as cells are in a tensional equilibrium physically connected and mechanically supported within the intracellular space [225].

Crosstalk between cell adhesion is important to the maintenance of tensional integrity and regulate many aspects of cell behaviour including proliferation, differentiation and migration [226], [227]. It is particularly important during regenerative processes such as wound healing which relies on the dynamic remodelling of cell adhesions [84]. Cellular biomechanical properties are strongly dependent on the interactions between the microenvironment consisting of the extracellular matrix and neighbouring cells and the integrity of the cytoskeleton in coupling the two interactions [228]. Cell-cell and cell-ECM adhesions are intricately engaged in a crosstalk between integrins and cadherins to modulate cellular functions [229]. Integrin-dependent actomyosin contractility modulates tension at E-cadherin mediated intercellular adhesions [230]–[232]. In addition, engagement of integrins with the ECM promotes myosin II activity and reinforcement of cadherin-based junctions through Src-kinase activation [230].

Cadherin-based junctions are equally important to integrin-based adhesions as traction forces increase in the presence of E-cadherin mediated cell-cell contacts and mechanical coupling between

cells [233] while strong cell-cell adhesion in colonies lead to peripheral localisations of traction forces [234]. The cadherin-activated Src-PI3K pathway stimulates traction forces arising from cell-ECM adhesions [231]. Perturbation of mechanotransduction at cell-cell adhesions results in integrin-mediated stiffening of cells through vinculin, a shared component of the force-transducing machinery at both adhesions [235]. Taken together, cell-cell and cell-matrix adhesions are intimately coupled with each other and favour spatial segregation in order to minimize intra- and inter-cellular forces [228], [236], [237].

1.4.1 Mechanosensing at the cell-cell and cell-ECM interface

Vinculin is a common to both cell-cell and cell-ECM adhesions and plays a role in bridging the adhesive elements with the contractile network within cells. Although biosensors based on Förster resonance energy transfer (FRET) have been developed for vinculin [238], [239], these have only been applied to mechanical stress sensing at the cell-ECM interface.

The ability of cells to sense and respond to mechanical stimuli originating from the ECM relies on integration and coordination of the outside with the inside of cells. Integrin-mediated complexes act as mechanosensors that transform externally applied forces to changes in cellular phenotype [240]. Focal adhesion stability and maturation is triggered by substrate stiffness which affect the actomyosin generated tensile properties of the cell and activate phosphorylation of protein kinases indicating that cells are able to sense their microenvironment and respond accordingly [241]. The ECM modulates cell shape and cytoskeletal tension through phosphorylation of myosin light chain kinase and actomyosin contractility [179]. Stiffness is perceived by cells at adhesion points by generating traction forces that contract the ECM. The strength of integrin-cytoskeletal linkages is dependent on matrix rigidity and biochemical composition [242] and is precisely the reason that cell spreading is perturbed in substrates that lack appropriate levels of matrix elasticity [243].

1.4.2 Cross-talk during cellular processes

Communication between different types of adhesion is essential to the integration of cellular forces not only during morphogenesis but also in the maintenance of normal physiology. Powered by NM II, the remodelling of the actin cytoskeleton leads to variations in cell tension and traction [244], [245]. For example, during Xenopus embryogenesis, cadherin adhesion signalling translates into actin reorganisation, myosin contractility and tissue tension which guides fibrillar matrix assembly [246]. Similarly, during wound healing, actomyosin cables connected to catenins in adherens junctions mechanically couple regions within the cell as well as neighbouring cells for coordinated movement along the wound axis [247], [248]. RhoA and ROCK mediate the contraction required during collective migration towards the wound [249], [250]. Tissue repair has been considered analogous in many ways to dorsal closure during embryonic morphogenesis which also requires RhoA [251], [252]. Although the activation of RhoA at cell-cell adhesions has been characterised for each of these events, the link to cell-matrix adhesions has not been made. It has been proposed that while RhoA activation has similar effects at individual adhesions, the activation of one type of adhesion is negatively correlated to the other giving rise to their spatial segregation [228], [236].

Integration of cellular forces across tissues, specifically epithelia, requires three fundamental criteria to be satisfied [253]. Firstly, the attachment between neighbours through cadherin-dependent adherens junctions is key to transmitting forces [254], [255]. Secondly, an intact cytoskeletal myosin meshwork within the cells to sustain forces forces [60]. And finally, coupling between adhesions and the contractile actomyosin-II cytoskeleton within individual cells to generate the forces necessary for cellular events.

1.5 Technical tools to investigate cortical tension

Micropatterning techniques were originally used in the late 1960's to manipulate cell adhesion but its use in cell biology settings were limited due to the use of complex and inaccessible material [256], [257]. Among the micropatterning techniques available, microcontact printing (μCP), originally developed by the Whitesides group [258], has emerged as the most popular and widely used [259]. μCP can be readily used in cell biology laboratories through the initial fabrication of photoresist masters with desired micropatterns or possession of masters or adhesive micropatterned chips that are commercially available. Briefly, μCP involves the use of an elastomeric stamp to print ECM protein patterns with micro-features onto culture substrates, whose unpatterned regions are rendered non-adhesive (Figure 1.5) [260].

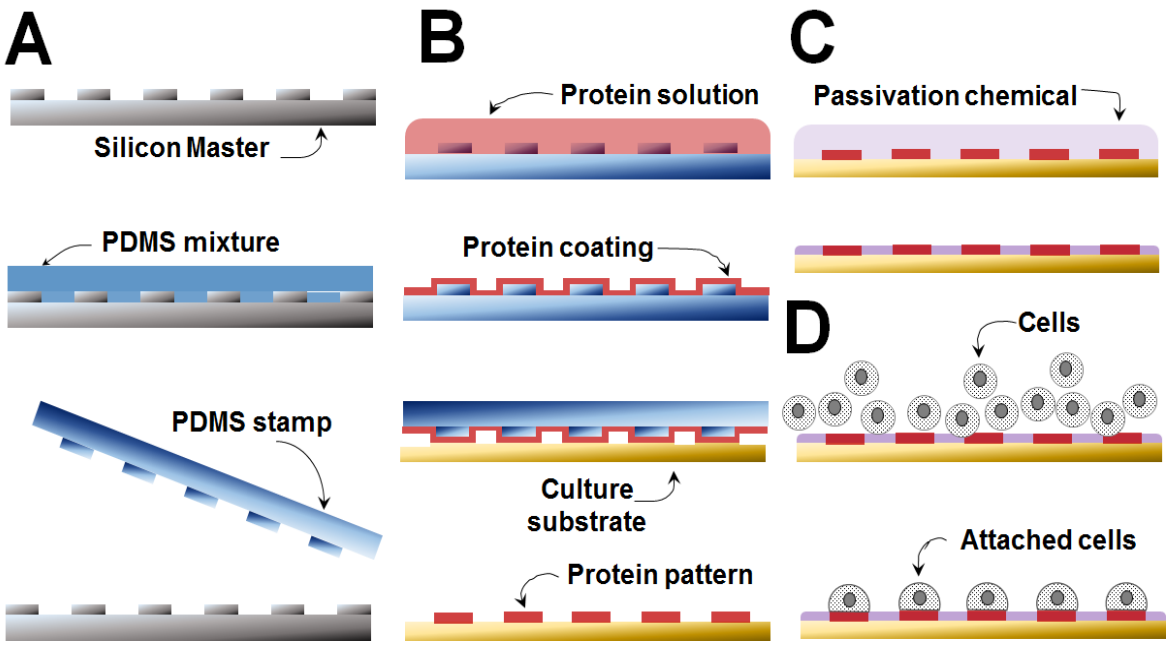

Figure 1.4: Schematic of microcontact printing procedure. (A) Replica casting of PDMS using the silicon master and curing of PDMS overnight to 60°C overnight to produce an elastomeric stamp with micropatterns. (B) Production of protein patterns on substrate surfaces by incubating stamps with the protein for 1 hour at room temperature, blowing the stamp dry and gently printing onto the substrate. (C) Passivation of non-patterned areas to avoid cell attachment. (D) Production of cellular micropatterns by seeding cells and allowing for attachment for 2 hours before changing the medium and leaving overnight for optimal spreading.

Culturing cells on unrestricted surfaces leads to the loss of reproducible cytoskeletal architecture as they provide homogenous, rigid, and uncontrolled adhesive possibilities. The study of cell mechanics and tensional equilibrium is compromised in such conditions due to the permanent disassembly and assembly of adhesions preventing the formation of steady-state structures [261]. In contrast, the confinement of cells within micropatterns imposes a stable and reproducible shape that can be used to precisely manipulate cytoskeletal architecture and mechanics [262]–[264].

Studies on micropatterns have addressed many processes that are crucial to tissue morphogenesis [265]. Intracellular assembly of cytoskeletal structures and orientation of polarity within single cells [266]–[268], and cell groups [269], [270] have been extensively studied. Polarity-driven cell migration has been studied on micropatterned surfaces for individual cells [271]–[274] and cell cohorts [275], [276]. Cell division has been studied in single cells to define the orientation of the division axis [277][278] and cell doublets to relate cell shape and division [279] as well as DNA segregation [280]. Studies of cell growth carried out on individual epidermal keratinocytes revealed that spatial confinement reduces cell growth [281] and can even lead to apoptosis in the case of endothelial cells [282]. Spreading, however, promotes cell growth [283], [284].

Differentiation is yet another area that has extensively utilised micropatterning as a tool to study shape-related behaviours of stem cells. Individual mesenchymal stem cell lineage is dependent on the level of contraction [285]. Keratinocyte differentiation on micropatterns is induced by reduced spreading [281] and presence of cell-cell contacts [286]. Thus illustrating that micropatterning is a powerful tool to address specific contributions of biophysical parameters to morphogenesis.

Micropatterning techniques allow for the recapitulation of *in vivo* cell microenvironments by imposing defined cell adhesion patterns with microscopic features similar to those encountered within tissues. Restricting the size and geometry of substrate regions to which cells attach to limits cell spreading and dictates the orientation of cytoskeletal fibres.

Single adhesive islands of micrometre scale have been utilised to study a myriad of cellular functions. When individual cells adhere to isolated micropatterned regions, focal adhesions mediate cell anchorage by physically coupling the ECM to the contractile actin cytoskeleton [287], [288]. Focal adhesions assemble asymmetrically at locations of highest tensional stress through cytoskeletal feedback mechanisms that direct their localisation [289]. The quantity, size and organization of focal adhesions is governed by cellular contractility that can be altered by the spreading and geometry imposed by micrpatterned islands. Increase in cell spreading preferentially promotes actin filament alignment due to tension moulding within the actin lattice and actin bundles align with the straight edges of the geometry [290]. Above a critical length of spreading, the formation of stress fibres triggers the growth and maturation of focal adhesions [291] and in turn promote the formation of lamellopodia and other membrane protrusions [263]. As spreading increases, larger focal adhesions accumulate and more stress fibres form, increasing the amount of traction forces exerted on the substrates by cells [292]. Tensional homeostasis is achieved as individual cells regulate these traction forces through feedback mechanisms [293], [294]. Individual, isolated adhesive micropatterned regions have studied the effect of cytoskeletal contractility on single cells as well as cell pairs and multicellular groups with the capacity for intercellular communication. The level of contractility imposed by different geometries depends on the spread area and the convexity of the cell edges and the number of apices [268], [295].

The four main types of microscopy techniques to detect intricate cell surface structures include optical microscopy, scanning electron microscopy (SEM), atomic force microscopy (AFM) and scanning ion conductance microscopy (SICM). Of these, SICM provides an attractive possibility to study the structural characteristics of cells as well as their mechanical properties due to its precedence over classical microscopy techniques as a non-contact live imaging modality [296].

Optical methods are hardly capable of reaching resolutions below 100 nm due to light diffraction limits and cannot directly image cell surfaces [297], [298]. These methods additionally pose the harmful

effects of prolonged light exposure to cells causing photo-toxicity and photo-bleaching in the case of fluorescence [299]. SEM has the capacity to image samples with resolutions between 0.5 and 10 nm, but cell surface probing requires samples to be dehydrated, fixed and stained with heavy chemicals thereby altering the morphology of cells and making cellular dynamic studies impossible [300]. AFM, on the other hand, is capable of imaging surfaces of biological samples at resolutions of 10-50 nm through a contact method that involves the cantilever tip of the microscope touching the sample [301], [302]. However, this method can disrupt the membrane and distort images due to height differences within the sample [303]. Additionally, dynamic processes can only be visualised at the expense of extended acquisition times and AFM has few applications in live imaging.

In contrast to the methods mentioned above, SICM offers the possibility of observing dynamic morphological changes of live cells through non-contact surface profiling [304]. The advantages of using SICM compared to other conventional techniques are three-fold; firstly, three dimensional (3D), high-resolution topographical changes could be imaged in real time, secondly, there is no harm caused to cells by light or heat exposure for long periods and thirdly, the non-invasiveness of the technique assures that cells undergo minimal mechanical damages[305]–[307]. The scanning speed is dependent on the area, surface features and resolution of the sample is generally faster. For example, a 10 x 10 µm scan of an adult ventricular myocyte with150 nm resolution generally takes only ~2-3 minutes [308].

Scanning ion conductance microscopy typically utilises a glass nanopipette of an inner tip diameter between 20-100 nm as the non-contact probe. The lower the tip size, the higher the resolution of the image being scanned [309]. The nanopipette contains an electrode within and is filled with an ionic solution allowing the flow of ions toward a second electrode when placed in medium with a biological sample. As the pipette approaches the sample, the ion flow is gradually restricted such that the ion current decreases [310]. Since the increase in tip resistance can be monitored before physical contact with the sample, the ion flow further acts as a feedback mechanism to prevent direct contact with the

sample by keeping the sample-pipette distance constant at a predefined set point (Figure 1.7). The scan then moves laterally in the XY direction with a controlled piezo stage whilst the ion conductance control system detects changes in the Z direction through the pipette displacement to reconstruct the 3D topography of live biological samples [304], [311]. Intricate features of the cell membrane can be reconstructed through this technique as the distance feedback control ensures that the pipette closely follows the surface.

The ability of cells to resist deformation and maintain a state of interfacial tension is derived from the intracellular network of filamentous polymers, i.e. the cytoskeleton [30]. Between cells that engage in intercellular interactions, there is junctional tension at the cell-cell interface in addition to the tension of the neighbouring cortices [312].Insight into the mechanics of cell contacts have been hampered by the availability of appropriate techniques to make direct measurements *in vivo* and *in vitro* on live samples. Indirect methods using tension sensors that rely on FRET and the elasticity of a spring connecting the flourophores are sensitive to pico-newton (pN) forces but this sensitivity makes calibration crucial to obtain absolute values of force measurements and involves introducing plasmids to the cells [126]. Other indirect methods involve force inference from image analysis which is largely theoretical [313] and laser ablation that involves severing the junctions and use of fluorescent probes [121]. Although these indirect methods provide vital insight into the molecular tension sustained by cadherin receptors at junctions, they do not provide absolute value for the adhesion tension at cell-cell contacts.

Recent advancements utilising a combination of optical tweezers with light-sheet microscopy measure pN scale tension at epithelial cell junctions in the early Drosophila embryo [314]. Although promising, this method requires the introduction of fluorescent beads, pre-calibration and specialised lasers and trapping equipment to gather data. Functionalised oil droplets have also been used as stress sensors and although harmless, generation of these droplets require fine chemistry and can be time-consuming [315]. Other examples include micromanipulation with the use of indenters [316] or

pipettes [317] and have measured junctional tension between cell monolayers or cell doublets respectively. Of particular interest, the strength of cadherin-dependent intercellular adhesions has been measured using a dual pipette assay on E-cadherin expressing doublets and has shed light on the role of the cytoskeleton in reinforcing contacts [125]. Although each of these techniques have great potential, a number of technical challenges limit their use in cell biology labs.

Measuring tension at the cell cortex is far less complicated and can be done using a number of techniques including those mentioned above. One of the most common methods of measuring membrane viscoelasticity utilises the AFM and involves directly contacting membrane surfaces with the cantilever tip itself or microspheres in between [318]. A modified version of the SICM, containing a pressure port for application of hydrostatic pressures to cell surfaces, allows the measurement of cortical tension through noncontact mechanical stimulation [311] and provides an attractive tool for the study of elastic compliance (Figure 1.6).

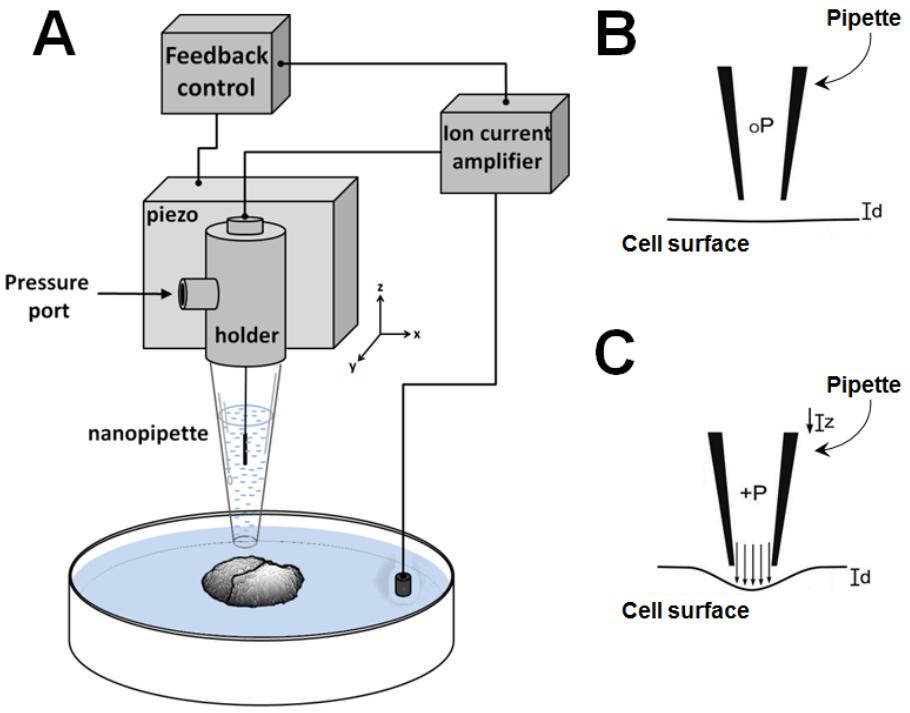

Figure 1.5: **Scanning ion conductance microscopy technique.** (A) Schematics of the systematic setup modified to include a pressure module for measurement of cellular compliance. (B) Non-contact pipette alignment with the cell surface to produce topographical images of cells on patterns. (C) Pressure application through pipette to displace the cell surface. Modified from image provided by Dr. Alonso- Sanchez, Imperial College London)

1.10 Hypothesis

Cell adhesions are coupled through an intricately linked cytoskeleton. Actomyosin contractility and GTPase signalling play a pivotal role in maintaining AJs and epithelial integrity. I hypothesise that actomyosin contractility and cortical tension are key regulators of the biophysical behaviour of neighbouring cells in confined areas and the way in which they interact with each other.

1.11 Aims

- Characterise cortical tension associated with different levels of geometry-dependent contractility
- Elucidate the effect of contractility on the migratory behaviours of cell pairs
- Explore the effect of peripheral actomyosin contractility imposed by substrate restrictions on junctional contractility
- Investigate the impact of increasing levels of contractility on junction properties

CHAPTER TWO:

Materials and methods

2.1 Cell Culture

2.1.1 Keratinocytes: Primary human keratinocytes isolated from the neonatal skin of a single donor (strain SF) were cultured from passages 2-6 on a feeder layer consisting of J2 Fibroblasts. The keratinocytes were maintained in FAD medium (DMEM:F12, BioWittaker, Lonza, Germany), supplemented with 10% fetal calf serum (FCS) (Sera Laboratories International Ltd, West Sussex, UK), 1.8 mM $CaCl_2$, 5 mM glutamine, 100 units/ml penicillin, 100 µg/ml streptomycin, 5 µg/ml insulin, 10 ng/ml epidermal growth factor (EGF), 0.5 µg/ml hydrocortisone (all Sigma-Aldrich) and 0.1 nM cholera toxin (Quadratech Diagnostics Ltd, Surrey, UK) at 37^{o}C and 5% CO_2 [319]. Mouse J2 3T3 fibroblasts were maintained in Dulbecco's modified medium (DMEM, Sigma-Aldrich) supplemented with 10% donor calf serum (Sera Laboratories International Ltd, West Sussex, UK) and 5 mM L-glutamine (Sigma-Aldrich). Confluent J2 fibroblasts were treated with 4 µg/ml mitomycin-C (Sigma-Aldrich) for at least two hours before trypsinising and seeding alongside keratinocytes as feeder layer. Keratinocytes were fed every other day and passaged weekly when cells reached 90% confluence.

2.2 Microcontact Printing

2.2.1 Preparation of elastomeric stamp with micropatterns

A silicon wafer master fabricated by photolithography (gift from Markus Textor, ETH Zürich) was used to make elastomeric stamps through replica casting polydimethylsiloxane (PDMS) (Dow Corning, Midland MI, USA). PDMS and the curing agent was combined in a 10:1 ratio, poured over the silicon master and cured at 60^{o}C overnight [320]. The resulting elastomeric stamp containing the micropattern was gently peeled off and stored in a closed container at room temperature. Prior to use, stamps were sonicated (Ultrasonic bath SW12H, Fisher Scientific) sequentially for a duration of 15 minutes each first in 70% ethanol, then acetone and finally in distilled water. The stamps were then blown dry under compressed air, oxidised in air plasma (200 mtorr) (Plasma Prep 5, Gala Instruments) and immediately coated with extracellular matrix proteins.

2.2.2 Coating stamps and printing onto substrates

Plasma activated stamps were coated with a 35 µl drop of 20 µg/ml fibronectin (Sigma-Aldrich) or collagen IV (BD Biosciences) for at least 1 hour at room temperature to allow adsorption of proteins. The stamps were then blown dry, inverted and placed in conformational contact with the substrate for 1 minute while applying gentle pressure. The stamp was then carefully removed and the substrate immersed in 0.5% (w/v) Pluronic® F127 (Sigma-Aldrich) in phosphate buffered saline (PBS) for 1 hour to passivate non-adhesive areas.

2.2.3 Cell deposition on to micropatterns

Substrates were washed with PBS three times after passivation and immersed for 30 minutes in PBS supplemented with 100 units/ml penicillin and 100 µg/ml streptomycin (Sigma-Aldrich). Keratinocytes were seeded at 2 x 10^4 cells/cm^2 in FAD medium immediately after trypsinization on to the substrates and allowed to attach for 2 hours. Unattached cells were removed by changing the medium after this time.

2.3 Substrate preparation

A number of different containers were used for culturing cells on micropatterns (Table 2.1). Initial experiments were conducted on 6-well untreated polystyrene plates (Nunc) since cells adhered well to the micropatterns and backfilling was successfully achieved with Pluronic® on these surfaces. Live microscopy experiments on cell doublets were performed on cells cultured in these plates with the use of a long working distance phase contrast objective lens. However, high resolution microscopy utilising objective lenses of short working distance was not possible in such plates due to the thickness of the bottom of the well. Extensive optimisation procedures were carried out in order to identify the best possible preparation for high resolution microscopy. The container chosen was dependent on the type of experiment but the adhering surface was always maintained as polystyrene coated glass surfaces either in well plates or dishes.

At first, 20mm circular areas that contained the micropatterned cells were punched out from 6-well plates. A glass coverslip was then mounted on the surface with mounting medium and allowed to dry before imaging. Several drawbacks were encountered with this method including the cells drying out, the wells breaking and creating uneven areas that would not hold coverslips making high resolution imaging impossible. Next, a different brand of untreated slides that were commercially specified for high resolution microscopy, Ibidi 2-well slides, were tried in order to eliminate hold punching. However, the Ibidi untreated surfaces could not be successfully passivated with Pluronic® and cells were not bounded by the micropatterned regions.

In an effort to maintain a consistent adhering surface for the cells while identifying the optimal container for high resolution microscopy, the cover of an untreated polystyrene 6-well plate was used to prepare a coating solution for glass coverslips. Final concentrations of 0.1%, 0.2%, 0.5%, 1% and 2% (w/v) polystyrene in toluene were tested for surface coating. While the lower concentrations were too dilute to evenly coat coverslips, the higher concentrations formed a thick layer that interfered with the imaging. 0.5% (w/v) polystyrene in toluene emerged as the optimal surface coating concentration since a thin even layer of surface coating could be obtained at such a concentration. The following sections describe the methodology in detail for preparing polystyrene coated coverslips for high resolution fluorescence microscopy experiments and the tailor made containers with polystyrene coated coverslips for scanning ion conductance microscopy (SICM) and fluorescence recovery after photobleaching (FRAP) experiments. The preparation of these plates were done with the help and advice of Dr. Julianna Lee (University of Hong Kong, Hong Kong).

2.3.1 Polystyrene coated coverslips

Square glass coverslips (20mm x 20mm, VWR) were cleaned with 70% ethanol and fully dried prior to coating. The polystyrene solution for coating was prepared by dissolving broken pieces of the cover of an untreated polystyrene 6-well plate (nunc) in toluene to a stock concentration of 25% (w/v). After rotating the glass vial with the 25% polystyrene in toluene solution overnight, it was further diluted in

toluene to a working concentration of 0.5% (w/v). Within a chemical fume hood, a thin layer of polystyrene was then coated on the coverslips using a 200 µl pipette tip without graduation marks so as to obtain a single fine layer on the coverslip. The opposite side of the glass coverslip was clearly marked with a permanent marker to identify the polystyrene coated side.

These coverslips were either used directly to culture cells by placing them in 6-well tissue culture plates or attaching onto 3cm dishes as described in the next section (2.3.2). Polystyrene coated coverslips were carefully retrieved from the wells using forceps and placed in a humid chamber for immunofluorescence staining (Section 2.4).

2.3.2 Tailor made 3cm dishes with polystyrene coated coverslips

Polystyrene coated coverslips as described in section 2.3.1 were used as the culture substrate and attached to the bottom of 3cm dishes to obtain thin bottomed dishes that were ideal for high resolution live microscopy. Culture dishes (3cm, Nunc) were drilled with 15mm diameter holes using special machinery and techniques by Mr Russell Stracey (RSM Workshop, Department of Materials, Imperial College London). The use of such a technique was necessary to avoid breakage and large cracks upon drilling. The dishes were then cleaned with 70% ethanol, dried and sterilised with UV in a biosafety cabinet for cell culture. Parafilm® was cut into 20mm x 20mm squares and round holes of 16 mm diameter were punched at the centre. The paper attached to the Parafilm® was removed and the centre of the Parafilm® placed in alignment with the drilled hole of the 3cm dish. The 20mm x 20mm polystyrene coated glass coverslips were then placed in alignment with the Parafilm® and placed on a heat block at 100^{o} to melt the Parafilm® and seal the dish to avoid leakage. Gentle pressure was applied to the sides of the hole within the dish to ensure contact between all the materials for sealing (Figure 2.1). These tailor made dishes were used for SICM and FRAP experiments that required live imaging of cells.

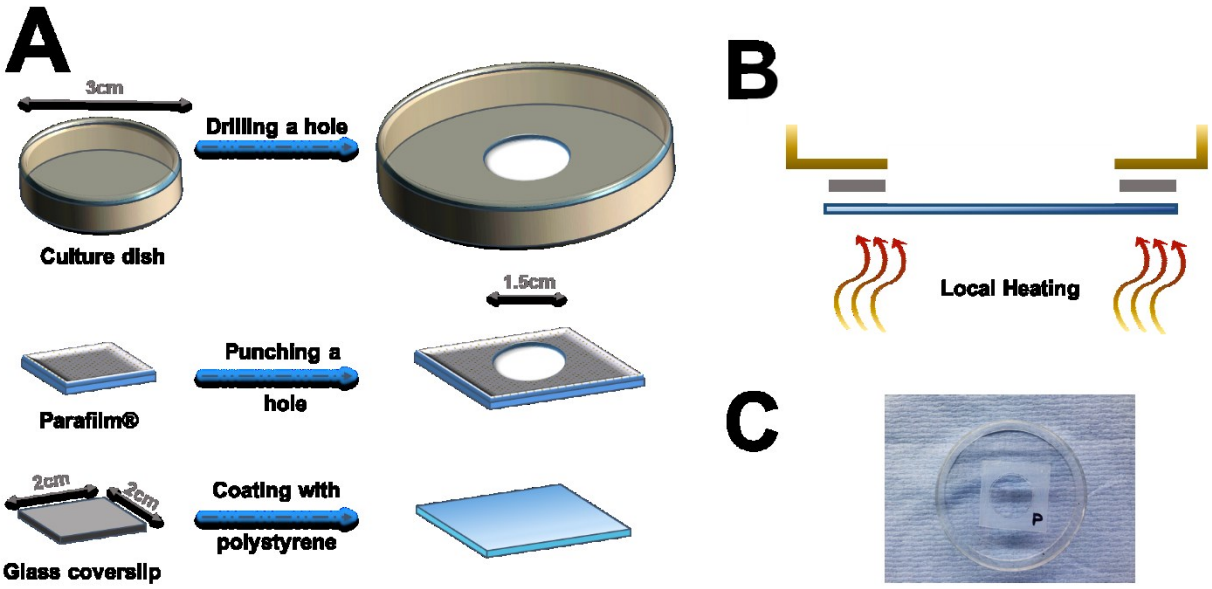

Figure 2.1: **Preparation of tailor made dishes with a thin bottom.** (A) Schematics of preparation of individual components for sealing (top view). (B) Alignment of components with the Parafilm® in between for heat sealing with local heating at 100°C (lateral view). (C) Photo of a completed tailor made dish.

Table 2.1: Substrate surfaces used for micropatterning

Surface (supplier)	Microscopy technique	Specific application (objective)
Untreated polystyrene plates – 6-well (Nunc, Thermo Scientific, Loughborough, UK)	Widefield	Phase contrast imaging of fixed samples (x10) and live cell videos (x40)
Polysyrene coated glass coverslips – 20mmx20mm (VWR, Leicestershire, UK)	Widefield and confocal	Immunofluorescece imaging of fixed samples in widefield (x20, x40) and confocal (x63 oil)
Tailor made container – 3cm dish (Nunc) with polysyrene coated coverslip (VWR) attached	WIdefield and confocal	Scanning of live cells for SICM (x20) and live imaging for FRAP (63x oil)
Ibidi untreated µ-slide – 2-well (ibidi GmbH, Planegg, Germany)	Widefield	N/A – only used for optimisation
Punched out wells of 6-well untreated polysyrene plates (Nunc)	Widefield	N/A – only used for optimisation

2.4 Immunoflourescence

2.4.1 PFA fixation: Cells were fixed with 3% paraformaldehyde (PFA) in PBS at room temperature for 10 minutes and blocked and permeabilised with 10% FCS in PBS containing 0.1% Triton X-100 respectively for a further 10 minutes washes at room temperature. Coverslips containing the cells were then incubated for at least 30 minutes with primary antibodies (Table 2.1) diluted in 10% FCS in PBS. After washing the coverslips in PBS three times, secondary antibodies (Table 2.2) diluted in 10% FCS in PBS were added onto the coverslips for at least a further 30 minutes. These steps were repeated for the subsequent antibodies in the case of double or triple staining. Coverslips were finally washed nine times in PBS and three times in water and mounted with Mowiol (Calbiochem, California, USA) on glass slides (Fisher Scientific UK Ltd, Loughborough, UK)

Table 2.2: Primary antibodies used for immunofluorescence staining

Primary antibody	Clone name	Supplier	Source	Dilution
E-cadherin	ECCD2	Invitrogen	Rat	1:750
E-cadherin	HECD1	Gift from M. Takeichi, Keio University, Japan	Mouse	1:1000
Phosph- Myosin Light Chain 2 (S19)	3675S	Cell Signalling	Mouse	1:1000

Table 2.3: Secondary antibodies and conjugates used for immunofluorescence staining

Conjugate	Supplier	Source	Dilution
Alexa Fluor 488 (AF488)-conjugated anti-mouse IgG	Jackson Immuno Research Laboratories	Goat	1:1000
Alexa Fluor 568 (AF568)-conjugated phalloidin	Molecular Probes		1:1000
DAPI	Sigma-Aldrich		1:3000
Indocarbocyanine (Cy3)-conjugated anti-mouse IgG	Jackson Immuno Research Laboratories	Donkey	1:3000
Indodicarbocyanine(Cy5)-conjugated anti-rat IgG	Jackson Immuno Research Laboratories	Donkey	1:400

2.5 cDNA transfection

For cDNA transfections, 0.5 µg plasmid DNA per coverslip were incubated at a ratio of 1:4 with FuGENE® HD transfection reagent (Promega, Madison WI, USA) in Opti-MEM® reduced serum medium (Life technologies, Paisley, UK) in a total volume of 50 µl. Tubes were vortexed for 10 seconds, centrifuged briefly and incubated at room temperature for 10 minutes. The medium was removed from the cells and replaced with 1 ml fresh FAD medium per 3cm dish. The transfection mixture was added to the cells and incubated for 24 hours before carrying out live microscopy.

Table 2.4: Expression vector

Coded protein	Plasmid	Source
Actin	pcDNA3.1-GFP	Gift from M. Bailly

2.6 Inhibitor assays

Cells were treated with 5 µM Y27632 (Sigma-Aldrich) for 5 minutes after overnight attachment of cells on to micropatterns. Cells were fixed immediately afterwards for immunofluorescence staining.

2.7 Microscopy

2.7.1 Image acquisition

Widefield microscopy: Images were acquired on a Zeiss Axio Observer inverted microscope using Zeiss ZEN 2012 (Flash Edition) (Carl Zeiss AG, Oberkochen, Germany) software. Immunofluorescence images were captured using either a 20x/0.8 DIC Plan Apochromat objective or a 40x/0.75 Ph2 EC Plan-Neofluar objective (Carl Ziess). Live videos were captured using a special long distance phase-contrast 40x/0.55 Ph2 LD A-Plan objective (Carl Zeiss).

Confocal microscopy: Images were acquired on a Zeiss LSM-780 inverted confocal laser scanning microscope using Zeiss ZEN 2012 (Black Edition) (Carl Zeiss AG, Oberkochen, Germany) software. High resolution still immunofluorescence images were obtained with a 63x/1.40 Oil DIC Plan-Apochromat objective (Carl Zeiss). For fluorescence recovery after photobleaching (FRAP) experiments, images

were acquired using a Zeiss LSM-510 inverted confocal microscope with Zeiss ZEN 2012 (Blue Edition) (Carl Zeiss AG, Oberkochen, Germany) software. The objective used for FRAP was also a 63x/1.40 Oil DIC Plan-Apochromat objective (Carl Zeiss).

2.7.2 Image analysis

Distances, areas and intensities: Images were analysed using Fiji (continuous release version) and custom made macros and plug-ins created by Mr Stephen Rothery (Facility for Imaging by Light Microscopy (FILM), Imperial College London).Two custom made macros were predominantly used for this work. Details of Macros will be provided in supplementary methods. Schematics of the methodology will be provided under the relevant results chapters. A description of each of the different parameters calculated is provided below, Images used for analysis were saved as composite images containing 4 different channels: Channel 1 (Nuclei), Channel 2 (E-cadherin / Phosphoylated myosin light chain (PMLC)), Channel 3 (F-actin) and Channel 4 (Phase contrast). Appropriate channels were extracted for the corresponding analyses.

Firstly, the Morphology Macro was used for measurement of parameters such as nuclear distance, nuclear area, and cell area and junction lengths on cells on micropatterns.

- Nuclear distance: grey scale images of the channel containing the nuclei were thresholded (extracted by pixel intensity). The centres of mass in the XY dimension were obtained for each of the nuclie in the format (x_1, y_1) and(x_2, y_2). The distance (d) between the two points calculated using the formula, $d = \sqrt{(x_2 - x_1)^2 + (y_2 - y_1)^2}$ (Figure 4.3)
- Nuclear area: grey scale images of the nuclei channel were thesholded and the area of each nucleus obtained using Fiji (Figure 4.5)
- Cell area: cell areas were calculated using the E-cadherin channel. The greyscale image containing the cell pair was used to draw a line through the junction to split the cells. The image was then thresholded and area for each image obtained using Fiji.

- Junction lengths: three different lengths were obtained using Fiji, the actual junction length, straight junction length, and edge-to-edge length as depicted in Figures 5.1 to 5.3. The actual junction length was obtained by drawing a line from the start to the end of the junction as seen from the greyscale E-cadherin image. The straight junction length was obtained by drawing a straight line between the two end point of the junctions and the edge-to-edge length obtained by extending the actual junction length to reach the edges of the cell borders.

Secondly, the Intensity Macro was used for measurement of intensities within the cell; cytoplasm and junction.

- E-cadherin intensity and density: To obtain the intensity at junctions, each greyscale image was thresholded to in a way to maximize the amount of E-cadherin junctional staining highlighted and minimise the amount of cytoplasmic staining highlighted. The cytoplasmic intensity was obtained by removing the junction region and thresholding the remaining cell. The density was obtained by measuring the area of the junction thresholded and taking the ratio of the intensity over the area.
- Actin intensity and density: E-cadherin images that were individually thresholded to cover the junction were converted to binary images and dilated by one pixel. These were then used as a mask to overlay on the actin channel to obtain the junctional pool of actin. The cytoplasmic intensity was obtained by removing the junctions and thresholding the remaining area. Densities were calculated by dividing the intensity by the measured areas for corresponding regions.

Cellular features: The presence of side fibres, lamella, thin bundles and junctional actin was qualitatively assessed on individual confocal images. Labelling with PMLC was assessed in a similar manner by comparing the presence of these structures in the PMLC channel side by side with the actin channel.

2.7.3 Calculation of cellular orientation preference

E-cadherin channels of images were assessed for the positioning of junctions and split into two categories for each of the square and triangular shapes. The categories were selected according to whether the junction passed through the edge or vertex of the shape. The number of cell pairs with junctions fulfilling each of the categories was then counted and multiplied by the probability of attaining that specific orientation. The probability of achieving either of the orientations was calculated by assuming that the junction always passes through the centre of the shape and dividing the shape into 5° °regions from the centre. For example, the probability of the junction passing through a vertex of a triangle was calculated by multiplying the number of vertices (i.e. 3) by 5 and then dividing this value by 360 to obtain a normalised probability per 5° region.

2.8 Cell Viability assay

2.8.1 Alamar Blue: Cell viability was assessed with the use of AlamarBlue® (Life Technologies) on 96-well plates (Corning). Keratinocytes were seeded at a density of 6.8-10 x 10^3 cells/cm^2 in FAD medium and allowed to proliferate for 48-72 hours until cells reached 70% confluence. Immediately prior to the assay, cells were briefly washed with versene (0.53 mM Ethylenediaminetetraacetic acid (EDTA) in PBS) and fresh medium replaced. Four types of medium were used for the assay which include FAD medium, FAD medium with 25 mM HEPES, FRAP medium (DMEM:F12 Phenol free, Life Technologies, Paisley, UK), supplemented with 10% fetal calf serum (FCS) (Sera Laboratories International Ltd, West Sussex, UK), 1.8 mM $CaCl_2$, 5 mM glutamine, 100 units/ml penicillin, 100 µg/ml streptomycin, 5 µg/ml insulin, 10 ng/ml epidermal growth factor (EGF), 0.5 µg/ml hydrocortisone (all Sigma-Aldrich) and 0.1 nM cholera toxin (Quadratech Diagnostics Ltd, Surrey, UK) and FRAP medium with 15 mM HEPES. Cells were incubated for 30 minutes with medium following addition of 10% Alamar Blue reagent directly onto the wells. The reagent was left on the cells for up to 6 hours in the dark either at 37°C and 5% CO_2 (inside the incubator) or at room temperature (outside the incubator). At hourly intervals from 1-6 hours, 100 µl of the medium on the cells was transferred to another 96-well plate (Sterilin). The

absorbance of the wells was read at 560/590 nm (excitation/emission) with a standard fluorometer (POLARstar Galaxy, BMG Labtech with FLUOstar Galaxy software).

2.9 Fluorescence recovery after photobleaching (FRAP)

The medium on the 3cm dish containing the transfected cells was removed immediately prior to the experiment and replaced with phenol-free FRAP medium. The Zeiss TempModule system was used to control the temperature (37°C) of the working system. Transfected doublets on micropatterns were then identified and selected using the 20x objective on the LSM-510 inverted confocal microscope. The dish was then carefully moved out of the way and the objective changed to 63x and a drop of oil added before replacing the dish in approximately the same position. A 5x optical zoom and 1064 x 1064 pixel resolution was used to isolate the pair of cells with the junction to be bleached. Two areas on the junction were selected with a rectangular size of 12x40 pixels and one of the areas were bleached while the other used as a control. Images were captured every 8 seconds with 5 pre-bleached images and 15 subsequent images after bleaching. Fiji was used to obtain values for the mean gray value and integrated densities for the bleached and non-bleached regions. Recovery curves were computed using these values normalised to the flouresence intensities before bleaching. The half-time and recovery were obtained from these recovery curves.

2.10 Scanning ion-conductance microscopy (SICM)

The SICM technique was carried out in collaboration with Prof. Julia Gorelik (Faculty of Medicine, National Heart & Lung Institute, Imperial College London). Dr. Jose Sanchez Alonso Mardones and Miss Georgina Heywood were both extensively involved in this work.

2.10.1 Image acquisition

Cells were identified using a 20x magnification objective to select for duplets. Cells were kept in 25mM HEPES at room temperature throughout the duration of the microscopy session and scanned using the Scanning ion-conductance microscope (Ionoscope Limited, London, UK). The micropipettes used for scanning were made from borosilicate glass capillaries (O.D.: 1.00mm, I.D.: 0.50mm, 7.5cm Length,

Intracel, UK) and were pulled using a laser puller (Sutter Instruments, P-2000), with a resistance between 15 – 40 MΩ. Images were then obtained by scanning an 80µm x 80µm area for the selected cell at low resolution. A higher resolution image was gained by scanning a 45µm x 45µm area at an increased resolution. All images were obtained using a hop amplification of 2,500nm, a fall rate of 35nm/ms and a feedback control set point of 7x0.1% (Piezo system, Jena, UK).

2.10.2 Testing mechanical properties of cell pairs

The cortical displacement and stiffness of cell pairs were tested by applying pressure to the cells at set locations. This was done using the same micropipette that was used for scanning. Compliance was measured at the centre of each cell, on micropatterns. To measure compliance the hop amplification and fall rate of the piezo had to be decreased to 300nm for the hop amplification and 30nm/ms for the fall rate. Around 15-40kPa pressure was applied to the cells, this was dependent on the pipette resistance as a lower pipette resistance indicated that the pipette tip width was quite large and too much pressure could damage the cells. Displacement that occurred due to the application of pressure was measured using Clampex (pClamp software, Molecular Devices, USA) [321].

2.10.3 Calculations

Young's Modulus: Data gained from applying pressure to the cells was used to calculate the Young's modulus (E) using the formula below:

$$h_{avg} = 16(1-v^2)\, R_{pip}\Delta P/(3\,\pi\, E)$$

Where, h_{avg} is the uniform displacement recorded by pClamp software, v is the Poisson ratio estimated as 0.5 assuming an incompressible material with small strains, ΔP is the pressure applied to the surface measured by a pressure meter, and R_{pip} is the pipette resistance calculated using the formula below [322],

$$R_{pip} = (\pi \bullet d/2 \bullet \tan(\phi/2) \bullet \rho)^{-1}$$

Where, d is the inner pipette tip diameter, ϕ is the tip of the cone angle (ϕ = 6.2° ± 0.5° Mean ± SD) [322] and ρ ~ 1.2 Sm^{-1} is the conductivity of the pipette in solution [323].

Cell volume, cell height and junction height: These parameters were calculated using the topographical images obtained from SICMImageViewer software which directly computes values for heights at any point on the cell surface. Volumes were calculated similarly by outlining the borders of each cell within the pair.

Recovery and relaxation: Percentage recovery and relaxation time were calculated from the pClamp recordings of the piezo displacement (Figure 3.3). Relaxation time was considered as the time taken to reach a stable baseline after the pressure stimulus start to reduce. The baseline reached after pressure application and relaxation was compared with the initial baseline, considering 100% as no change in displacement between the initial baseline and the recovered baseline. When the baseline after the stimulus was more than 90%, a full recovery was considered. When this baseline was less than 90% of the initial baseline, recovery was considered partial.

2.11 Statistics

Data was statistically analysed using GraphPad Prism v5.04 (GraphPad Software, Inc., La Jolla, CA, USA) and Matlab R2014a (The MathWorks, Inc., Cambridge, UK). Data generally appeared normally distributed. Therefore, parametric tests were used throughout this thesis. Data originating from repeated experiments were analysed by t-test or one-way ANOVA. One-way ANOVA was followed by the Tukey post-hoc analysis to obtain p-values of statistical significance.

CHAPTER THREE:

Biophysical parameters and cortical stiffness variations according to geometric constraints.

3.1 Rationale

Cell mechanics play a pivotal role in maintaining structural and functional integrity of tissues [30] and deviations from physiological values, particularly for cell elasticity, can be identified as distinct phases of cancer progression [324]. Cell elasticity is mainly defined by the actin cytoskeleton [325], [326] and precisely engineered microenvironments that impose regular shapes and cytoskeletal organisations can be used to manipulate cell behaviour and mechanics in vitro in a reproducible manner [265], [295].

Cells are mechanically coupled to each other to establish and maintain equilibrium and function as a cohesive unit within tissues [327]. Cell motility is influenced by cell-cell and cell-matrix interactions as well as intrinsic cellular properties [328]. Cellular contractility governed by the geometry and spatial constraints imposed upon cells impacts collective migration [329], [330]. Furthermore, the coupling of contractile forces between neighbouring cells plays a vital role in coordinating cell motility [331]. The role of cell-cell adhesions in coordinating and directing cell motility [276] and the contraction of 'leader cells' to guide cohesive colonies along defined tracks [332] are two phenomena that are of utmost importance in dissecting the biophysical mechanisms of cell motility.

Epithelial cells exhibit collective migration during development [251], [333], wound healing [334], [335], and cancer metastasis [336], [337]. Particularly in metastasis, cells detach from primary tumours as single cells or multiple cells with intact cell-cell contacts as seen in tissue samples and infiltrate surrounding tissues to colonise distinct sites [338]. In light of this, the coordinated motility of MDCK cell sheets cultured on removable microstencils was shown to be a combination of individual behaviours of single 'leader' cells and collective behaviours of 'follower' cells mechanically coupled through cell-cell contacts to maintain epithelial integrity [335]. Collective and individual motility driven by colony dispersal into single migratory cells has further been assessed utilising a novel assay which utilises uniform, circular shaped wounds to determine diverse levels of invasiveness of three cancer cell lines [339].

The role of cellular tension in determining how cells interact and communicate with each other remain elusive throughout the literature. Appropriate control of cell-cell contacts and cell-matrix adhesions is essential for the establishment of the distinct epithelial morphology [340]. Culturing cells on micropatterns of different sizes and shapes has been used to precisely manipulate their microenvironment and directly impact cell growth, differentiation and migration [265]. Mechanical properties of cells grown in micropatterns may thus provide vital information on how cell tension is regulated by geometric restrictions.

Mechanical mapping of cell elasticity by AFM has revealed its dependence on cell spread area, substrate stiffness and actin distributions [341]. A recent study by Rigato et al. reported variations in Young's moduli related to adhesion geometry when single cell elasticity of epithelial cells (hTERT-RPE1) cultured on different adhesive geometries of triangular cell shape were measured by AFM [342]. Apart from this publication, all other studies related to the mechanical properties of epithelial cells have been done on unrestricted surfaces using AFM. A further study of cell mechanics on single keratinocytes of varying origin measured elasticity of the cell membrane and cytoplasm with an AFM probe modified with a large microsphere for pressure application [318].

SICM allows the non-invasive imaging of live cell surfaces with fine lateral resolution such that precise 3D topographical cell profiles can be obtained [343], [344]. Such high resolution surface nano-topographies allow for visualisation of fine structures such as microvilli, cilium, endocytic pits and tight junctions [345]. In addition to providing insight into visual architecture and morphological parameters, SICM can also be used to infer cellular mechanical properties such as cell viscoelasticity as revealed by a study on A6 toad kidney epithelial cell monolayers [304], [311].

In this chapter I shed light on the behaviour and mechanical properties of keratinocyte cell pairs cultured in a minimalistic model system that couples both cell-matrix and cell-cell interactions on differentially imposed cytoskeletal tensions. In my minimal model system cell pairs are allowed to interact with each other in a permissive manner within a defined microenvironment. Unlike single

cells on micropatterns, doublets shed light on the influence of cell-cell contacts in determining mechanical properties and migratory behaviours whilst spatially constrained to recapitulate tissue-like variability in contractility. In this chapter, I address how varying levels of contraction of cells influences properties critical for collective migration. More specifically, we correlate the morphological heterogeneity of cells grown on circular, square and triangular micropatterns with their dynamic cellular movements and contractile properties.

3.2 Hypothesis and aims

I hypothesise that the tension constraints imposed by different geometric shapes, directly affect individual cellular mechanics and dynamics. In order to study the relationship between cell shape and intracellular tension and how these affect cell movement, I aimed to:

(i) characterise spreading of keratinocyte doublets on confined micropatterns of different sizes to define the optimal pattern area suitable for future experiments

(ii) correlate cellular stiffness (Young's moduli) and recovery mechanics with shape

(iii) explore the movement of cell pairs in response to cell shape and tension

3.3 Results

3.3.1 Keratinocytes attach in multiples to single micropatterns of varying shapes and sizes

In order to evaluate the optimal size for attachment of doublets of keratinocytes to micropatterns of circular, square and triangular shapes, six different sizes ranging from 300 μm^2 to 1300 μm^2 were tested. Protein transfer efficiency from the PDMS stamp to the substrate surface was assessed with the use of FITC labelled Collagen I micro-printed on to the substrates and imaged using a widefield fluorescence microscope (Figure 3.1A). Attachment and spreading of one or two keratinocytes per micropattern were analysed for six different sizes with the use of phase contrast microscopy on fixed cells (Figure 312B).

An area of 1300 μm^2 for circular, square and triangular shaped micropatterns was selected as the optimal size to confine doublets of keratinocytes. It was observed that cells attached in multiple numbers occupying 1-4 cells per micropattern despite spatial restrictions (Figure 3.1C). Two different extracellular matrix compositions, fibronectin and Collagen IV, were tested for optimal keratinocyte attachment (data not shown). Of these, fibronectin micropatterns were more consistent for protein transfer and subsequent attachment of cells and was the chosen extracellular matrix for further experimentation.

3.3.2 Addition of HEPES buffer to standard medium improves cellular responses

For experiments on the SICM, cells were maintained at room temperature throughout the procedure due to the lack of a heating/CO_2 chamber. A medium change was avoided so that changes in intracellular dynamics due to serum replenishment were minimised. Addition of 25 µM HEPES to buffer the pH of the medium did not affect the morphology of cells at room temperature or at 37°C, 5% CO_2 (Figure 3.2A). AlamarBlue® was used as a nontoxic, quantitative and colorimetric indicator of cellular metabolic activity [346]. Visible differences in colour over time confirmed changes in activity in cells within the incubator or

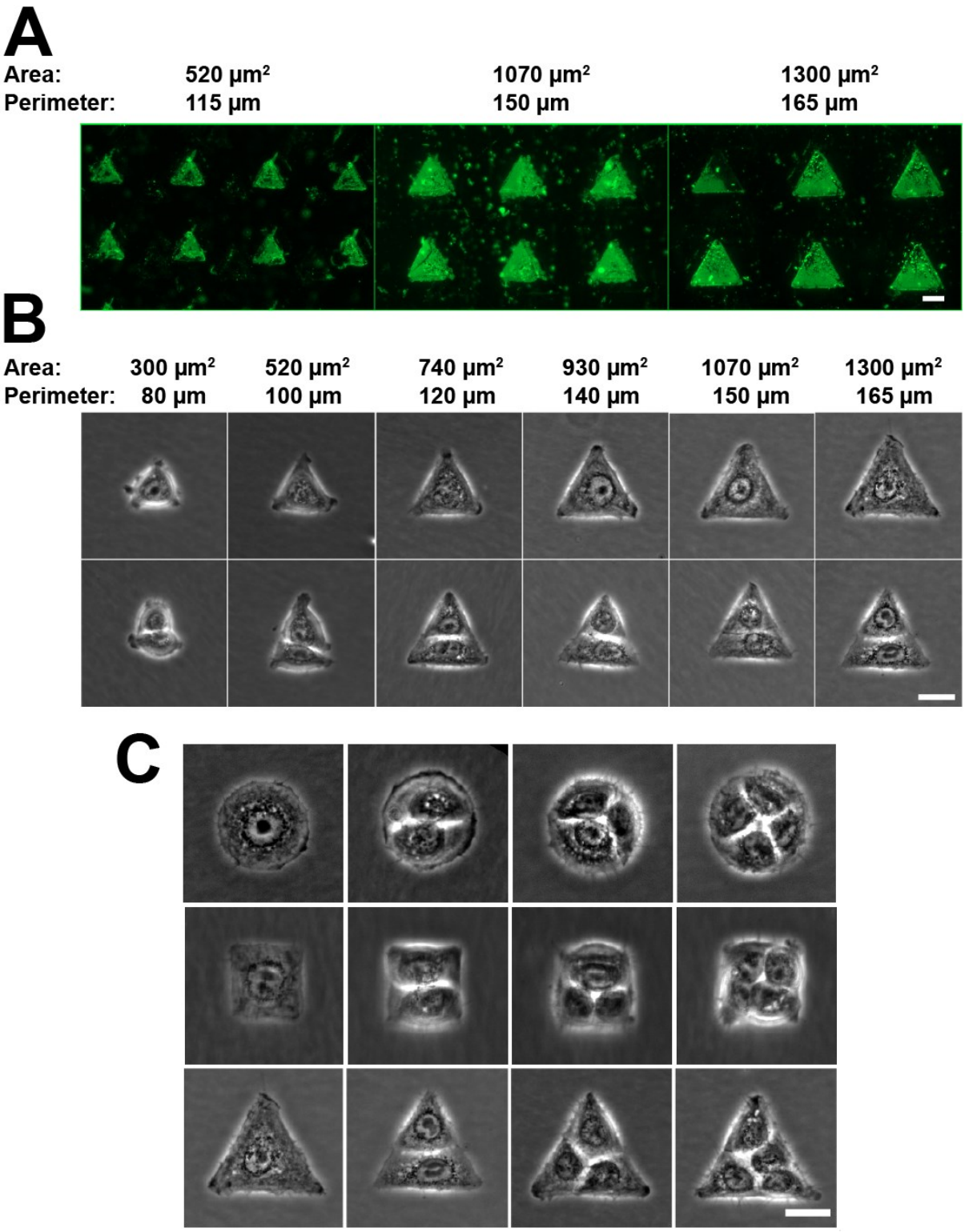

Figure 3.1: Multiple cells attach to micropatterns of varying sizes and shapes. Images of fixed cells were taken on an inverted widefield microscope 20 hours post seeding. (A) Immunoflouresce images of FITC CollagenI labelled triangular micropatterns of different sizes. (B) Brightfield images of keratinocytes attached in single cells and doublets on triangular micropattern islands of six different areas ranging from 300 – 1300 μm^2. (C) Brightfield images of 1-4 keratinocytes attached per micropattern of circular, square and triangular shapes of area 1300 μm^2. Scale bars represent 20 μm.

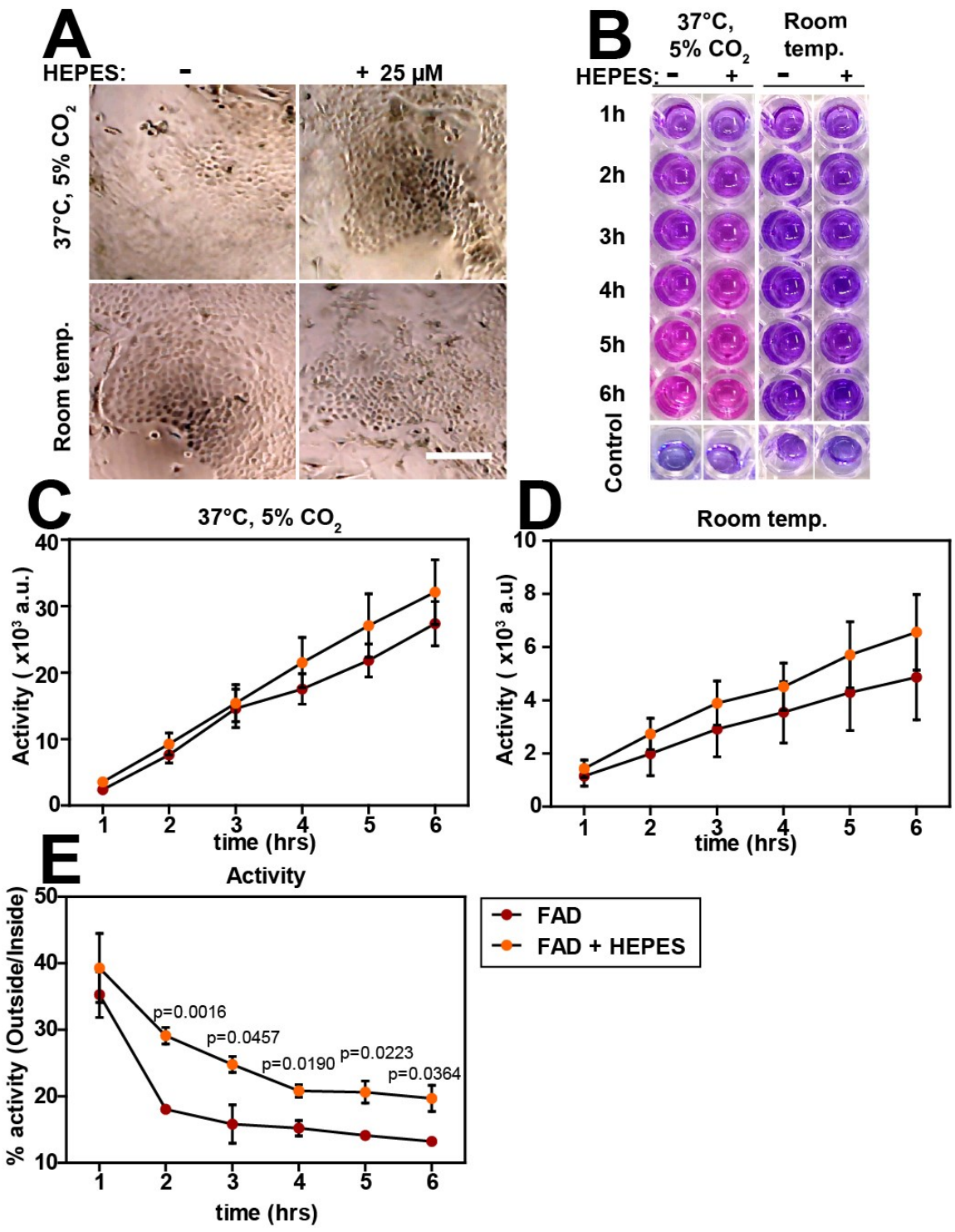

Figure 3.2: The use of standard medium containing HEPES is better suited for experiments at room temperature. Keratinocytes were cultured as monolayers and treated with AlamarBlue® for up to 6 hours and the resulting absorbance measured. (A) Brightfield images of cells in incubated at 37°C, 5% CO2 (top row) or at room temperature (bottom row) with or without the addition of HEPES. (B) Visible colour changes of cells containing AlamarBlue® from 1-6 hours. Control wells are those that did not contain cells. Metabolic activity measured inside (C) and outside (D) the incubator from 1-6 hrs. (E) Percentage activity at room temp. compared to 37°C, 5% CO2 with and without HEPES. Scale bar represents 200 µm. Graphs show mean values. Error bars represent SEM. Data are representative of 3 independent experiments.

at room temperature (Figure 3.2B). The metabolic activity of cells kept in medium containing 25 µM HEPES was always higher than in standard medium both at 37°C, 5% CO_2 (Figure 3.3C) or room temperature (Figure 3.2D).

Cellular metabolic activity at 37°C, 5% CO_2 was more than three-fold higher from 2-6 hours when compared to that at room temperature. The percentage of metabolic activity at room temperature compared to 37°C, 5% CO_2 was significantly higher for 2-4 hours in cells cultured in the medium with HEPES than without (Figure 3.2E). These results indicate that prolonged experiments at room temperature carried out with the addition of HEPES to the medium of cells improves cellular responses in general and should be used for consistent cellular dynamics with live cell imaging.

Cells were maintained at room temperature in pH buffered medium which contained 25 µm HEPES [33] for SICM experiments. Despite previous reports of the significantly slow rate of E-cadherin contact formation at a temperature of 19°C [34], cells cultured at room temperature did not show any visible detrimental changes in morphology or activity for up to 6h (Figure 3.3). SICM experiments were conducted at room temperature for durations of up to 3 hours in a single sitting whilst ensuring cells grown on the three different shapes were kept at the same conditions and were randomly selected for imaging.

3.3.3 SICM provides insight into the biophysical parameters of cells constrained by different geometric shapes

To gain insight into the biophysical properties of cells, high resolution three dimensional images of live keratinocytes on micropatterns were acquired using SICM. SICM experiments were carried out in collaboration with Prof. Julia Gorelik (Imperial College London) with the modified technique developed in her lab. Dr. Jose Sanchez-Alonso and Miss Georgina Heywood conducted experiments on the SICM, analysed the data and contributed to computing graphs. I prepared the cells on the micropatterns and contributed to analysis and quantification.

Doublets were selected randomly for scanning and, in general, keratinocytes exhibited a convoluted morphology with an uneven, convex cell surface (Figure 3.3). In addition to obtaining 3D morphological surface maps of cells, in this study, SICM was used for measurements of cell height, volume, and membrane compliance. Height measurements were directly obtained through the raster image (Z-displacement) whilst volume measurements were calculated by integrating the Z-displacement in X and Y directions of the cells [347]. For both measurements, it was assumed that the entire basal surface of cells was in close contact with the substrate. To test the mechanical properties of cells, force was generated at the tip of the nanopipette by a pressure source through hydraulic jets applied to indent surface membranes and study their mechanical properties [311]. The pipette follows the indentation as a function of the applied pressure and quantitatively probes the cell cortex surface without direct contact. The Young's modulus of elasticity can be determined by the effective force and distance.

The maximum heights of cells in the three shapes appeared similar (Figure 3.3A). The doublet profiles on each of the micropatterns were such that the maximum cell height was observed at the centres of each of the cells (lighter regions) while there was a dip in cell heights at the junction between cell pairs or at the periphery of the cells (darker regions) (Figure 3.3B-C). From these images, it was noted that heights of cell pairs display similarity in cells grown on circular and square shaped micropaterns while individual cell heights on triangles show a discrepancy where one of the cells is clearly taller than the other. The three different views also enabled the visualisation of height and volume of cells grown on the different shapes (Figure 3.3). Such detailed images were used for the quantification of the aforementioned parameters of the figures that follow. Cell heights and volumes were measured from cell profiles obtained as shown in Figure 3.3 using SICMImageViewer software. There were no discernible differences in mean cell heights or volumes between the different micropattern shapes (Figure 3.4A). Graphs of mean volume and height can be found in supplementary methods (S.2) and show no statistical significance in either parameter between the different shapes.

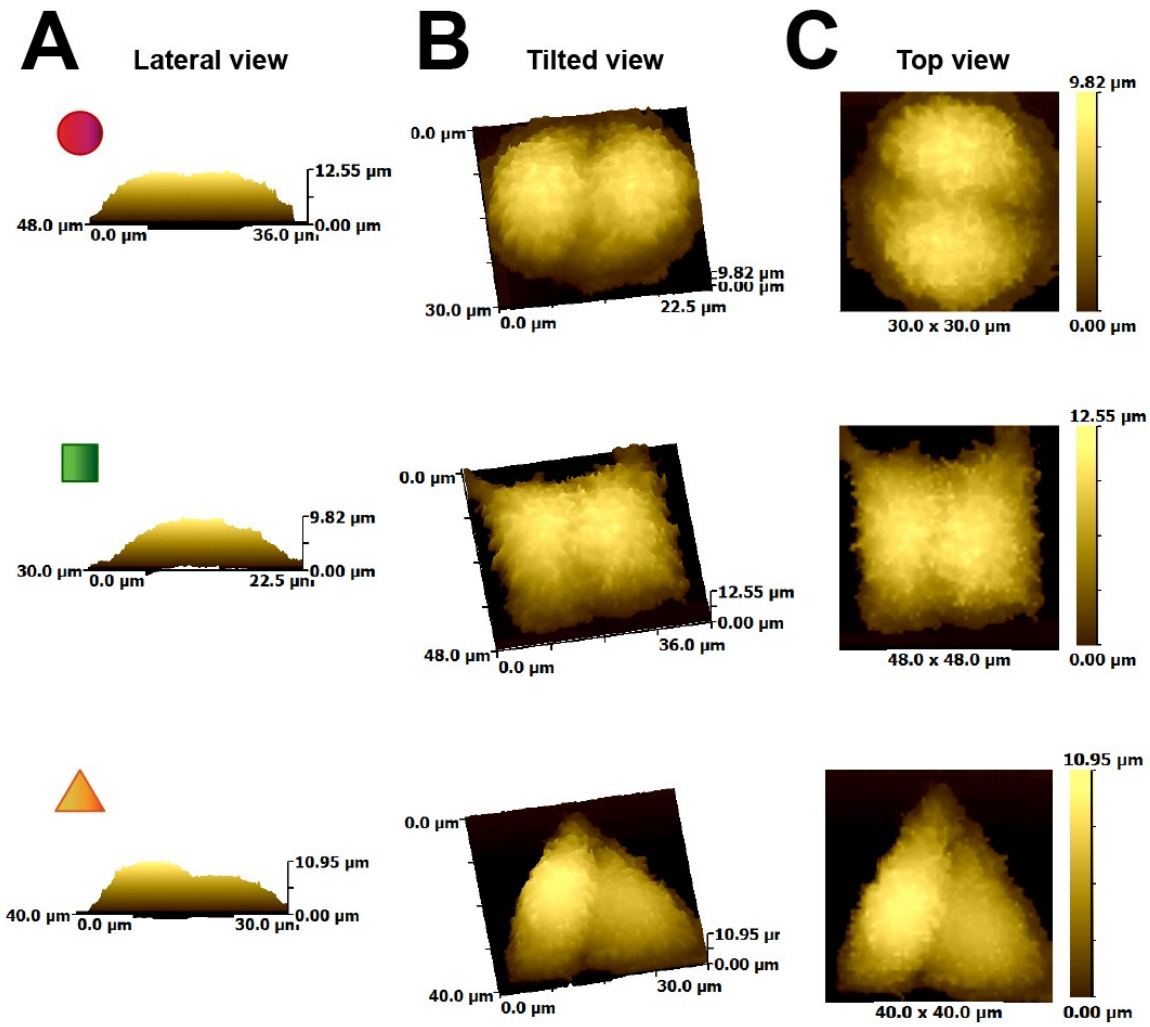

Figure 3.3: Three dimensional cell profiles obtained by scanning ion conductance microscopy (SICM). Keratinocytes were seeded onto micropatterns and allowed to attach and spread overnight, SICM was then used to generate high resolution profiles of cells in standard medium containing 25 µM HEPES. Images were processed using SICMImageViewer software to obtain three different views. (A) Lateral view, (B) tilted view and (C) top view of cells cultured on circular, square and triangular shaped micropatterns respectively (top to bottom of each column). Scale on the right shows a measure of height by colour where the maximum heights are 9.82 µm, 12.55 µm and 10.95 µm for cells on circular, square and triangular shaped micropatterns respectively. Images were acquired and processed by Dr Sanchez-Alonso. Cells were cultured on micropatterns and transported by myself.

Frequency distributions of cell heights indicated that cells on both triangular and square shapes had a peak height of ~9.8 µm while cells on circular shapes show a larger spread of cell heights (Figure 3.4B – left). However, volumes of cells displayed varying distributions for each of the three shapes: circles had the largest spread in volume while squares had a smaller spread with a clear peak volume of ~2500 μm^3 (Figure 3.4B – right). These observations led me to determine if height and volume were correlated to each other such that differences in volumes could be attributable to differences in heights. Indeed, positive correlations between cell height and volume were discovered in all three shapes with the strongest correlation observed in doublets grown on circular shapes ($R^2 = 0.7911$) and the weakest correlation detected on keratinocytes grown on triangular shapes ($R^2 = 0.340$) (Figure 3.4C).

3.3.4 Cortical stiffness of keratinocytes vary according to geometric constraints

There are known differences in cytoskeletal tension of single cells driven by changes in cell shape. Here I addressed biophysical properties of two cells on micropatterns such as cellular displacement in response to pressure application and the resulting stiffness. Application of pressure to the cortex of cells in duplets on the three shapes resulted in the displacement of the cell cortex (Figure 3.5A). Cells cultured on circles showed a significantly higher displacement in response to the applied pressure than those on square and triangular shapes (Figure 3.5B). Since pipette resistance varied between measurements, the data was normalised for Young's moduli estimations which takes into account the effective force and displacement of the pipette. Young's moduli demonstrated that cells grown on circles were least stiffer with a mean value of 8.8 kPa, which was almost two-fold lower than those on square (14.4 kPa) or triangular (16.1 kPa) shaped micropatterns (Figure 3.5C).

A

	Mean	SD	SE	Mean	SD	SE	Mean	SD	SE
Height (μm)	10.04	2.75	0.41	9.71	1.65	0.23	9.86	1.61	0.27
Volume (μm³)	2507	971	143.2	2527	730	103.3	2396	688	114.7

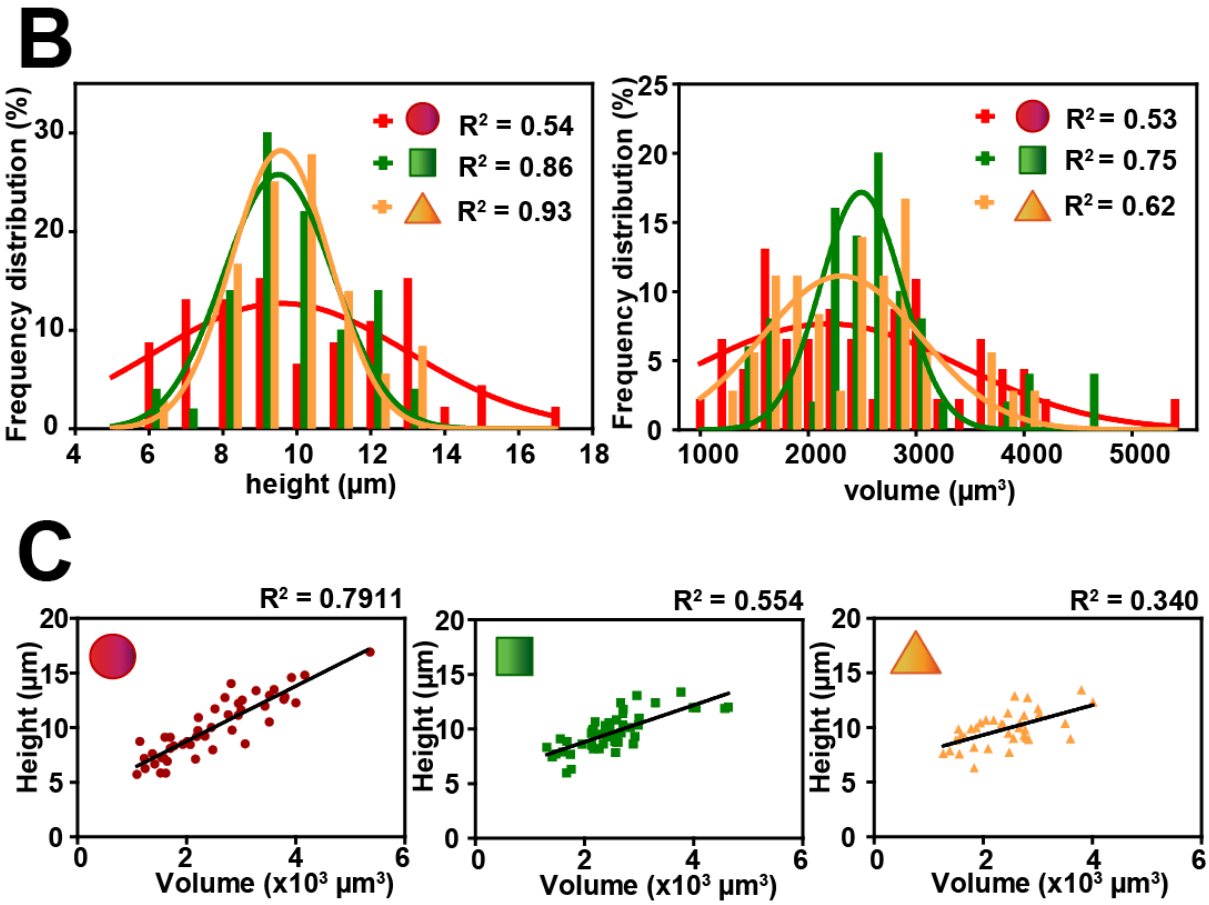

Figure 3.4: Cells grown on different shaped micropatterns have remarkably similar heights and volumes but follow different distributions. Cell height and volume were calculated using SICMImageViewer software. (A) Table of average cell heights and volumes showing the mean, standard deviation (SD) and standard error of the means (SEM) for each of the three shapes. (B) Frequency distribution graphs for height (left) and volume (right). (C) Correlation graphs of height to volume for cells grown on circular, square and triangular shapes patterns respectively (left to right). R^2 values for the best-fit lines are shown within (B) or on the top right (C) of each graph. Dr. Sanchez-Alonso contributed to acquisition, analysis and interpretation of data.

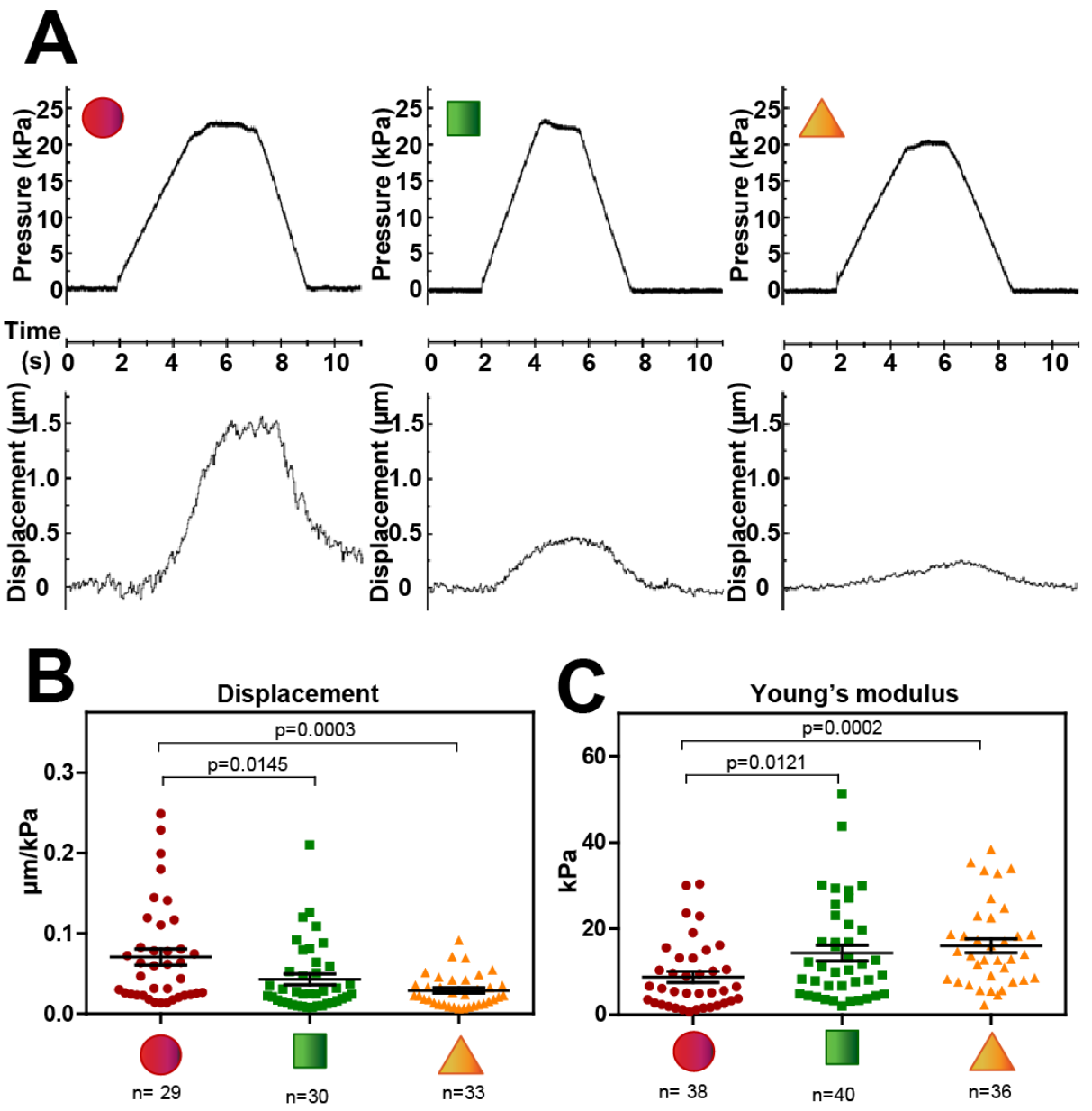

Figure 3.5: Cells grown on triangular and square shaped micropatterns are stiffer (less compliant) than those on circular micropatterns. Pressure was applied to the cortex of each cell in a pair with the use of a modified scanning ion-conductance microscope and the resulting displacement micrographs computed using Clampex (pClamp software). (A) Pressure (top row) and displacement (bottom row) line traces for cells seeded on circular, square and triangular shaped patterns respectively (left to right). (B) Quantification of displacement of the cellular cortex. (C) Quantification of Young's modulus. Graphs represent values per cell. Error bars represent SEM. Data were analysed statistically by one-way ANOVA followed by Tukey post-hoc test. N numbers for individual cells are shown below each of the shapes. Data are representative of 4 independent experiments. Dr. Sanchez-Alonso contributed acquisition, analysis and interpretation of data.

3.3.5 Efficiency of recovery and relaxation to baseline is affected by cell shape

To gain further insight into the behaviour of doublets in response to the externally applied pressure, displacement micrographs for each shape were closely examined. The displacement of cell membranes in response to pressure application revealed differences in the time required for relaxation and to return to baseline state (before pressure application) (Figure 3.6A). Relaxation time refers to the time taken for cells to reach the baseline displacement from the time the pressure applied starts to decrease. This parameter was significantly lower in the cells grown on triangular shapes (3.9 s) in comparison to cells on both circular and square shapes (5.2 s and 4.8 s respectively) (Figure 3.6B). The fact that cells grown on triangles have the highest Young's modulus and recover fastest implies that these cells are most resistant to changes in height as a result of the pressure and are therefore less elastic. Conversely, cells grown on circles, have the highest elasticity. They not only deform the most in response to pressure but also take the longest to recover due to the greater displacement of their cortices.

The average recovery, which refers to the final displacement as a percentage of the baseline value before pressure application, was highest for cells on triangular shapes at 94.7%, next in squares at 89.7% and lowest in circles at 84.5% (Figure 3.6C). The efficiency of cell recovery to baseline was further assessed through the percentage of cells that recover more or less than 90% (Figure 3.7D). A majority of cells on all three different shapes recovered more than 90% and cells on triangles had the greatest majority of 82% while those on circles and squares were 53% and 60% respectively. It is likely that cells grown on triangular micropatterns recover more efficiently as they have more resistance to deformations, their cortices displace less and they recover faster than cells on circles. In contrast, cells sharing a circular micropattern are more elastic and undergo greater changes to their cortices making full recovery harder to achieve.

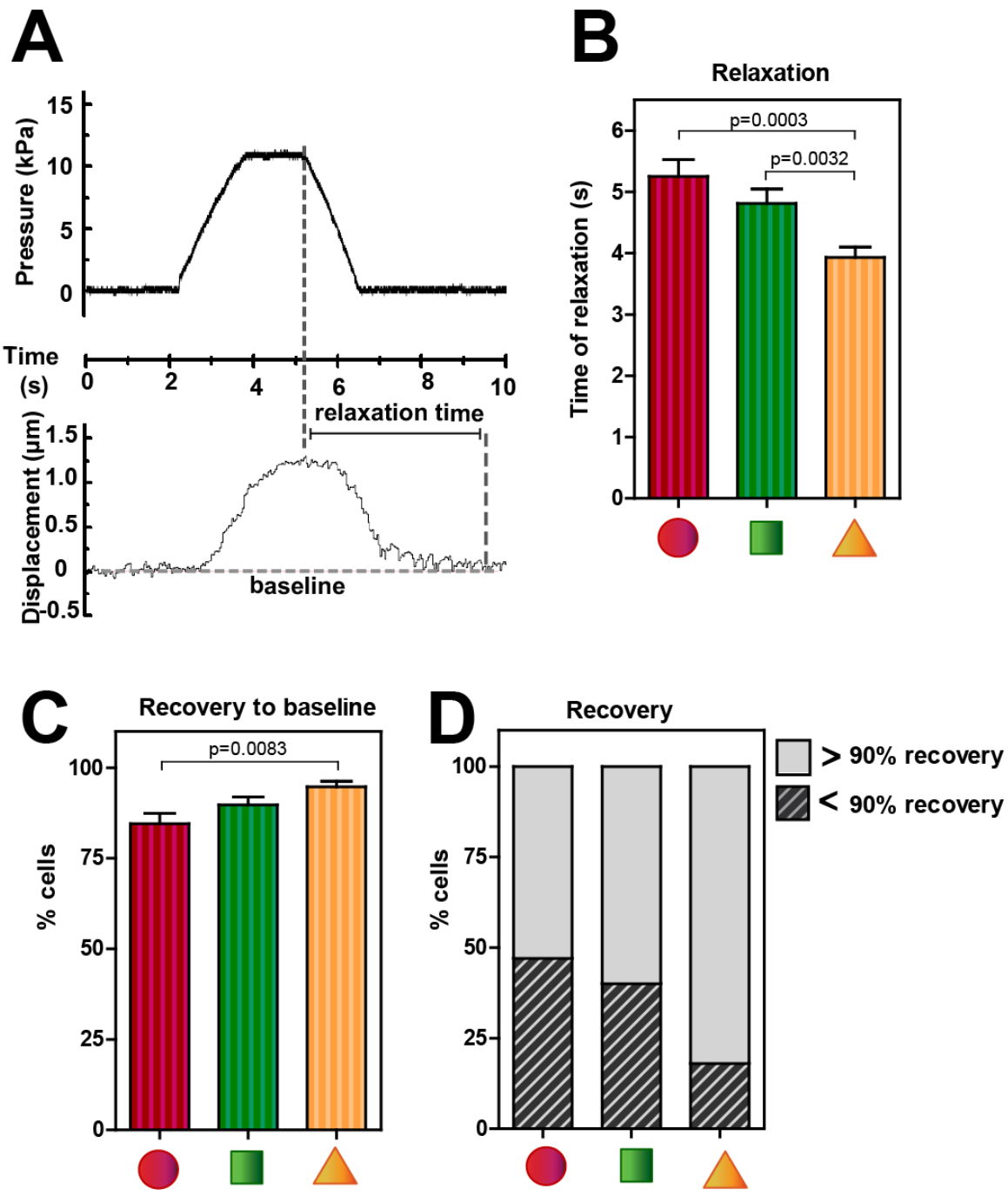

Figure 3.6: Cells grown on circular micropatterns have a longer relaxation time and recover less efficiently than those on triangular and square shaped micropatterns. The relaxation time and recovery to baseline compliance were computed with the use of pressure and displacement micrographs in Clampex (pClamp software). (A) Pressure (top left) and displacement (bottom left) line traces for a typical cell indicating the baseline and relaxation time measurements. (B) Quantification of relaxation time. (C) Quantification of the percentage of cells that recovered to baseline. (D) Graph of percentages of cells that recover more or less than 90% of the baseline value. Graphs represent the mean with error bars indicating SEM. Data were analysed statistically by one-way ANOVA followed by Tukey post-hoc test. Data are representative of 4 independent experiments. Dr. Sanchez-Alonso contributed acquisition, analysis and interpretation of data.

3.3.6 Cell height and volume differ within a pair of cells sharing the same micropattern

The varying displacement of the cortices, recovery dynamics and stiffness of doublets in micropatterns of different shapes lead me to look at individual cells within a pair occupying the same micropattern to perceive shape-imposed differences on neighbours. There was a wide range of values of volume and height displayed through individual measurements of cells in each shape (Fig.3.4 B, C). This raised the question whether cells sharing the same micropattern behave differently to its neighbours despite having the same adhesive area available to them to initially attach to. Individual cell height and volume were quantified for cell pairs on the same micropattern. Indeed, there is a clear distinction of values between neighbours for both height and volume despite similar average values on each micropattern for both parameters. Individual cell heights and volumes were calculated by separating the cells through the junction between them and mapping each cell to its partner to depict differences in values (Figure 3.7A and B).

It was observed that while all cell pairs in a particular shape have a discrepancy in their cell heights, the difference was statistically significant for cells cultures on square and triangular shaped micropatterns (Figure 3.7C). To quantify the significance of the trends observed, the difference in values were calculated for each cell pair within a pattern and plotted (Figure 3.8A). The difference in cell heights was significantly higher in cells grown on triangular micropatterns compared to square shapes.

Individual cell volumes within a micropattern were also significantly different within each micropattern (Figure 3.7B and C– right). However, cell volumes were not distinct between micropatterns (Figure 3.8B). Heights and volumes have been quantified in this chapter, adhesion areas of cells will be quantified in Chapter 4.

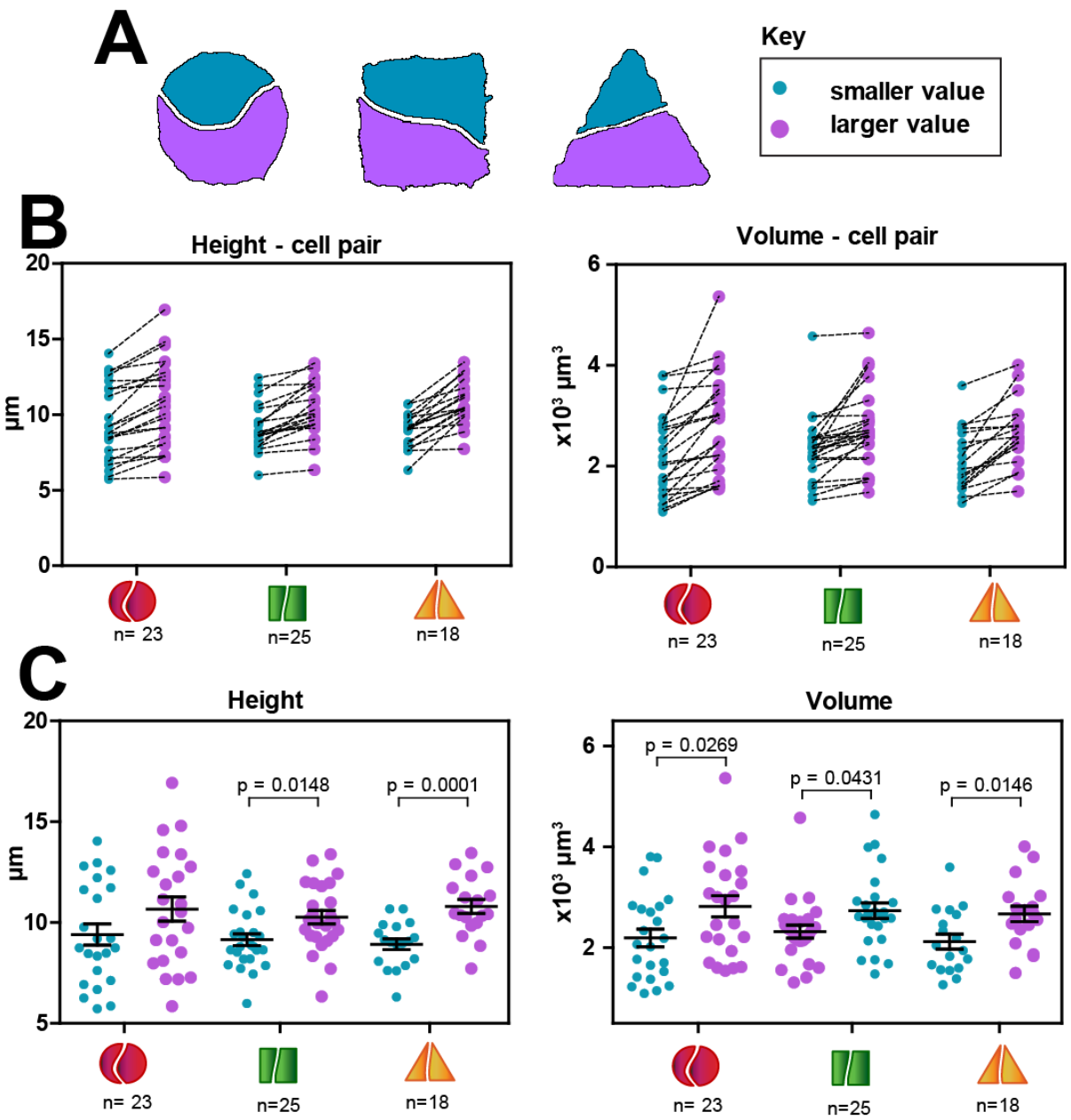

Figure 3.7: Cell pairs grown on different shaped micropatterns have different heights and volumes to each other. Cell height and volume were calculated using SICMImageViewer software. (A) Schematic of cells on micropatterns. (B) Measurements obtained for individual cells sharing a micropattern were then ranked according to their value for height (left) or volume (right), and represented as pairs of cells joined with an interconnecting line. (C) Graph of average height (left) and volume (right) of cell pairs sharing a micropattern. N = number of cell pairs. Data were statistically analysed using an unpaired t-test for doublets in each geometry. Data are representative of 4 independent experiments. Dr. Sanchez-Alonso contributed to analysis and interpretation of data.

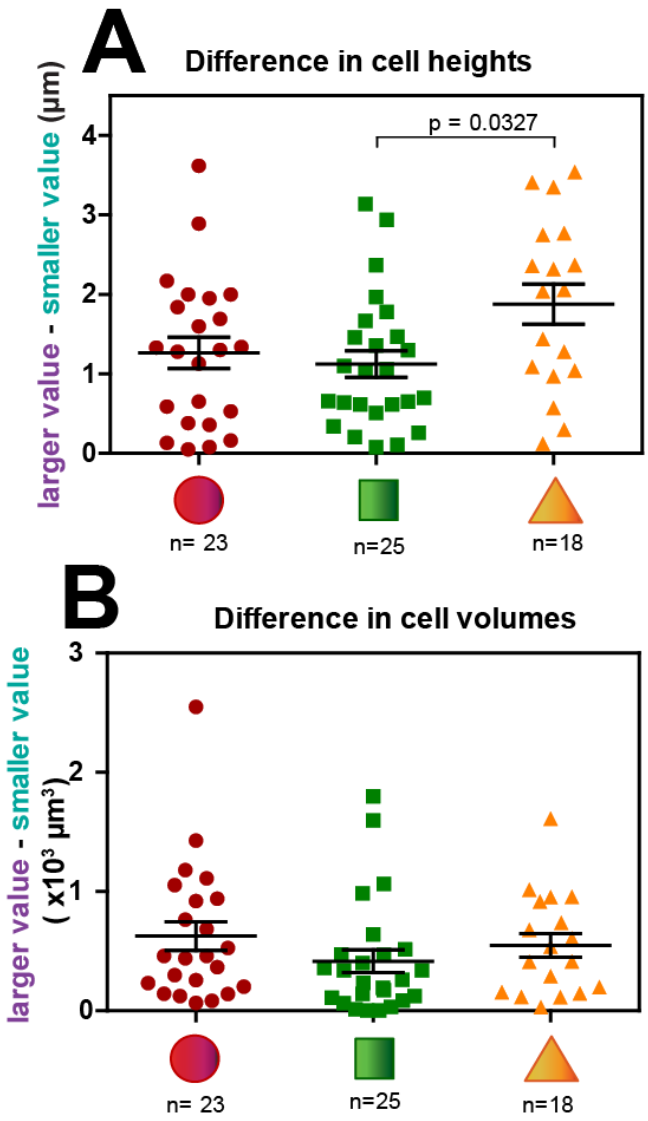

Figure 3.8: The difference between cell heights is larger in cells grown on triangular micropatterns compared to those on square shaped micropatterns. Cell height and volume per cell pair were calculated using SICMImageViewer software. (A) Quantification of difference in height between each cell in a pair. (B) Quantification of difference in volume between each cell in a pair. Error bars show SEM. Data were analysed statistically by one-way ANOVA followed by Tukey post-hoc test. N = numbers of cell pairs analysed and are shown below each of the shapes. Data are representative of 4 independent experiments.

3.3.7 The Young's moduli of cell pairs vary in difference but not in ratio between the different shapes

The results obtained so far suggest that cells grown on triangular micropatterns have the highest Young's modulus values (Figure 3.5C). The heights and volumes, of individual cells in a triangular micropattern are also significantly distinct. This led me to question whether there would be variations on cortical tension between cells sharing different micropattern shapes. Young's moduli of cells within a pair were mostly dissimilar on those on square and triangular shaped micropatterns but this difference was statistically significant only between cell pairs on the square shape (Figure 3.9B). However when comparisons were made between geometries, the differences between Young's moduli of cell pairs grown on triangles (5.5 kPa) and squares (5.0 kPa) were almost twice as high compared to that in circles (2.1 kPa) (Figure 3.9C).

Furthermore, there was no correlation between the cortical tension of a cell in a pair with its height or volume (Figure 3.10). I concluded that the differences in Young's moduli between cell pairs in square and triangle shapes could not be attributed to height and volume of corresponding cells but are likely to be a result of the intrinsic properties of these cells, possibly the inherent tension imposed by the different geometries.

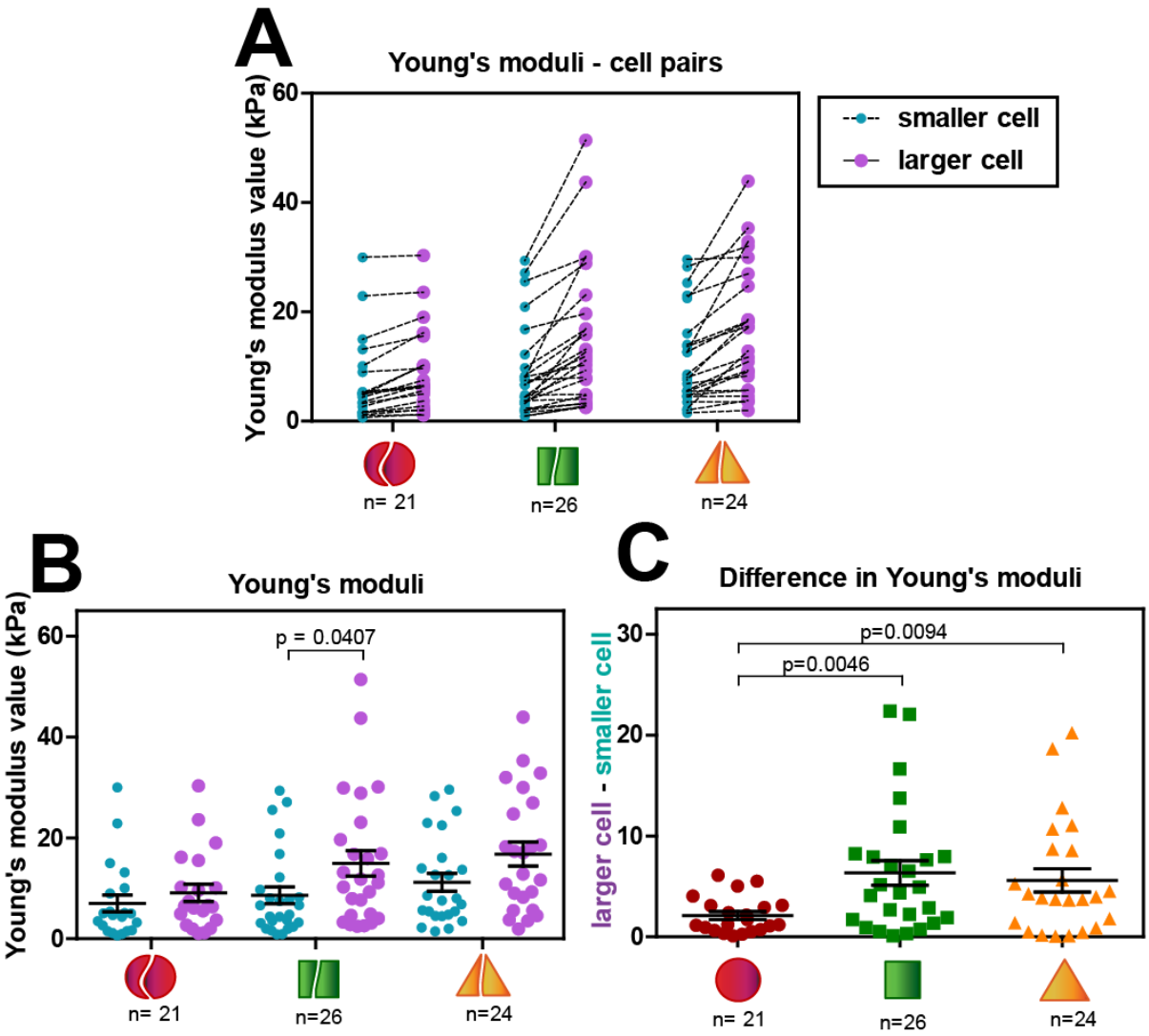

Figure 3.9: Cells grown on different shaped micropatterns have different Young's moduli to each other. Young's moduli for each cell within a pair was calculated using displacement micrographs computed using Clampex (pClamp software). (A) Graph of Young's moduli of pairs of cells joined with an interconnecting line to represent those sharing the same micropattern. The values are measurements of each cell in a pair. (B) Graph of average Young's modli of cell pairs sharing a micropattern. Data were statistically analysed using an unpaired t-test. (C) Quantification of the differences in Young's moduli between each cell in a pair. N = numbers of cell pairs analysed and are shown below each of the shapes.Error bars show SEM. Data were analysed statistically by one-way ANOVA followed by Tukey post-hoc test. Data are representative of 4 independent experiments. Dr. Sanchez-Alonso contributed to analysis and interpretation of data.

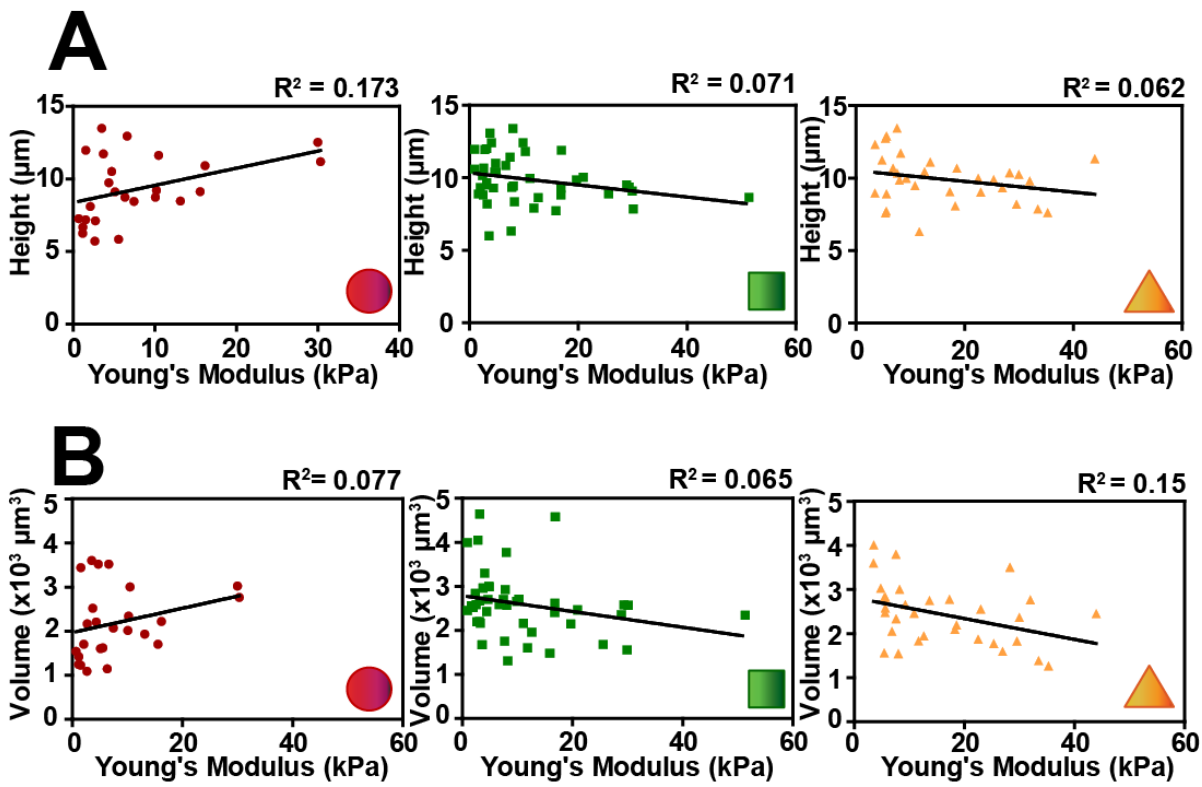

Figure 3.10: There are no significant correlations between Young's modulus with either height or volume of each cell. Correlation graphs of Young's modulus to height (A) and volume (B) for cells grown on circular, square and triangular shapes patterns respectively (left to right). R^2 values for the best fit lines are shown on the top right of each graph. Data are representative of 4 independent experiments. Dr. Sanchez-Alonso contributed to analysis and interpretation of data.

3.3.8 Cell pairs change their speed and direction of movement according to geometric shape

Changes in the cortical stiffness of cells due to variations in cell shape revealed that the dynamic behaviour of cells also differs between shapes. As seen previously, doublets recover differently after deformations caused by pressure application. To unravel the behaviour of live doublets on the three shapes without any external physical stimuli, phase contrast time lapse microscopy was used. Doublets of keratinocytes seeded on micropatterns of circular, square and triangular shapes were seen to dynamically move around each other. Over a period of 2.5 hours, during which video microscopy was carried out, cells rotate around each other by coordinating the orientations of junctions (Figure 3.11). Angles of junctions between the cells were computed with the use of Fiji (image analysis software) to calculate variations with time (Figure 3.12A). Resulting angle-time graphs were computed for each cell pair to obtain average angular speeds (Figure 3.12B). The results indicated that on average, cells grown on circles move around each other 0.6 °/min faster than those on squares which in turn move slightly faster (0.12°/min) than cells on triangles (Figure 3.12C).

It was also evident from the live videos that cells changed their direction of movement (clockwise to anticlockwise and vice versa) within each micropattern. Cells moving on circles were the most persistent with an average change in direction of 0.5 changes while cells on triangle changed their direction of movement at least twice (Figure 3.12D). The results indicate that cells dynamically rotate around each other such that cells grown on circles rotate at the fastest speed with the highest persistence, while cells on triangles rotate at a slower speed with the least persistence.

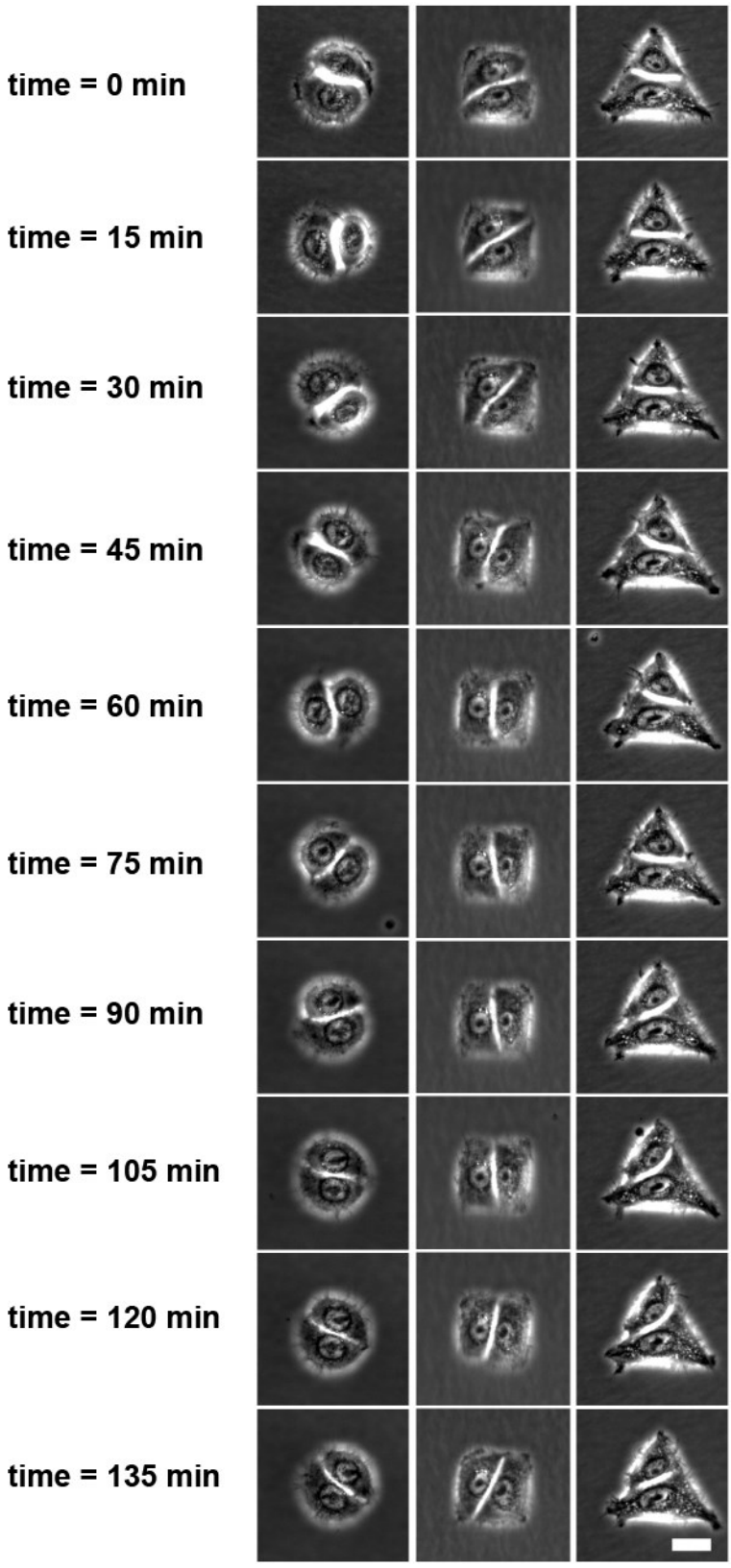

Figure 3.11: Movement of cell pairs on circular, square and triangular shaped micropatterns. Keratinocytes were seeded in the three different shapes and after 18 hours, cells were filmed by phase contrast time lapse video microscopy. Still images were captured every 5 minutes for 2.5 hours. (A) Representative images of doublets of cells grown on circular, square and triangular shaped patterns from 0-135 minutes. Scale bar represents 20 µm.

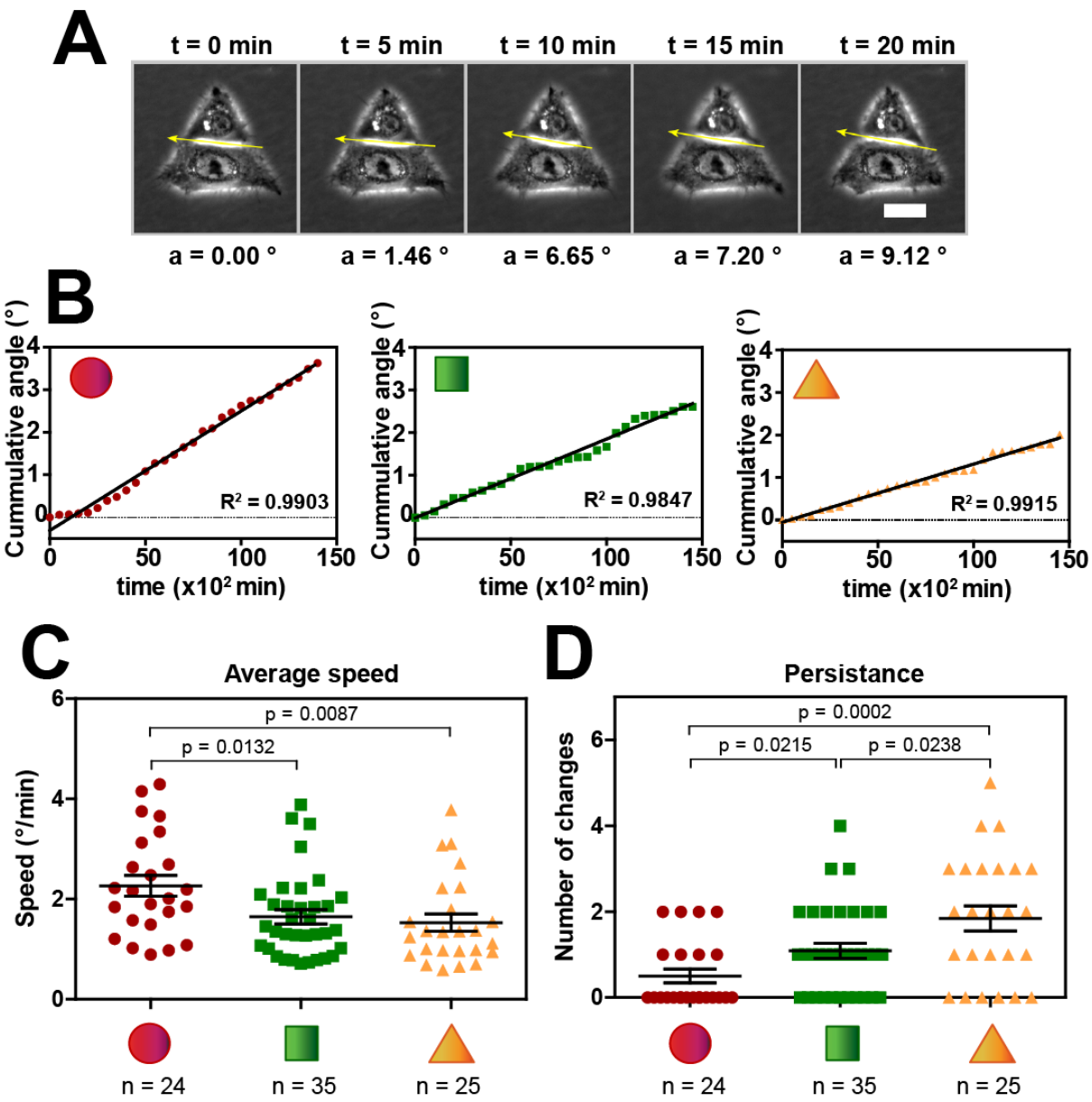

Figure 3.12: Cells grown on circular shaped micropatterns move faster than those on triangular and square shaped patterns and tend not to change the direction of movement. Angle of the junction between cells for each time point were measured using Fiji (image analysis software) and the resulting speed calculated. (A) Images of cells on a triangular shaped pattern with an arrow drawn parallel to the junction. Angle calculations relative to time zero positioning of the junction are shown below still images. Time in minutes is shown on top. Scale bar represents 20 µm. (B) Representative graphs of cumulative angle over time for cells grown on circular, square and triangular patterns (left to right). Values represent data points per cell for each of the shapes (C) Average speed of cells. (D) Changes in the direction of cell movement (persistence). . Values in C and D are per junction calculated as shown in (A). Error bars represent SEM. Data were analysed statistically by one-way ANOVA followed by Tukey post-hoc test. N = numbers of junctions per cell pair analysed and are shown below each of the shapes. Data are representative of 3 independent experiments.

3.4. Discussion

3.4.1 Keratinocyte cell pairs attach and spread optimally on micropatterns of 1300 μm² area

Here, the attachment of primary human keratinocytes was optimised to three different micropattern shapes: circles, squares and triangles, all of which expose the same adhesive area for cell attachment. Appropriate control experiments were performed to ensure that the adhesive area exposed by all three different geometries contained a homogenous distribution and equal density of ECM proteins to allow a fair comparison between shapes without bias from extracellular ligand presentation as these parameters have been shown to affect cell behaviour [179], [348]. Six different areas were tested and an area of ~1300 μm² emerged as the optimal micropattern area to contain well attached and spread keratinocyte doublets (Figure 3.2). This size is consistent with previous studies with mammary epithelial cells cultured in cell pairs in square shaped micropatterns of 35 μm width (1225 μm² area) [236] and MDCK cells grown in pairs on rectangular areas of 1225 μm² [237]. The importance of restricting primary keratinocytes in a specific cell area has been highlighted in past studies which show that (1) terminal differentiation of single keratinocytes is promoted by reduced contact with substratum [281] and (2) founding keratinocytes above a certain size (20 μm in diameter) lose their ability to form clones and instead commit to further enlargement and terminal differentiation [349]. Thus, it is important that cells are cultured in conditions of appropriate restrictions to mimic physiological spatial confinement to ensure a more relaxed state with imposed contractility [179].

3.4.2 SICM provides insights into morphological and mechanical properties of cell pairs

We used SICM to study the micro-features of keratinocyte cell surfaces cultured as doublets in spatially restricted geometries. 3D morphological imaging of cells on micropatterns has never been done before and provides informative insight into features defined by cell shape. Additionally, SICM is a non-invasive method that can acquire high resolution surface nano-topographies at short time scales. In our case, a 30 x 30 μm scan took approximately 5 minutes similar to other studies with comparable scanning areas and resolutions [308]. The 3D topographical maps of keratinocytes on circular, square and triangular micropatterns clearly depict surface characteristics such as membrane

protrusions on the free surface of cells in all three shapes. The average cell height and volume measured on the three different shapes does not differ, but follows different distributions (Figure 3.5). The average volume of ~2500 μm^3 obtained for human keratinocytes in this study is consistent with previously measured volumes of single fish epidermal keratocytes using two different techniques (2060 μm^3 and 2210 μm^3); integration of height maps obtained by AFM and fluorescence displacement respectively [350]. However, the height of fish keratocytes (3.65 µm) could not be compared as they spread extensively compared to cells restricted on micropatterns. The apical height reconstructed through fluorescent confocal microscopy of primary keratinocytes cultured in our lab has been reported to be 10 µm [351], which is in line with the average cell heights reported in my study for all three shapes. Lulevich et al. also measured by AFM a compatible average cell height of 10 µm for human keratinocytes grown as single cells [318]. Despite the lack of height measurements for cells on micropatterns, our results reveal that cell pairs which are differentially restricted maintain the cell heights as recorded for keratinocytes in alternative culture conditions.

In an earlier study, Watt and Green found that primary keratinocytes attaching to collagen coated coverslips exhibited a range of different cell sizes from 5-45 µm in diameter and separation by density gradient centrifugation yielded 12 µm as the peak diameter established by most keratinocytes [352]. Similarly, Kalaji et al. revealed a distribution of keratinocyte cell areas ranging from 2-14 x 10^3 pixels with the highest frequency occurring at 4 x 10^3 pixels [116]. Although our study restricts the adhesion areas of keratinocytes and are grown in doublets compared to cells in a monolayer, cells continue to display heterogeneity in sizes as shown by their heights and volumes measured through SICM.

Analysis of individual cell heights and volumes of doublets sharing the same micropattern reveals that indeed there are inconsistencies in height and volume between neighbouring cells in all three of the micropatterns. One such cell frequently exhibits a higher value compared to its neighbour implying that these two cells follow different distributions and can therefore be separated into distinct classes. When frequency histograms were plotted for each class, the distributions varied between them in

square and triangular geometries more than circles (data not shown). In line with this, the difference, calculated between two neighbouring cells in a micropattern, is exacerbated on cell pairs cultured on the squares and triangles. These results indicate that the geometry of cell pairs affects cell morphology such that a decrease in the vertex angle of shapes (from circles to squares to triangles) coincides with a greater discrepancy in cell height and volume. These results cannot be compared with previous studies as heights and volumes of isolated cell pairs have not been reported before. Thus our results provide novel insights into the behaviour of keratinocytes in response to varying geometries.

The mechanical properties of human keratinocyte cell pairs were measured for the very first time in this study to compute values for the Young's moduli of cells cultured on circular, square and triangular shaped micropatterns. Here we used the measurement of cell cortex stiffness as a surrogate to the measurement of membrane elasticity at junctions. The SICM technique assumes measurement of flat, freely deformable surfaces but junctions form between cells in their lateral domain and cannot be flat. In the case of cell pairs within a micropattern, junctions between cells are not always linear and the upper limit of the lateral junction height may not always be directly approachable through the surface, due to differing conformations of cell pairs. Direct application of pressure at junctions was therefore avoided in order to alleviate these complications.

A typical plot profile of pressure over time shows that the pressure applied to the cells was between 20-25 kPa with the use of a slow pressure ramp (Figure 3.5A). The use of a slow pressure ramp ensured that cell health could be continuously monitored and the pressure adjusted accordingly to prevent force induced blebs as seen with single keratinocyte cells that were compressed using AFM [318]. Cells on circles have the lowest Young's modulus of 8.8 kPa with deformations of 0.7 µm. This value is comparable to Young's moduli measurements of A6 toad epithelium kidney cells obtained by SICM (7.8 kPa for deformations of 0.75 µm) [304] and MDCK cells obtained by AFM (5-7 kPa) [353]. However, the Young's moduli for cells grown on triangles (16.1 kPa) and squares (14.3 kPa) were at least 60% higher than those in circles. The higher cell tension observed in cell doublets cultured on square and

triangular shaped micropatterns is consistent with the higher contractility, determined by the peripheral actin stress fibre density (quantified in the next Chapter), reported for single cells grown on similar geometric shapes [265].

A separate study of isolated single keratinocytes grown on expansive areas of culture dishes reported much larger Young's moduli values of at least 120 kPa for primary cells (Normal human keratinocytes, NHK) and comparable values of ~ 22 kPa for cell-lines (NEB-1 and KEB-7) measured by a modified AFM probe containing a hemisphere [318]. The difference in values with those obtained by SICM may be due to differences in techniques, adhesive surface area and number of cells. Therefore one needs to exercise caution when comparing cells cultured on micropatterns with those that are not, as restrictions in shape impose varying cytoskeletal tensions to cells and thereby alter their elastic moduli.

Young's moduli values computed for individual cells within a pattern varied between each other such that one cell could be classed as 'stiffer' than the other. Distinct classes were obtained from the fact that they followed different frequency distributions (data not shown). The difference between values of Young's modulus was significantly higher in cell pairs cultured in squares and triangles compared to those on circles. Interestingly, a minority of cell pairs (20-30%) in squares and triangles exhibit a large difference in the value of their Young's modulus (i.e. one cell is much stiffer than the other). Although rare, the existence of such cases likely contribute to the significant differences observed seen between shapes.

The analysis of recovery of cells after pressure application has never been studied in depth previously and provide invaluable information into the behaviour of cells upon pressure application. Sanchez et al. reported pressure and deformation graphs for studies on red blood cells, epithelial cells and neurons but detailed analyses of the aforementioned parameters were not included [311]. Our results show that cells on the triangular micropatterns, which exhibit the lowest elastic compliance, display the fastest relaxation and most efficient recovery possibly because of their smaller displacements.

Cells grown on circles are highly compliant (more elastic) and therefore more deformable (higher displacement). Their surface membranes take longer to reach the baseline as they are displaced more and do not recover as effectively.

In addition to the global values of Young's modulus elasticity of cell pairs across the different shapes, individual cells on the same micropattern elicit discrepancies in all three of the different shapes. When quantified, cell pairs on triangles have a significantly larger difference in Young's moduli between the two cells sharing the same micropattern. Furthermore, and there are no significant correlations between the Young's modulus of an individual cell with either its height or volume. These results indicate that the biophysical properties displayed by cell pairs on the different micropatterns may be attributable to the inherent cytoskeletal tensions imposed on them and are independent of morphological cell parameters such as height and volume.

3.4.2 Dynamics of cell pairs differ according to the tensions imposed by shape restrictions

Here I studied how changes in cytoskeletal tensions mediated by spatial restrictions of cells grown on circular, square and triangular micropatterns affect cell motility in doublets. My studies show that the speed and direction of movement of cell pairs within micropatterns vary according to the geometries they attach to. However, all cell pairs unanimously exhibit a continuous rotational motion. Collective rotational motion has been reported in many biological processes involving migration [354]–[358]. This rotational phenomenon plays a pivotal role in the formation of a spherical geometry during morphogenesis of mammary epithelial cells [359], while the loss of this rotational motion is pre-eminent in cancer cells [360]. The tendency of two cells to rotate around their geometric centre while maintaining directionality has been termed 'symmetry breaking' of the intrinsically random and therefore 'symmetrical' motion that individually cultured single cells display [328], [361].

The motion can be either clockwise or anticlockwise with equal probability depending on initial conditions [362]. Three minimal conditions that cells must satisfy in order to entertain this phenomenon are (1) spatial restriction where motile cells are cultured in defined microenvironments,

(2) persistence where cells move in the same direction and (3) dynamic coupling where a cell exhibits an increased propensity to follow its neighbour upon physical contact [361], [363]. The importance of the latter parameter was first observed by Verchovsky when mechanical induction by tapping the 'back' of a cell with a pipette lead to polarized forward motion [364]. Additionally, Li and Sun showed that chemical signalling between cells is not essential for rotational motion and that mechanical cues brought about by the geometric shapes and material properties of substrates which affect cell elasticity, contraction and adhesion are the determining factors [331], [362], [365]. Our results suggest that symmetry-breaking brought about by the mechanical coupling of doublets is best achieved in cells cultured in circles as they maintain the highest directional persistence while being constrained [328].

A physical model to explain the behaviour of constrained cell-cell clusters predicts that persistent steady rotation of cell pairs predominantly depends on actomyosin forces while the sigmoidal shape of the cell-cell junction is mostly attributed to cortical tension [363]. These studies were done with either bovine capillary endothelial or NIH 3T3 cell pairs cultured on circular and square shaped micropatterns ranging from 30-50 µm in diameter and width respectively [328], [361]. In contrast, NBT-II tumour derived epithelial cells plated on unpatterned glass in 2-8 cell clusters failed to exhibit sigmoidal cell-cell interfaces [366]. As the number of cells in the cluster increases from 2-8, the rotary migration and its persistence decreases and is inversely correlated with cell contractility. These data are consistent with our results that show cells on circular shapes display the lowest contractility, and the highest directional persistence. The absence of the sigmoidal junction interface between some of the epithelial cells may be a result of the short junction widths observed between them compared to endothelial cells cultured on micropatterns [363]. The junctional interface between primary keratinocytes cultured on micropatterns in our study is not always sigmoidal, but displays a certain extent of curvature. Morphological features of junctions including junction curvature and width will be addressed in depth in Chapter 5.

Similar to the rotation of single cells [367] and doublets [328], [361], speed and coherence (persistence) of nuclei rotation of single cells on circular micropatterns are drastically reduced when actomyosin contractility was lowered with the use of blebbistatin [367]. The absolute angular velocity of the nucleus is inversely correlated to contractility such that the nuclei of single cells on triangular micropatterns exhibit the slowest rotation while those on circular micropatterns have the highest. These results can be explained using a hydrodynamics approach, in which the nucleus is modelled as a rigid inclusion in the fluidic cytoplasm enriched with active filaments and intrinsic stresses. Perturbation of the actomysoin network leads to incoherence brought about by disorganised fibres within the cytoplasm. Peripheral actomyosin fibres may play a more structural role in confining the nucleus through enhanced friction supressing its motion. Rotating nuclei have attracted attention for decades [368], [369] but the notion of a rigid nucleus passively responding to active cytoplasmic stresses [367] facilitated by the microtubule motor dynein [370], [371] is recent. The principal mechanism of rotation of the cells causing intracellular flows that in turn rotate the nuclei has been proposed to be driven by the interaction between dynein and the microtubules [370]. Insight into nuclear positioning in cells cultured in the different shapes will be provided in Chapter 4.

In conclusion, I have shown in this chapter that the mechanical properties of cell pairs and their motility are geometry-dependent such that cells on square and triangular shapes stiffer. Membrane tension does not correlate with cell height or volume and is thus likely to be driven by the cortical constituency (eg. Actomyosin filament distribution). In addition, neighbouring cells sharing the same micropattern display different Young's moduli values, particularly on geometric shapes imposing the highest tension. In line with the observations on rotating nuclei and the physical explanations above, my study shows that the average angular speed and directional persistence of rotation of cell pairs negatively correlates with cell stiffness, suggesting that the geometry of cells and their stiffness plays an important role in affecting the dynamic behaviour of cell pairs.

CHAPTER FOUR:

Cytoskeletal organization and positioning of cells, organelles and junctions driven by geometric shape.

4.1 Rationale

Each tissue in the body comprises unique arrays of cells held together by the extracellular matrix (ECM) which has a specific composition and fibrillar architecture giving rise to distinct mechanical microenvironments [372], [373]. Cellular traction forces, exerted by actomyosin interactions and transmitted to the ECM through stress fibres and focal adhesions, maintain tensional homeostasis [294] and direct many cellular functions [374]. Traction forces play a pivotal role in morphogenesis, wound repair and disease and are regulated by actomyosin-generated tension dependant on cell size and shape [375]. Cell morphology regulates the magnitude of traction forces such that higher forces are generated when cells spread on large patterns of micropost arrays [376]. Additionally, these forces are determined by the geometry of the cells (distance from centre to perimeter) and regulated by focal adhesions [377].

Microcontact printing was originally used by Ingber and Whitesides to study the relationship between individual cell shape and their cytoskeletal structure by generating adhesive islands of varying geometries and sizes [289], [378]. Cells are able to sense the shape of ECM patterns and generate spatial cues that guide the deposition of new ECM and preferentially extend lamellapodia dictated by the geometric features encountered [379]. Parker et al. observed that individual cells cultured on square adhesive islands were able to sense edges and extended lamellapodia at corners as the diagonal offers a longer axis along which the cell may spread [263]. This increase in cell spreading preferentially promotes actin filament alignment due to tension moulding within the actin lattice and actin bundles align with the straight edges of the geometry [290]. Conversely, cells on circles contain no such edges owing to the radial symmetry of the shape and instead, extended cell processes at random points along their circumference [263]. Thus, the local curvature of the perimeter affects cellular architecture such that concave features promote the assembly of stress fibres whilst convex features encourage the assembly of lamellopodia [380].

Cells on different geometries exhibit morphologically distinct patterns of contractility determined by the underlying actomyosin network. Myosin II is essential for actin dynamics, bundle assembly and the stability of cytoskeletal shape due to the contraction dependent alignment and organization of the actin filaments [381]. Modulating the adhesive areas of the pattern geometry alters the distribution of stress fibres [295]. Inhibition of myosin function leads to more concave cell borders, suggesting that (i) contractile stress fibres oppose membrane tension at cell borders and that (ii) focal adhesions are unevenly distributed on non-migrating cells [295] and (iii) cells develop large tensions at bridges between micropatterned adhesion sites and these are enriched with actin and myosin filaments. Inhibition of either myosin II or actin polymerisation collapsed the actomyosin network and hence the bridges [382].

The microenvironment of a cell comprises of two spatially segregated regions, the extracellular matrix and neighbouring cells [228]. However, both of these regions cooperate extensively through signalling between the cell-matrix and cell-cell adhesions facilitated by the intricately linked actomyosin network of epithelial cells [383]. Modulation of cell-ECM traction forces through extracellular matrix ligands and substrate stiffness affects the endogenous tension at cell-cell contacts of MDCK cells such that cell-matrix and cell-cell forces are positively correlated [231]. Using a system of microfabricated force sensors, Liu et al showed that endothelial cell-cell tugging forces, which occur perpendicular to the junction, grew upon myosin activation and induce increases in adherens junction length in Bowtie micropatterns [124]. In this system, the Bowtie pattern was used to capture two cells and promote interaction between them. Furthermore, the ECM also has an impact on the spatial organisation of cell-cell contacts such that junctions positioned themselves on areas deprived of ECM to resist large perpendicular tensional forces from the ECM to increase junctional stability [236].

Mechanical forces exerted on surface adhesion receptors, whether it be integrins for cell-matrix forces or cadherins for cell-cell forces propagate to the cytoplasm and nucleus through the intimately connected cytoskeletal filaments [384]. The nucleus, possibly the most prominent cellular organelle,

is sensitive to forces that act from the microenvironment such that its shape, size and cellular location are affected [270], [385]–[387].

It is clear that previous studies of cell pairs on micropatterns have exclusively focused on quantitative classifications of cytoskeletal tension rather than the structural organisation of actin and myosin, which are fundamental to cellular contractility. These studies have also used different types of cells, substrates, spatial constraints and ECM adhesion ligands and the interdependence of cell-matrix and cell-cell forces has not been consistently addressed. In this chapter, we focus on the shape-dependent, peripheral actomyosin network of primary keratinocyte cell pairs and how this affects the actomyosin network at the junctions between them.

4.2 Hypothesis and aims

I hypothesise that the actomyosin contractility dictated by cell shape, impacts the behaviour of cells and the positioning of nuclei and intercellular junctions. In order to study the characteristics of shape imposed contractility of cells, I aimed to:

(i) characterise the pattern of the actomyosin network of cell pairs at the cell peripheries and cell-cell junctions
(ii) determine the effect of cell shape on how doublets distribute the space available to them (cell area and nuclear area)
(iii) investigate the positioning of the junction between cells and determine preference in orientation
(iv) examine the distance between nuclei to correlate effects of tension on the positioning of nuclei

4.3 Results

4.3.1 Cell pairs on different geometric patterns follow similar actin distributions to single cells

The cytoskeleton is the key to the mechanical integrity of cells: the filamentous polymer network modulates cell mechanics, migration and signalling events that can modulate a myriad of functions [30]. Identification of specific cellular structures within cell pairs for comparison between the three different geometric shapes necessitated the use of confocal microscopy. Images taken with a confocal microscope had much higher resolution than its widefield counterpart and could be used for three-dimensional reconstructions. Similar to cells cultured in the absence of calcium, preventing cell-cell contact formation [388], E-cadherin receptors on single cells displayed diffused staining throughout the cytoplasm as expected without cell-cell adhesion. F-actin staining of single keratinocytes attached to square and triangular shaped micropatterns clearly illustrated the accumulation of thick stress fibres on the edges of these geometries compared to single cells on circular micropatterns, which had more dispersed actin [295] (Figure 4.1A).

E-cadherin accumulated at the cell-cell contacts of doublets attached on all three shapes as seen in Figure 4.1B. Thick F-actin stress fibres remained at the edges of cell pairs grown in square and triangular shaped micropatterns despite the presence of a junction between them. Cells on circular micropatterns had more dispersed actin around the edges of the shape as seen for single keratinocytes. Two populations of actin are generally present in the vicinity of epithelial junctions, junctional actin directly at the junctions and thin bundles parallel to junctions [25]. There was a distinct presence of thin bundles adjacent to cell-cell contacts in doublets seeded on square and triangular micropatterns, suggesting that the peripheral actin distributions contribute to rearrangement of actin at cell-cell contacts.

To confirm the peripheral actin distributions seen previously, fluorescence intensity heatmaps were generated. These represent average signal intensities of many micropatterned cells on the same shape, from which intensity data at any spatial location within the cell can be obtained. E-cadherin

heat maps of single cells on micropatterns showed dispersed staining throughout the cytoplasm with no clear increase in any particular location (Figure 4.2A – left). F-actin intensity was much higher at cell peripheries corresponding to edges of the geometric shapes for cells grown on square and triangular shaped micropatterns. Cells grown on circles had a more random distribution of F-actin without major hot spots (Figure 4.2A - right). The heat maps of E-cadherin for doublets clearly indicated the redistribution of much of the E-cadherin to cell-cell contacts between two cells grown on micropatterns of all three shapes (Figure 4.2B- left). Accumulation of F-actin at the edges of the micropattern as previously seen with in Figure 4.1B was clear for cells grown on the square and triangular shaped micropatterns. The variability of the superimposed F-actin on the different images made it is impossible to differentiate between the different actin populations at junctions. Taken together these results indicate that the shape-imposed cytoskeletal organization of actin as seen in single micropatterned cells [265], [295] is maintained even in the presence of cell-cell contacts between neighbouring cells.

4.3.2 Inter-nuclear distance between cell pairs is affected by geometry

The striking patterns of thick stress fibres aligning with the borders of square and triangular shapes strongly suggest that these geometric shapes impose tensional constraints on cells. I next investigated whether such enhanced contractile forces impact on the positioning of the nucleus (Figure 4.3A), using as a read out the inter-nuclear distance. Nuclear positioning has been shown to be affected by integrin engagement with the ECM [266], [277] as well as cadherin binding at neighbouring cells [270].

The distance between nuclei of cells sharing the same micropatterns was quantified by thresholding the two nuclei of cells in the DAPI channel and calculating the distance between their centres using FIJI image analysis software (Figure 4.3B). The inter-nuclear distance of cell pairs on squares (14.9 µm) was significantly higher than those on circles but lower than that on triangles. These results indicate that an increased tension observed in triangles and squares correlates with nuclei locating themselves further apart within cell pairs.

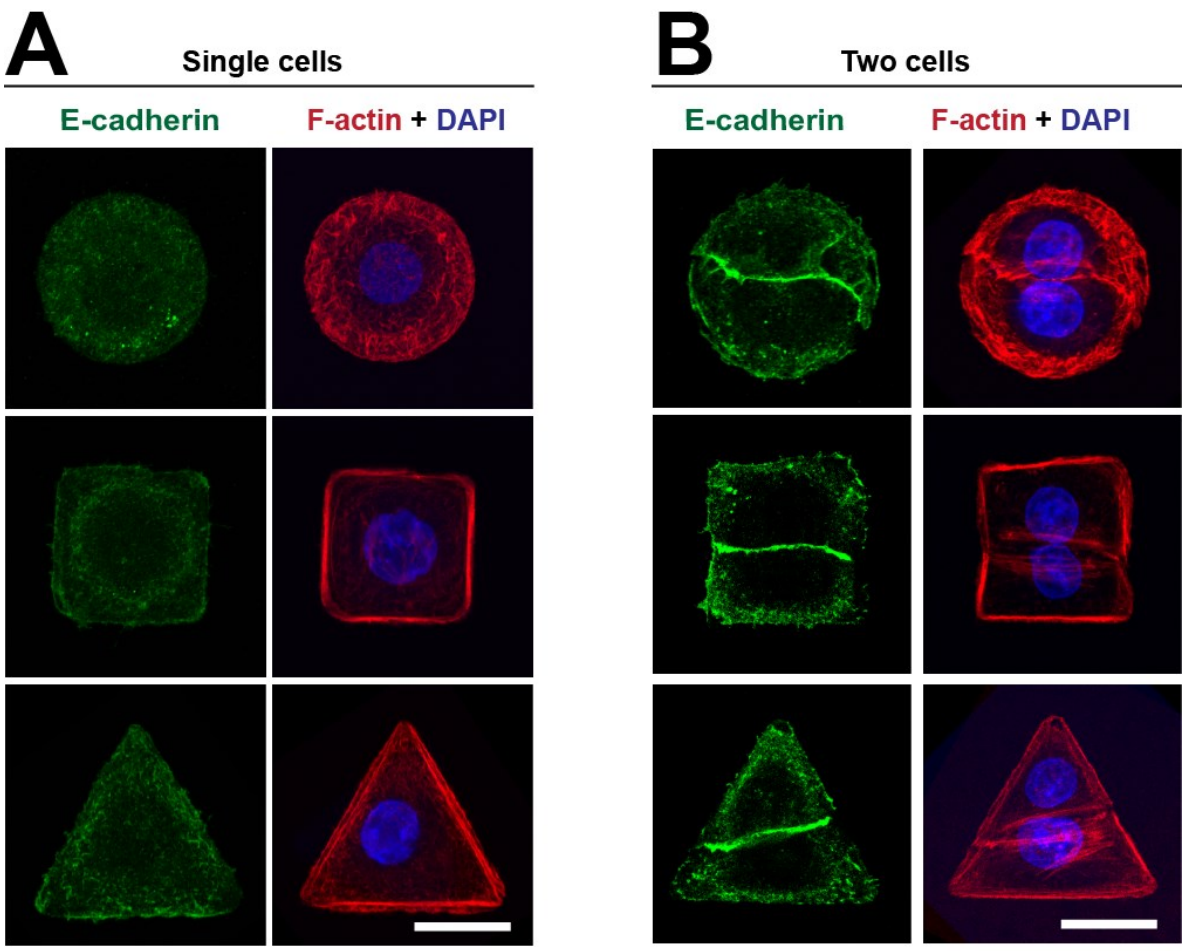

Figure 4.1: Cell pairs grown on micropatterns have similar pattern of peripheral actin labelling as single cells. Keratinocytes were co-stained for E-cadherin (green), F-actin (red) and nuclei (blue). Images were taken on a confocal microscope and the two z-planes of best focus with clear staining summed in FIJI. Immunofluorescence images of single cells (A) or cell pairs (B) grown on circular, square and triangular (top to bottom of column) shaped micropatterns. Scale bars represent 20 µm.

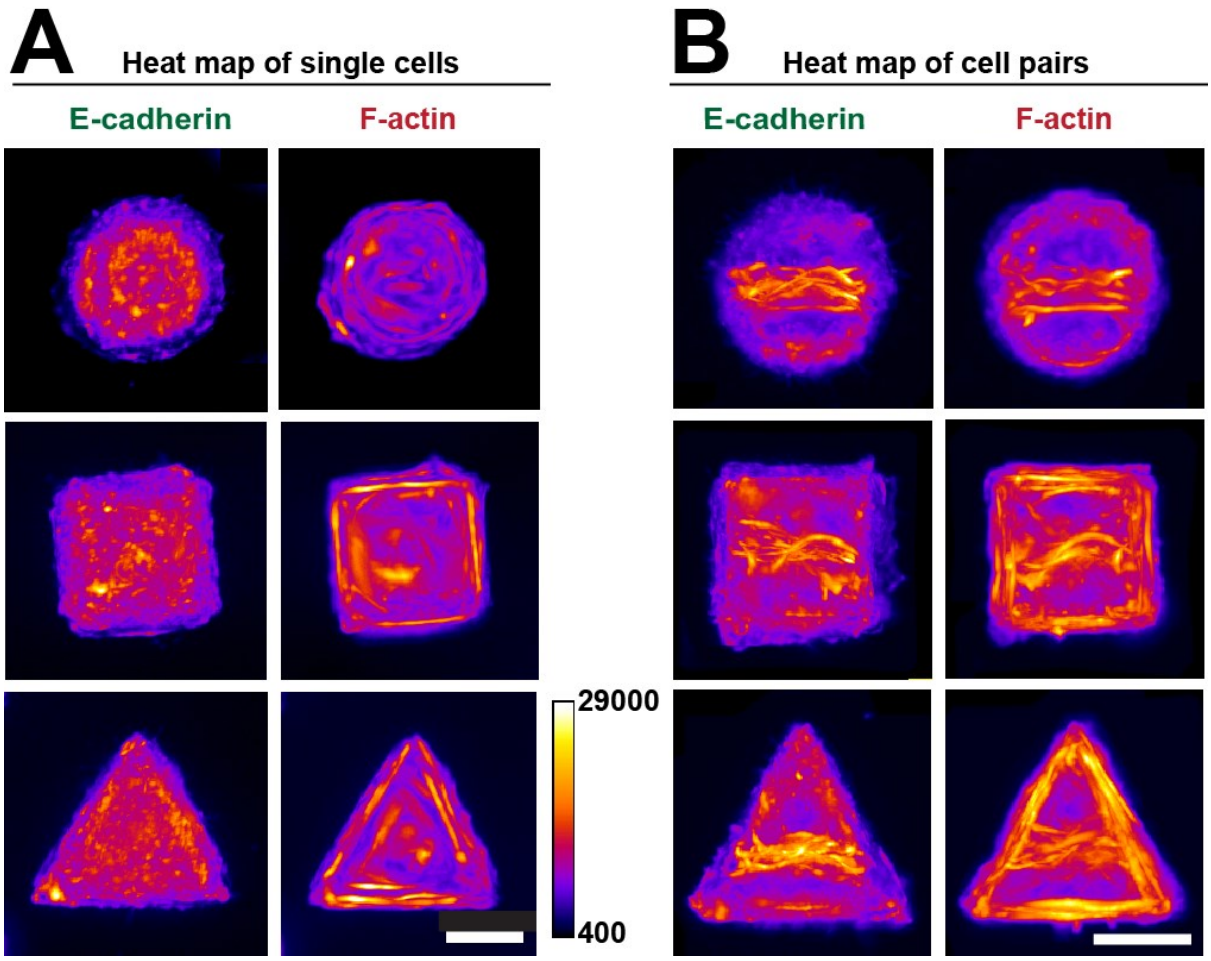

Figure 4.2: Heat maps show actin stress fibres at the periphery for square and triangular shaped micropatterns containing single cells or doublets. Images of keratinocytes stained for E-cadherin (right) or F-actin (left) were overlaid on top of each other to create a stack on Fiji, these were then projected onto a single slice with maximum intensity to create the heat maps. Heat maps of single cells (A) or cell pairs (B) grown on circular, square and triangular (top to bottom of column) shaped micropatterns. Scale bars represent 20 µm. Number of cells per heat map was 20-30 from a single experiment.

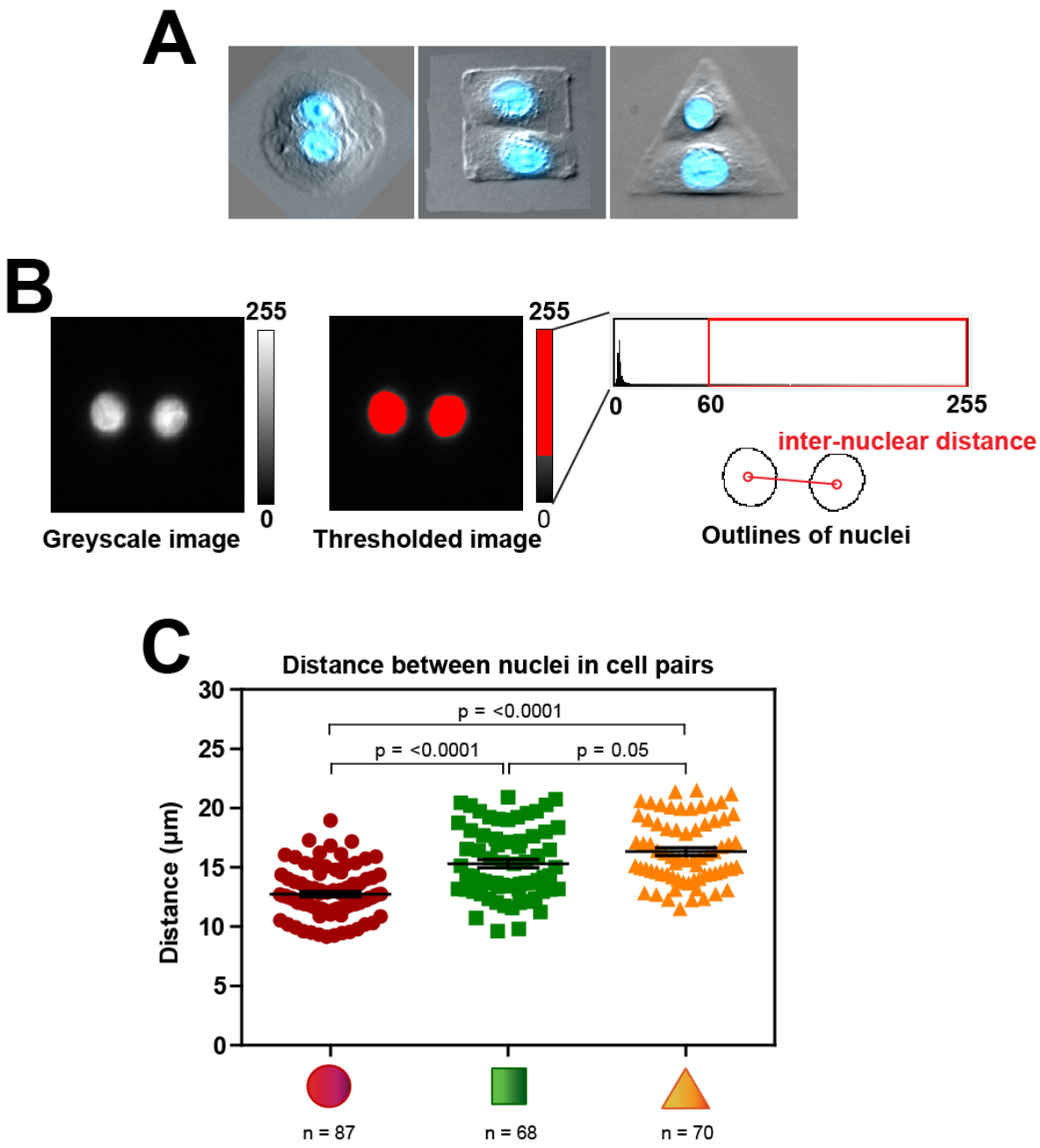

Figure 4.3: Nuclei of cell pairs grown on square and triangular shaped micropatterns are positioned further apart than those on circular micropatterns. Distance between nuclei were calculated using Fiji. (A) Phase-contrast (grey) images of keratinocytes stained for nuclei (blue) on circular, square and triangular shaped micropatterns (left to right of row). (B) Quantification technique on Fiji involved converting the image to greyscale (left), thresholding the nuclei represented by the brighter regions (middle) and calculating the inter-nuclear distance (bottom-right) between the centres of nuclear outlines. (C) Quantification of inter-nuclear distance between cell pairs grown on different geometric shaped micropatterns. Graph represents values per pair of nuclei. Error bars show SEM. Data were analysed statistically by one-way ANOVA followed by Tukey post-hoc test. N = numbers of cell pairs analysed and are shown below each of the shapes. Data are representative of 4 independent experiments.

4.3.3 Cell areas differ between a cell pair on the same micropattern

In the previous chapter, I have shown that cell heights and volumes vary significantly among doublets sharing a micropattern of different geometry (Figure 3.8). This result implies that cell areas must vary between neighbours so that the differences in height may be compensated to some extent. To gain insight into how cells share the availability of space within the adhesive region of the micropatterns, individual cell areas were measured. The area enclosed by the cytoskeleton was selected and the two cells were split by their junction (Figure 4.4A), separated according to size and plotted pairwise to obtain Figure 4.4B. All cell pairs within a micropattern have significantly dissimilar areas to each other. When the difference in areas was compared between shapes, there was a significantly larger difference of at least 52 μm^2 between cell areas of pairs grown on triangular micropatterns (219.4 μm^2) compared to those on square (167.1 μm^2) and circular (155.6 μm^2) micropatterns (Figure 4.5A). The total areas covered by doublets on micropatterns were also similar in all three shapes (Figure 4.5B). Thus, I concluded that cells do not share the space available to them equally and that cell pairs on triangles have a greater area discrepancy between neighbours consistent with what was seen for cell heights.

4.3.4 Area of nuclei are similar within cell pairs in the different geometric shapes

As cellular mechanical forces affect nuclear size [385], [386], [389], I next interrogated whether differences in cell areas carried through to nuclear areas. Nuclear areas were measured using Fiji by thresholding the brighter nuclei to obtain the two areas within a cell pair enclosed by their outlines (Figure 4.6A), and separating according to size and ranking as described above (Figure 4.6B and C). Although there were significant differences between the areas of nuclei of a cell pair within each geometric shape, further quantification revealed that the difference (~28 µm) in nuclear areas were not significant between the three shapes (Figure 4.6D). Total nuclear area also remained similar between the shapes (Figure 4.6E). We concluded that the individual fluctuations of nuclear areas within doublets did not significantly differ between shapes.

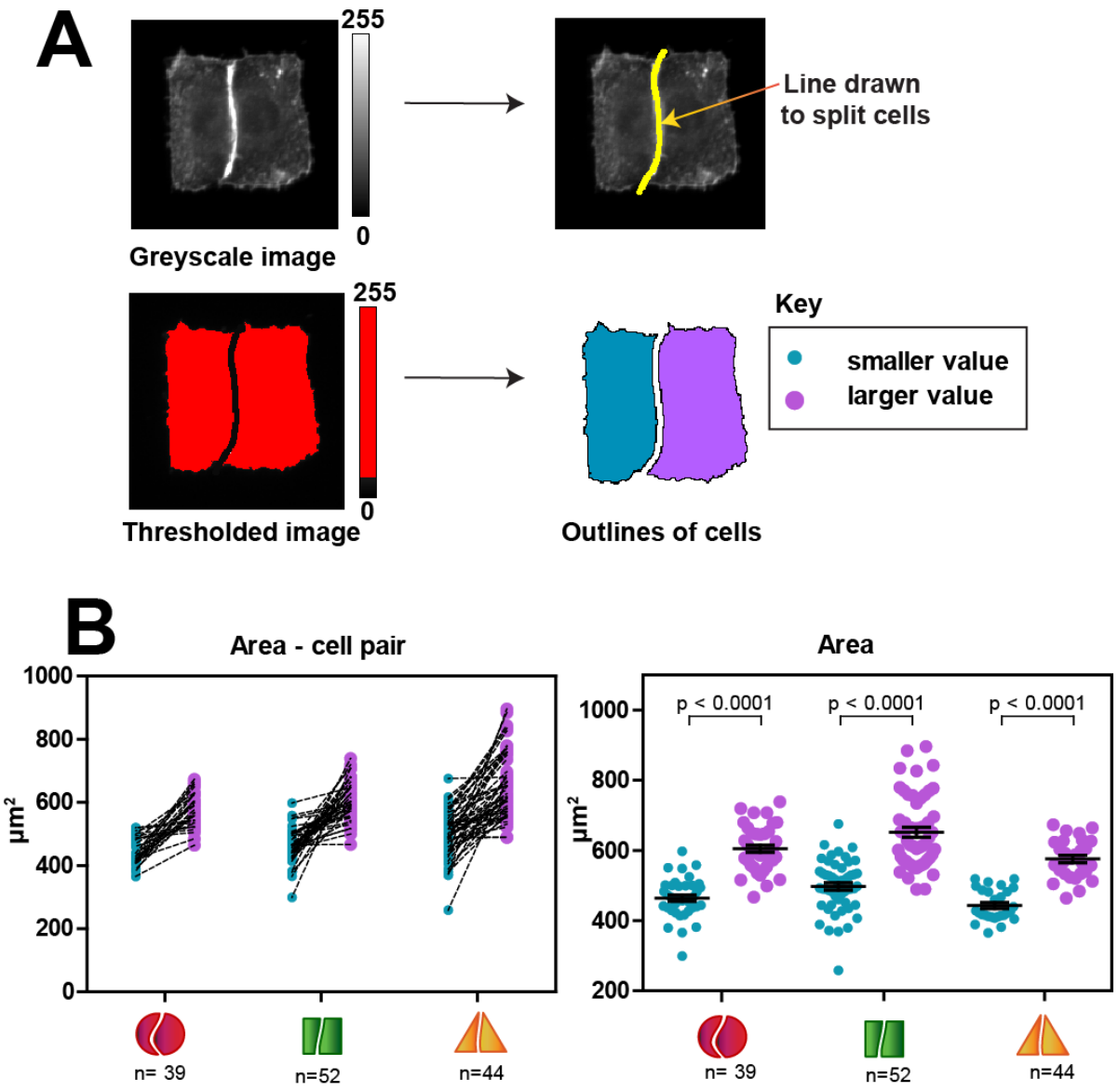

Figure 4.4: **Cell pairs grown on all three shapes have discrepancies in areas.** Cell areas were calculated using Fiji. (A) Quantification technique on Fiji involved converting the image to greyscale (top left), drawing a line through the junction to split the cells (top right), thresholding the cell contained by the cell boundary (bottom left) and obtaining areas for each cell in a pair. (B) Graph of areas of cell pairs are shown with an interconnecting line to represent those sharing the same micropattern (left) and mean areas of larger and smaller cells (right). N = numbers of cell pairs analysed for each of the shapes. Data are representative of 1 independent experiment.

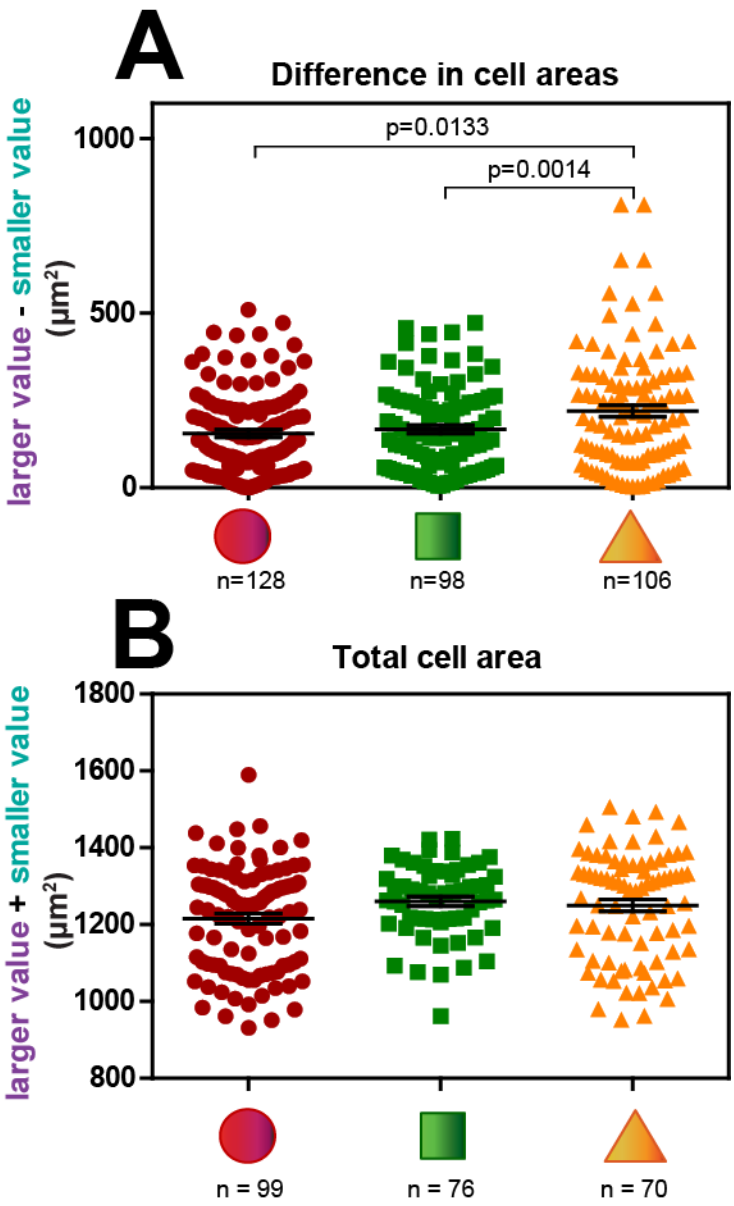

Figure 4.5: The difference between areas of cell pairs is larger in cells grown on triangular micropatterns compared to those on circular and square shaped micropatterns. Individual cell area within a cell pair was calculated using Fiji software as shown in Figure 4.4. Quantification of difference in area between each cell in a pair (A) and total area of both cells (C). Graphs represent values per cell pair. Error bars show SEM. Data were analysed statistically by one-way ANOVA followed by Tukey post-hoc test. N = numbers of cell pairs analysed and are shown below each of the shapes. Data are representative of 4 independent experiments.

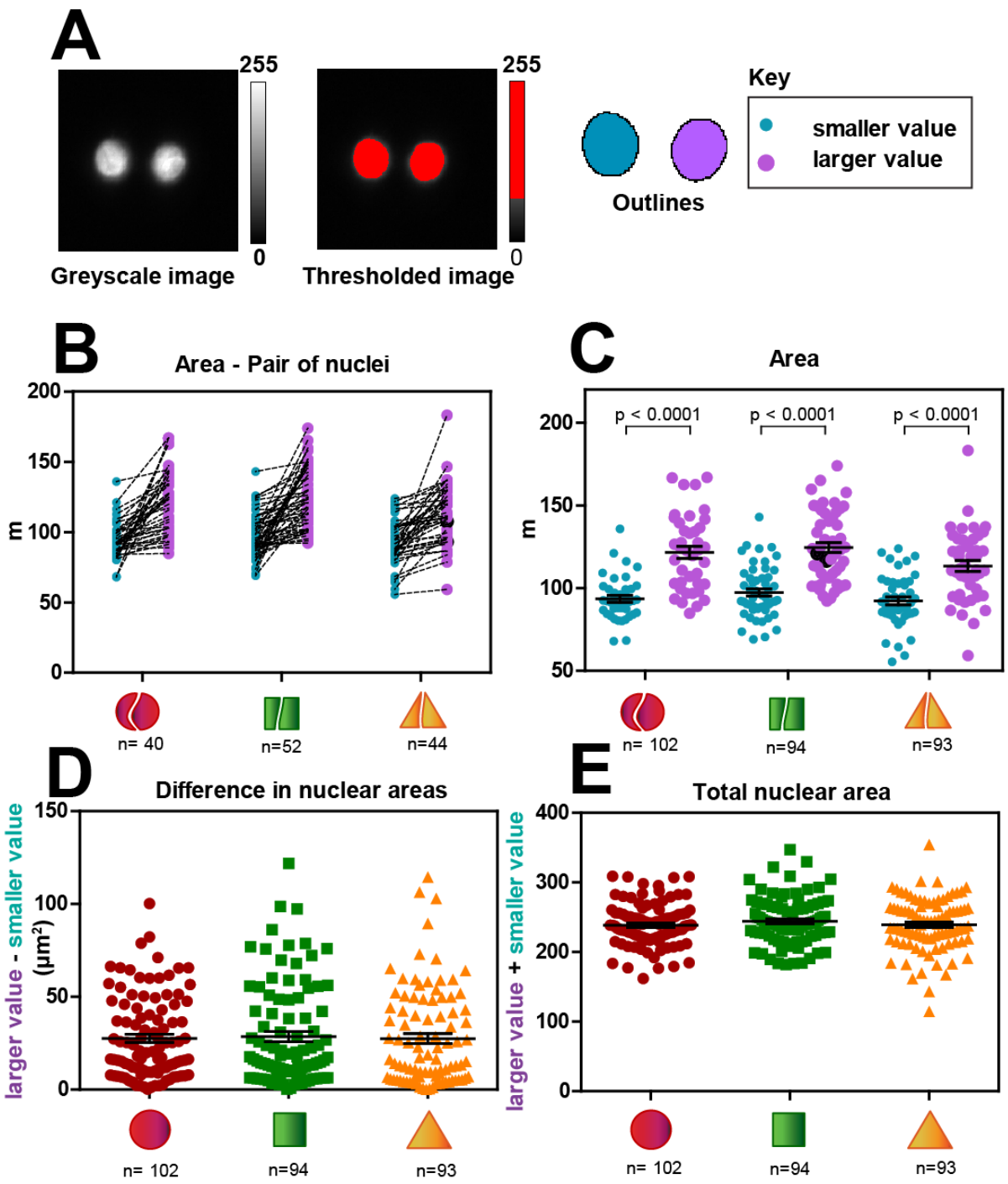

Figure 4.6: Nuclear area of cell pairs grown on the different shapes are similar. Nuclear areas were calculated using Fiji. (A) Quantification technique involved converting the image to greyscale (top left), thresholding the nuclei represented by the brighter regions (middle) and calculating the areas of nuclei enclosed by the outlines (bottom right). Graph of individual nuclear areas of cell pairs are shown with an interconnecting line to represent those sharing the same micropattern (B) and their means (C). Means were analysed statistically using an unpaired t-test. (D) Quantification of the difference in area between each nucleus cell in a pair (D) and total area (E). Data were analysed statistically by one-way ANOVA followed by Tukey post-hoc test. Graphs represent values per cell pair. Error bars show SEM. N = numbers of cell pairs analysed and are shown below each of the shapes. Data are representative of 4 independent experiments.

4.3.5 Cell pairs on squares and triangles show a preference in junction orientation

My data suggests that space is not equally shared by neighbours as the areas of individual cells are distinct both within a micropattern and between geometric shapes. I investigated whether these discrepancies would also extend to the way in which cells contact with each other, in particular, I addressed how these contacts are oriented within the micropattern and whether junction height is achieved and maintained in each of the geometric shapes. Junctions between cell pairs grown on square and triangular shapes fitted into two possible orientations. In contrast, cell doublets seeded on circular shapes had only one pattern: junctions spanning the equator region of the circle. (Figure 4.7A). A majority of cell pairs on square shaped micropatterns form their junction such that it spans opposing edges (82%) compared to junctions that pass through adjacent edges (18%). In the case of cells grown on triangles, a majority formed junctions through adjacent edges (88%) whilst the rest of the junctions were formed passing through an edge and vertex (12%) (Supplementary Figure S.2). However, since the probability of the junctions passing through the vertex of either the square or triangular shape is much lower than that passing any of the edges, the orientation percentages were compared to the probability of attaining each 5° region to yield Figure 4.7C. This result shows that cell pairs with junctions passing through a vertex is in fact 12% and 8% higher for squares and triangles respectively compared to the predicted probability of attaining such an orientation. In addition, we looked at whether junction height was distinct in different micropattern shapes, since cell heights were seen to vary in Chapter 3. In collaboration with Dr. Alonso-Mardones (Prof. Gorelik laboratory), SICM cell profiles acquired using SICMImageViewer software (Figure 3.4) were used to obtain the lateral height of junctions as indicated in Figure 4.8A. There was no apparent difference in junction heights between the different micropattern shapes with mean values of 7.2 µm, 6.48 µm and 6.47 µm for cell pairs grown on circular, square and triangular patterns respectively (Figure 4.8B). I next normalised junction height to the average height of the two cells within the micropattern. This analysis revealed no significant difference between the three different shapes, where the height of junctions is on average 32% shorter than the height at the top of the neighbouring cells (Figure 4.8C).

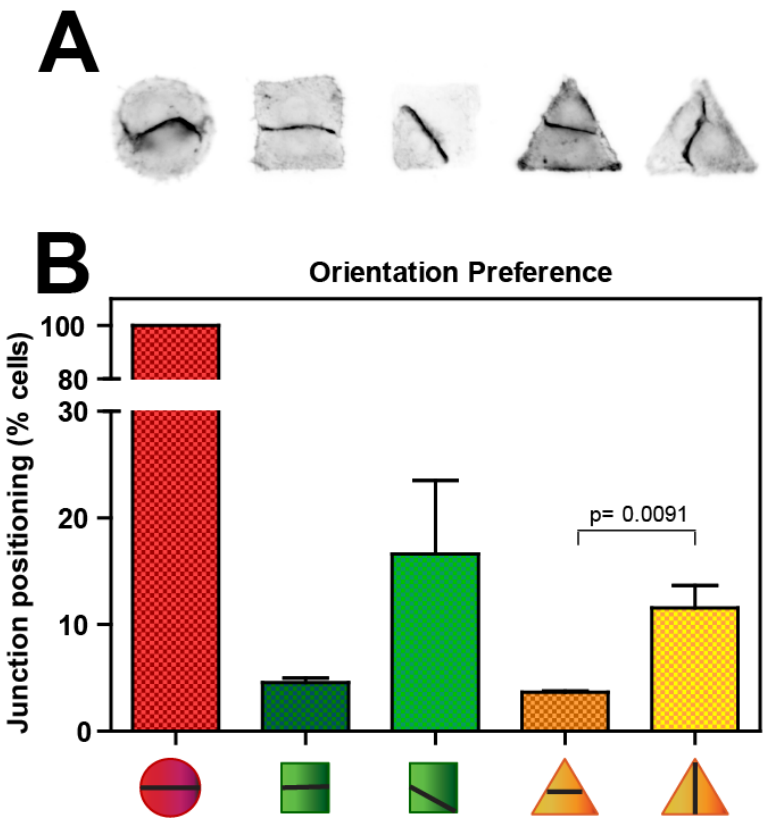

Figure 4.7: Cell pairs grown on square and triangular shaped micropatterns have preferences on the positioning of junctions between them. (A) Inverted immunofluorescence images of E-cadherin staining depicting different orientations of junctions for cells pairs on the three different shapes. (B) Quantification of percentage of cells (normalised to probability) achieving a given orientation of junctions. Error bars show SEM. Data were analysed statistically using t-tests for the two different orientations within a single shape (square or triangle). Data are representative of 4 independent experiments.

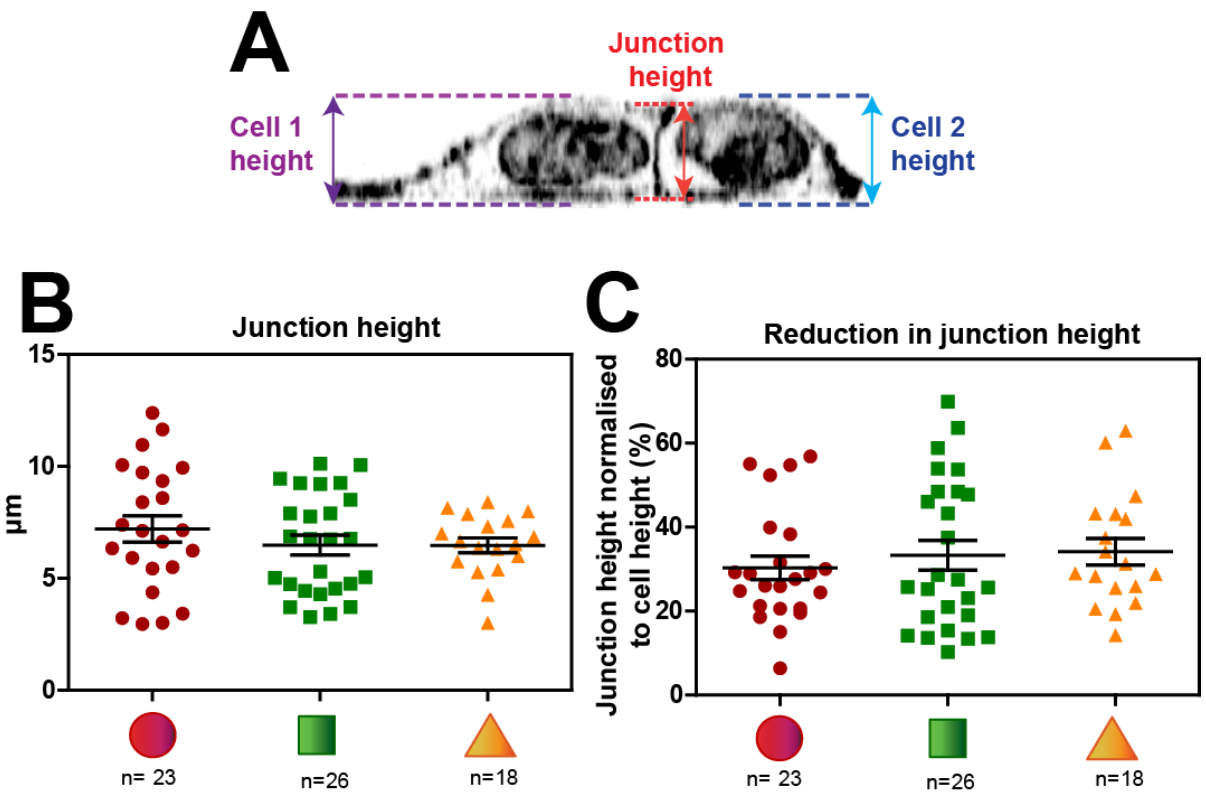

Figure 4.8: **Cells grown on different shaped micropatterns have similar junction heights but follow distinct distributions.** Cells were imaged using SICM and junction height calculated using SICMImageViewer software. (A) Inverted orthogonal confocal image of cell pair grown on a triangular micropattern stained with E-cadherin, F-actin and DAPI illustrating heights of interest. Quantification of averages of junction height per cell pair (B) and junction height per cell pair normalised to the average height of both cells sharing a micropattern (C). Graphs represent values per cell pair. Error bars show SEM. Data were analysed statistically by one-way ANOVA followed by Tukey post-hoc test. N = numbers of cell pairs analysed.

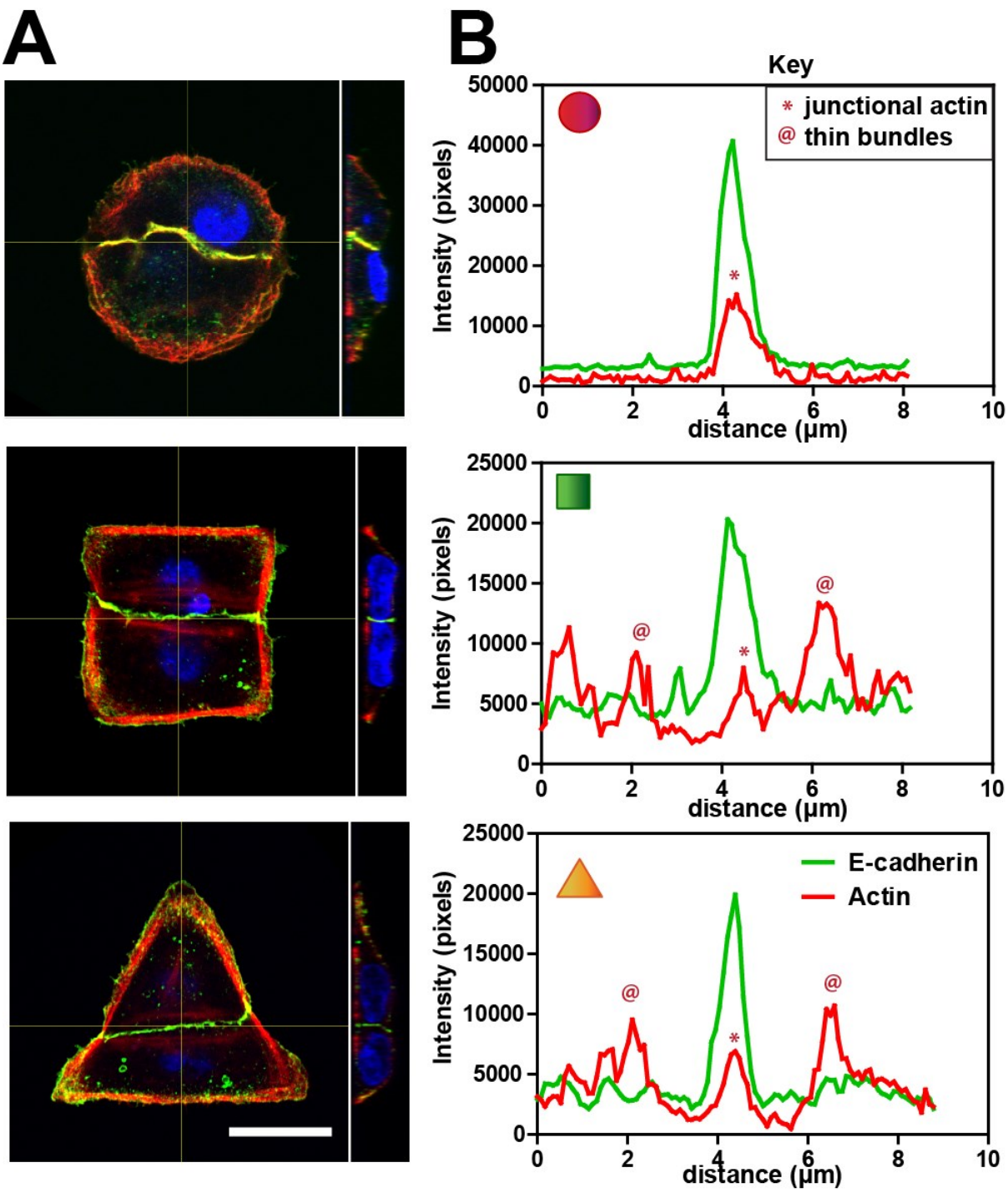

Figure 4.9: **Thin actin bundles are present on either side of the junction in cells grown on circular, square and triangular shaped micropatterns.** Keratinocytes were co-stained for E-cadherin (green), F-actin (red) and nuclei (blue). Images were taken on a confocal microscope and seven consecutive Z-planes of best focus were summed for each of the shapes in Fiji. Immunofluorescence images of cell pairs (A) grown on circular, square and triangular (top to bottom of column) shaped micropatterns with their respective E-cadherin and F-actin line traces through the junction extending to 4 µm on either side. Scale bars represent 20 µm. Images are representatives from one experiment.

4.3.7 Cells on square and triangular shaped micropatterns contain actin thin bundles

Epithelial polarisation is accompanied by an increase in the height of junctions, a process that requires actin contractility. Our lab has previously shown that the contractile actin population is found on circumferential thin bundles that compact towards cell-cell contacts [116]. Preventing contraction pharmacologically or via depletion of ROCK proteins results in cells that did not reach the full lateral height [116]. My previous data demonstrated a smaller spread in junction heights on the square and triangular shapes (Figure 4.8). Here, I investigated whether the parallel thin bundles were more consistent in these shapes. Confocal images of doublets grown on each micropattern were taken and line scans were drawn across the junctional area (Figure 4.9). Junctions between cell pairs always contained junctional actin in cells grown on all three geometric shapes. However, there was a distinct presence of thin actin bundles on either side of the junction of doublets grown on square and triangular shaped micropatterns (depicted by actin peaks marked with '@').

I next addressed the implications of higher contraction for the characteristic organization of epithelial cytoskeleton: the overall prevalence among different samples of junctional actin and parallel thin bundles. A majority of cells (78%) grown on square and triangular shaped micropatterns had thin bundles on either side of the junction while only 50% of cell pairs grown on circles contain thin bundles (Figure 4.12). Junctional actin was present in all cells that have cell-cell contacts. Since the presence of thin bundles adjacent to junctions implies that the junctions have increased adhesion tension [84],

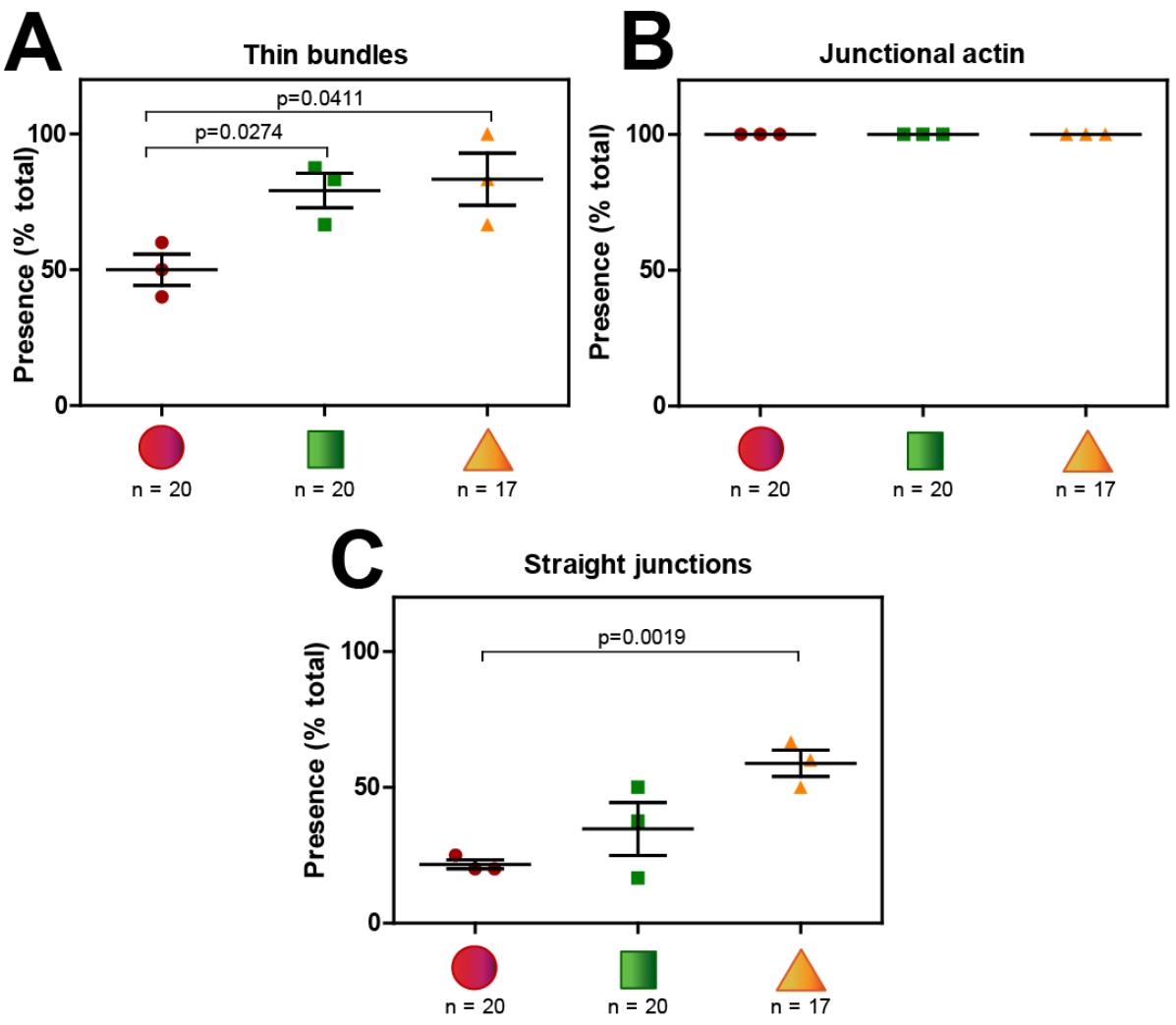

Figure 4.10: **A higher percentage of cells contain thin bundles when grown on square or triangular shaped micropatterns, while straight junctions are found predominantly on cells on triangular shapes.** Quantification of actin thin bundles (A) and junctional actin (B) for the three different shapes. (C) Quantification of percentage of straight junctions in the three different shapes. Graphs represent average values per experiment. Error bars show SEM. N = total number of cell pairs analysed per geometry. Data were analysed statistically by one-way ANOVA followed by Tukey post-hoc test. Data are representative of 3 independent experiments.

I quantified the proportions of straight junctions within cell-pairs as increased interfacial tension favours straight junctions to minimize contact area. Junctions of doublets grown on triangular shapes have significantly higher percentages of straight junctions (59%) compared to cells grown on circles (22%). Cells on squares (35%) also have straighter junctions between them compared to circles. Further analysis of junction configuration will be addressed in Chapter 5.

4.3.8 Myosin light chain II staining of cells unravels similar peripheral cell profiles to F-actin

Phosphorylated myosin light chain II (PMLC), was used as a marker of cytoskeletal contractility of keratinocytes for confirmation of cell shape induced differences in contraction between the three shapes. Thick stress fibres at the edges of the geometries in single cells cultured on square and triangular shaped micropatterns are labelled with PMLC (Figure 4.10A). In contrast, single cells on circular micropatterns had an abundance of peripheral lamella that were labelled with PMLC.

Cell pairs grown on the three different geometric shapes exhibited similar contractile structures to what was seen with single cells despite cell-cell contacts between neighbouring cells (Figure 4.10B), in line with my previous observation (Figure 4.1). F-actin side fibres were very often present in squares and triangles, but absent in circles (Figure 4.11). Lamella at the micropattern periphery was almost always present in circles (96%), but found in low abundance in cell pairs on triangular (48%) and square (29%) shaped micropatterns. PMLC labelling at stress fibres and lamella follows the same profile across different geometric shape (Figure 4.11 C and D). In conclusion, the cytoskeletal structure varies largely in a shape-dependent manner. Contractility, defined by the presence of actin stress fibres, labelled with the contractile marker: PMLC, at cell edges is high in square and triangular shaped micropatterns, while cells grown on circular micropatterns exhibit peripheral lamella instead giving rise to the characteristic low contractility known to this shape. Short, randomly oriented actin fibres at the cell peripheries were defined as lamella in my study.

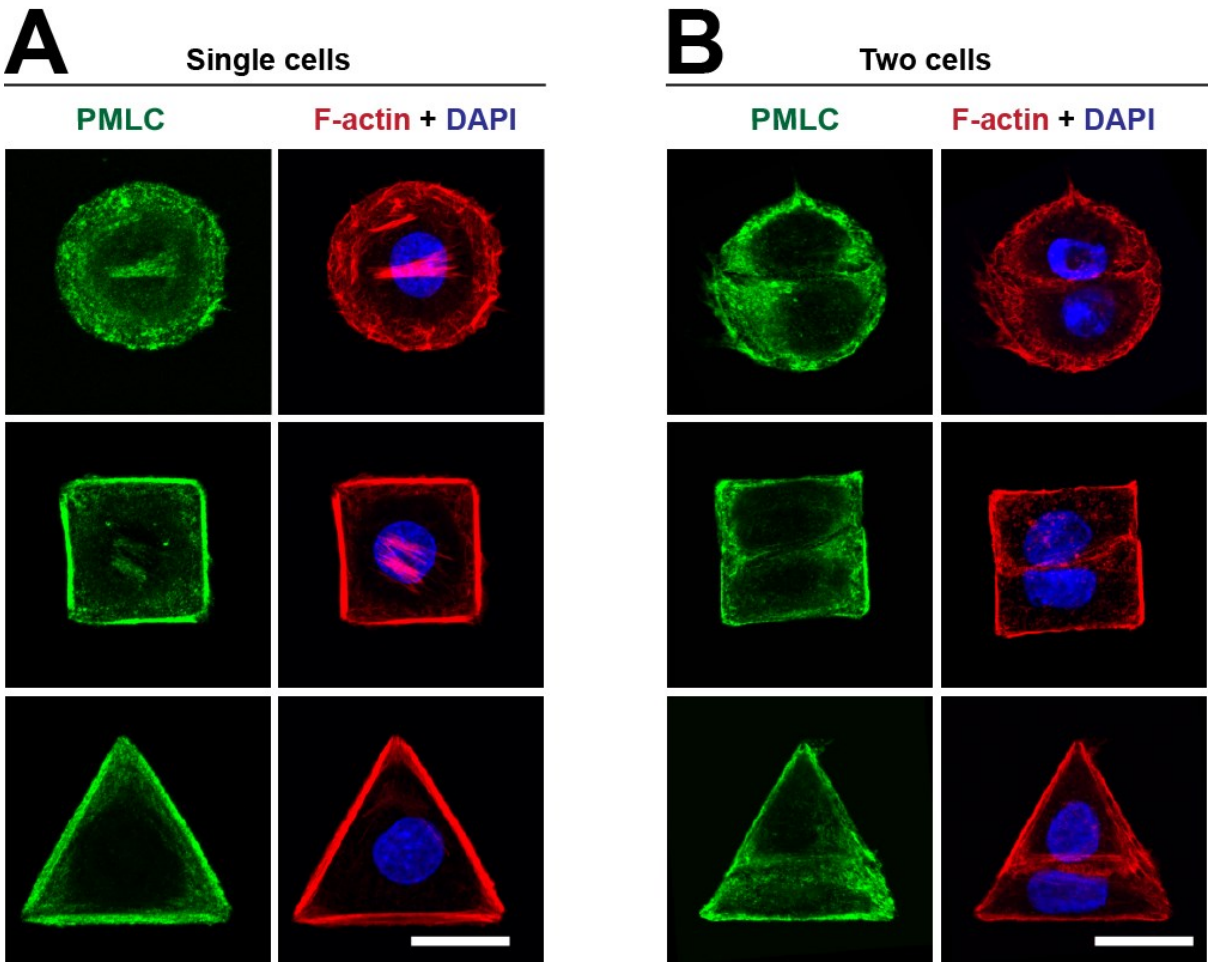

Figure 4.11: **Cell pairs grown on micropatterns have similar pattern of peripheral PMLC labelling as single cells.** Keratinocytes were co-stained for PMLC (green), F-actin (red) and nuclei (blue). Images were taken on a confocal microscope and the two z-planes of best focus with clear staining summed in FIJI. Immunofluorescence images of single cells (A) or cell pairs (B) grown on circular, square and triangular (top to bottom of column) shaped micropatterns. Scale bars represent 20 µm.

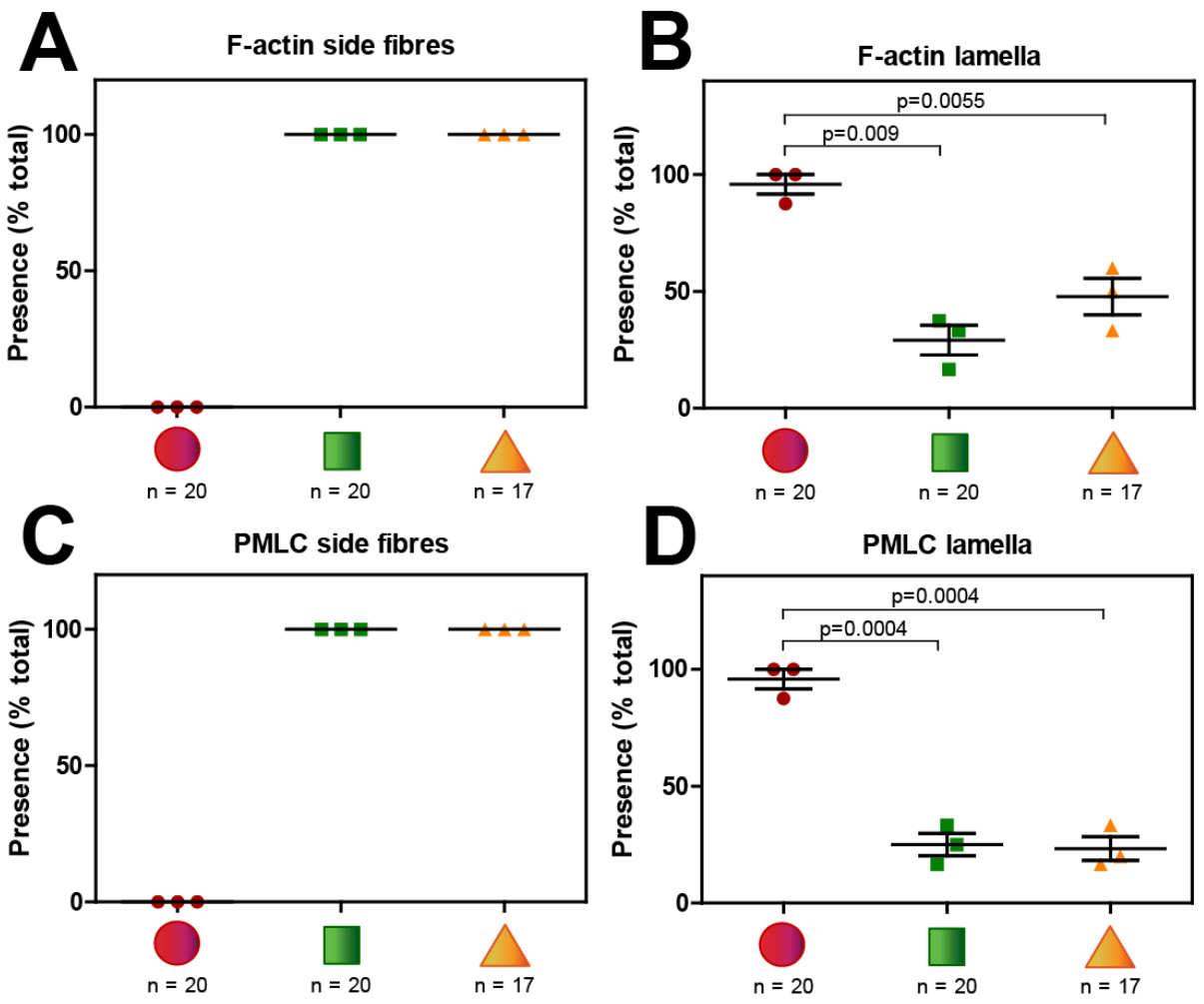

Figure 4.12: **Cells grown on circular shapes do not have stress fibres at their periphery, but rather lamella.** Quantification of F-actin side fibres (A) and lamella (B) for the three different shapes. Quantification of PMLC side fibres (C) and lamella (D) for the three different shapes. Graphs represent average values per experiment. Error bars show SEM. N = total number of cell pairs analysed per geometry. Data were analysed statistically by one-way ANOVA followed by Tukey post-hoc test. Data are representative of 3 independent experiments.

4.3.9 Contractility of actin populations is determined by geometric shape

I next addressed the contractile properties exhibited by the actin populations within varying shapes. Similar to F-actin (Figure 4.10A), the majority of doublets on square and triangular shapes contained PMLC labelling at thin bundles while only 50% of cells on circular micropatterns have PMLC labelling at thin bundles indicating that thin bundles are mostly contractile when present (Figure 4.13A). Further analysis confirmed that all thin bundles were in fact labelled with PMLC (data not shown). Interestingly, PMLC labelling at junctions was low (~32%) for cell pairs on all three different geometries (Figure 4.13B) consistent with previous studies on epithelial monolayers [25].

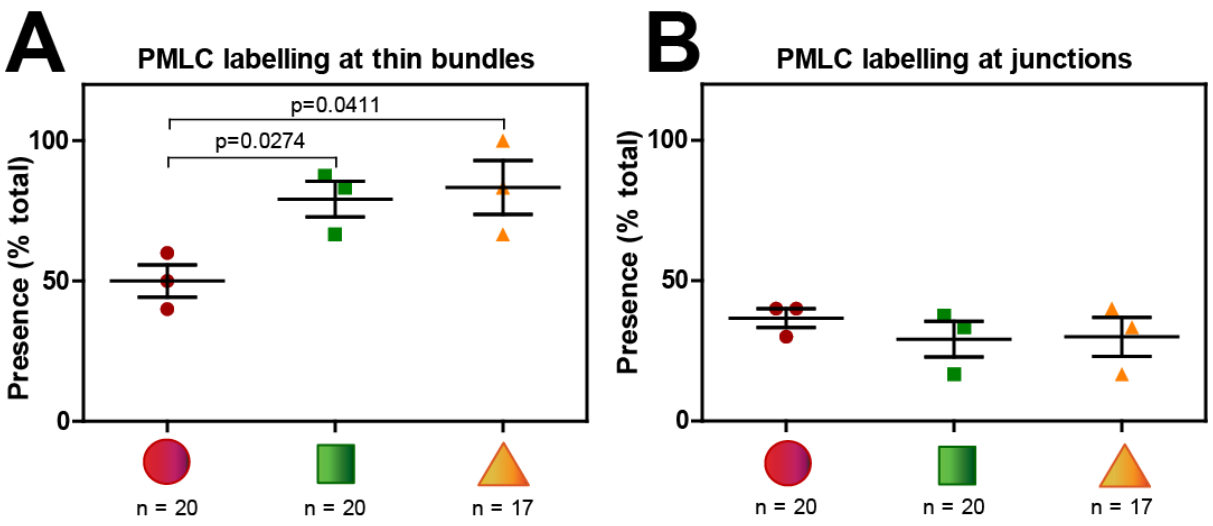

Figure 4.13: **A higher percentage of cells have PMLC labelling at thin bundles when grown on square or triangular shaped micropatterns.** Quantification of PMLC labelling at the thin bundles (A) or at junctions (B). Graphs represent average values per experiment. Error bars show SEM. N = total number of cell pairs analysed per geometry. Data were analysed statistically by one-way ANOVA followed by Tukey post-hoc test. Data are representative of 3 independent experiments.

4.3.10 Higher percentage of thin bundles corresponds to higher percentage of straight junctions

The abundance of thin bundles and straight junctions in cell pairs grown on triangular shaped micropatterns suggested that these parameters were related to one another. Firstly, I looked at the averages of individual experiments for which thin bundles were plotted against straight junctions (Figure 4.14A). As the average number of micropatterns with cells containing thin bundles increased, the presence of straight junctions increased accordingly for cell pairs in all three shapes. Secondly, I looked at the averages per shape with corresponding data spreads. Here, I found that the averages of thin bundles and straight junctions were higher for doublets on squares and triangles compared to those on circles (Figure 4.14B) confirmed by the previous results (Figure 4.10). Thirdly, we calculated the percentage of cell doublets containing thin bundles and among those, the amount that also have straight junctions. The percentage of cells with thin bundles that also have straight junctions increases with increasing contractility from 20% in circles, 35% in squares and 53% in triangles.

PMLC labelling of thin bundles also closely correlated with the presence of straight junctions (data not shown). Averages per shape showed the highest percentages for cells on triangles and the lowest for cells on circles. Cells with PMLC at thin bundles and concomitant straight junctions also showed a similar trend to that observed previously demonstrating that thin bundles labelled with PMLC are specifically associated with straight junctions for cell pairs in triangles, to a lesser extent in cells grown on squares and the least for those in circles.

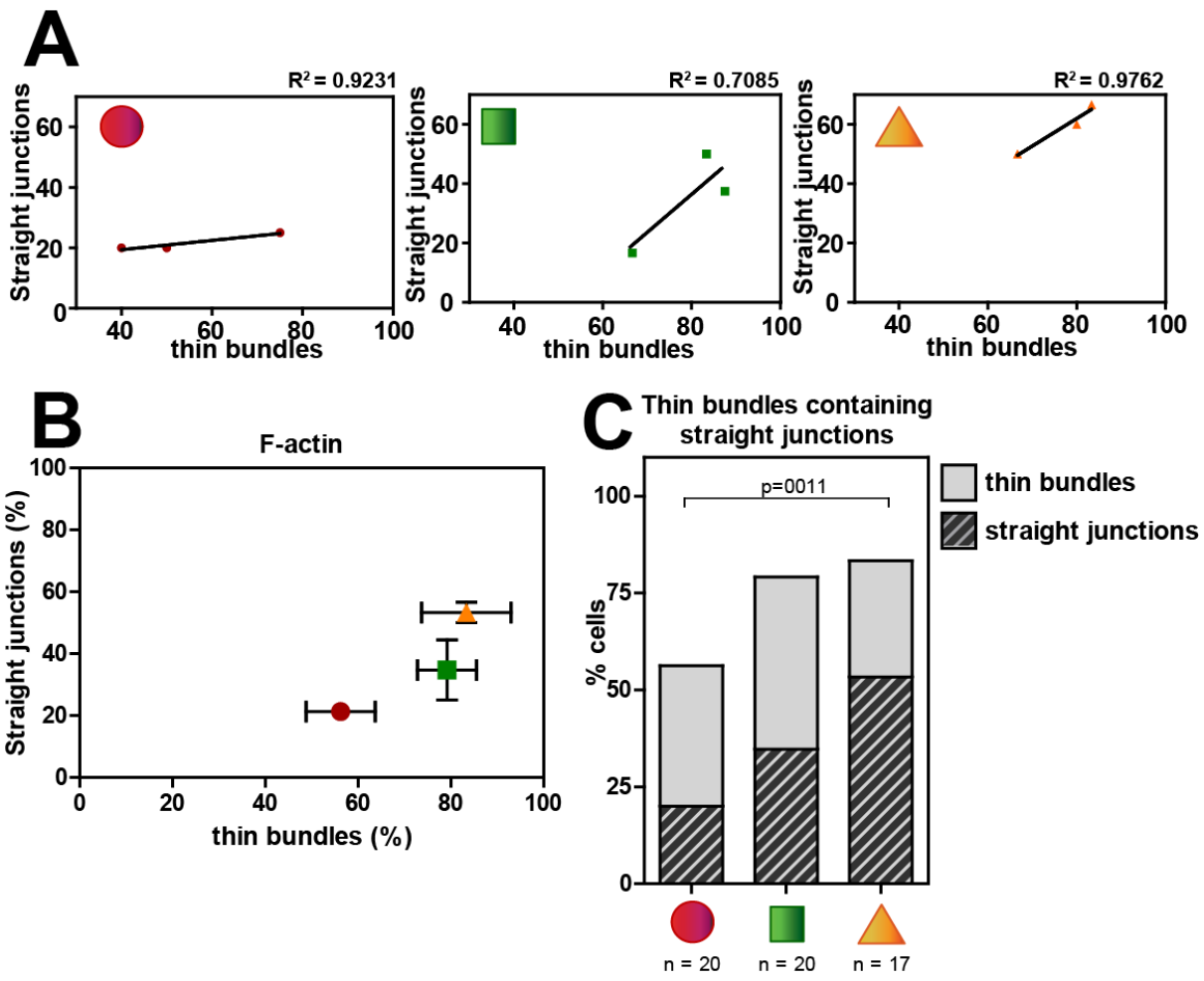

Figure 4.14: Average percentage of cells containing thin bundles and straight junctions are higher in doublets grown on square and triangular shaped micropatterns. (A) Correlation of the percentage of cells with thin bundles or straight junctions per shape in individual experiments. (B) Averages of experiments. (C) Graph of percentage of cells that contain thin bundles and the proportion of cells that also have straight junctions. Data are average values from 3 independent experiments.

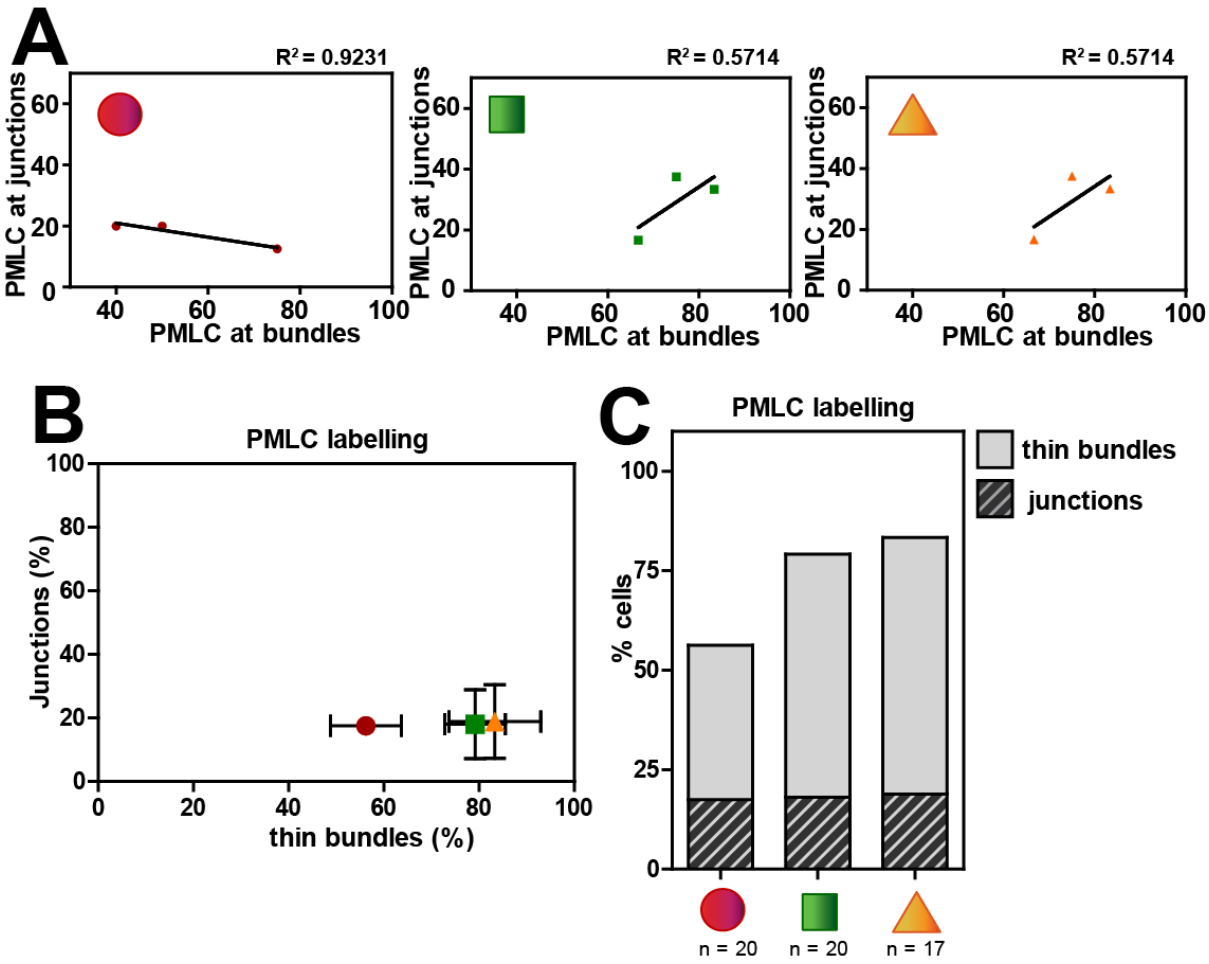

Figure 4.15: **Average percentage of cells containing PMLC labelling at thin bundles and junctions are similar in all three shapes.** (A) Correlation of the percentage of cells with PMLC labelling at thin bundles or junctions per shape in individual experiments. (B) Averages of experiments. (C) Graph of percentage of cells that are labelled with PMLC at thin bundles and the proportion of cells that also have labelling of PMLC at junctions. Data are average values from 3 independent experiments.

4.3.11 PMLC labelling at thin bundles and junctions are dependent on shape

I next tested whether there is a correlation between PMLC labelling at junctions and at thin bundles, depend on geometric shape. When individual experiments are plotted, the amount of cells grown on circles containing PMLC labelling at junctions is inversely correlated with those that have PLMC at thin bundles. In contrast, cells grown on square and triangular shaped micropatterns showed a positive correlation (Figure 4.16). Averages per shape showed that PMLC labelling at junctions is equally low for all three shapes. In contrast, the percentage of cells containing thin bundles labelled with PMLC increased as the contractility of the geometries increased. Analysis of concomitant PMLC labelling at junctions and thin bundles revealed that cells grown on all three shapes had consistently low levels of labelling at junctions (~18%) despite the increasing appearance of thin bundles with increasing shape-related contractility. These results suggest that an increase in thin bundle contractility has no effect on PMLC labelling at junctions.

4.4. Discussion

4.4.1 Cell pairs maintain shape imposed F-actin distributions similar to single cells

This chapter largely focuses on defining the precise consequences and biological impact of the actomyosin contractility enforced on doublets by three different geometries. Of the two main components of the contractile network, I first looked at the F-actin polymer scaffold and then the myosin II regulatory proteins to gain insight into the behaviour of cell pairs forced into particular shapes.

Micropatterning of cell pairs creates a minimal model system to explore the effects of cytoskeletal tension on a single junction. The contractility imposed by circular, square and triangular shaped micropatterns have been widely studied in the context of individual cells [265], [295], [380]. Here, I used for the first time that primary keratinocytes cultured on different geometries with the same adhesive area. Although cell pairs on square shaped micropatterns with varying aspect ratios have been studied in the context of adhesions before [236], [237], the fine cytoskeletal architecture relating to actin and myosin filaments was not addressed. I have used cell pairs on varying geometric shapes to show that contractility increments from the circle to square shape and then furthermore to the triangular shape, with its acute angles. I found that morphologically distinct patterns of contractility are conserved in cell pairs with junctions when compared to single cells [295]. Cell pairs grown on square and triangular micropatterns maintain the thick F-actin stress fibre composition at the edges of the geometries while the circular shape preserves the short randomly oriented peripheral F-actin fibres despite the formation of a junction at the interface between adherent keratinocytes. Staining cell pairs on the different geometries for vinculin showed that large focal adhesions develop at the vertices of the shape (data not shown) where the stress fibres terminate. Thus focal adhesions may play a role in anchoring the stress fibres at the vertices and aligning them with the edges of the geometry to increase contractility. The increased contractility as determined by the accumulation of peripheral stress fibers which securely anchor the cells to the extracellular matrix is likely to be the cause of the increased cortical tension of cells in these shapes as seen in Chapter 3.

4.4.2 Cellular contractility determines positioning of nuclei and cells

A past study utilised inter-nuclear distance as an indicator of live cell kinematics (speed and direction of cell repulsion) driven by reorganization of actin filaments [390] while others have used this parameter to determine cleavage furrow tension and constriction during cytokinesis [391], [392]. Here I used inter-nuclear distance as an indirect measure of cell tension as it is intricately linked through cytoskeletal fibres to the actomyosin networks at the cell peripheries and cell-cell contacts. Increasing contractility as determined by different geometric shapes,, significantly correlated with increased distance between nuclei such that, nuclei of doublets cultured on triangular shapes are furthest apart.

Nuclear-centrosomal orientation of MDCK cells is affected by cell confinement on circular micropatterns of varying sizes and ECM composition that modulate spreading and contractility [393]. Low cell confinement (increased spreading and contractility) maintained the positioning of centrosomes at the cell centre and nuclei close to the junctions (low inter-nuclear distance). On the contrary, high cell confinement (reduced cell spreading and contractility) positioned centrosomes toward the cell junctions and the nuclei away. In these cells, lumen formation was initiated between the cells independent of actin contractility and increased junction tension caused nuclei to be positioned far apart [167], [269]. Lumen formation occurs when individually polarised cells differentiate and acquire collective apicobasal polarity during epithelial morphogenesis [394]. Conversely, in less confined cell pairs, the positioning of the nuclei depended on the fine balance between the pathways that control peripheral and junctional actin [393]. Inhibition of the kinase Par-4/LKB1 via the RhoA-Rho kinase-myosin II pathway induced peripheral contractility and thereby determined the positioning of the nuclei. I reason that tension-related differences generated by geometric confinement may also impact on a number of cellular responses, particularly as a mechanism to counterbalance forces. I assessed the influence of increased contraction on the sharing of space available on each micropattern, changes in nuclear area, positioning of junctions and efficiently epithelial polarisation (junction height).

Although cell pairs on micropatterns have been studied before and images suggest that areas of cell pairs are similar, in depth analysis of cellular occupation had not been included in the results [236], [237]. Assuming that the majority of cell pairs are in a stable configuration at the time of fixation, cells do not share the area available to them equally but rather adhere disproportionately with one cell attaching to a larger area than its partner and thereby falling into different classes as confirmed by the distinct frequency distributions. The difference in adhesive areas of individual cells is more pronounced in doublets on triangular micropatterns with the greatest contractility where one of the cells occupies an area 17% larger than its neighbour. It is worth noting that this difference is mediated by the few cell pairs (6%) which show much larger discrepancies to one another. Although this is a rare occurrence, it is only seen within triangles and is likely a feature attributed to its inherent contractility which favours one cell to be much larger than its neighbour. Areas of nuclei of cells sharing a micropattern also show discrepancies when differences are compared within but not between geometric shapes. This is in line with an extensive study of the nucleus showing that shape and size is interrelated to cellular factors including cell volume [385]. My finding is the first to disclose discrepancies between adhesion areas of cell pairs and their nuclei on micropatterns.

4.4.3 Positioning but not height of junctions is affected by cell contractility

It is expected that variations in the positioning of cells would lead to differences in the orientation of cell-cell contacts in order to spatially accommodate the doublets. The study by Tseng et al clearly shows that doublets which are cultured on 35µm x 35µm square micropatterns with a 10µm strip of peripheral adhesive area orient their nucleus-nucleus axis randomly such that junctions form in a plethora of different angles [236]. In my study, cell pairs on square and triangular geometric shapes have a preference in positioning their junctions such that areas are not equally distributed between two neighbours. This affects the resultant polygonal shape of the doublets such that individual cells within the pattern prefer at least one of the doublets to have the triangular shape. Indeed, this result compliments previous findings that show that in a monolayer,~10% of keratinocytes acquire square shape after assembly of junctions while only about 1% have triangular shapes [116]. However, the

percentage of cells with junctions passing through vertices, which are known points of accumulated tension [295], [395] is higher than the predicted probability. However, this calculation was based on the assumption that the junction always passes through the centre of the shape. Although this limits the otherwise infinite possibilities in which the junction could orient, the actual probabilities are likely to deviate from those calculated here.

The distinct contractility of geometric shapes did not interfere with junction height. Similar junction height of average of 6.7 µm is observed among all shapes, consistent with the previously reported 6.2 µm lateral junction height in primary human keratinocytes [351]. However, rather interestingly, junction heights between cell pairs follow different distributions in the three shapes: the spread and peak value of heights show shape-related disparities suggesting that contractility may be coupled with the pairwise orientation of the cells in determining the optimal junctional height.

4.4.4 The two populations of actin and PMLC at cell-cell junctions

Two spatially distinct actin populations; junctional actin and peripheral thin bundles have been identified upon cell-cell contact induction and are known to play varying roles during epithelial polarization [25]. These two actin populations are also found in cell pairs cultured on the three different geometries. The majority of cells on square and triangular shapes clearly show a presence of thin bundles adjacent to the junctions on either side. In contrast, most doublets on the least contractile circular shape micropattern exhibit only junctional actin. Interestingly, my results illustrate that: (I) junctional actin precedes the formation of thin bundles as previously shown [25]; and (ii) assembly of junctions is not sufficient to remodel F-actin as parallel thin bundles. It seems that increased tension in the cell body is also required for the appropriate junctional architecture.

Contractility visualisations of cells on micropatterns have relied single-handedly on F-actin staining in previous studies [236], [265], [396]. Here I unravel, for the first time, decorations of peripheral and junctional F-actin with PMLC. At cell-cell contacts, hardly any labelling of junctional actin with PMLC is visible, while thin bundles when present are labelled with PMLC, consistent with their contractile

nature. Contractile forces at junctions are generally resisted by adhesive forces which transmit tension [397]. Interestingly, the high contractility imposed on cell pairs by the triangular shape coupled with contractile thin bundles impact on the configuration of junctions as seen in Chapter 5, suggesting that global contractility of cell pairs plays a role in determining distinct patterns of junction contractility.

There maybe two possibilities as to how the peripheral acto-myosinII integrates with that of the junctions. The presence of peripheral stress fibres on the square and triangular shapes may lead to an increased cortical tension which is transmitted towards the cell-cell contacts and dictate the precise nature of the actin architecture at the junctions. Alternatively, there might be mechanical coupling between stress fibers and the acto-myosinII associated with the adherens junctions through an intact medial meshwork that extends between these adhesions. Further experiments related to junction formation are necessary to conclude which of these possibilities is favoured. Actin filaments in the cytoskeleton have long been characterised as the main supporters of tensile forces [398], [399] and direct links between adhesions, acin filaments and the nucleus have been shown to be involved even in long range force transmission [400]. Although evidence supports that crosstalk between cell=cell and cell-matrix adhesions is vital to mechanotransduction, precisely how forces are integrated and transmitted remains to be explored. The tensile acto-mysoinII meshworks, as seen during Drosophila epithelial morphogenesis, may at least in part account for the coupling between the cytoskeletons of the neighbours through cell-cell adhesions [60] but the degree to which these extend to cell-matrix adhesions in individual cells remain unclear.

In conclusion, I have identified that peripheral contractility and cortical tension imposed through distinct geometries correlate with contractility at junctions without affecting average junction height. Characteristic parallel thin bundle populations in epithelial cells are perturbed in cells with lower contractility, without an impact on the junction formation or total F-actin levels at cadherin complexes. I have also discovered that doublets occupy different areas of the micropatterns giving rise to variations in junction orientation, at least in the shapes with higher contractility.

CHAPTER FIVE:

Junction configuration, levels of junctional markers and shape-driven role of actomyosin contractility

5.1 Rationale

Cell morphology is partially controlled by the magnitude of traction forces generated by mechanically interacting with the substrate [241]. These actively generated contractile forces are highly dependent on the actin-myosin cytoskeleton and its regulators and at equilibrium, accounts to a net force of zero in single cells [376]. For two cells in contact with each other, the force remains zero as the cell-matrix traction forces are equal but opposite in magnitude to the intercellular tugging force at cell-cell contacts [124]. In endothelial cell pairs cultured on an array of patterned elastomeric microneedles, the tugging force, is perpendicular to the intercellular boundary and positively correlates with the size of junctions. Inhibition of myosin activation leads to a decrease in cell-cell tugging forces and contact size[124]. These cell-cell adhesions trigger many signalling events through Rho GTPases to regulate cell mechanics [401]. Actomyosin driven initiation, expansion and completion of cell-cell adhesion contacts have been shown to be regulated by the localisation of activities of Rho and Rac [17].

The Rho GTPases, Rho and Rac, are critical to cadherin-dependent adhesion in epithelial cells and inhibition of endogenous activity perturbs E-cadherin accumulation at cell-cell contacts [105], [402]. Actomyosin contractility at junctions is generated through the phosphorylation of MLC and through the Rho effector, ROCK and is necessary for E-cadherin localisation to cell-cell contacts [21]. However, other studies show that ROCK inhibition via the Y27632 compound has no effect on AJ assembly in epithelial cells [403]. The contradictory findings are explained by the differential effects of actomyosin contractility according to AJ localisation. Some filaments run perpendicular to junctions and pull them radially, thereby disrupting junctions [84] while the majority form linear thin bundles adjacent to cell-cell contacts [25]. Despite affecting junction composition, the formation and maintenance of AJ depend on the actomyosin contractility generated by ROCK and myosin II and affects the rearrangement of AJs during neoplastic transformation by altering directions of tension at cell-cell contacts [162].

The role of ROCK mediated contraction has been widely studied in epithelial morphogenesis in *Drosphila.* Junctional actomyosin plays a pivotal role in stabilization of junction length during junction shrinkage in *Drosophila* germband extension to attain cell intercalation [121], [404], [405]. ROCK is recruited to membranes via the actin-binding protein, Shroom3 and contributes to apical constriction by inducing the contraction of the circumferential actin belt causing junction shrinkage [406], [407]. In MDCK epithelial cells, Shroom localises to the apical region and alters F-actin distribution and formation of the contractile actomyosin network facilitating cell shape changes to achieve polarity [408].

The role of actomyosin contractility and underlying tension on determining the structure of junctions has not been addressed in previous reports. However, the participation of the Rho-ROCK pathway in enhancement of contraction has been studied on single cells on micropatterns [295], [382], [409]. Stress fibre contraction is activated by Rho through myosin-dependent cross-linking and is particularly important to stabilise the convexity of membranes when cells form bridges between adhesive sites [382], Integrin based adhesions are excluded beneath the centre of E-cadherin junctions of MDCK cell pairs on unrestricted substrates and localised to the distal ends of cell-cell contact edges [17]. Cells may adopt such an arrangement to avoid the large perpendicular tensional forces from the ECM at intercellular junctions and spatially organise contacts away from the cell-ECM adhesion sites and maintain stability [236].

Although it is known that AJs are under contraction through a ROCK-dependent pathway, and that contractility is crucial for remodelling during morphogenesis, the precise impact of contractility on stationary epithelial cell junctions remains elusive. The intricate balance between cell-ECM and cell-cell forces determines the structure and stability of junctions. Actomyosin contractility governs tension within the cell and at adhesive interfaces through the interconnected network of actin and myosin fibres. Here our model system provides a unique opportunity to characterise and dissect which morphological parameters of junctions are influenced by increased cortical tension.

5.2 Hypothesis and aims

I hypothesise that appropriate maintenance of intercellular junctions is facilitated by the level of actomyosin contractility. In order to gain insight into the composition and dynamics of junctions. I aimed to:

(i) characterise the length, linearity and coverage of junctions (junction configuration) and E-cadherin and actin at junctions (junction composition) of cell pairs within each micropattern

(ii) examine the role of contractility in determining junction configuration and composition by inhibition of contraction using Y27632

(iii) determine actin molecular dynamics at cell-cell junctions of doublets in each shape

5.3 Results

5.3.1 Contractility affects morphological features of junctions

Cell pairs grown on micropatterns with higher contractility (square and triangular shapes) indicate a bias in the spatial organisation of junctions towards a specific orientation (Chapter 4 – Figure 4.7). Inspired by this result, I carried out an in depth analysis of junction morphological features such as length, linearity and coverage of cell pairs in the three geometrically distinct micropatterns. Here, I measured the absolute values for junction length of cell-pairs cultured on different shapes. Cell doublets grown on circles had a mean junction length of 37.24 µm (Figure 5.1). Shape-driven contractility negatively correlated with junction length. Junction length of doublets decreased significantly by 6% and 16% when cells were grown on square and triangular shaped micropatterns respectively compared to circular shaped micropatterns. Thus, shape-driven contractility negatively correlated with junction length.

We next investigated whether cortical tension modulated by imposed constraints on cells, have an impact on the curvature of junctions. To measure the extent to which the junctions resemble a straight-line a linearity index is defined as the ratio of the minimum distance between the junction end-points to the actual junction length [169], [410] (Figure 5.2). Indeed, junction linearity correlated positively with cortical tension such that junctions between doublets on triangular shaped micropatterns were significantly more linear (have a significantly lower linearity index) than those on square and circular shaped micropatterns where the cell-cell contacts were more curved. Cell pairs on triangular shaped micropatterns with higher contractility and cortical tension form junctions that are shorter and straighter.

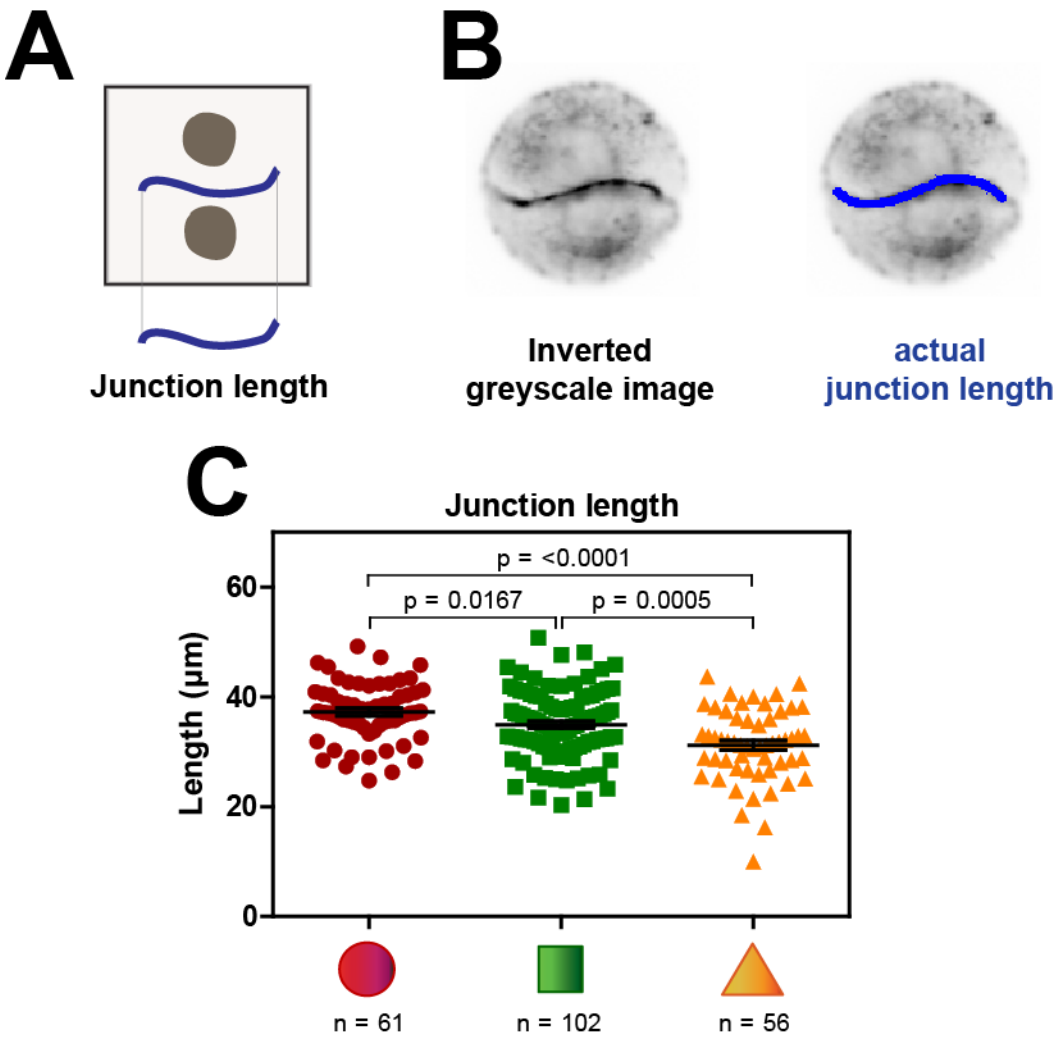

Figure 5.1: **Junction length decreases with increase in contractility.** Keratinocytes were cultured on micropatterns and the E-cadherin channel used for quantifications (A) Schematic defining junction length (B) Inverted greyscale image of a cell pair cultured on a circular micropattern (left) depicting the actual junction length (right). (C) Quantification of actual length of intercellular junctions of keratinocyte cell pairs. Graphs represent values per cell pair. Data were analysed statistically by one-way ANOVA followed by Tukey post-hoc test. N = numbers of cell pairs analysed and are shown below each of the shapes. Error bars represent SEM. Data are representative of 5 independent experiments.

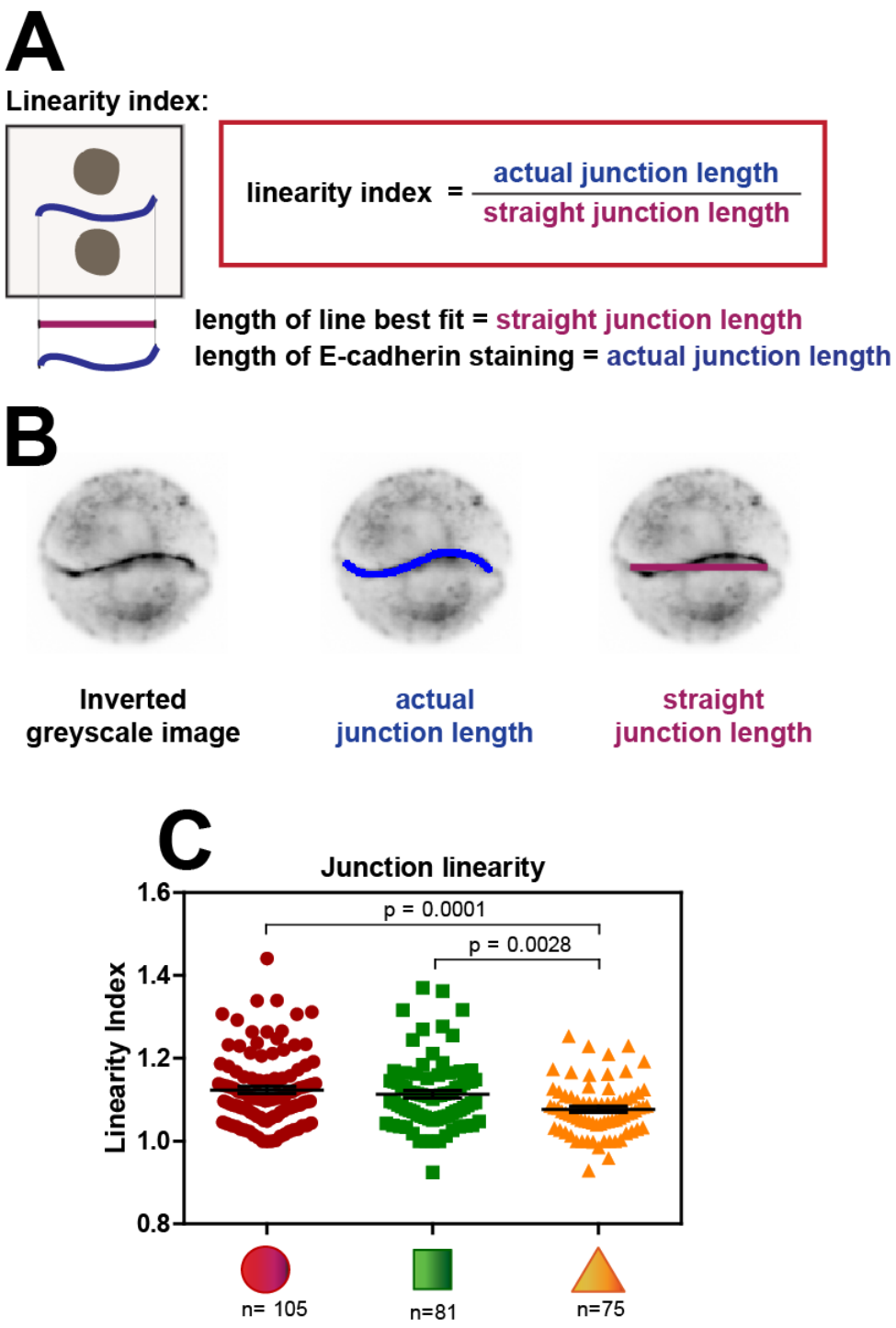

Figure 5.2: Junctions between cell pairs grown on triangular patterns are significantly straighter. Keratinocytes were cultured on micropatterns and measurements at junctions performed using the Ecadherin staining. (A) Schematic defining the linearity index which measures how straight a junction is. (B) Inverted greyscale image of a cell pair cultured on a circular micropattern (left) depicting the actual junction length (middle) and the junction length measured by drawing a straight line between the two end-points of the junction (right). (C) Quantification of junction linearity. Graphs represent values per cell pair. Data were analysed statistically by one-way ANOVA followed by Tukey post-hoc test. N = numbers of cell pairs analysed and are shown below each of the shapes. Error bars represent SEM. Data are representative of 5 independent experiments

I next examined junction coverage which measures the extent to which a cell-cell contact spans the entirety of the interface between the two cells limited by the edges of the geometry. This is defined as the ratio of the junction length to the edge length. There were no significant differences in junction coverage between doublets on the three shapes, which all had a mean 83% coverage (Figure 5.3). Taken together, these results suggest that junction length and linearity but not coverage correlate with on global cellular contractility.

5.3.2 Levels of E-cadherin receptors and F-actin at junctions vary in the different geometric shapes

Since junction configuration shows a clear association with cellular contractility, I next investigated whether the E-cadherin and actin levels at junctions are affected. Intensity and density were measured as described in Figure 5.4 using Fiji image analysis software. Briefly, intensities were measured by thresholding the E-cadherin at junctions and overlaying the outline of this threshold with the actin channel to obtain junctional actin intensity values. Additionally, I quantified the cytosolic intensities of E-cadherin and actin. The absolute intensity values together with the density of the junctional markers per unit area of the actual junction (i.e. area of E-cadherin staining) were computed.

E-cadherin intensity was significantly higher by 48% and 35% at the cell-cell contacts of doublets cultured on circular and square shaped micropatterns respectively compared to those on the triangular micropatterns (Figure 5.5). Noteworthy, E-cadherin intensity at junctions were at least two-fold higher than in the rest of the cell (in the case of triangles). The density of E-cadherin receptors at junctions followed a similar, yet less pronounced, increase by 43% and 22% on circular and square shaped micropatterns respectively compared to those on the triangular micropatterns. In contrast, the cytosolic intensity of E-cadherin receptors showed an opposite trend to the levels at the junctions. Cytosolic E-cadherin decreased by 33% and 18% in cell pairs grown on circular and square shaped micropatterns respectively compared to triangles (7.3×10^3 a.u.).

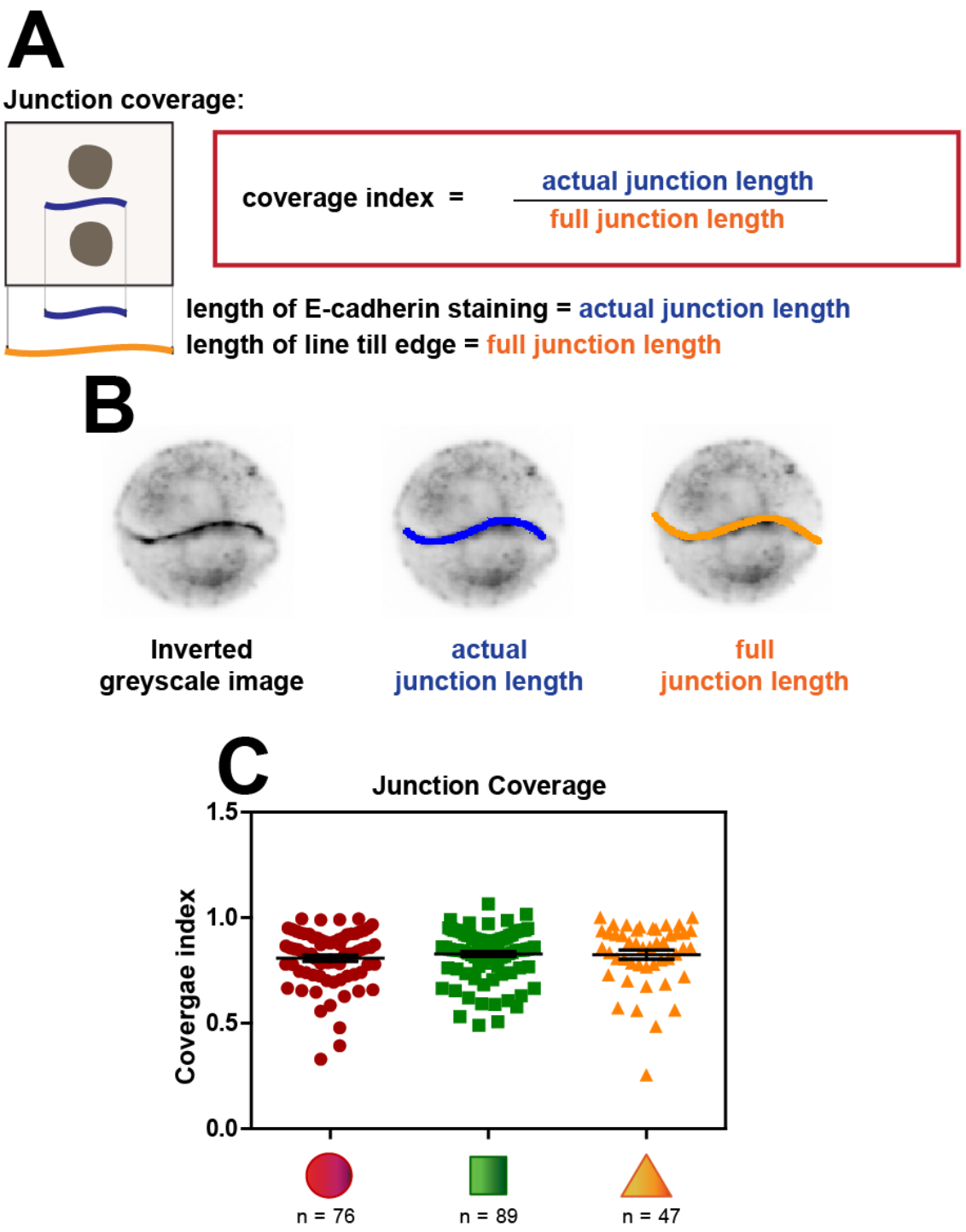

Figure 5.3: Junction coverage is similar across the different geometries. Keratinocytes were cultured on micropatterns and the E-cadherin channel used for quantifications. (A) Schematic defining the coverage index which measures to what extent the junction spans to the edges of the geometric shape. (B) Inverted greyscale image of a cell pair cultured on a circular micropattern (left) depicting the actual junction length (middle) and the junction length measured by extending to the nearest edge of the geometry (right). (C) Quantification of junction covergae. Graphs represent values per cell pair. Data were analysed statistically by one-way ANOVA followed by Tukey post-hoc test. N = numbers of cell pairs analysed and are shown below each of the shapes. Error bars represent SEM. Data are representative of 5 independent experiments.

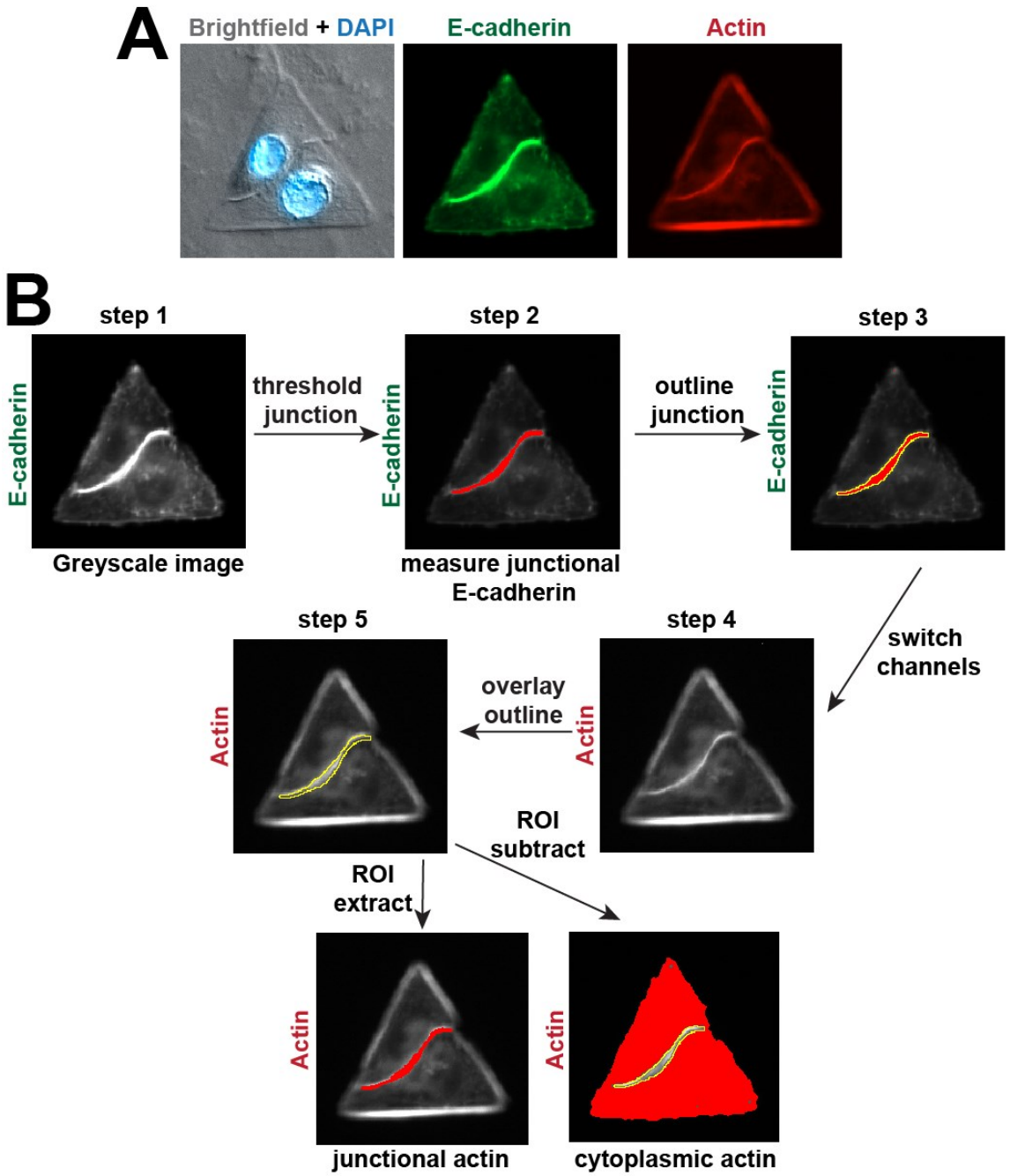

Figure 5.4: **Methodology for quantification of junctional and cytoplasmic markers.** Keratinocytes were co-stained for E-cadherin (green), F-actin (red) and nuclei (blue) and imaged on a widefield microscope. (A) Representative immunoflourescence images of doublets cultured on triangular micropatterns. (B) Quantification technique involved converting the E-cadherin image to greyscale (step 1), thresholding the junction and measuring E-cadherin levels (step 2), obtaining the outline of the junction (step 3), switching channels to the actin greyscale image (step 4), overlaying the junctional outline on the actin channel (step 5). Junction outline was extracted from F-actin image to generate the parameter junctional action and the remaining F-actin staining to produce the parameter cytoplasmic actin.

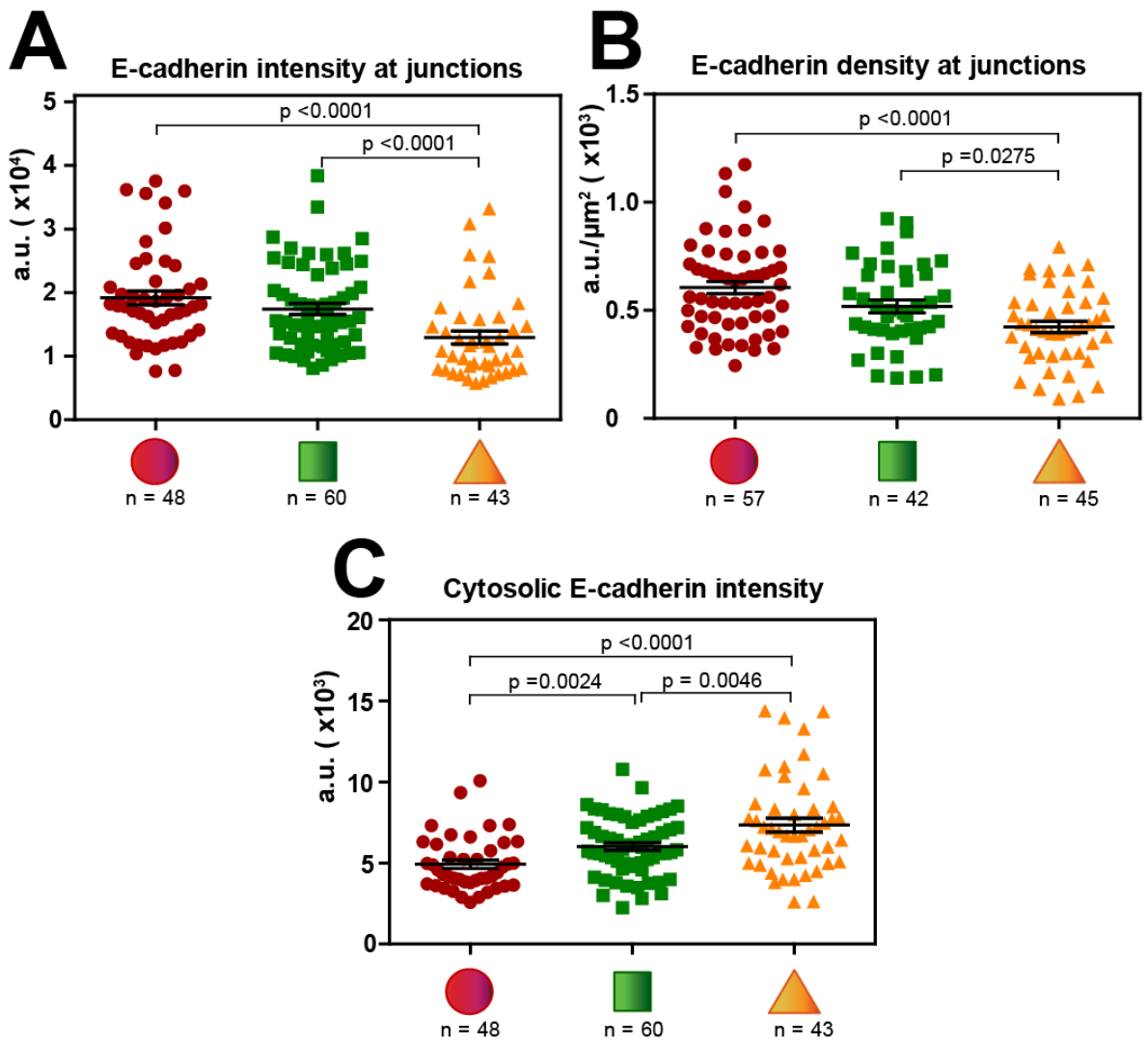

Figure 5.5: Cell pairs on triangular micropatterns have lower levels of E-cadherin at junctions compared to those on square and circular micropatterns. E-cadherin levels were quantified as described in Figure 5.4. Quantification of junctional E cadherin intensity (A) and density (intensity per unit area along the junction, B). (C) E-cadherin intensity in the cytoplasm excluding the junction. Graphs represent values per cell pair. Data were analysed statistically by one-way ANOVA followed by Tukey post-hoc test. N = numbers of cell pairs analysed and are shown below each of the shapes. Error bars represent SEM. Data are representative of 3 independent experiments.

Junctional F-actin intensity levels revealed that it was 39% higher at the cell-cell contacts of doublets cultured on circular shaped micropatterns compared to those on triangular micropatterns (Figure 5.6). The density of F-actin (F-actin per unit area) at junctions were significantly higher by 28% and 19% on circles compared to both triangular and square shaped micropatterns. The cytosolic intensity of F-actin was sustained at 8 x 10^3 a.u. across doublets grown on the three different geometric shapes. It is clear that recruitment of E-cadherin receptors and F-actin to junctions exhibit shape related differences.

5.3.3 Inhibition of contraction through Y27632 alters junction configuration and E-cadherin recruitment to junctions

The results above indicate that shape-driven contractility, which is dependent on the underlying cytoskeletal organization, plays a role in shaping the profile of junctions. To address the effect of actomyosin force, I antagonised cytoskeletal tension by treatment of cell pairs on micropatterns with the Y27632 compound (a Rho kinase inhibitor) and investigated its effect on junction configuration and recruitment of junctional markers. Y27632 treatment perturbs junction contractility by abolishing thin bundles adjacent to junctions [21], [25]. The concentration and time for treatment with the Y27632 compound was optimised on micropatterns (data not shown) such that the thin bundles disappeared without affecting E-cadherin at junctions or the retracting from the geometric shape. In my study, 5 µM Y27632 was used for 5 minutes to inhibit contraction.

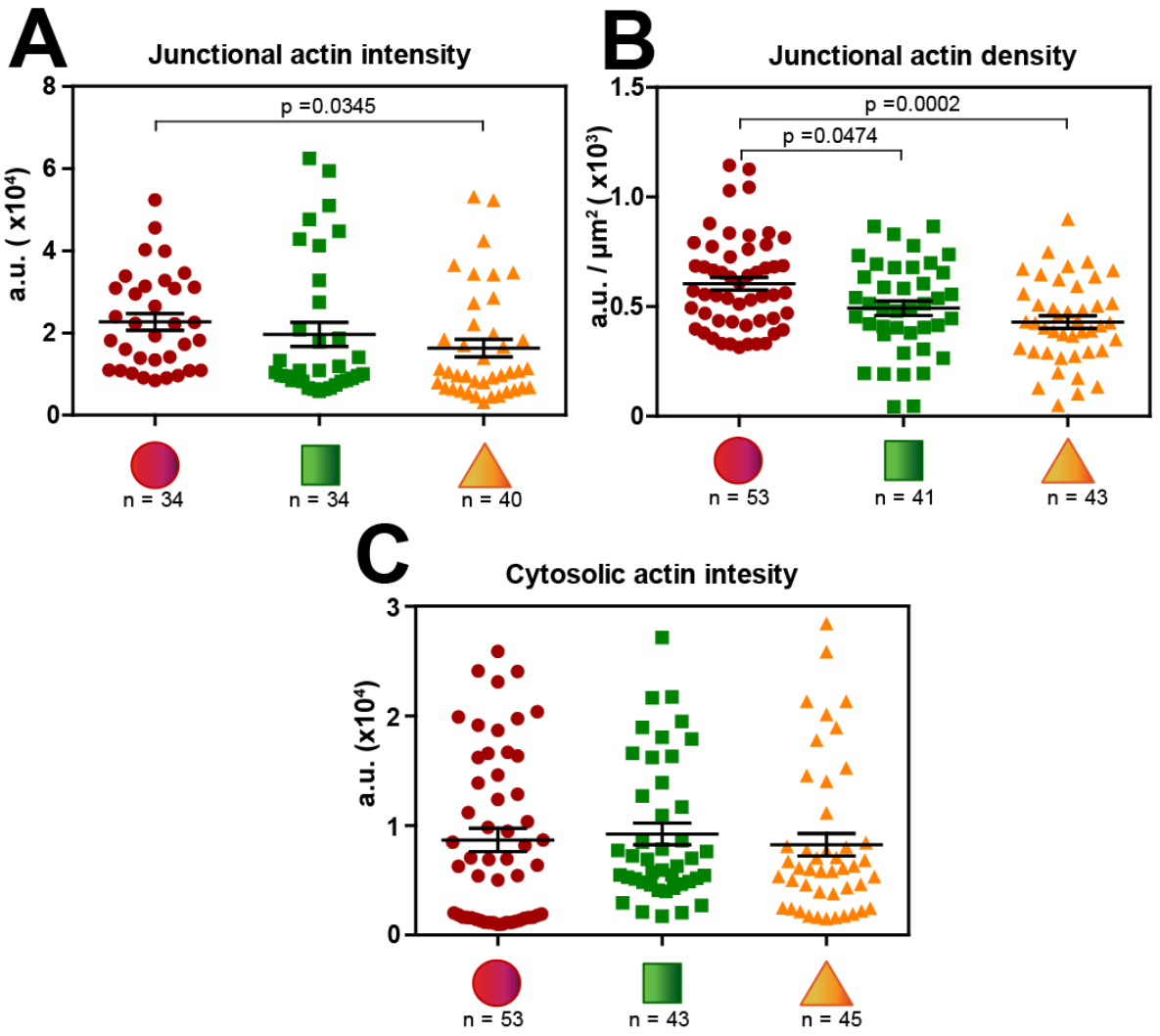

Figure 5.6: Cell pairs on triangular micropatterns have lower levels of actin at junctions compared to those on circular micropatterns. Actin levels were quantified as described in Figure 5.4 (steps 3-5). Quantification of junctional actin intensity (A) and density (intensity per unit area along the junction, B). (C) Actin intensity in the cytoplasm excluding the junction. Graphs represent values per cell pair. Data were analysed statistically by one-way ANOVA followed by Tukey post-hoc test. N = numbers of cell pairs analysed and are shown below each of the shapes. Error bars represent SEM. Data representative of 3 independent experiments.

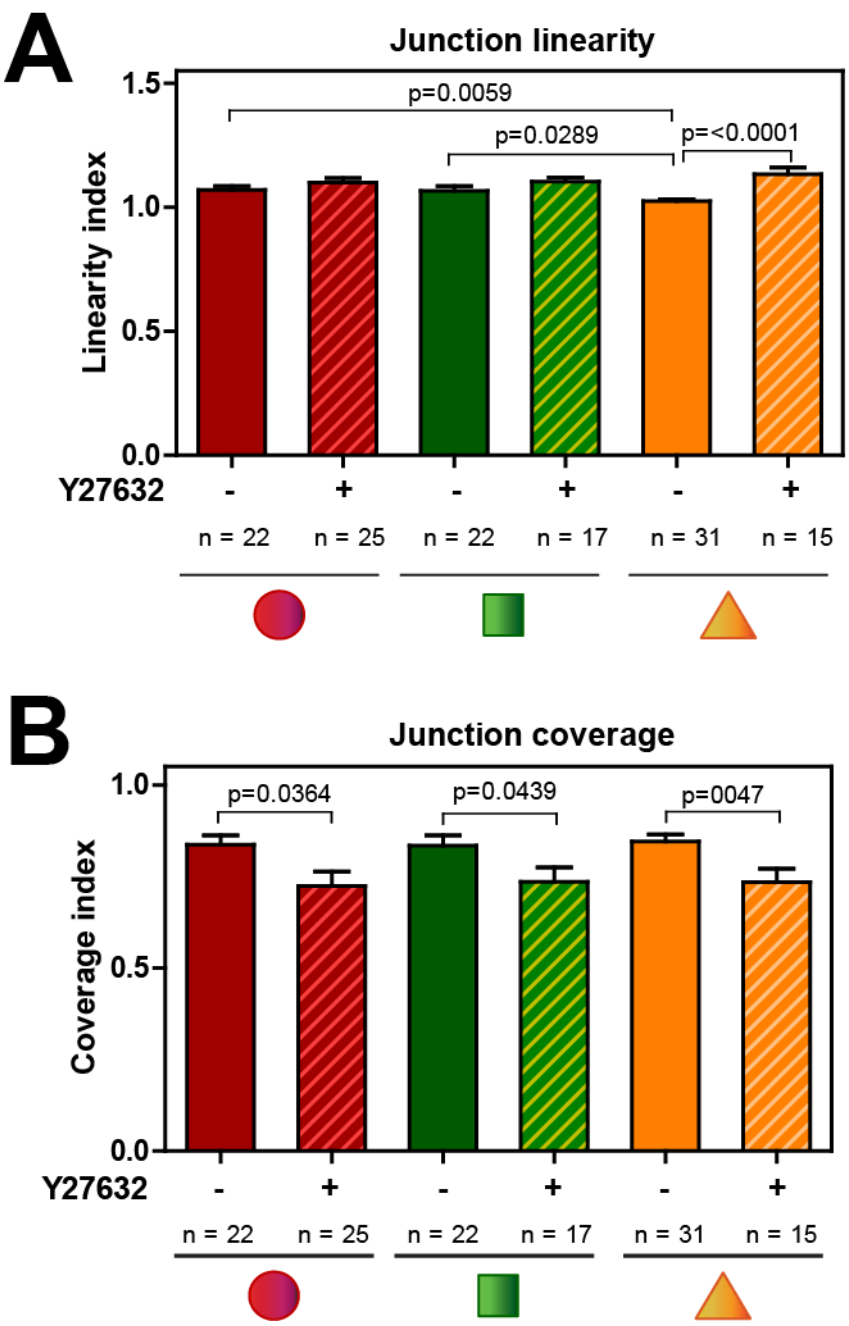

Figure 5.7: Contribution of contractility for formation of straight junctions and coverage of micropattern width by junctions. Keratinocytes were treated with 5 µm Y27632 for 5 minutes, 20 hours after seeding onto micropatterned coverslips. Control cells (represented with the '-' sign) were those that had no inhibitor added. Quantification of junction linearity (A) and coverage (B) for cell pairs on micropatterns of the different geometries with or without the addition of Y27632. Graphs represent values per cell pair. Data were analysed statistically by one-way ANOVA followed by Tukey post-hoc test. N = numbers of cell pairs analysed and are shown below each of the shapes. Error bars represent SEM. Data are representative of 3 independent experiments.

The linearity index of junctions in cell pairs cultured on triangular micropatterns significantly decreased upon addition of Y27632. Junction curvature was similar with that of cell pairs grown on circular and square shapes with or without the addition of Y27632. Interestingly, junction coverage significantly decreased for cell pairs cultured on all three different geometries such that junction coverage dropped by 10% upon inhibition of contraction across the different geometries (Figure 5.7).

With respect to junctional levels of E-cadherin receptors, intensity significantly increased by 63%. Upon inhibition with the Y27632 compound. This value closely matched with the values observed at junctions in cell pairs grown on circular micropatterns with and without the addition of Y27632 and square patterns with the addition of Y27632. The density of E-cadherin receptors showed an interesting trend, whereby higher densities were observed for all three of the geometric shapes upon addition of the Y27632 (Figure 5.8). This increase was more pronounced at junctions in cell pairs cultured on square (54%) and triangular (49%) shapes respectively. Conversely, junctional actin intensity and density did not show any significant changes upon addition of the Y27632 compound for cell pairs grown on any of the shapes. Thus, my study indicate that inhibition of contraction through Y27632 decreases contact length of junctions and increases junctional E-cadherin density across the geometric shapes These effects were independent of junctional actin recruitment.

5.3.4 Junctional actin dynamics vary according to shape-imposed contractility

Inhibition of contraction with Y27632 did not yield significant changes in junction at actin levels. Previous results indicate that shape related differences could be largely attributed to actomyosin contractility. I investigated the mobility of actin at junctions through FRAP to deduce actin dynamics.

For FRAP experiments, cells were maintained in phenol-free medium to avoid interference with the fluorescence signal. Microscopy was carried out at 37°C in a heating chamber without the control of CO_2. Addition of 25 µM HEPES to buffer the pH of the medium did not affect the morphology of cells at room temperature compared to those maintained at 37°C, 5% CO_2 (Figure 5.10). Colour changes

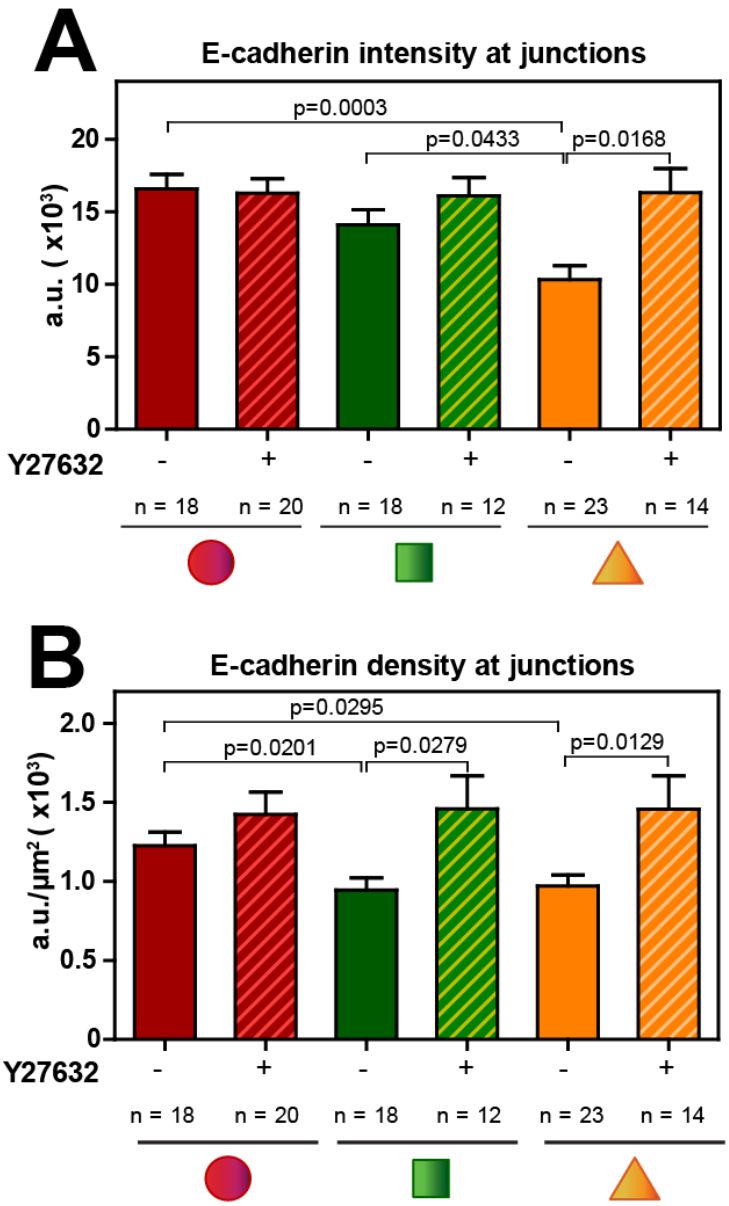

Figure 5.8: E-cadherin levels at junctions increase upon addition of Y27632. Keratinocytes were treated with 5 µm Y27632 for 5 minutes, 20 hours after seeding onto micropatterned coverslips. Control cells (represented with the '-' sign) were those that had no inhibitor added. E-cadherin levels were quantified as described in Figure 5.4. Quantification of junctional E cadherin intensity (A) and density (intensity per unit area along the junction, B). Graphs represent values per cell pair. Data were analysed statistically by one-way ANOVA followed by Tukey post-hoc test. N = numbers of cell pairs analysed and are shown below each of the shapes. Error bars represent SEM. Data representative of 3 independent experiments of 3 independent experiments.

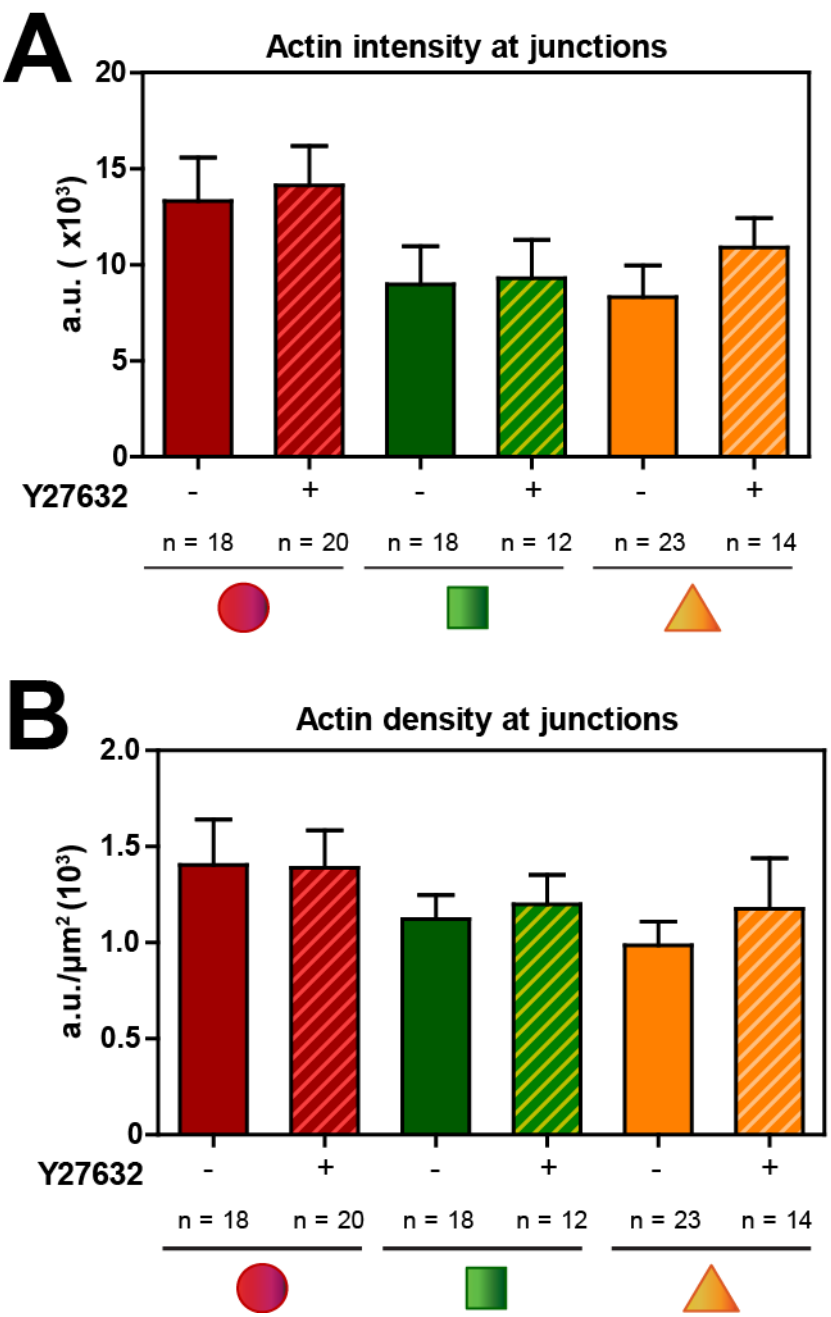

Figure 5.9: Actin levels at junctions do not change signnificantly upon addition of Y27632. Keratinocytes were treated with 5 µm Y27632 for 5 minutes, 20 hours after seeding onto micropatterned coverslips. Control cells (represented with the '-' sign) were those that had no inhibitor added. Actin levels were quantified as described in Figure 5.4. Quantification of junctional actin intensity (A) and density (intensity per unit area along the junction, B). Graphs represent values per cell pair. Data were analysed statistically by one-way ANOVA followed by Tukey post-hoc test. N = numbers of cell pairs analysed and are shown below each of the shapes. Error bars represent SEM. Data representative of 3 independent experiments of 3 independent experiments.

with the AlamarBlue® assay indicated changes in activity in cells within the incubator or at room temperature. The metabolic activity of cells kept in FRAP medium with or without 25 µM HEPES did remained similar at room temperature or 37°C, 5% CO2.

Cellular responses at 37°C, 5% CO_2 were also more than three-fold higher from 2-6 hours when compared to that at room temperature. The percentage of activity at room temperature compared to 37°C, 5% CO_2 was significantly higher at 2 hours and 5-6 hours in cells cultured in the medium with HEPES than without (Figure 5.10E). These results indicate that prolonged experiments at room temperature carried out with the addition of HEPES to the medium of cells improves cellular responses in general and should be used for consistent cellular dynamics with live cell imaging. Although FRAP experiments were conducted within a heating chamber at 37°C, the positive effect of buffering the pH with 25 µm HEPES addition was clear from our results. Experiments were carried out for durations of up to 2 hours in a single sitting whilst ensuring cells grown on the three different shapes were kept at the same conditions and were randomly selected for imaging.

FRAP experiments were controlled such that the bleaching region was maintained at a pre-defined size at the same relative position along the junction of transfected cells for all cells analysed. Transfections of micropatterns with GFP-actin revealed that cell pairs were randomly transfected such that either one cell or both cells in a doublet contained the plasmid (Figure 5.11). Recovery curves (integrated density ratio over time) were similar for junctions bleached in both scenarios (Figure 5.11B). Fluorescent recovered up to an average of 80%, at which point most cells had reached their maximum recovery. The halftime of recovery corresponds to the time point at which the florescence intensity has reached half the value of the final recovered intensity. It was similar for cells in a pair whether transfected singly or doubly. Likewise, the maximum recovery levels were unchanged.

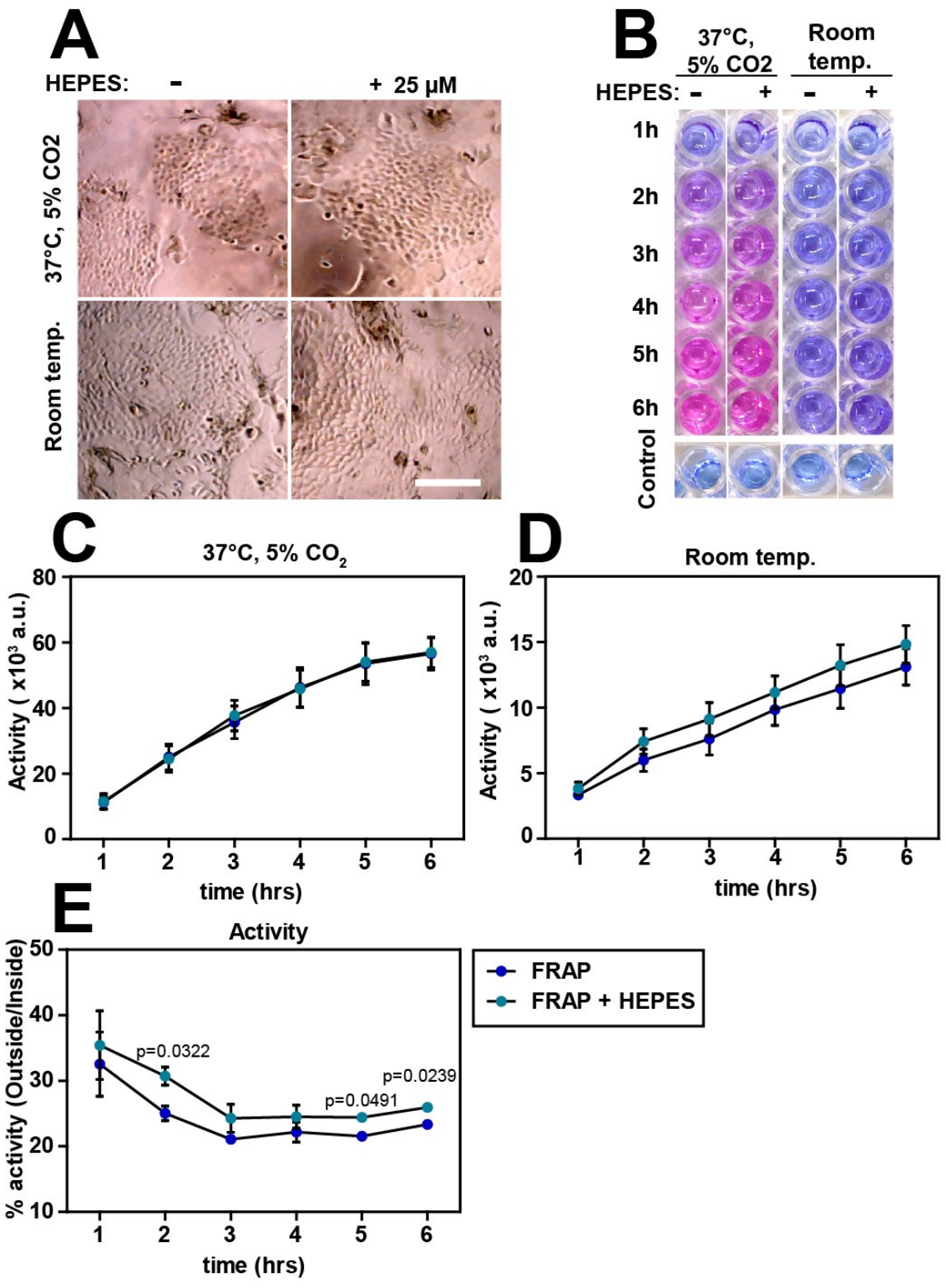

Figure 5.10: The use of FRAP medium containing HEPES is better suited for experiments at room temperature. Keratinocytes were cultured as monolayers and treated with AlamarBlue® for up to 6 hours and the resulting absorbance measured. (A) Brightfield images of cells incubated at 37°C, 5% CO_2 (top row) or at room temperature (bottom row) with or without the addition of HEPES. (B) Visible colour changes of cells containing AlamarBlue® from 1-6 hours. Control wells are those that did not contain cells. Metabolic activity measured inside (C) and outside (D) the incubator from 1-6 hrs. (D) Activity of cells with and without HEPES over a period of 6 hrs. Scale bar represents 200 µm. Graphs show mean values. Error bars represent SEM. Data representative of 3 independent experiments.

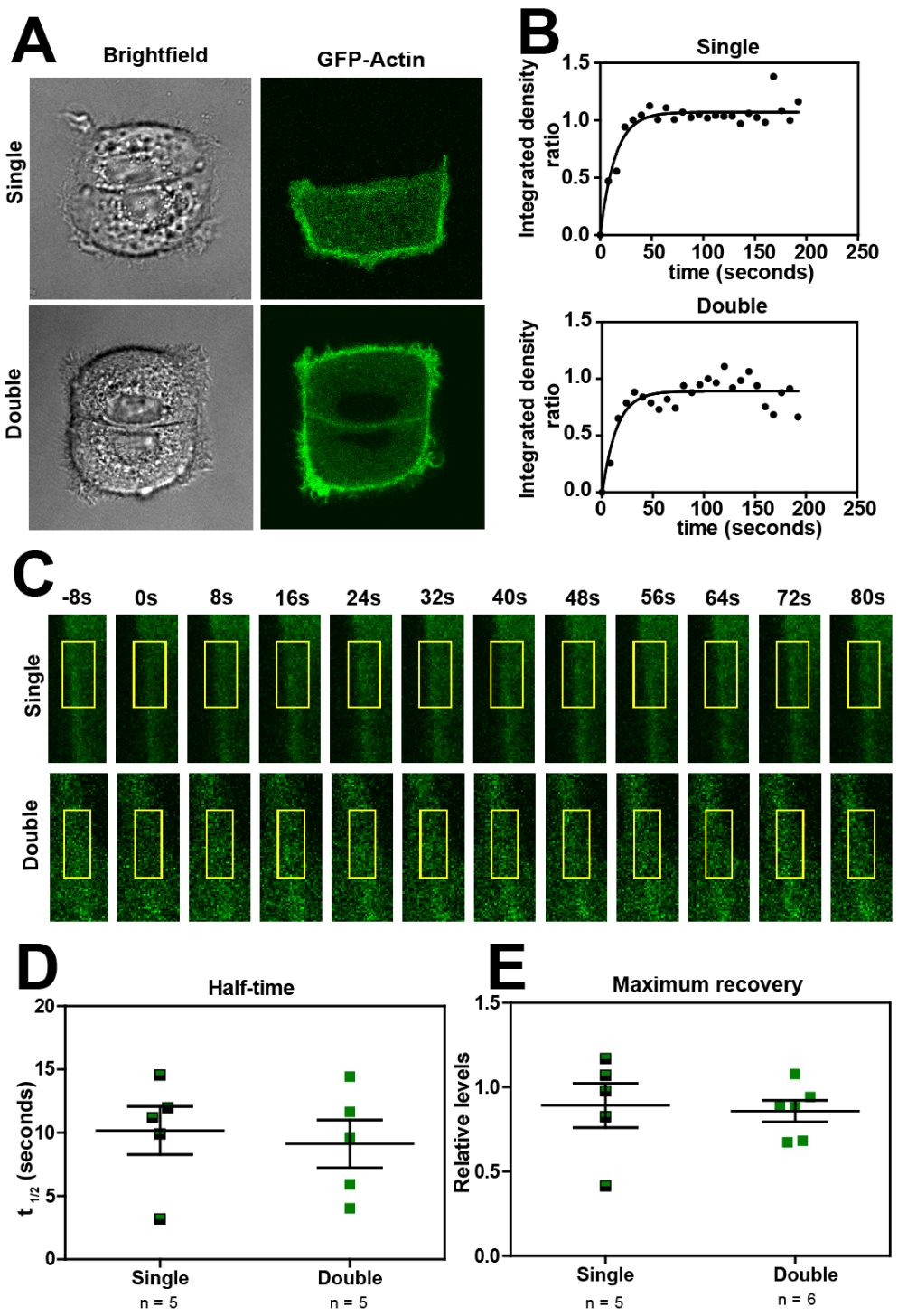

Figure 5.11: The half-time and recovery of single or double transfected cells grown on square shaped micropatterns do not significantly differ. FRAP was carried out 18 hours after transfection with GFP-Actin construct. (A) Brightfield and confocal images of doublets with one cell (top-right) or both cells (bottom-left) transfected. (B) Recovery curves for single (top) and double (bottom) transfected cells. (C) Recovery panels before (-8s), during (0s) and after (8-80s) photobleaching. Bleached area is represented within the yellow rectangle. (D) Half time of recovery. (E) Maximum recovery at which the curve plateaus. Scale bar represents 20 µm. Graphs show mean values. Data were analysed statistically by a student's t-test. Error bars represent SEM. Data representative of 2 independent experiments.

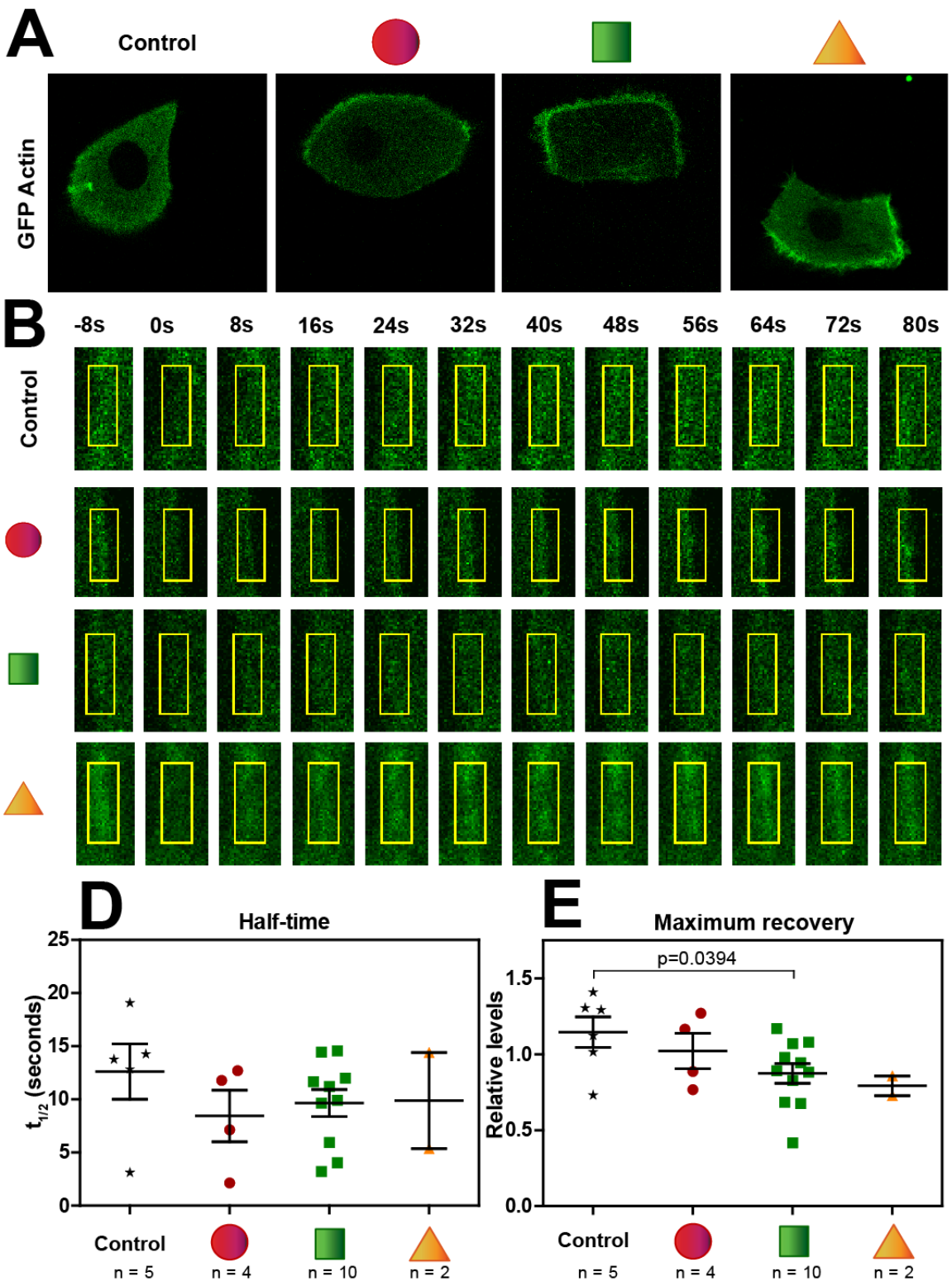

Figure 5.12: **Fluorescence recovery after photobleaching of junctional actin in cells grown on micropatterns.** FRAP was carried out 18 hours after transfection with GFP-Actin construct at the junctions of either single or double transfected cells. (A) Immunoflourescence images of doublets with a single transfected cell. (B) Recovery panels before (-8s), during (0s) and after (8-80s) photobleaching. Bleached area is represented within the yellow rectangle. (D) Half time of recovery. (E) Maximum recovery at which the curve plateaus. Scale bar represents 20 µm. Graphs show mean values. Error bars represent SEM. Data representative of 2 independent experiments.

Since the number of cells transfected on a given micropattern did not affect actin dynamics parameters measured, results from cell pairs grown on all three geometric micropatterns were computed and pooled together for comparison between the shapes. Control keratinocytes were maintained on unpatterned and unrestricted areas to allow for comparison with those confined in micropatterns. Fluorescent images of doublets transfected with GFP-actin in the three different shapes illustrate, as expected, that cell pairs maintain the shape despite expressing the vector (Figure 12A). The fluorescent intensity panels also show that cells bleach and recover efficiently despite the level of shape restriction and contractility (Figure 5.11B).

The half time of recovery was consistent on cell pairs grown on the three different geometric micropatterns and lower compared to the unrestricted control cells. However, data were not statistically significant due to the lack of power (n numbers). Interestingly, the maximum recovery levels showed shape-related differences. Maximum recovery at junctions correlated negatively with contractility. Recovery was highest in the circles and lowest in the triangles although the results did not show significance due to the low number of junctions analysed. When unrestricted control cells were compared to those on micropatterns, junctions of cell pairs grown on square micropatterns recovered significantly less than that of control cells. The graph represents data from only two independent experiments. Yet, controls and cell pairs on square micropatterns had the highest number of data points and exhibited significance. These results indicate shape-dependent control of actin dynamics such that an increase in contractility decreases the fraction of mobile actin molecules.

5.4 Discussion

5.4.1 Shape imposed cellular contractility affects junction configuration of doublets

Junction configuration encompasses three distinct morphological features of junctions including their length, linearity and coverage. These three different aspects of stabilised junctions will be discussed in the following paragraphs.

Epithelial cells arrange themselves in a hexagonal array characterised by the honey-comb like pattern to minimize their surface contact with surrounding cells [411][412]. Previous studies in our lab demonstrate heterogeneity of cell shapes and sizes on monolayers, but absolute values for junction lengths have not been reported [116]. Other studies only report vertical junction length shrinkage during cell intercalation during *Drosophila* embryogenesis [121]. For the first time we report the length of junctions of keratinocyte cell pairs when forced into different geometric shapes which differ significantly according to the geometry and imposed contractility.

Junction length: A recent study showed that MDCK epithelial cell pairs cultured on rectangular and I-shaped micropatterns of increasing size and aspect ratio regulated junction length through forces at the cell-cell contacts [413]. In contrast to my study, Sim et al. investigated the effect of varying cell spread area and aspect ratio of rectangular shaped micropatterns on cell forces [413]. The study reported that cell-ECM and cell-cell forces increase with spread area and aspect ratio but that junction length was differentially regulated. I have used micropatterns of the same spread area yet varying shapes therefore cell-cell forces calculated in their study may not be applicable to ours.

The 35 µm wide square (rectangle with aspect ratio 1:1) micropatterns which closely corresponds with that of mine which have a width of 36 µm, housed cell pairs with an average junction length of ~31 µm compare to the 35 µm length obtained in my study. An increase in aspect ratios on rectangular micropatterns corresponded to an increase in cell-cell forces without affecting junction lengths. This was explained by the continuation of the rectangular adhesive area at the distal ends of the cell-cell contacts, which play a role in anchoring the adhesive complexes and expanding junction lengths.

Different to my study in which the entire square shaped area consisted of adhesive ECM ligands for attachment of cell pairs, in their study, the adhesive region was restricted to a 10µm strip along the perimeter. Sim et al. also compared cell pairs grown on I shaped micropatterns, where edges of junctions could not be anchored by cell-ECM contacts on the pattern. Increasing the aspect ratio through elongation of I-shaped micropatterned regions resulted in sustained cell-cell forces and decreased junction lengths indicating that increasing contractility affects junction length.

In contrast, cell-cell forces and junction lengths do not correlate in unconstrained MDCK cell pairs that are able to freely migrate and change their cell shape and orientation on collagen-coated polyacrylamide gels [231]. Cell-cell forces remain constant while junctions remodel and change contact lengths by as much as 30% over 60 minutes. This is largely due to the uneven distribution of forces along the contact length, which cannot be deciphered through the net force vector used to measure cell-cell forces. Cell-cell contact retraction at the edges of calcium depleted cell pairs ascertain that a large fraction of the force accumulate at the contact vertices.

Also, the junction length of endotheilial cell pairs seeded on bowtie micropatterns is correlated with the magnitude of cell-cell forces which are also called intercellular tugging forces [124]. However, global cellular contractility measured through traction forces exerted on microneedles, shows no correlation to the length of junctions. These results indicate that the local tugging forces between cell pairs alone control changes in junction length. The contrasting results between the two studies can be explained by differences in cell type, cadherin type, junction geometry and structure of the underlying actin cytoskeleton at junctions: epithelial cells contain actin thin bundles, while endothelial cells have stress fibres [414].

Junction linearity: Epithelial cells have cell boundaries with a linear morphology to maintain such a low energy configuration. Depletion of Tuba, a Cdc42-specific GEF, leads to undulation of cell junctions and loss of the geometric configuration of epithelial cells [169]. Here, I reveal that increased contractility favours the formation of linear junctions such that junctions between cell pairs on

triangular shape bare the closest resemblance to straight lines. This result could be explained by the fact that the actin cytoskeleton regulates the viscoelasticity of the cell cortex to maintain surface tension necessary to form the cell-cell contacts [415]. Thus, my results imply that increased cortical tension brought about by increased contractility promotes the formation of straight junctions.

In contrast, between the majority of cell pairs cultured on circular micropatterns, the junction resembles a continuous 'S' shape resulting in a curved and slack phenotype. This sigmoidal cell-cell interface was first observed by Bragwynne et al. in dynamic bovine capillary endothelial cells cultured on 30-50 µm circular islands [361][328]. The curved junction formation in endothelial cells was predominantly attributed to the cortical tension and to a lesser extent to the actomyosin forces [363]. Interfacial deformations increase as cortical tensions decrease similar to my findings with cells grown on circles. However, fibroblasts cultured in the same way presented a straight cell-cell boundary showing cell specific remodelling of cell-cell interfaces [328]. The failure to produce this interfacial deformation, as seen in fibroblasts, was due to high cortical tension and short interfacial widths [363]. Since large stresses are necessary to deform rigid membranes (high cortical tension), the short, linear junction lengths could be explained by weak cell-cell adhesions relative to cortical tension giving rise to short interfacial distances designed to minimize the stresses [363].

Junction coverage: has not been explicitly mentioned in previous publications but is of interest to determine how efficiently junctions form across the length of the interface of neighbouring cells confined within micropatterns. As a measure of comparison, approximate junction coverage values were calculated using the data of Sim et al. on MDCK cells cultured on I-shape micropatterns that form a square shape when spread optimally [413]. I-shape pattern widths of 35 µm or 45 µm in width corresponded to coverage values of 63% and 66% respectively. Junction coverage values for cell pairs cultured on the three different geometric shapes in our study were consistent at 83%. The difference in cell types (primary keratinocytes versus simple epithelial MDCK cells) and the extra cellular matrix

coating area (whole geometric shape versus partial I-shaped region) could be reasons for the discrepancy between the two studies.

Taken together, my study shows that junction length and linearity are inversely correlated to contractility of cell pairs while junction coverage remains unchanged between shapes. Cell pairs across the shapes do not continue junctions to span the edges and it is, therefore, not a shape-dependent phenomenon. These parameters have not been collectively assessed on cell pairs in previous studies and hence for the first time show that cell contractility and tension affect junction configuration.

5.4.2 Levels of E-cadherin and actin at junctions are affected by contractility

Our study shows that the intensity and density of E-cadherin and actin at junctions negatively correlate with cellular contractility: junctions between cell pairs grown on triangular micropatterns contain significantly lower levels of E-cadherin receptors and actin (Figures 5.5-6). E-cadherin and actin intensity at junctions have not been addressed in the context of varying cellular contractility in previous studies with the use of different geometric micropatterns. MDCK cell pairs grown on rectangular shaped micropatterns of different aspect ratios (elongations), with corresponding increases in both the cell-ECM and cell-cell forces, were reported to have a decrease in average E-cadherin intensity along cell-cell contacts with forced elongation of cell pairs [413]. A further study reported that endogenous cell-cell forces in MDCK cell pairs measured through traction force microscopy does not correlate with the integrated E-cadherin intensity at the interface [231]. In agreement with this result, Bazellieres et al. showed that the rate of intercellular force build up is controlled by E-cadherin but not the magnitude of the cell-cell force itself [416]. Together, these results indicate that cell-ECM forces are the dominant force associated with contractility regulating the levels of E-cadherin receptors.

5.4.3 Contraction inhibition impairs junction morphology and recruitment of E-cadherin

The ROCK inhibitor Y27632 is a well-known disruptor of the actomysosin network and is used in many studies to antagonise the cytoskeletal tension [417]. Disruption of actomyosin–generated contractility

in individual RPE1 cells cultured on triangular shaped adhesive islands did not alter cell shape on continuous adhesive edges but cells cultured on concave micropatterns with different adhesive geometries underwent dramatic shape changes with profoundly sagging membrane borders [295]. Here for the first time, I inhibit contraction of cell pairs to determine the effects on both the configuration and molecular make up of junctions. Despite cell pairs maintaining their shapes in all three of the different geometries, contractility-dependent effects on junctions were erased specifically in the triangular shapes. The linearity index of cell-cell contacts between doublets in triangular micropatterns increased to levels seen in circular micropatterns indicating that the loss of cytoskeletal tension results in the undulation of junctions.

Junction coverage was perturbed in cell pairs cultured on all three geometric shapes such that coverage fell by 10%. A recent paper reported that treatment with Y27632 resulted in significantly shorter junctions in cell pairs cultured in bowtie shaped micropatterns and cells in monolayers [124]. Although this study measured junction length instead of junction coverage as we did, both results implicate that cells do not efficiently form junctions across the intercellular interface and specifically in micropatterns, do not span the edges of the geometric shape. RhoA and actomyosin have been shown to drive initiation, expansion, and completion of cell-cell contacts through their activity at contact edges [17]. Impairment of actomysoin contractility may thus contribute to a deficiency in expanding the cell-cell contacts to reach the edges and cover the entire cell boundary.

The intensity of E-cadherin at junctions significantly increases in cell pairs upon disruption of cytoskeletal tension when grown on the square and triangular shaped micropatterns such that intensity levels match with that seen on the circular micropatterns. However, the density of E-cadherin at junctions increases significantly on the square and triangular micropattern shapes to a level above that found in cell pairs cultured on the circular shaped micropatterns control (i.e. without treatment with Y27632). These results imply that the density of E-cadherin clusters increases with inhibition of contraction.

Both actin intensity and density showed no significant changes upon addition of the Y27632 compound and junctional levels remained low for cell pairs cultured on the square and triangular shapes.

Interestingly, my results show that levels of E-cadherin (intensity and density) at junctions is lower with increased tension. However, it would be expected that with an increase in cell tension, endocytic rates would decrease as it would be harder to deform the membrane and E-cadherin would accumulate along the adhesion. To support this hypothesis, it has been shown in MDCK cells by de Beco et al. that E-cadherin turnover rates increase with increased contact stress [150]. The discrepancy in results may be explained by the fact that my cells have a single neighbour compared to cells in a monolayer which have multiple neighbours and a variety of influential factors. Additionally, junctions were quantified with widefield images and not confocal images which could indicate E-cadherin levels along the lateral region through height reconstructions. De Beco et al. also showed that there were asymmetric turnover rates for cells with varying contractility induced by the overexpression of RhoA. Since my results indicate that discrepancies in cellular tension between cell pairs on triangular shapes is significant, this is likely transferred to the junction where contractility maybe asymmetric and affects the level of cadherins. It is also worth noting that an increase in contractility favours shorter junctions that do not span the edges of the shape. Although both the E-cadherin intensity and density were quantified in my study, neither showed an increase with contractility. Cadherin accumulation may therefore be influenced by more than cortical tension.

5.4.4 The mobility of actin molecules is perturbed by increases in acto-myosinII contractility

FRAP involves the irreversible bleaching of fluorescent molecules and subsequent recording of the recovery of fluorescence through the redistribution of surrounding non-bleached molecules [418]. The two parameters can be deduced from FRAP experiments; the mobile fraction of fluorescent molecules (maximum recovery) and the rate of mobility (half time) [419]. In my study, I observed the mobility of

GFP-actin molecules at cell junctions both in unconstrained keratinocytes and those confined within micropatterns.

My results indicate that although the rate of mobility of actin molecules remain unchanged at the junctions between the various samples, the half-life for actin turnover (10 seconds) maybe more rapid than that observed at the leading edge of migrating keratinocytes (23 seconds) [420] and at the contractile ring of llC-PK1 kidney tubule cells (26 seconds) [421]. My results also revealed that the mobile fraction of actin molecules is contractility-dependent. Unrestricted cells contained the largest fraction of dynamic actin while this fraction decreases with increase in contractility. In agreement with my findings, the mobility of actin (maximal percentage and rate of recovery) that makes up the junctional bands of cells declined progressively with the increase in age-related accumulation of F-actin that thickens the bundles [422]. The decrease in actin turnover due to higher cortical tension reduces mobility of E-cadherin molecules and increased accumulation at junctions [151]. Although my results support the decrease in actin turnover with increase in cortical tension, E-cadherin levels at junctions are not increased. This implies that there may be additional factors involved in cadherin dynamics which may affect the rate for E-cadherin removal from adhesions. In conclusion, I have shown that higher contractility and cortical tension favours shorter and straighter junction lengths. The minimization of distance in the triangles is dependent on actomyosin-generated tension and perturbation leads to undulation similar to circles which have curved junctions. Abolishment of thin bundle contractility also leads to lower junction coverage across the shapes suggesting that junction extension is perturbed. Actin dynamics at junctions alter with geometry such that, contractility negatively correlates with actin mobility.

CHAPTER SIX:

General discussion, summary and future directions

6.1 General discussion

Culturing cells on different shapes offer the possibility of imposing varying levels of contractility upon them and driving a myriad of cellular functions. Cell-ECM adhesion signalling in single cells cultured on micropatterned islands can be controlled by varying the type and density of the ECM and the spread area. Culturing cell pairs on micropatterns have the added possibility of controlling cell-cell adhesion signalling and creating a minimalistic system through which both types of signalling could be evaluated. In this study, I have cultured primary keratinocyte cell pairs on micropatterns of three different geometries; circles, squares and triangles with the same adhesive area and extracellular matrix ligand (i.e. same ECM ligand density).

A summary of findings related to the shape-imposed characteristics pertained by the doublets is shown in Table 6.1. Contractility of cell pairs is altered through the shape imposed upon the doublets. The circular shape imposes the least contractility as can be seen by the absence of stress fibres and randomly oriented peripheral actomyosin lamella. Squares impose a higher contractility owing to thick side stress fibres parallel to the edges together with the focal adhesion sites at the 90° vertices. Triangles impose the highest contractility because of the thick stress fibres aligned with the edges combined with the focal adhesion sites concentrated at the acute 60° vertices. These results are in line with the contractility reported on single cells [263], [290], [380] which remain unchanged when cell pairs are cultured on the different geometries instead.

My study has shown that shape-driven actomyosin contractility influences the viscoelastic properties of cell pairs as measured using SICM. This is the first time such measurements have been conducted on micropatterned cells be it single or more cells. Height and volume of individual cells show no correlation with cortical tension. Therefore, differences in cortical tension can be attributed to shape-driven contractility of cell pairs and the organisation of contractile actin fibres which positively correlates with cortical tension. In line with this, cells that possess the least contractility are highly deformable and thus take the longest time to relax to their initial state.

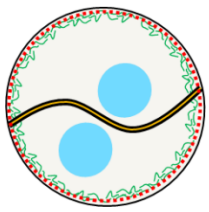

Circle

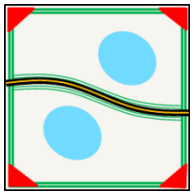

Square

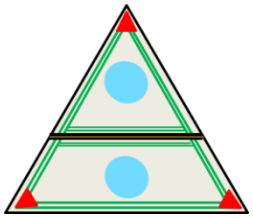

Triangle

Cellular Characteristics			
Cell height (µm)	10.04	9.71	9.86
Cell volume (µm^3)	2507	2527	2396
Nuclear distance (µm)	12.47	14.90	15.90
Young's Modulus (kPa)	8.8	14.4	16.1
Cellular dynamics			
Angular changes (Nº)	0.5	1.1	1.8
Speed (°/min)	2.26	1.65	1.53
Junction Characteristics			
Junction height (µm)	7.20	6.49	6.47
Linearity index	1.123	1.113	1.076
Junction coverage	0.825	0.828	0.825
Junction length (µm)	37.24	34.93	31.17
E-cadherin intensity	19,182	17,420	12,922
E-cadherin density	0.605	0.518	0.423
Actin intensity	22,677	19,632	16,313
Actin density	0.605	0.493	0.423
Contractility features			
F-actin side fibres (%)	0	100	100
PMLC side fibres (%)	0	100	100
F-actin lamella (%)	100.00	29.17	47.78
PMLC lamella (%)	100.00	25.00	23.33
Thin bundles (%)	50.00	79.17	76.67
Junctional actin (%)	100	100	100
PMLC labelling at bundles (%)	50.00	79.17	76.67
PMLC labelling at junctions (%)	36.67	29.17	30.00
Straight junctions (%)	21.67	34.72	58.89
Inhibition of contraction			
Linearity index	No change	No change	Increased
Junction coverage	Decreased	Decreased	Decreased
E-cadherin intensity	No change	No change	Increased
E-cadherin density	No change	Increased	Increased
Actin intensity	No change	No change	No change
Actin density	No change	No change	No change

Table 6.1: **Summary of characteristics of cells grown on different geometries.** The results are colour coded according to relative levels when compared to each other. Grey denotes no significant differences were observed between shapes. Yellow depicts the lowest value, red the highest and orange the intermediate when compared amongst the three different geometries.

Although our study did not explicitly measure junction tension, contractility at junctions were assessed via immunofluorescence staining of actin and PMLC and their presence at the junction and adjacent to junctions (thin bundles). Although junctions of cell pairs on all three different geometries contained actin at junctions, the vast majority of these were not labelled with myosin. Consistent with our previous reports on cell monolayers, my current results on micropatterns reinforce the finding that junctional actin is not contractile [116]. However, there is a discrepancy on the presence of thin bundles adjacent to junctions based on global cell contractility. When present, the thin bundles are always labelled with PMLC (i.e. contractile). The majority of intercellular junctions of doublets acquiring the square and triangular shapes have contractile thin bundles aligned with the junctions, while only half of the junctions of cell pairs grown on circular micropatterns contain parallel thin bundles. My results show that peripheral and junctional acto-myosinII contractility correlate with each other. This could be a result of either (1) peripheral contractility dictating junction contractility through signalling pathways or (2) integration of the two adhesive regions by actin filament meshwork in the cortex as seen during morphogenesis [60].

Junction configuration and composition (E-cadherin and F-actin levels) are also influenced by cellular and junctional contractility. The length of junctions and the linearity index (the curvature of junctions) exhibit a negative correlation with contractility. As contractility sensed at the junctions increases, such as in doublets cultured on the triangular shapes, their cell-cell contacts contain the highest tension, and have straighter and shorter junctions to minimize the area of contact between neighbouring cell pairs. Since cells cultured on triangles also display a preference in junction positioning, meaning they could have longer junctions if they positioned themselves differently, cell pairs on this shape actively minimize their junction length as a result of contractility/cortical tension. These changes in morphological parameters are accompanied by a corresponding decrease in the density of E-cadherin. The inhibition of thin bundle contraction (since these disappear upon treatment with Y27632) impairs junction composition and configuration such that junctions span a lesser distance between the edges (junction coverage) and have more E-cadherin receptors per junctional area. Cells grown on triangular

micropatterns also lose the linearity of their junctions (increased their linearity index) upon inhibition of contraction.

In line with this, nuclei are positioned furthest apart in triangles as a result of the combination of an increased contractility and tension at the junctions and within the cellular cortices. Since the positions of nuclei are balanced by both peripheral and junctional forces [393], our results imply that cell-cell forces may be the dominant forces that displaces the nuclei further apart. However, further measurements on junctional tension per se are needed in order to support this interpretation.

The composition of junctional proteins show an equally interesting dependence on cell geometry. Contractility at the cell cortex and thin bundles may play a critical role in determining the levels of junctional proteins. Both the density and intensity of E-cadherin at junctions is highest for cell pairs grown on the circular micropatterns, which impose the least contractility. These results infer that the decrease in thin bundle contraction beside the junctions enhances the recruitment of E-cadherin and actin to the intercellular contacts, while allowing junctions to increase their length and have a loser and slack (highest linearity index) appearance. This result contradicts previous findings which report an increase in junction length and E-cadherin accumulation with increase in junction tension. Such an increase in tension would also support the fact that a stiffer membrane is harder to deform and would lead to lower rates of endocytosis and more cadherin accumulation. However, my results show that an increased contractility both at the cell peripheries and junction and higher cortical tension correlate with shorter junction lengths and less E-cadherin at junctions. The asymmetric tension at junctions mediated by disproportionate neighbours as seen with cell pairs in the triangular shape may influence junction length and E-cadherin levels.

In addition to the structural features of the cell pairs and their junctions, cellular dynamics also demonstrate geometry dependence. Cell pairs cultured in the least contractile circular micropatterns frequently display a sigmoidal interface and rotate faster with the highest directional persistence. Our data are in line with previous reports that indicate coupling between the rotational behaviour and a

sigmoidal cell-cell interface [328], [361], [363]. The effect of contractility has not been addressed in previous dynamic studies and for the first time I have shown that increase in cortical tension leads to cell pairs rotating at lower speeds with more changes in angular direction.

Although F-actin levels at junctions are progressively reduced with higher cortical tension, inhibition of contraction by Y27632 does not significantly interfere with total F-actin levels at contact sites. Yet, the actin dynamics at the junction are modified by contractility-dependent effects. The mobile fraction of actin molecules (represented by the maximum recovery during FRAP) appears to decrease with higher contraction although further confirmation with more replicates is necessary to justify the trend. This implies that the junctional actin which is largely non-contractile (poor labelling with PMLC), becomes increasingly immobile with geometry driven generation of thin bundles and cortical tension. A combination of cell size, spread area and the number of neighbours maintain a specific actomyosin generated contractility in cells to optimize cell packing [6], [7] highlighting that individual junction configurations and compositions are optimised for structure specific functions. Taken together, my results have profound implications on how cellular tension determines junction characteristics of primary cell pairs, which is critical to maintaining proper functionality of epithelial tissues and organs.

6.2 Summary

In summary, I have shown that shape-driven contractility determines a myriad of features both within and between cell pairs. Cell contractility negatively correlates with junction configuration (linearity and length) and composition (recruitment of E-cadherin and actin). In turn, these characteristics determine cell motility and migration. A summary of the key findings are illustrated in Figure 6.1. The novel findings of my thesis are:

I. Peripheral actomyosin contractility determines cell tension, appearance of contractile thin bundles and junction tension of cell pairs.
II. Junction configuration and composition are contractility-dependent parameters
III. Positioning of nuclei is dependent on the balance between peripheral and junctional forces.
IV. Cellular dynamics and F-actin mobility at junctions are affected by acto-myosinII contractility

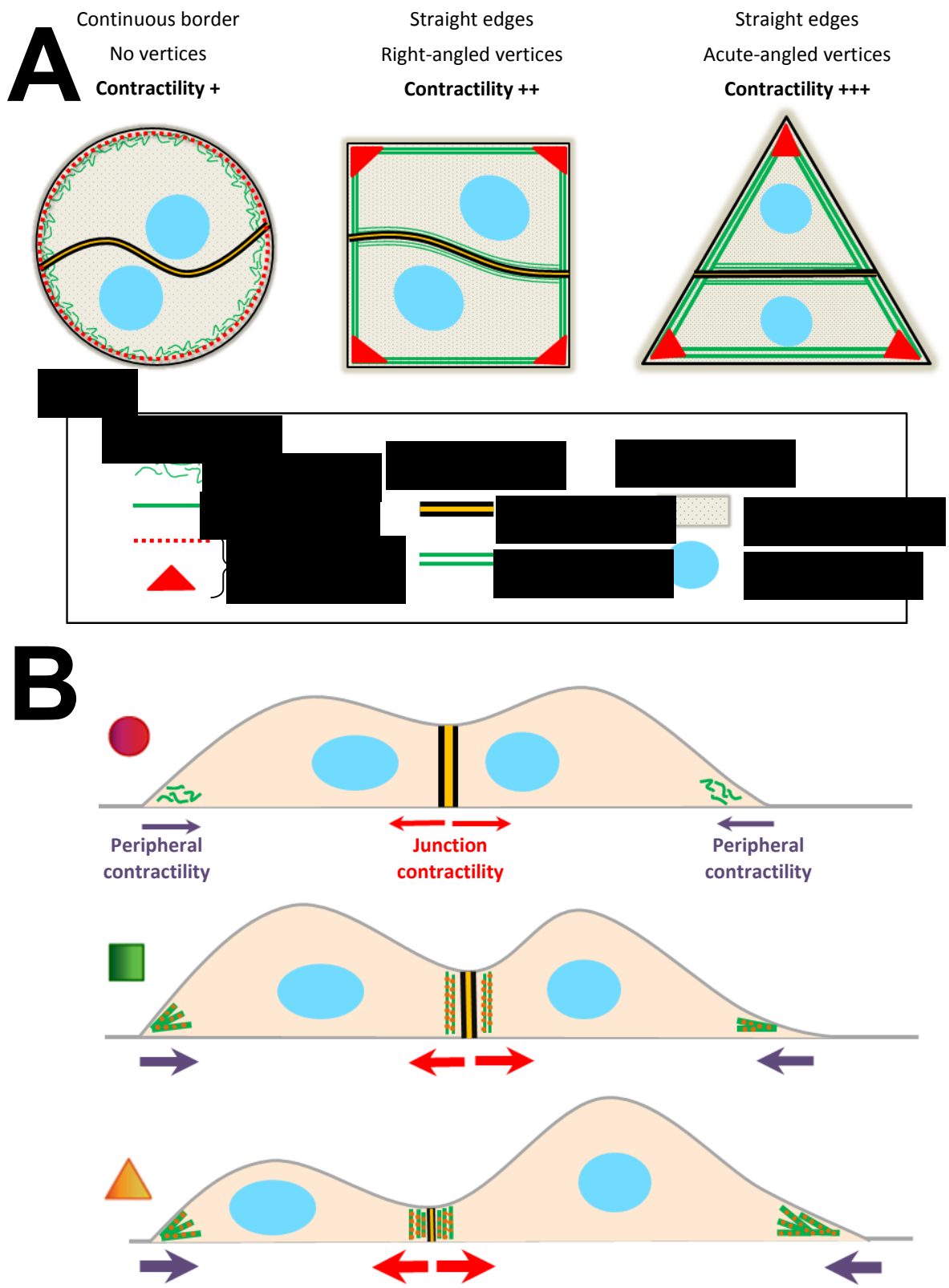

Figure 6.1: Model for contractility-dependant cell characteristics. High peripheral contractility induces increases in cell tension, junction contraction and junction tension and displaces nuclei further apart as shown in the schematic of top (A) and lateral (B) views

6.3 Future directions

The model system established by my work provides a minimal unit of junction regulation with vast implications for the dissection of signalling pathways with impact on cell-cell contact functionality. Further work is essential to strengthen my results. Due to the need for extensive optimisation of transfections on micropatterns and time constraints, I could not observe statistical significance specifically in the FRAP experiments which nevertheless show a clear trend. More experiments need to be conducted in order to increase 'N' numbers and perform valid statistical analyses.

My results strongly suggest that junctional tension is increased as shape driven contractility of cells increase. However, I have not conducted measurements of viscoelasticity at junctions with SICM or otherwise, due to technical limitations within our system. Junction tension on the different geometries need to be addressed quantitatively in order to definitively conclude my interpretations.

My work on cell motility has provided promising results in the realm of how cell contractility determines cell behaviour. However, it was limited to addressing only the speed and directionality of cell pairs due to restrictions within the quality of images that only allowed us to manually quantify the above parameters in Fiji. We are currently collaborating with Dr Andrew Loza (Washington University, St. Louis, U.S.A) to automatically quantify further parameters including the time the cell pair spends in a particular orientation, areas of cells at each time frame and overall motion (as a velocity measurement). Andrew has developed the automated program (Figure 6.2A) in Matlab which has been optimised and tested by myself. It is ready for systematic experimental analysis, which unfortunately could not be done due to time constraints. We are also collaborating with Prof. Sean Sun (John Hopkins University, Baltimore, U.S.A) in order to model the contractility-dependent preference of junction orientation and area sharing of the micropatterns by cell doublets. Although an initial model has been produced to relate space occupation of doublets with surface tension and contractility (Figure 6.2B), further experimentation is needed to strengthen these predictions with data on cellular dynamics combined with contractility inhibition.

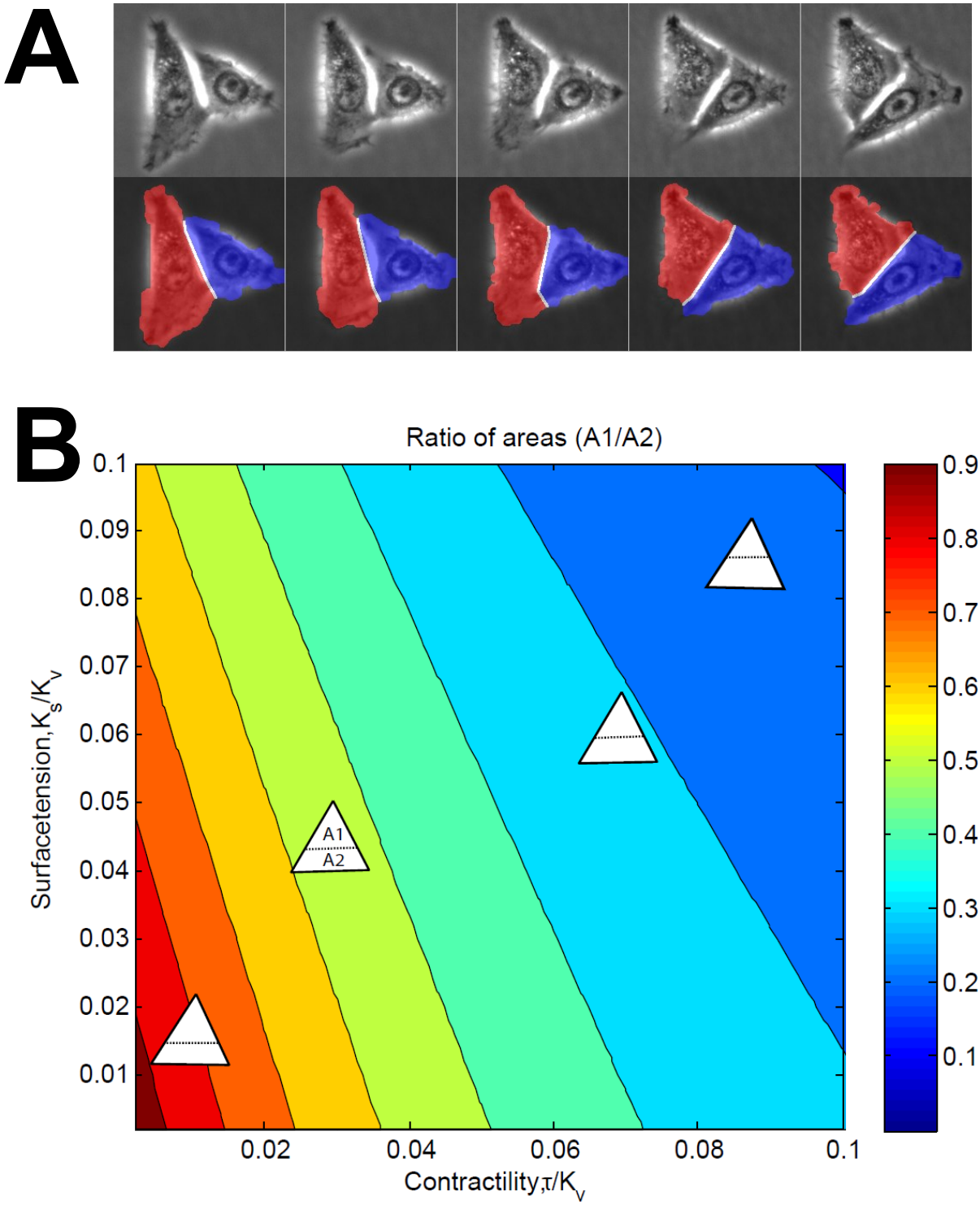

Figure 6.2: **Automated image analysis and modelling of cells grown on triangular micropatterns.** (A) First five frames depicting an initial test of the automated cell detection in Matlab (Program provided by Dr Andrew Loza, Washington University). (B) Model of contractility and tension dependent distribution of cell areas (Model provided by Prof Sean Sun, John Hopkins University) of cell pairs on triangular micropatterns.

References

[1] D. W. Powell, “Barrier function of epithelia.,” *Am. J. Physiol.*, vol. 241, no. 4, pp. G275–G288, 1981.

[2] a. H. Redi, “Morphogenesis and Tissue Engineering of Bone,” *Tissue Eng.*, vol. 6, no. 4, pp. 351–359, 2000.

[3] R. E. Dawes-Hoang, “Folded Gastrulation, Cell Shape Change and the Control of Myosin Localization,” *Development*, vol. 132, no. 18, pp. 4165–4178, 2005.

[4] S. D. Joshi and L. A. Davidson, “Epithelial machines of morphogenesis and their potential application in organ assembly and tissue engineering.,” *Biomech. Model. Mechanobiol.*, vol. 11, no. 8, pp. 1109–21, Nov. 2012.

[5] B. M. Gumbiner, “Epithelial morphogenesis,” *Cell*, vol. 69, no. 3, pp. 385–387, 1992.

[6] F. Schöck and N. Perrimon, “Molecular mechanisms of epithelial morphogenesis.,” *Annu. Rev. Cell Dev. Biol.*, vol. 18, no. 1, pp. 463–493, 2002.

[7] C. M. Niessen, D. Leckband, and A. S. Yap, “Tissue organization by cadherin adhesion molecules: dynamic molecular and cellular mechanisms of morphogenetic regulation.,” *Physiol. Rev.*, vol. 91, no. 2, pp. 691–731, Apr. 2011.

[8] S. Yonemura, “Cadherin-actin interactions at adherens junctions.,” *Curr. Opin. Cell Biol.*, vol. 23, no. 5, pp. 515–22, Oct. 2011.

[9] S. K. Wu, G. a Gomez, M. Michael, S. Verma, H. L. Cox, J. G. Lefevre, R. G. Parton, N. a Hamilton, Z. Neufeld, and A. S. Yap, “Cortical F-actin stabilization generates apical-lateral patterns of junctional contractility that integrate cells into epithelia.,” *Nat. Cell Biol.*, vol. 16, no. 2, pp. 167–78, Feb. 2014.

[10] S. Hong, R. B. Troyanovsky, and S. M. Troyanovsky, “Spontaneous assembly and active disassembly balance adherens junction homeostasis.,” *Proc. Natl. Acad. Sci. U. S. A.*, vol. 107, no. 8, pp. 3528–33, Feb. 2010.

[11] A. Vaezi, C. Bauer, V. Vasioukhin, and E. Fuchs, “Actin cable dynamics and Rho/Rock orchestrate a polarized cytoskeletal architecture in the early steps of assembling a stratified epithelium.,” *Dev. Cell*, vol. 3, no. 3, pp. 367–81, Sep. 2002.

[12] F. M. Mason, M. Tworoger, and A. C. Martin, “Apical domain polarization localizes actin-myosin activity to drive ratchet-like apical constriction.,” *Nat. Cell Biol.*, vol. 15, no. 8, pp. 926–36, 2013.

[13] S. Tojkander, G. Gateva, and P. Lappalainen, “Actin stress fibers-assembly, dynamics and biological roles.,” *J. Cell Sci.*, vol. 125, no. Pt 8, pp. 1855–64, Apr. 2012.

[14] Y. Cai, O. Rossier, N. C. Gauthier, N. Biais, M.-A. Fardin, X. Zhang, L. W. Miller, B. Ladoux, V. W. Cornish, and M. P. Sheetz, “Cytoskeletal coherence requires myosin-IIA contractility.,” *J. Cell Sci.*, vol. 123, no. Pt 3, pp. 413–23, Feb. 2010.

[15] Y. Aratyn-Schaus, P. W. Oakes, and M. L. Gardel, “Dynamic and structural signatures of lamellar actomyosin force generation.,” *Mol. Biol. Cell*, vol. 22, no. 8, pp. 1330–9, Apr. 2011.

[16] W. Luo, C. Yu, Z. Z. Lieu, J. Allard, A. Mogilner, M. P. Sheetz, and A. D. Bershadsky, “Analysis of the local organization and dynamics of cellular actin networks.,” *J. Cell Biol.*, vol. 202, no. 7, pp. 1057–73, Sep. 2013.

[17] S. Yamada and W. J. Nelson, “Localized zones of Rho and Rac activities drive initiation and expansion of epithelial cell cell adhesion,” *J. Cell Biol.*, vol. 178, no. 3, pp. 517–527, 2007.

[18] S. Tojkander, G. Gateva, and P. Lappalainen, “Actin stress fibers - assembly, dynamics and biological roles.,” *J. Cell Sci.*, vol. 125, no. Pt 8, pp. 1855–1864, 2012.

[19] M. Opas and V. I. Kalnins, “Spatial distribution of cortical proteins in cells of epithelial sheets.,” *Cell Tissue Res.*, vol. 239, no. 2, pp. 451–4, Jan. 1985.

[20] P. Maupin, C. L. Phillips, R. S. Adelstein, and T. D. Pollard, “Differential localization of myosin-II isozymes in human cultured cells and blood cells.,” *J. Cell Sci.*, vol. 107 (Pt 1, pp. 3077–90, Nov. 1994.

[21] A. M. Shewan, M. Maddugoda, A. Kraemer, S. J. Stehbens, S. Verma, E. M. Kovacs, and A. S. Yap, “Myosin 2 is a key Rho kinase target necessary for the local concentration of E-cadherin at cell-cell contacts.,” *Mol. Biol. Cell*, vol. 16, no. 10, pp. 4531–42, Oct. 2005.

[22] A. M. Castillo, R. Lagunes, M. Urban, E. Frixione, and I. Meza, “Myosin II-actin interaction in MDCK cells: role in cell shape changes in response to Ca2+ variations.,” *J. Muscle Res. Cell Motil.*, vol. 19, no. 5, pp. 557–74, Jun. 1998.

[23] K. L. Weber, R. S. Fischer, and V. M. Fowler, “Tmod3 regulates polarized epithelial cell morphology.,” *J. Cell Sci.*, vol. 120, no. Pt 20, pp. 3625–32, Oct. 2007.

[24] T. J. Widmann and C. Dahmann, “Dpp signaling promotes the cuboidal-to-columnar shape transition of Drosophila wing disc epithelia by regulating Rho1.,” *J. Cell Sci.*, vol. 122, no. Pt 9, pp. 1362–73, May 2009.

[25] J. Zhang, M. Betson, J. Erasmus, K. Zeikos, M. Bailly, L. P. Cramer, and V. M. M. Braga, “Actin at cell-cell junctions is composed of two dynamic and functional populations,” *J. Cell Sci.*, vol. 118, no. 23, pp. 5549–5562, 2005.

[26] T. D. Pollard, L. Blanchoin, and R. D. Mullins, “Molecular mechanisms controlling actin filament dynamics in nonmuscle cells.,” *Annu. Rev. Biophys. Biomol. Struct.*, vol. 29, pp. 545–76, Jan. 2000.

[27] H. N. Higgs, “Formin proteins: a domain-based approach.,” *Trends Biochem. Sci.*, vol. 30, no. 6, pp. 342–53, Jun. 2005.

[28] E. D. Goley and M. D. Welch, “The ARP2/3 complex: an actin nucleator comes of age.,” *Nat. Rev. Mol. Cell Biol.*, vol. 7, no. 10, pp. 713–26, Oct. 2006.

[29] J. A. Cooper and D. Sept, “New insights into mechanism and regulation of actin capping protein.,” *Int. Rev. Cell Mol. Biol.*, vol. 267, pp. 183–206, Jan. 2008.

[30] D. A. Fletcher and R. D. Mullins, “Cell mechanics and the cytoskeleton,” *Nature*, vol. 463, no. 7280, pp. 485–492, 2010.

[31] M. Bovellan, Y. Romeo, M. Biro, A. Boden, P. Chugh, A. Yonis, M. Vaghela, M. Fritzsche, D. Moulding, R. Thorogate, A. J??gou, A. J. Thrasher, G. Romet-Lemonne, P. P. Roux, E. K. Paluch, and G. Charras, “Cellular control of cortical actin nucleation,” *Curr. Biol.*, vol. 24, no. 14, pp. 1628–1635, 2014.

[32] C. Le Clainche and M.-F. Carlier, “Regulation of actin assembly associated with protrusion and adhesion in cell migration.,” *Physiol. Rev.*, vol. 88, no. 2, pp. 489–513, Apr. 2008.

[33] S. Jansen, A. Collins, C. Yang, G. Rebowski, T. Svitkina, and R. Dominguez, “Mechanism of actin filament bundling by fascin.,” *J. Biol. Chem.*, vol. 286, no. 34, pp. 30087–96, Aug. 2011.

[34] Y. Feng and C. A. Walsh, “The many faces of filamin: a versatile molecular scaffold for cell motility and signalling.,” *Nat. Cell Biol.*, vol. 6, no. 11, pp. 1034–8, Nov. 2004.

[35] K. Burridge and E. S. Wittchen, “The tension mounts: stress fibers as force-generating mechanotransducers.,” *J. Cell Biol.*, vol. 200, no. 1, pp. 9–19, Jan. 2013.

[36] M. Ikebe and D. J. Hartshorne, “The role of myosin phosphorylation in the contraction-relaxation cycle of smooth muscle.,” *Experientia*, vol. 41, no. 8, pp. 1006–10, Aug. 1985.

[37] G. M. Cooper, “Actin, Myosin, and Cell Movement,” *Cell A Mol. approach*, no. 2nd edition, 2000.

[38] A. R. Bresnick, “Molecular mechanisms of nonmuscle myosin-II regulation.,” *Curr. Opin. Cell Biol.*, vol. 11, no. 1, pp. 26–33, Feb. 1999.

[39] E. Golomb, X. Ma, S. S. Jana, Y. A. Preston, S. Kawamoto, N. G. Shoham, E. Goldin, M. A. Conti, J. R. Sellers, and R. S. Adelstein, “Identification and characterization of nonmuscle myosin II-C, a new member of the myosin II family.,” *J. Biol. Chem.*, vol. 279, no. 4, pp. 2800–8, Jan. 2004.

[40] K. C. Holmes, *Myosins*, vol. 7. Dordrecht: Springer Netherlands, 2007.

[41] M. Kovács, F. Wang, A. Hu, Y. Zhang, and J. R. Sellers, “Functional divergence of human cytoplasmic myosin II: kinetic characterization of the non-muscle IIA isoform.,” *J. Biol. Chem.*, vol. 278, no. 40, pp. 38132–40, Oct. 2003.

[42] F. Wang, M. Kovacs, A. Hu, J. Limouze, E. V Harvey, and J. R. Sellers, “Kinetic mechanism of non-muscle myosin IIB: functional adaptations for tension generation and maintenance.,” *J. Biol. Chem.*, vol. 278, no. 30, pp. 27439–48, Jul. 2003.

[43] B. I. Gerashchenko, K. Ueda, M. Hino, and H. Hosoya, “Phosphorylation at threonine-18 in addition to phosphorylation at serine-19 on myosin-II regulatory light chain is a mitosis-specific event.,” *Cytometry*, vol. 47, no. 3, pp. 150–7, Mar. 2002.

[44] M. Ikebe and D. J. Hartshorne, “Phosphorylation of smooth muscle myosin at two distinct sites by myosin light chain kinase.,” *J. Biol. Chem.*, vol. 260, no. 18, pp. 10027–31, Aug. 1985.

[45] R. Craig, R. Smith, and J. Kendrick-Jones, “Light-chain phosphorylation controls the conformation of vertebrate non-muscle and smooth muscle myosin molecules.,” *Nature*, vol. 302, no. 5907, pp. 436–9, Jan. .

[46] T. Watanabe, H. Hosoya, and S. Yonemura, “Regulation of myosin II dynamics by phosphorylation and dephosphorylation of its light chain in epithelial cells.,” *Mol. Biol. Cell*, vol. 18, no. 2, pp. 605–16, Feb. 2007.

[47] Y. Mizuno, E. Isotani, J. Huang, H. Ding, J. T. Stull, and K. E. Kamm, “Myosin light chain kinase activation and calcium sensitization in smooth muscle in vivo.,” *Am. J. Physiol. Cell Physiol.*, vol. 295, no. 2, pp. C358–64, Aug. 2008.

[48] M. Amano, M. Ito, K. Kimura, Y. Fukata, K. Chihara, T. Nakano, Y. Matsuura, and K. Kaibuchi, “Phosphorylation and activation of myosin by Rho-associated kinase (Rho-kinase).,” *J. Biol. Chem.*, vol. 271, no. 34, pp. 20246–9, Aug. 1996.

[49] K. Riento and A. J. Ridley, “Rocks: multifunctional kinases in cell behaviour.,” *Nat. Rev. Mol. Cell Biol.*, vol. 4, no. 6, pp. 446–56, Jun. 2003.

[50] M. Maekawa, T. Ishizaki, S. Boku, N. Watanabe, A. Fujita, A. Iwamatsu, T. Obinata, K. Ohashi, K. Mizuno, and S. Narumiya, “Signaling from Rho to the actin cytoskeleton through protein kinases ROCK and LIM-kinase.,” *Science*, vol. 285, no. 5429, pp. 895–8, Aug. 1999.

[51] F. Li and H. N. Higgs, “The mouse Formin mDia1 is a potent actin nucleation factor regulated by autoinhibition.,” *Curr. Biol.*, vol. 13, no. 15, pp. 1335–40, Aug. 2003.

[52] N. Watanabe, T. Kato, a Fujita, T. Ishizaki, and S. Narumiya, “Cooperation between mDia1 and ROCK in Rho-induced actin reorganization.,” *Nat. Cell Biol.*, vol. 1, no. 3, pp. 136–143, 1999.

[53] J. M. Sawyer, J. R. Harrell, G. Shemer, J. Sullivan-Brown, M. Roh-Johnson, and B. Goldstein, “Apical constriction: a cell shape change that can drive morphogenesis.,” *Dev. Biol.*, vol. 341, no. 1, pp. 5–19, May 2010.

[54] T. Nishimura, H. Honda, and M. Takeichi, “Planar cell polarity links axes of spatial dynamics in neural-tube closure.,” *Cell*, vol. 149, no. 5, pp. 1084–97, May 2012.

[55] T. Nishimura and M. Takeichi, “Shroom3-mediated recruitment of Rho kinases to the apical cell junctions regulates epithelial and neuroepithelial planar remodeling.,” *Development*, vol. 135, no. 8, pp. 1493–502, Apr. 2008.

[56] M. Vicente-Manzanares, X. Ma, R. S. Adelstein, and A. R. Horwitz, “Non-muscle myosin II takes centre stage in cell adhesion and migration,” *Nat. Rev. Mol. Cell Biol.*, vol. 10, no. 11, pp. 778–790, 2009.

[57] A. C. Martin, M. Kaschube, and E. F. Wieschaus, “Pulsed contractions of an actin–myosin network drive apical constriction,” *Nature*, vol. 457, no. 7228, pp. 495–499, 2009.

[58] J. Solon, A. Kaya-Copur, J. Colombelli, and D. Brunner, “Pulsed forces timed by a ratchet-like mechanism drive directed tissue movement during dorsal closure.,” *Cell*, vol. 137, no. 7, pp. 1331–42, Jul. 2009.

[59] M. Roh-Johnson, G. Shemer, C. D. Higgins, J. H. McClellan, A. D. Werts, U. S. Tulu, L. Gao, E. Betzig, D. P. Kiehart, and B. Goldstein, “Triggering a cell shape change by exploiting preexisting actomyosin contractions.,” *Science*, vol. 335, no. 6073, pp. 1232–5, Mar. 2012.

[60] A. C. Martin, M. Gelbart, R. Fernandez-Gonzalez, M. Kaschube, and E. F. Wieschaus, “Integration of contractile forces during tissue invagination,” *J. Cell Biol.*, vol. 188, no. 5, pp. 735–749, 2010.

[61] J. K. Sawyer, W. Choi, K.-C. Jung, L. He, N. J. Harris, and M. Peifer, “A contractile actomyosin network linked to adherens junctions by Canoe/afadin helps drive convergent extension.,” *Mol. Biol. Cell*, vol. 22, no. 14, pp. 2491–508, Jul. 2011.

[62] J. K. Sawyer, N. J. Harris, K. C. Slep, U. Gaul, and M. Peifer, “The Drosophila afadin homologue Canoe regulates linkage of the actin cytoskeleton to adherens junctions during apical constriction.,” *J. Cell Biol.*, vol. 186, no. 1, pp. 57–73, Jul. 2009.

[63] J. N. Jodoin and A. C. Martin, “Epithelial Contractility: A Crowning Achievement,” *Dev. Cell*, vol. 37, no. 1, pp. 3–4, 2016.

[64] M. Michael, J. C. M. Meiring, B. R. Acharya, D. R. Matthews, S. Verma, S. P. Han, M. M. Hill, R. G. Parton, G. A. Gomez, and A. S. Yap, “Coronin 1B Reorganizes the Architecture of F-Actin Networks for Contractility at Steady-State and Apoptotic Adherens Junctions.,” *Dev. Cell*, vol. 37, no. 1, pp. 58–71, Apr. 2016.

[65] B. M. Gumbiner, “Cell adhesion: The molecular basis of tissue architecture and morphogenesis,” *Cell*, vol. 84, no. 3, pp. 345–357, 1996.

[66] V. Braga, “Epithelial Cell Shape: Cadherins and Small GTPases,” *Exp. Cell Res.*, vol. 261, no. 1, pp. 83–90, 2000.

[67] J. M. Anderson and C. M. Van Itallie, “Physiology and function of the tight junction.,” *Cold Spring Harb. Perspect. Biol.*, vol. 1, no. 2, p. a002584, Aug. 2009.

[68] S. Terry, M. Nie, K. Matter, and M. S. Balda, “Rho signaling and tight junction functions.,” *Physiology (Bethesda).*, vol. 25, no. 1, pp. 16–26, Feb. 2010.

[69] C. M. Niessen and C. J. Gottardi, “Molecular components of the adherens junction.,” *Biochim. Biophys. Acta*, vol. 1778, no. 3, pp. 562–71, Mar. 2008.

[70] D. Garrod and M. Chidgey, “Desmosome structure, composition and function.,” *Biochim. Biophys. Acta*, vol. 1778, no. 3, pp. 572–87, Mar. 2008.

[71] B. N. G. Giepmans and S. C. D. van Ijzendoorn, “Epithelial cell-cell junctions and plasma membrane domains.,” *Biochim. Biophys. Acta*, vol. 1788, no. 4, pp. 820–31, Apr. 2009.

[72] B. M. Gumbiner, “Regulation of cadherin-mediated adhesion in morphogenesis,” *Nat. Rev. Mol. Cell Biol.*, vol. 6, no. 8, pp. 622–634, 2005.

[73] J. M. Halbleib and W. J. Nelson, “Cadherins in development: cell adhesion, sorting, and tissue morphogenesis.,” *Genes Dev.*, vol. 20, no. 23, pp. 3199–214, Dec. 2006.

[74] E. Stepniak, G. L. Radice, and V. Vasioukhin, “Adhesive and signaling functions of cadherins and catenins in vertebrate development.,” *Cold Spring Harb. Perspect. Biol.*, vol. 1, no. 5, p. a002949, Nov. 2009.

[75] M. Takeichi, “The cadherins: cell-cell adhesion molecules controlling animal morphogenesis.,” *Development*, vol. 102, no. 4, pp. 639–55, Apr. 1988.

[76] D. B. Ivanov, M. P. Philippova, and V. A. Tkachuk, “Structure and functions of classical cadherins.,” *Biochem. Biokhimiia*, vol. 66, no. 10, pp. 1174–86, Oct. 2001.

[77] H. Oda and M. Takeichi, “Evolution: structural and functional diversity of cadherin at the adherens junction.,” *J. Cell Biol.*, vol. 193, no. 7, pp. 1137–46, Jun. 2011.

[78] T. Harris, *Adherens Junctions: from Molecular Mechanisms to Tissue Development and Disease*. Springer Science & Business Media, 2012.

[79] H. Wakita, S. Shirahama, and F. Furukawa, “Distinct P-cadherin expression in cultured normal human keratinocytes and squamous cell carcinoma cell lines.,” *Microsc. Res. Tech.*, vol. 43, no. 3, pp. 218–23, Nov. 1998.

[80] D. F. Jarrard, R. Paul, A. van Bokhoven, S. H. Nguyen, G. S. Bova, M. J. Wheelock, K. R. Johnson, J. Schalken, M. Bussemakers, and W. B. Isaacs, “P-Cadherin is a basal cell-specific epithelial marker that is not expressed in prostate cancer.,” *Clin. Cancer Res.*, vol. 3, no. 11, pp. 2121–8, Nov. 1997.

[81] J. C. Wu, C. W. Gregory, and R. M. DePhilip, “P-cadherin and E-cadherin are co-expressed in MDCK cells.,” *Biochem. Biophys. Res. Commun.*, vol. 195, no. 3, pp. 1329–35, Sep. 1993.

[82] Y. Takai, W. Ikeda, H. Ogita, and Y. Rikitake, “The immunoglobulin-like cell adhesion molecule nectin and its associated protein afadin.,” *Annu. Rev. Cell Dev. Biol.*, vol. 24, pp. 309–42, Jan. 2008.

[83] Y. Tanaka, H. Nakanishi, S. Kakunaga, N. Okabe, T. Kawakatsu, K. Shimizu, and Y. Takai, “Role of nectin in formation of E-cadherin-based adherens junctions in keratinocytes: analysis with the N-cadherin dominant negative mutant.,” *Mol. Biol. Cell*, vol. 14, no. 4, pp. 1597–609, Apr. 2003.

[84] M. Takeichi, “Dynamic contacts: rearranging adherens junctions to drive epithelial remodelling.,” *Nat. Rev. Mol. Cell Biol.*, vol. 15, no. 6, pp. 397–410, Jun. 2014.

[85] M. Overduin, T. S. Harvey, S. Bagby, K. I. Tong, P. Yau, M. Takeichi, and M. Ikura, “Solution structure of the epithelial cadherin domain responsible for selective cell adhesion.,” *Science*, vol. 267, no. 5196, pp. 386–9, Jan. 1995.

[86] M. Overduin, K. I. Tong, C. M. Kay, and M. Ikura, “1H, 15N and 13C resonance assignments and monomeric structure of the amino-terminal extracellular domain of epithelial cadherin.,” *J. Biomol. NMR*, vol. 7, no. 3, pp. 173–89, May 1996.

[87] B. Nagar, M. Overduin, M. Ikura, and J. M. Rini, “Structural basis of calcium-induced E-cadherin rigidification and dimerization.,” *Nature*, vol. 380, no. 6572, pp. 360–4, Mar. 1996.

[88] S. A. Kim, C.-Y. Tai, L.-P. Mok, E. A. Mosser, and E. M. Schuman, “Calcium-dependent dynamics of cadherin interactions at cell-cell junctions.,” *Proc. Natl. Acad. Sci. U. S. A.*, vol. 108, no. 24, pp. 9857–62, Jun. 2011.

[89] O. Hiroki, “Evolution of the cadherin-catenin complex.,” *Subcell. Biochem.*, vol. 60, pp. 9–35, Jan. 2012.

[90] A. S. Yap, M. S. Crampton, and J. Hardin, “Making and breaking contacts: the cellular biology of cadherin regulation.,” *Curr. Opin. Cell Biol.*, vol. 19, no. 5, pp. 508–14, Oct. 2007.

[91] A. Hartsock and W. J. Nelson, “Adherens and tight junctions: structure, function and connections to the actin cytoskeleton.,” *Biochim. Biophys. Acta*, vol. 1778, no. 3, pp. 660–9, Mar. 2008.

[92] M. Watabe-Uchida, N. Uchida, Y. Imamura, A. Nagafuchi, K. Fujimoto, T. Uemura, S. Vermeulen, F. van Roy, E. D. Adamson, and M. Takeichi, “α-Catenin-Vinculin Interaction Functions to Organize the Apical Junctional Complex in Epithelial Cells,” *J. Cell Biol.*, vol. 142, no. 3, pp. 847–857, Aug. 1998.

[93] S. D. Hansen, A. V Kwiatkowski, C.-Y. Ouyang, H. Liu, S. Pokutta, S. C. Watkins, N. Volkmann, D. Hanein, W. I. Weis, R. D. Mullins, and W. J. Nelson, “αE-catenin actin-binding domain alters actin filament conformation and regulates binding of nucleation and disassembly factors.,” *Mol. Biol. Cell*, vol. 24, no. 23, pp. 3710–20, Dec. 2013.

[94] S. Yamada, S. Pokutta, F. Drees, W. I. Weis, and W. J. Nelson, “Deconstructing the cadherin-catenin-actin complex.,” *Cell*, vol. 123, no. 5, pp. 889–901, Dec. 2005.

[95] E. E. Weiss, M. Kroemker, A. H. Rüdiger, B. M. Jockusch, and M. Rüdiger, “Vinculin is part of the cadherin-catenin junctional complex: complex formation between alpha-catenin and vinculin.,” *J. Cell Biol.*, vol. 141, no. 3, pp. 755–64, May 1998.

[96] S. Yonemura, Y. Wada, T. Watanabe, A. Nagafuchi, and M. Shibata, “alpha-Catenin as a tension transducer that induces adherens junction development.,” *Nat. Cell Biol.*, vol. 12, no. 6, pp. 533–42, Jun. 2010.

[97] J. McCormack, N. J. Welsh, and V. M. M. Braga, “Cycling around cell-cell adhesion with Rho GTPase regulators.,” *J. Cell Sci.*, vol. 126, pp. 379–91, 2013.

[98] M. J. Wheelock and K. R. Johnson, “Cadherin-mediated cellular signaling,” *Curr. Opin. Cell Biol.*, vol. 15, no. 5, pp. 509–514, 2003.

[99] W. J. Nelson, “Regulation of cell-cell adhesion by the cadherin-catenin complex.,” *Biochem. Soc. Trans.*, vol. 36, no. Pt 2, pp. 149–55, Apr. 2008.

[100] Z. Xie and D. D. Bikle, “The recruitment of phosphatidylinositol 3-kinase to the E-cadherin-catenin complex at the plasma membrane is required for calcium-induced phospholipase C-gamma1 activation and human keratinocyte differentiation.,” *J. Biol. Chem.*, vol. 282, no. 12, pp. 8695–703, Mar. 2007.

[101] T. Watanabe, K. Sato, and K. Kaibuchi, “Cadherin-mediated intercellular adhesion and signaling cascades involving small GTPases.,” *Cold Spring Harb. Perspect. Biol.*, vol. 1, no. 3, p. a003020, Sep. 2009.

[102] C. L. Adams, W. J. Nelson, and S. J. Smith, “Quantitative analysis of cadherin-catenin-actin reorganization during development of cell-cell adhesion.,” *J. Cell Biol.*, vol. 135, no. 6 Pt 2, pp. 1899–911, Dec. 1996.

[103] V. Vasioukhin, C. Bauer, M. Yin, and E. Fuchs, “Directed actin polymerization is the driving force for epithelial cell-cell adhesion.,” *Cell*, vol. 100, no. 2, pp. 209–19, Jan. 2000.

[104] C. L. Adams, Y. T. Chen, S. J. Smith, and W. J. Nelson, “Mechanisms of epithelial cell-cell adhesion and cell compaction revealed by high-resolution tracking of E-cadherin-green fluorescent protein.,” *J. Cell Biol.*, vol. 142, no. 4, pp. 1105–19, Aug. 1998.

[105] V. M. Braga, L. M. Machesky, A. Hall, and N. A. Hotchin, “The small GTPases Rho and Rac are required for the establishment of cadherin-dependent cell-cell contacts.,” *J. Cell Biol.*, vol. 137, no. 6, pp. 1421–31, Jun. 1997.

[106] F. M. Helwani, E. M. Kovacs, A. D. Paterson, S. Verma, R. G. Ali, A. S. Fanning, S. A. Weed, and A. S. Yap, “Cortactin is necessary for E-cadherin-mediated contact formation and actin reorganization.,” *J. Cell Biol.*, vol. 164, no. 6, pp. 899–910, Mar. 2004.

[107] E. M. Kovacs, R. G. Ali, A. J. McCormack, and A. S. Yap, “E-cadherin homophilic ligation directly signals through Rac and phosphatidylinositol 3-kinase to regulate adhesive contacts.,” *J. Biol. Chem.*, vol. 277, no. 8, pp. 6708–18, Feb. 2002.

[108] S. Verma, A. M. Shewan, J. A. Scott, F. M. Helwani, N. R. den Elzen, H. Miki, T. Takenawa, and A. S. Yap, “Arp2/3 activity is necessary for efficient formation of E-cadherin adhesive contacts.,” *J. Biol. Chem.*, vol. 279, no. 32, pp. 34062–70, Aug. 2004.

[109] S. Yamada, S. Pokutta, F. Drees, W. I. Weis, and W. J. Nelson, “Deconstructing the Cadherin-Catenin-Actin Complex,” *Cell*, vol. 123, no. 5, pp. 889–901, 2005.

[110] F. Drees, S. Pokutta, S. Yamada, W. J. Nelson, and W. I. Weis, “Alpha-catenin is a molecular switch that binds E-cadherin-beta-catenin and regulates actin-filament assembly.,” *Cell*, vol. 123, no. 5, pp. 903–15, Dec. 2005.

[111] D. L. Rimm, E. R. Koslov, P. Kebriaei, C. D. Cianci, and J. S. Morrow, “Alpha 1(E)-catenin is an actin-binding and -bundling protein mediating the attachment of F-actin to the membrane adhesion complex.,” *Proc. Natl. Acad. Sci. U. S. A.*, vol. 92, no. 19, pp. 8813–7, Sep. 1995.

[112] A. Kobielak and E. Fuchs, “Alpha-catenin: at the junction of intercellular adhesion and actin dynamics.,” *Nat. Rev. Mol. Cell Biol.*, vol. 5, no. 8, pp. 614–25, Aug. 2004.

[113] W. Meng and M. Takeichi, “Adherens junction: molecular architecture and regulation.,” *Cold Spring Harb. Perspect. Biol.*, vol. 1, no. 6, p. a002899, Dec. 2009.

[114] J. A. Scott, A. M. Shewan, N. R. den Elzen, J. J. Loureiro, F. B. Gertler, and A. S. Yap, “Ena/VASP proteins can regulate distinct modes of actin organization at cadherin-adhesive contacts.,” *Mol. Biol. Cell*, vol. 17, no. 3, pp. 1085–95, Mar. 2006.

[115] E. M. Kovacs, M. Goodwin, R. G. Ali, A. D. Paterson, and A. S. Yap, “Cadherin-directed actin assembly: E-cadherin physically associates with the Arp2/3 complex to direct actin assembly in nascent adhesive contacts.,” *Curr. Biol.*, vol. 12, no. 5, pp. 379–82, Mar. 2002.

[116] R. Kalaji, A. P. Wheeler, J. C. Erasmus, S. Y. Lee, R. G. Endres, L. P. Cramer, and V. M. M. Braga, “ROCK1 and ROCK2 regulate epithelial polarisation and geometric cell shape.,” *Biol. Cell*, vol. 104, no. 8, pp. 435–51, Aug. 2012.

[117] W. Engl, B. Arasi, L. L. Yap, J. P. Thiery, and V. Viasnoff, “Actin dynamics modulate mechanosensitive immobilization of E-cadherin at adherens junctions.,” *Nat. Cell Biol.*, vol. 16, no. 6, pp. 587–94, 2014.

[118] M. Cavey, M. Rauzi, P.-F. Lenne, and T. Lecuit, “A two-tiered mechanism for stabilization and immobilization of E-cadherin.,” *Nature*, vol. 453, no. 7196, pp. 751–756, 2008.

[119] A. S. Yap, W. M. Brieher, M. Pruschy, and B. M. Gumbiner, “Lateral clustering of the adhesive ectodomain: a fundamental determinant of cadherin function.,” *Curr. Biol.*, vol. 7, no. 5, pp. 308–15, May 1997.

[120] A. S. Yap, C. M. Niessen, and B. M. Gumbiner, “The juxtamembrane region of the cadherin cytoplasmic tail supports lateral clustering, adhesive strengthening, and interaction with p120ctn.,” *J. Cell Biol.*, vol. 141, no. 3, pp. 779–89, May 1998.

[121] M. Rauzi, P.-F. Lenne, and T. Lecuit, “Planar polarized actomyosin contractile flows control epithelial junction remodelling.,” *Nature*, vol. 468, no. 7327, pp. 1110–4, Dec. 2010.

[122] Q. le Duc, Q. Shi, I. Blonk, A. Sonnenberg, N. Wang, D. Leckband, and J. de Rooij, “Vinculin potentiates E-cadherin mechanosensing and is recruited to actin-anchored sites within adherens junctions in a myosin II-dependent manner.,” *J. Cell Biol.*, vol. 189, no. 7, pp. 1107–15, Jun. 2010.

[123] B. Ladoux, E. Anon, M. Lambert, A. Rabodzey, P. Hersen, A. Buguin, P. Silberzan, and R.-M. Mège, “Strength dependence of cadherin-mediated adhesions.,” *Biophys. J.*, vol. 98, no. 4, pp. 534–42, Feb. 2010.

[124] Z. Liu, J. L. Tan, D. M. Cohen, M. T. Yang, N. J. Sniadecki, S. A. Ruiz, C. M. Nelson, and C. S. Chen, “Mechanical tugging force regulates the size of cell-cell junctions,” *Proc. Natl. Acad. Sci.*, vol. 107, no. 22, pp. 9944–9949, May 2010.

[125] Y. S. Chu, W. a Thomas, O. Eder, F. Pincet, E. Perez, J. P. Thiery, and S. Dufour, “Force measurements in E-cadherin-mediated cell doublets reveal rapid adhesion strengthened by actin cytoskeleton remodeling through Rac and Cdc42,” *J. Cell Biol.*, vol. 167, no. 6, pp. 1183–1194, 2004.

[126] O. G. Shcherbakova, W. I. Weis, B. L. Pruitt, W. James, A. R. Dunn, N. Borghi, M. Sorokina, and W. J. Nelson, "Correction for Borghi et al., E-cadherin is under constitutive actomyosin-generated tension that is increased at cell-cell contacts upon externally applied stretch," *Proc. Natl. Acad. Sci.*, vol. 109, no. 46, pp. 19034–19034, Oct. 2012.

[127] D. Cai, S.-C. Chen, M. Prasad, L. He, X. Wang, V. Choesmel-Cadamuro, J. K. Sawyer, G. Danuser, and D. J. Montell, "Mechanical feedback through E-cadherin promotes direction sensing during collective cell migration.," *Cell*, vol. 157, no. 5, pp. 1146–59, May 2014.

[128] D. E. Leckband and J. de Rooij, "Cadherin adhesion and mechanotransduction.," *Annu. Rev. Cell Dev. Biol.*, vol. 30, pp. 291–315, Jan. 2014.

[129] D. E. Leckband, Q. le Duc, N. Wang, and J. de Rooij, "Mechanotransduction at cadherin-mediated adhesions.," *Curr. Opin. Cell Biol.*, vol. 23, no. 5, pp. 523–30, Oct. 2011.

[130] W. A. Thomas, C. Boscher, Y.-S. Chu, D. Cuvelier, C. Martinez-Rico, R. Seddiki, J. Heysch, B. Ladoux, J. P. Thiery, R.-M. Mege, and S. Dufour, "α-Catenin and vinculin cooperate to promote high E-cadherin-based adhesion strength.," *J. Biol. Chem.*, vol. 288, no. 7, pp. 4957–69, Feb. 2013.

[131] S. Huveneers and J. de Rooij, "Mechanosensitive systems at the cadherin-F-actin interface.," *J. Cell Sci.*, vol. 126, no. Pt 2, pp. 403–13, Jan. 2013.

[132] K. Taguchi, T. Ishiuchi, and M. Takeichi, "Mechanosensitive EPLIN-dependent remodeling of adherens junctions regulates epithelial reshaping.," *J. Cell Biol.*, vol. 194, no. 4, pp. 643–56, Aug. 2011.

[133] P. D. McCrea and B. M. Gumbiner, "Purification of a 92-kDa cytoplasmic protein tightly associated with the cell-cell adhesion molecule E-cadherin (uvomorulin). Characterization and extractability of the protein complex from the cell cytostructure.," *J. Biol. Chem.*, vol. 266, no. 7, pp. 4514–20, Mar. 1991.

[134] E. M. Shore and W. J. Nelson, "Biosynthesis of the cell adhesion molecule uvomorulin (E-cadherin) in Madin-Darby canine kidney epithelial cells.," *J. Biol. Chem.*, vol. 266, no. 29, pp. 19672–80, Oct. 1991.

[135] A. I. Ivanov, A. Nusrat, and C. A. Parkos, "Endocytosis of epithelial apical junctional proteins by a clathrin-mediated pathway into a unique storage compartment.," *Mol. Biol. Cell*, vol. 15, no. 1, pp. 176–88, Jan. 2004.

[136] T. L. Le, A. S. Yap, and J. L. Stow, "Recycling of E-cadherin: a potential mechanism for regulating cadherin dynamics.," *J. Cell Biol.*, vol. 146, no. 1, pp. 219–32, Jul. 1999.

[137] N. Akhtar and N. A. Hotchin, "RAC1 regulates adherens junctions through endocytosis of E-cadherin.," *Mol. Biol. Cell*, vol. 12, no. 4, pp. 847–62, Apr. 2001.

[138] Z. Lu, S. Ghosh, Z. Wang, and T. Hunter, "Downregulation of caveolin-1 function by EGF leads to the loss of E-cadherin, increased transcriptional activity of beta-catenin, and enhanced tumor cell invasion.," *Cancer Cell*, vol. 4, no. 6, pp. 499–515, Dec. 2003.

[139] D. M. Bryant, M. C. Kerr, L. A. Hammond, S. R. Joseph, K. E. Mostov, R. D. Teasdale, and J. L. Stow, “EGF induces macropinocytosis and SNX1-modulated recycling of E-cadherin.,” *J. Cell Sci.*, vol. 120, no. Pt 10, pp. 1818–28, May 2007.

[140] M. Desclozeaux, J. Venturato, F. G. Wylie, J. G. Kay, S. R. Joseph, H. T. Le, and J. L. Stow, “Active Rab11 and functional recycling endosome are required for E-cadherin trafficking and lumen formation during epithelial morphogenesis.,” *Am. J. Physiol. Cell Physiol.*, vol. 295, no. 2, pp. C545–56, Aug. 2008.

[141] J. G. Lock and J. L. Stow, “Rab11 in recycling endosomes regulates the sorting and basolateral transport of E-cadherin.,” *Mol. Biol. Cell*, vol. 16, no. 4, pp. 1744–55, Apr. 2005.

[142] M. A. Davis, R. C. Ireton, and A. B. Reynolds, “A core function for p120-catenin in cadherin turnover.,” *J. Cell Biol.*, vol. 163, no. 3, pp. 525–34, Nov. 2003.

[143] M. Peifer and A. S. Yap, “Traffic control: p120-catenin acts as a gatekeeper to control the fate of classical cadherins in mammalian cells.,” *J. Cell Biol.*, vol. 163, no. 3, pp. 437–40, Nov. 2003.

[144] K. Xiao, D. F. Allison, M. D. Kottke, S. Summers, G. P. Sorescu, V. Faundez, and A. P. Kowalczyk, “Mechanisms of VE-cadherin processing and degradation in microvascular endothelial cells.,” *J. Biol. Chem.*, vol. 278, no. 21, pp. 19199–208, May 2003.

[145] K. Xiao, J. Garner, K. M. Buckley, P. A. Vincent, C. M. Chiasson, E. Dejana, V. Faundez, and A. P. Kowalczyk, “p120-Catenin regulates clathrin-dependent endocytosis of VE-cadherin.,” *Mol. Biol. Cell*, vol. 16, no. 11, pp. 5141–51, Nov. 2005.

[146] P. Z. Anastasiadis, “p120-ctn: A nexus for contextual signaling via Rho GTPases.,” *Biochim. Biophys. Acta*, vol. 1773, no. 1, pp. 34–46, Jan. 2007.

[147] Y. T. Chen, D. B. Stewart, and W. J. Nelson, “Coupling assembly of the E-cadherin/beta-catenin complex to efficient endoplasmic reticulum exit and basal-lateral membrane targeting of E-cadherin in polarized MDCK cells.,” *J. Cell Biol.*, vol. 144, no. 4, pp. 687–99, Mar. 1999.

[148] S. Dupre-Crochet, A. Figueroa, C. Hogan, E. C. Ferber, C. U. Bialucha, J. Adams, E. C. N. Richardson, and Y. Fujita, “Casein kinase 1 is a novel negative regulator of E-cadherin-based cell-cell contacts.,” *Mol. Cell. Biol.*, vol. 27, no. 10, pp. 3804–16, May 2007.

[149] M. Sharma and B. R. Henderson, “IQ-domain GTPase-activating protein 1 regulates beta-catenin at membrane ruffles and its role in macropinocytosis of N-cadherin and adenomatous polyposis coli.,” *J. Biol. Chem.*, vol. 282, no. 11, pp. 8545–56, Mar. 2007.

[150] S. de Beco, J.-B. Perney, S. Coscoy, and F. Amblard, “Mechanosensitive Adaptation of E-Cadherin Turnover across adherens Junctions.,” *PLoS One*, vol. 10, no. 6, p. e0128281, Jan. 2015.

[151] J. de Rooij, “Cadherin adhesion controlled by cortical actin dynamics.,” *Nat. Cell Biol.*, vol. 16, no. 6, pp. 508–10, 2014.

[152] V. M. M. Braga, “Cell – cell adhesion and signalling,” *Curr. Opin. Cell Biol.*, vol. 14, pp. 546–556, 2002.

[153] A. Nusrat, M. Giry, J. R. Turner, S. P. Colgan, C. A. Parkos, D. Carnes, E. Lemichez, P. Boquet, and J. L. Madara, “Rho protein regulates tight junctions and perijunctional actin organization in polarized epithelia.,” *Proc. Natl. Acad. Sci. U. S. A.*, vol. 92, no. 23, pp. 10629–33, Nov. 1995.

[154] M. Bruewer, “RhoA, Rac1, and Cdc42 exert distinct effects on epithelial barrier via selective structural and biochemical modulation of junctional proteins and F-actin,” *AJP Cell Physiol.*, vol. 287, no. 2, pp. C327–C335, Mar. 2004.

[155] E. Sahai and C. J. Marshall, “RHO-GTPases and cancer.,” *Nat. Rev. Cancer*, vol. 2, no. 2, pp. 133–42, Feb. 2002.

[156] J. Waschke, V. Spindler, P. Bruggeman, D. Zillikens, G. Schmidt, and D. Drenckhahn, “Inhibition of Rho A activity causes pemphigus skin blistering.,” *J. Cell Biol.*, vol. 175, no. 5, pp. 721–7, Dec. 2006.

[157] V. M. Braga and A. S. Yap, “The challenges of abundance: epithelial junctions and small GTPase signalling.,” *Curr. Opin. Cell Biol.*, vol. 17, no. 5, pp. 466–74, Oct. 2005.

[158] S. Eaton, P. Auvinen, L. Luo, Y. N. Jan, and K. Simons, “CDC42 and Rac1 control different actin-dependent processes in the Drosophila wing disc epithelium.,” *J. Cell Biol.*, vol. 131, no. 1, pp. 151–64, Oct. 1995.

[159] J. A. Tunggal, I. Helfrich, A. Schmitz, H. Schwarz, D. Günzel, M. Fromm, R. Kemler, T. Krieg, and C. M. Niessen, “E-cadherin is essential for in vivo epidermal barrier function by regulating tight junctions.,” *EMBO J.*, vol. 24, no. 6, pp. 1146–56, Mar. 2005.

[160] E. Sahai and C. J. Marshall, “ROCK and Dia have opposing effects on adherens junctions downstream of Rho.,” *Nat. Cell Biol.*, vol. 4, no. 6, pp. 408–15, Jun. 2002.

[161] K. Takaishi, T. Matozaki, K. Nakano, and Y. Takai, “Multiple downstream signalling pathways from ROCK, a target molecule of Rho small G protein, in reorganization of the actin cytoskeleton in Madin-Darby canine kidney cells.,” *Genes Cells*, vol. 5, no. 11, pp. 929–936, Nov. 2000.

[162] D. V Ayollo, I. Y. Zhitnyak, J. M. Vasiliev, and N. a Gloushankova, “Rearrangements of the actin cytoskeleton and E-cadherin-based adherens junctions caused by neoplasic transformation change cell-cell interactions.,” *PLoS One*, vol. 4, no. 11, p. e8027, 2009.

[163] M. Smutny, H. L. Cox, J. M. Leerberg, E. M. Kovacs, M. A. Conti, C. Ferguson, N. a Hamilton, R. G. Parton, R. S. Adelstein, and A. S. Yap, “Myosin II isoforms identify distinct functional modules that support integrity of the epithelial zonula adherens.,” *Nat. Cell Biol.*, vol. 12, no. 7, pp. 696–702, 2010.

[164] E. Sahai and C. J. Marshall, “ROCK and Dia have opposing effects on adherens junctions downstream of Rho,” *Nat.Cell Biol.*, vol. 4, no. 1465–7392 (Print), pp. 408–415, 2002.

[165] S. Verma, S. P. Han, M. Michael, G. a Gomez, Z. Yang, R. D. Teasdale, A. Ratheesh, E. M. Kovacs, R. G. Ali, and A. S. Yap, “A WAVE2-Arp2/3 actin nucleator apparatus supports junctional tension at the epithelial zonula adherens.,” *Mol. Biol. Cell*, vol. 23, no. 23, pp. 4601–10, 2012.

[166] V. W. Tang and W. M. Brieher, “α-Actinin-4/FSGS1 is required for Arp2/3-dependent actin assembly at the adherens junction.,” *J. Cell Biol.*, vol. 196, no. 1, pp. 115–30, Jan. 2012.

[167] M. Georgiou, E. Marinari, J. Burden, and B. Baum, “Cdc42, Par6, and aPKC Regulate Arp2/3-Mediated Endocytosis to Control Local Adherens Junction Stability,” *Curr. Biol.*, vol. 18, no. 21, pp. 1631–1638, Nov. 2008.

[168] E. M. Kovacs, S. Verma, R. G. Ali, A. Ratheesh, N. a Hamilton, A. Akhmanova, and A. S. Yap, “N-WASP regulates the epithelial junctional actin cytoskeleton through a non-canonical post-nucleation pathway.,” *Nat. Cell Biol.*, vol. 13, no. 8, pp. 934–943, 2011.

[169] T. Otani, T. Ichii, S. Aono, and M. Takeichi, “Cdc42 GEF Tuba regulates the junctional configuration of simple epithelial cells,” *J. Cell Biol.*, vol. 175, no. 1, pp. 135–146, 2006.

[170] S. Zigmond, “Formin ’ adherens junctions,” vol. 6, no. 1, pp. 12–14, 2004.

[171] A. I. Ivanov, M. Bachar, B. A. Babbin, R. S. Adelstein, A. Nusrat, and C. A. Parkos, “A unique role for nonmuscle myosin heavy chain IIA in regulation of epithelial apical junctions.,” *PLoS One*, vol. 2, no. 7, p. e658, Jan. 2007.

[172] S. Citi, D. Spadaro, Y. Schneider, J. Stutz, and P. Pulimeno, “Regulation of small GTPases at epithelial cell-cell junctions,” *Mol. Membr. Biol.*, vol. 28, no. 7–8, pp. 427–444, 2011.

[173] L. Carramusa, C. Ballestrem, Y. Zilberman, and A. D. Bershadsky, “Mammalian diaphanous-related formin Dia1 controls the organization of E-cadherin-mediated cell-cell junctions.,” *J. Cell Sci.*, vol. 120, no. Pt 21, pp. 3870–82, Nov. 2007.

[174] C. C. F. Homem and M. Peifer, “Diaphanous regulates myosin and adherens junctions to control cell contractility and protrusive behavior during morphogenesis.,” *Development*, vol. 135, no. 6, pp. 1005–1018, 2008.

[175] A. Kobielak, H. A. Pasolli, and E. Fuchs, “Mammalian formin-1 participates in adherens junctions and polymerization of linear actin cables,” *Nat. Cell Biol.*, vol. 6, no. 1, pp. 21–30, 2004.

[176] B. L. Goode and M. J. Eck, “Mechanism and Function of Formins in the Control of Actin Assembly,” Jun. 2007.

[177] S. J. Warner and G. D. Longmore, “Distinct functions for Rho1 in maintaining adherens junctions and apical tension in remodeling epithelia,” *J. Cell Biol.*, vol. 185, no. 6, pp. 1111–1125, 2009.

[178] T. Rozario and D. W. DeSimone, “The extracellular matrix in development and morphogenesis: a dynamic view.,” *Dev. Biol.*, vol. 341, no. 1, pp. 126–40, May 2010.

[179] T. R. Polte, G. S. Eichler, N. Wang, and D. E. Ingber, “Extracellular matrix controls myosin light chain phosphorylation and cell contractility through modulation of cell shape and cytoskeletal prestress.,” *Am. J. Physiol. Cell Physiol.*, vol. 286, no. 3, pp. C518–28, Mar. 2004.

[180] C.-L. Guo, M. Ouyang, J.-Y. Yu, J. Maslov, A. Price, and C.-Y. Shen, “Long-range mechanical force enables self-assembly of epithelial tubular patterns.,” *Proc. Natl. Acad. Sci. U. S. A.*, vol. 109, no. 15, pp. 5576–82, Apr. 2012.

[181] H. Lodish, A. Berk, S. L. Zipursky, P. Matsudaira, D. Baltimore, and J. Darnell, “Cell-Matrix Adhesion.” W. H. Freeman, 2000.

[182] L. M. Sterk, C. A. Geuijen, L. C. Oomen, J. Calafat, H. Janssen, and A. Sonnenberg, “The tetraspan molecule CD151, a novel constituent of hemidesmosomes, associates with the integrin alpha6beta4 and may regulate the spatial organization of hemidesmosomes.,” *J. Cell Biol.*, vol. 149, no. 4, pp. 969–82, May 2000.

[183] D. Tsuruta, T. Hashimoto, K. J. Hamill, and J. C. R. Jones, “Hemidesmosomes and focal contact proteins: functions and cross-talk in keratinocytes, bullous diseases and wound healing.,” *J. Dermatol. Sci.*, vol. 62, no. 1, pp. 1–7, Apr. 2011.

[184] P. Benny, C. Badowski, E. B. Lane, and M. Raghunath, “Making More Matrix: Enhancing the Deposition of Dermal–Epidermal Junction Components *In Vitro* and Accelerating Organotypic Skin Culture Development, Using Macromolecular Crowding,” *Tissue Eng. Part A*, vol. 21, no. 1–2, pp. 183–192, 2015.

[185] H. Larjava, L. Koivisto, and L. Häkkinen, “Keratinocyte Interactions with Fibronectin during Wound Healing.” Landes Bioscience, 2000.

[186] F. M. Watt, “Role of integrins in regulating epidermal adhesion, growth and differentiation.,” *EMBO J.*, vol. 21, no. 15, pp. 3919–26, Aug. 2002.

[187] L. P. Cramer, M. Siebert, and T. J. Mitchison, “Identification of novel graded polarity actin filament bundles in locomoting heart fibroblasts: implications for the generation of motile force.,” *J. Cell Biol.*, vol. 136, no. 6, pp. 1287–305, Mar. 1997.

[188] E. Lazarides and K. Burridge, “Alpha-actinin: immunofluorescent localization of a muscle structural protein in nonmuscle cells.,” *Cell*, vol. 6, no. 3, pp. 289–98, Nov. 1975.

[189] J. C. Adams, “Formation of stable microspikes containing actin and the 55 kDa actin bundling protein, fascin, is a consequence of cell adhesion to thrombospondin-1: implications for the anti-adhesive activities of thrombospondin-1.,” *J. Cell Sci.*, vol. 108 (Pt 5, pp. 1977–90, May 1995.

[190] K. Wang, J. F. Ash, and S. J. Singer, “Filamin, a new high-molecular-weight protein found in smooth muscle and non-muscle cells.,” *Proc. Natl. Acad. Sci. U. S. A.*, vol. 72, no. 11, pp. 4483–6, Nov. 1975.

[191] J. V. Small, K. Rottner, I. Kaverina, and K. I. Anderson, “Assembling an actin cytoskeleton for cell attachment and movement,” *Biochim. Biophys. Acta - Mol. Cell Res.*, vol. 1404, no. 3, pp. 271–281, Sep. 1998.

[192] P. Hotulainen and P. Lappalainen, “Stress fibers are generated by two distinct actin assembly mechanisms in motile cells.,” *J. Cell Biol.*, vol. 173, no. 3, pp. 383–94, May 2006.

[193] H. B. Schiller, M.-R. Hermann, J. Polleux, T. Vignaud, S. Zanivan, C. C. Friedel, Z. Sun, A. Raducanu, K.-E. Gottschalk, M. Théry, M. Mann, and R. Fässler, “β1- and αv-class integrins cooperate to regulate myosin II during rigidity sensing of fibronectin-based microenvironments.,” *Nat. Cell Biol.*, vol. 15, no. 6, pp. 625–36, Jun. 2013.

[194] S. K. Mitra, D. A. Hanson, and D. D. Schlaepfer, “Focal adhesion kinase: in command and control of cell motility.,” *Nat. Rev. Mol. Cell Biol.*, vol. 6, no. 1, pp. 56–68, Jan. 2005.

[195] C. K. Choi, M. Vicente-Manzanares, J. Zareno, L. A. Whitmore, A. Mogilner, and A. R. Horwitz, “Actin and alpha-actinin orchestrate the assembly and maturation of nascent adhesions in a myosin II motor-independent manner.,” *Nat. Cell Biol.*, vol. 10, no. 9, pp. 1039–50, Sep. 2008.

[196] B. Short, “Stress fibers guide focal adhesions to maturity,” *J. Cell Biol.*, vol. 196, no. 3, p. 301, 2012.

[197] M. Vicente-Manzanares, C. K. Choi, and A. R. Horwitz, “Integrins in cell migration--the actin connection.,” *J. Cell Sci.*, vol. 122, no. Pt 2, pp. 199–206, Jan. 2009.

[198] J. D. Humphries, P. Wang, C. Streuli, B. Geiger, M. J. Humphries, and C. Ballestrem, “Vinculin controls focal adhesion formation by direct interactions with talin and actin.,” *J. Cell Biol.*, vol. 179, no. 5, pp. 1043–57, Dec. 2007.

[199] A. del Rio, R. Perez-Jimenez, R. Liu, P. Roca-Cusachs, J. M. Fernandez, and M. P. Sheetz, “Stretching single talin rod molecules activates vinculin binding.,” *Science*, vol. 323, no. 5914, pp. 638–41, Jan. 2009.

[200] J. C. Friedland, M. H. Lee, and D. Boettiger, “Mechanically activated integrin switch controls alpha5beta1 function.,” *Science*, vol. 323, no. 5914, pp. 642–4, Jan. 2009.

[201] S. Narumiya, T. Ishizaki, and N. Watanabe, “Rho effectors and reorganization of actin cytoskeleton.,” *FEBS Lett.*, vol. 410, no. 1, pp. 68–72, Jun. 1997.

[202] P. Aspenström, A. Fransson, and J. Saras, “Rho GTPases have diverse effects on the organization of the actin filament system.,” *Biochem. J.*, vol. 377, no. Pt 2, pp. 327–37, Jan. 2004.

[203] A. Hall and C. D. Nobes, “Rho GTPases: molecular switches that control the organization and dynamics of the actin cytoskeleton.,” *Philos. Trans. R. Soc. Lond. B. Biol. Sci.*, vol. 355, no. 1399, pp. 965–70, Jul. 2000.

[204] S.-T. Sit and E. Manser, “Rho GTPases and their role in organizing the actin cytoskeleton.,” *J. Cell Sci.*, vol. 124, no. Pt 5, pp. 679–83, Mar. 2011.

[205] A. J. Ridley and A. Hall, “The small GTP-binding protein rho regulates the assembly of focal adhesions and actin stress fibers in response to growth factors.,” *Cell*, vol. 70, no. 3, pp. 389–99, Aug. 1992.

[206] A. J. Ridley, H. F. Paterson, C. L. Johnston, D. Diekmann, and A. Hall, “The small GTP-binding protein rac regulates growth factor-induced membrane ruffling.,” *Cell*, vol. 70, no. 3, pp. 401–10, Aug. 1992.

[207] R. Kozma, S. Ahmed, A. Best, and L. Lim, “The Ras-related protein Cdc42Hs and bradykinin promote formation of peripheral actin microspikes and filopodia in Swiss 3T3 fibroblasts.,” *Mol. Cell. Biol.*, vol. 15, no. 4, pp. 1942–52, Apr. 1995.

[208] C. D. Nobes and A. Hall, “Rho, rac, and cdc42 GTPases regulate the assembly of multimolecular focal complexes associated with actin stress fibers, lamellipodia, and filopodia.,” *Cell*, vol. 81, no. 1, pp. 53–62, Apr. 1995.

[209] Z. Zhao and E. Manser, “PAK and other Rho-associated kinases--effectors with surprisingly diverse mechanisms of regulation.,” *Biochem. J.*, vol. 386, no. Pt 2, pp. 201–14, Mar. 2005.

[210] M. Chrzanowska-Wodnicka and K. Burridge, “Rho-stimulated contractility drives the formation of stress fibers and focal adhesions.,” *J. Cell Biol.*, vol. 133, no. 6, pp. 1403–15, Jun. 1996.

[211] J. K. Liao, M. Seto, and K. Noma, “Rho kinase (ROCK) inhibitors.,” *J. Cardiovasc. Pharmacol.*, vol. 50, no. 1, pp. 17–24, Jul. 2007.

[212] M. Amano, M. Nakayama, and K. Kaibuchi, “Rho-kinase/ROCK: A key regulator of the cytoskeleton and cell polarity,” *Cytoskeleton*, vol. 67, no. 9, pp. 545–554, 2010.

[213] T. Ishiuchi and M. Takeichi, “Willin and Par3 cooperatively regulate epithelial apical constriction through aPKC-mediated ROCK phosphorylation.,” *Nat. Cell Biol.*, vol. 13, no. 7, pp. 860–6, Jul. 2011.

[214] W. P. Daley, E. M. Gervais, S. W. Centanni, K. M. Gulfo, D. a Nelson, and M. Larsen, “ROCK1-directed basement membrane positioning coordinates epithelial tissue polarity.,” *Development*, vol. 139, no. 2, pp. 411–22, 2012.

[215] T. Leung, X. Q. Chen, E. Manser, and L. Lim, “The p160 RhoA-binding kinase ROK alpha is a member of a kinase family and is involved in the reorganization of the cytoskeleton.,” *Mol. Cell. Biol.*, vol. 16, no. 10, pp. 5313–27, 1996.

[216] T. Ishizaki, M. Naito, K. Fujisawa, M. Maekawa, N. Watanabe, Y. Saito, and S. Narumiya, “p160ROCK, a Rho-associated coiled-coil forming protein kinase, works downstream of Rho and induces focal adhesions,” *FEBS Lett.*, vol. 404, no. 2–3, pp. 118–124, 1997.

[217] A. Yoneda, H. a B. Multhaupt, and J. R. Couchman, “The Rho kinases I and II regulate different aspects of myosin II activity,” *J. Cell Biol.*, vol. 170, no. 3, pp. 443–453, 2005.

[218] D. Thumkeo, J. Keel, T. Ishizaki, M. Hirose, K. Nonomura, H. Oshima, M. Oshima, M. M. Taketo, and S. Narumiya, “Targeted disruption of the mouse rho-associated kinase 2 gene results in intrauterine growth retardation and fetal death.,” *Mol. Cell. Biol.*, vol. 23, no. 14, pp. 5043–55, Jul. 2003.

[219] K. Riento, N. Totty, P. Villalonga, R. Garg, R. Guasch, and A. J. Ridley, “RhoE function is regulated by ROCK I-mediated phosphorylation.,” *EMBO J.*, vol. 24, no. 6, pp. 1170–80, Mar. 2005.

[220] N. Rath and M. F. Olson, “Rho-associated kinases in tumorigenesis: re-considering ROCK inhibition for cancer therapy.,” *EMBO Rep.*, vol. 13, no. 10, pp. 900–8, Oct. 2012.

[221] S. R. Peyton, C. M. Ghajar, C. B. Khatiwala, and A. J. Putnam, “The emergence of ECM mechanics and cytoskeletal tension as important regulators of cell function.,” *Cell Biochem. Biophys.*, vol. 47, no. 2, pp. 300–20, Jan. 2007.

[222] P. A. Janmey, J. P. Winer, M. E. Murray, and Q. Wen, “The hard life of soft cells.,” *Cell Motil. Cytoskeleton*, vol. 66, no. 8, pp. 597–605, Aug. 2009.

[223] D. E. Ingber, “The riddle of morphogenesis: a question of solution chemistry or molecular cell engineering?,” *Cell*, vol. 75, no. 7, pp. 1249–52, 1993.

[224] D. E. Ingber, “Mechanical control of tissue morphogenesis during embryological development,” *Int. J. Dev. Biol.*, vol. 50, no. 2–3, pp. 255–266, 2006.

[225] D. E. Ingber, “Tensegrity II. How structural networks influence cellular information processing networks,” *J. Cell Sci.*, vol. 116, no. 8, pp. 1397–1408, 2003.

[226] B. Geiger, A. Bershadsky, R. Pankov, K. M. Yamada, and B. G. Correspondence, “Transmembrane extracellular matrix– cytoskeleton crosstalk,” *Nat. Rev. Mol. Cell Biol.*, vol. 2, no. November, pp. 793–805, 2001.

[227] E. Brown and E. Dejana, “Cell-to-cell contact and extracellular matrix,” *Curr. Opin. Cell Biol.*, vol. 15, no. 5, pp. 505–508, 2003.

[228] M. Burute and M. Thery, “Spatial segregation between cell-cell and cell-matrix adhesions.,” *Curr. Opin. Cell Biol.*, vol. 24, no. 5, pp. 628–36, Oct. 2012.

[229] G. F. Weber, M. a Bjerke, and D. W. DeSimone, “Integrins and cadherins join forces to form adhesive networks.,” *J. Cell Sci.*, vol. 124, no. Pt 8, pp. 1183–93, 2011.

[230] C. Martinez-Rico, F. Pincet, J.-P. Thiery, and S. Dufour, “Integrins stimulate E-cadherin-mediated intercellular adhesion by regulating Src-kinase activation and actomyosin contractility.,” *J. Cell Sci.*, vol. 123, no. Pt 5, pp. 712–22, Mar. 2010.

[231] V. Maruthamuthu, B. Sabass, U. S. Schwarz, and M. L. Gardel, “Cell-ECM traction force modulates endogenous tension at cell–cell contacts,” *Proc. Natl. Acad. Sci. U. S. A.*, vol. 108, pp. 4708–4713, 2011.

[232] J. de Rooij, “Integrin-dependent actomyosin contraction regulates epithelial cell scattering,” *J. Cell Biol.*, vol. 171, no. 1, pp. 153–164, Oct. 2005.

[233] A. Jasaitis, M. Estevez, J. Heysch, B. Ladoux, and S. Dufour, “E-cadherin-dependent stimulation of traction force at focal adhesions via the Src and PI3K signaling pathways.,” *Biophys. J.*, vol. 103, no. 2, pp. 175–84, Jul. 2012.

[234] A. F. Mertz, Y. Che, S. Banerjee, J. M. Goldstein, K. A. Rosowski, S. F. Revilla, C. M. Niessen, M. C. Marchetti, E. R. Dufresne, and V. Horsley, “Cadherin-based intercellular adhesions organize epithelial cell-matrix traction forces.,” *Proc. Natl. Acad. Sci. U. S. A.*, vol. 110, no. 3, pp. 842–7, Jan. 2013.

[235] J. L. Bays, X. Peng, C. E. Tolbert, C. Guilluy, A. E. Angell, Y. Pan, R. Superfine, K. Burridge, and K. A. DeMali, “Vinculin phosphorylation differentially regulates mechanotransduction at cell-cell and cell-matrix adhesions.,” *J. Cell Biol.*, vol. 205, no. 2, pp. 251–63, Apr. 2014.

[236] Q. Tseng, E. Duchemin-Pelletier, A. Deshiere, M. Balland, H. Guillou, O. Filhol, and M. Théry, "Spatial organization of the extracellular matrix regulates cell-cell junction positioning.," *Proc. Natl. Acad. Sci. U. S. A.*, vol. 109, no. 5, pp. 1506–11, Jan. 2012.

[237] J. Yong, J. Moeller, K. C. Hart, and D. Ramallo, "Spatial Distribution of Cell-Cell and Cell-ECM Adhesions Regulates Force Balance while Maintaining E-cadherin Molecular Tension in Cell Pairs."

[238] C. Grashoff, B. D. Hoffman, M. D. Brenner, R. Zhou, M. Parsons, M. T. Yang, M. a McLean, S. G. Sligar, C. S. Chen, T. Ha, and M. a Schwartz, "Measuring mechanical tension across vinculin reveals regulation of focal adhesion dynamics.," *Nature*, vol. 466, no. 7303, pp. 263–266, 2010.

[239] F. Meng, T. M. Suchyna, and F. Sachs, "A fluorescence energy transfer-based mechanical stress sensor for specific proteins in situ.," *FEBS J.*, vol. 275, no. 12, pp. 3072–87, Jun. 2008.

[240] S. P. Carey, J. M. Charest, and C. A. Reinhart-King, "Forces During Cell Adhesion and Spreading: Implications for Cellular Homeostasis," *Stud Mechanobiol Tissue Eng Biomater*, vol. 2, no. September 2010, pp. 153–171, 2011.

[241] N. Q. Balaban, U. S. Schwarz, D. Riveline, P. Goichberg, G. Tzur, I. Sabanay, D. Mahalu, S. Safran, a Bershadsky, L. Addadi, and B. Geiger, "Force and focal adhesion assembly: a close relationship studied using elastic micropatterned substrates.," *Nat. Cell Biol.*, vol. 3, no. 5, pp. 466–472, 2001.

[242] D. Choquet, D. P. Felsenfeld, and M. P. Sheetz, "Extracellular matrix rigidity causes strengthening of integrin-cytoskeleton linkages.," *Cell*, vol. 88, no. 1, pp. 39–48, Jan. 1997.

[243] R. J. Pelham, "Cell Locomotion and Focal Adhesions Are Regulated by the Mechanical Properties of the Substrate," pp. 348–350, 1998.

[244] D. E. Ingber, "Tensegrity and Mechanostransduction," *J. Bodyw. Mov. Ther.*, vol. 12, no. 3, pp. 198–200, 2008.

[245] D. E. Ingber, "Tensegrity I. Cell structure and hierarchical systems biology.," *J. Cell Sci.*, vol. 116, no. Pt 7, pp. 1157–1173, 2003.

[246] B. J. Dzamba, K. R. Jakab, M. Marsden, M. A. Schwartz, and D. W. DeSimone, "Cadherin adhesion, tissue tension, and noncanonical Wnt signaling regulate fibronectin matrix organization.," *Dev. Cell*, vol. 16, no. 3, pp. 421–32, Mar. 2009.

[247] Y. Danjo and I. K. Gipson, "Actin 'purse string' filaments are anchored by E-cadherin-mediated adherens junctions at the leading edge of the epithelial wound, providing coordinated cell movement.," *J. Cell Sci.*, vol. 111 (Pt 2, pp. 3323–32, Nov. 1998.

[248] W. M. Bement, P. Forscher, and M. S. Mooseker, "A novel cytoskeletal structure involved in purse string wound closure and cell polarity maintenance.," *J. Cell Biol.*, vol. 121, no. 3, pp. 565–78, May 1993.

[249] J. Brock, K. Midwinter, J. Lewis, and P. Martin, “Healing of incisional wounds in the embryonic chick wing bud: characterization of the actin purse-string and demonstration of a requirement for Rho activation.,” *J. Cell Biol.*, vol. 135, no. 4, pp. 1097–107, Nov. 1996.

[250] M. Tamada, T. D. Perez, W. J. Nelson, and M. P. Sheetz, “Two distinct modes of myosin assembly and dynamics during epithelial wound closure.,” *J. Cell Biol.*, vol. 176, no. 1, pp. 27–33, Jan. 2007.

[251] P. Martin and S. M. Parkhurst, “Parallels between tissue repair and embryo morphogenesis.,” *Development*, vol. 131, no. 13, pp. 3021–34, Jul. 2004.

[252] N. Harden, M. Ricos, Y. M. Ong, W. Chia, and L. Lim, “Participation of small GTPases in dorsal closure of the Drosophila embryo: distinct roles for Rho subfamily proteins in epithelial morphogenesis.,” *J. Cell Sci.*, vol. 112 (Pt 3, pp. 273–84, Feb. 1999.

[253] C. G. Vasquez and A. C. Martin, “Force transmission in epithelial tissues.,” *Dev. Dyn.*, vol. 245, no. 3, pp. 361–71, Mar. 2016.

[254] N. Gorfinkiel and A. M. Arias, “Requirements for adherens junction components in the interaction between epithelial tissues during dorsal closure in Drosophila.,” *J. Cell Sci.*, vol. 120, no. Pt 18, pp. 3289–98, Sep. 2007.

[255] M. S. Hutson, Y. Tokutake, M.-S. Chang, J. W. Bloor, S. Venakides, D. P. Kiehart, and G. S. Edwards, “Forces for morphogenesis investigated with laser microsurgery and quantitative modeling.,” *Science*, vol. 300, no. 5616, pp. 145–9, Apr. 2003.

[256] S. B. Carter, “Haptotactic islands,” *Exp. Cell Res.*, vol. 48, no. 1, pp. 189–193, Oct. 1967.

[257] A. Harris, “Behavior of cultured cells on substrata of variable adhesiveness,” *Exp. Cell Res.*, vol. 77, no. 1–2, pp. 285–297, Mar. 1973.

[258] G. P. López, H. a Biebuyck, R. Härter, a Kumar, and G. M. Whitesides, “Fabrication and imaging of two-dimensional patterns of proteins adsorbed on self-assembled monolayers by scanning electron microscopy,” *J. Am. Chem. Soc.*, vol. 115, no. 23, pp. 10774–10781, 1993.

[259] S. Alom Ruiz and C. S. Chen, “Microcontact printing: A tool to pattern,” *Soft Matter*, vol. 3, no. 2, p. 168, 2007.

[260] M. Thery and M. Piel, “Adhesive Micropatterns for Cells: A Microcontact Printing Protocol,” *Cold Spring Harb. Protoc.*, vol. 2009, no. 7, p. pdb.prot5255–pdb.prot5255, 2009.

[261] T. D. Pollard and G. G. Borisy, “Cellular motility driven by assembly and disassembly of actin filaments.,” *Cell*, vol. 112, no. 4, pp. 453–65, Feb. 2003.

[262] R. Singhvi, a Kumar, G. P. Lopez, G. N. Stephanopoulos, D. I. Wang, G. M. Whitesides, and D. E. Ingber, “Engineering cell shape and function.,” *Science*, vol. 264, no. 5159, pp. 696–698, 1994.

[263] K. K. Parker, A. L. Brock, R. J. M. Cliff Brangwynne, N. Wang, E. Ostuni, N. A. Geisse, J. C. Adams, and A. D. E. I. George M. Whitesides, “Directional control of lamellipodia extension by

constraining cell shape and orienting cell tractional forces," *FASEB J.*, vol. 16, no. 10, pp. 1195–1204, Aug. 2002.

[264] N. Wang and D. E. Ingber, "Control of cytoskeletal mechanics by extracellular matrix, cell shape, and mechanical tension.," *Biophys. J.*, vol. 66, no. 6, pp. 2181–9, 1994.

[265] M. Théry, "Micropatterning as a tool to decipher cell morphogenesis and functions.," *J. Cell Sci.*, vol. 123, no. Pt 24, pp. 4201–13, Dec. 2010.

[266] M. Théry, V. Racine, M. Piel, A. Pépin, A. Dimitrov, Y. Chen, J.-B. Sibarita, and M. Bornens, "Anisotropy of cell adhesive microenvironment governs cell internal organization and orientation of polarity.," *Proc. Natl. Acad. Sci. U. S. A.*, vol. 103, no. 52, pp. 19771–6, 2006.

[267] A. Pitaval, Q. Tseng, M. Bornens, and M. Théry, "Cell shape and contractility regulate ciliogenesis in cell cycle-arrested cells," *J. Cell Biol.*, vol. 191, no. 2, pp. 303–312, 2010.

[268] J. James, E. D. Goluch, H. Hu, C. Liu, and M. Mrksich, "Subcellular curvature at the perimeter of micropatterned cells influences lamellipodial distribution and cell polarity," *Cell Motil. Cytoskeleton*, vol. 65, no. 11, pp. 841–852, 2008.

[269] R. A. Desai, L. Gao, S. Raghavan, W. F. Liu, and C. S. Chen, "Cell polarity triggered by cell-cell adhesion via E-cadherin.," *J. Cell Sci.*, vol. 122, no. Pt 7, pp. 905–11, Apr. 2009.

[270] I. Dupin, E. Camand, and S. Etienne-Manneville, "Classical cadherins control nucleus and centrosome position and cell polarity," *J. Cell Biol.*, vol. 185, no. 5, pp. 779–786, 2009.

[271] F. Pouthas, P. Girard, V. Lecaudey, T. B. N. Ly, D. Gilmour, C. Boulin, R. Pepperkok, and E. G. Reynaud, "In migrating cells, the Golgi complex and the position of the centrosome depend on geometrical constraints of the substratum.," *J. Cell Sci.*, vol. 121, no. Pt 14, pp. 2406–2414, 2008.

[272] G. Mahmud, C. J. Campbell, K. J. M. Bishop, Y. a. Komarova, O. Chaga, S. Soh, S. Huda, K. Kandere-Grzybowska, and B. a. Grzybowski, "Directing cell motions on micropatterned ratchets," *Nat. Phys.*, vol. 5, no. 8, pp. 606–612, 2009.

[273] X. Jiang, D. a Bruzewicz, A. P. Wong, M. Piel, and G. M. Whitesides, "Directing cell migration with asymmetric micropatterns.," *Proc. Natl. Acad. Sci. U. S. A.*, vol. 102, no. 4, pp. 975–8, 2005.

[274] J. Su, R. R. Brau, X. Jiang, G. M. Whitesides, M. J. Lange, and P. T. C. So, "Geometric confinement influences cellular mechanical properties II -- intracellular variances in polarized cells.," *Mol. Cell. Biomech.*, vol. 4, no. 2, pp. 105–118, 2007.

[275] A. Saez, M. Ghibaudo, A. Buguin, P. Silberzan, and B. Ladoux, "Rigidity-driven growth and migration of epithelial cells on microstructured anisotropic substrates.," *Proc. Natl. Acad. Sci. U. S. A.*, vol. 104, no. 20, pp. 8281–6, 2007.

[276] K. E. Worley, D. Shieh, and L. Q. Wan, "Inhibition of cell–cell adhesion impairs directional epithelial migration on micropatterned surfaces," *Integr. Biol.*, vol. 7, pp. 1–4, 2015.

[277] M. Théry, V. Racine, A. Pépin, M. Piel, Y. Chen, J.-B. Sibarita, and M. Bornens, “The extracellular matrix guides the orientation of the cell division axis.,” *Nat. Cell Biol.*, vol. 7, no. 10, pp. 947–53, Oct. 2005.

[278] A. Jime, V. Racine, M. Bornens, F. Ju, M. Théry, A. Jiménez-Dalmaroni, F. Jülicher, and M. Thery, “Experimental and theoretical study of mitotic spindle orientation,” *Nature*, vol. 447, no. 7143, pp. 493–496, 2007.

[279] M. Théry and M. Bornens, “Cell shape and cell division,” *Curr. Opin. Cell Biol.*, vol. 18, no. 6, pp. 648–657, 2006.

[280] S. Yennek, M. Burute, M. Théry, and S. Tajbakhsh, “Cell Adhesion Geometry Regulates Non-Random DNA Segregation and Asymmetric Cell Fates in Mouse Skeletal Muscle Stem Cells,” *Cell Rep.*, vol. 7, no. 4, pp. 961–970, 2014.

[281] F. M. Watt, P. W. Jordan, and C. H. O’Neill, “Cell shape controls terminal differentiation of human epidermal keratinocytes.,” *Proc. Natl. Acad. Sci. U. S. A.*, vol. 85, no. 15, pp. 5576–80, 1988.

[282] C. S. Chen, M. Mrksich, S. Huang, G. M. Whitesides, and D. E. Ingber, “Geometric control of cell life and death.,” *Science*, vol. 276, no. 5317, pp. 1425–1428, 1997.

[283] a. Mammoto, S. Huang, K. Moore, P. Oh, and D. E. Ingber, “Role of RhoA, mDia, and ROCK in Cell Shape-dependent Control of the Skp2-p27kip1 Pathway and the G1/S Transition,” *J. Biol. Chem.*, vol. 279, no. 25, pp. 26323–26330, 2004.

[284] S. Huang, C. S. Chen, and D. E. Ingber, “Control of cyclin D1, p27(Kip1), and cell cycle progression in human capillary endothelial cells by cell shape and cytoskeletal tension,” *Mol. Biol. The.Cell*, vol. 9, no. 11, pp. 3179–3193, 1998.

[285] R. McBeath, D. M. Pirone, C. M. Nelson, K. Bhadriraju, and C. S. Chen, “Cell shape, cytoskeletal tension, and RhoA regulate stem cell lineage commitment,” *Dev. Cell*, vol. 6, no. 4, pp. 483–495, 2004.

[286] J. L. Charest, J. M. Jennings, W. P. King, A. P. Kowalczyk, and A. J. García, “Cadherin-mediated cell-cell contact regulates keratinocyte differentiation.,” *J. Invest. Dermatol.*, vol. 129, no. 3, pp. 564–572, 2009.

[287] S. K. Sastry and K. Burridge, “Focal adhesions: a nexus for intracellular signaling and cytoskeletal dynamics.,” *Exp. Cell Res.*, vol. 261, no. 1, pp. 25–36, Nov. 2000.

[288] N. Wang, J. P. P. Butler, and D. E. E. Ingber, “Mechanotransduction across the cell surface and through the cytoskeleton.,” *Science*, vol. 260, no. 5111, pp. 1124–1127, 1993.

[289] C. S. Chen, J. L. Alonso, E. Ostuni, G. M. Whitesides, and D. E. Ingber, “Cell shape provides global control of focal adhesion assembly,” *Biochem. Biophys. Res. Commun.*, vol. 307, no. 2, pp. 355–361, Jul. 2003.

[290] D. E. Ingber, “Cellular tensegrity: defining new rules of biological design that govern the cytoskeleton.,” *J. Cell Sci.*, vol. 104 (Pt 3, no. 3, pp. 613–27, Mar. 1993.

[291] A. D. Bershadsky, N. Q. Balaban, and B. Geiger, “Adhesion-Dependent Cell Mechanosensitivity,” *Annu. Rev. Cell Dev. Biol.*, vol. 19, no. 1, pp. 677–695, 2003.

[292] J. L. Tan, J. Tien, D. M. Pirone, D. S. Gray, K. Bhadriraju, and C. S. Chen, “Cells lying on a bed of microneedles: an approach to isolate mechanical force.,” *Proc. Natl. Acad. Sci. U. S. A.*, vol. 100, no. 4, pp. 1484–9, Feb. 2003.

[293] R. A. Brown, R. Prajapati, D. A. McGrouther, I. V Yannas, and M. Eastwood, “Tensional homeostasis in dermal fibroblasts: mechanical responses to mechanical loading in three-dimensional substrates.,” *J. Cell. Physiol.*, vol. 175, no. 3, pp. 323–32, Jun. 1998.

[294] B. Eckes and T. Krieg, “Regulation of connective tissue homeostasis in the skin by mechanical forces.,” *Clin. Exp. Rheumatol.*, vol. 22, no. 3 Suppl 33, pp. S73–6, Jan. .

[295] M. Théry, A. Pépin, E. Dressaire, Y. Chen, and M. Bornens, “Cell distribution of stress fibres in response to the geometry of the adhesive environment,” *Cell Motil. Cytoskeleton*, vol. 63, no. 6, pp. 341–355, 2006.

[296] Y. E. Korchev, C. L. Bashford, M. Milovanovic, I. Vodyanoy, and M. J. Lab, “Scanning ion conductance microscopy of living cells.,” *Biophys. J.*, vol. 73, no. 2, pp. 653–8, Aug. 1997.

[297] P. C. Moe, P. Blount, and C. Kung, “Functional and structural conservation in the mechanosensitive channel MscL implicates elements crucial for mechanosensation.,” *Mol. Microbiol.*, vol. 28, no. 3, pp. 583–92, May 1998.

[298] K. I. Willig, R. R. Kellner, R. Medda, B. Hein, S. Jakobs, and S. W. Hell, “Nanoscale resolution in GFP-based microscopy.,” *Nat. Methods*, vol. 3, no. 9, pp. 721–3, Oct. 2006.

[299] M. Hermann, O. Nussbaumer, R. Knöfler, P. Hengster, W. Nussbaumer, and W. Streif, “Real-Time Live Confocal Fluorescence Microscopy as a New Tool for Assessing Platelet Vitality.,” *Transfus. Med. Hemother.*, vol. 37, no. 5, pp. 299–305, Jan. 2010.

[300] U. Brunk, V. P. Collins, and E. Arro, “The fixation, dehydration, drying and coating of cultured cells of SEM.,” *J. Microsc.*, vol. 123, no. Pt 2, pp. 121–31, Aug. 1981.

[301] P. J. de Pablo and M. Carrión-Vázquez, “Imaging biological samples with atomic force microscopy.,” *Cold Spring Harb. Protoc.*, vol. 2014, no. 2, pp. 167–77, Feb. 2014.

[302] S. Vahabi, B. Nazemi Salman, and A. Javanmard, “Atomic force microscopy application in biological research: a review study.,” *Iran. J. Med. Sci.*, vol. 38, no. 2, pp. 76–83, Jun. 2013.

[303] H. X. You, J. M. Lau, S. Zhang, and L. Yu, “Atomic force microscopy imaging of living cells: a preliminary study of the disruptive effect of the cantilever tip on cell morphology.,” *Ultramicroscopy*, vol. 82, no. 1–4, pp. 297–305, Feb. 2000.

[304] M. J. Lab, a. Bhargava, P. T. Wright, and J. Gorelik, “The Scanning Ion Conductance Microscope (SICM) for Cellular Physiology,” *AJP Hear. Circ. Physiol.*, pp. 1–11, 2012.

[305] T. Ushiki, M. Nakajima, M. Choi, S.-J. Cho, and F. Iwata, “Scanning ion conductance microscopy for imaging biological samples in liquid: a comparative study with atomic force microscopy and scanning electron microscopy.,” *Micron*, vol. 43, no. 12, pp. 1390–8, Dec. 2012.

[306] J. Seifert, J. Rheinlaender, P. Novak, Y. E. Korchev, and T. E. Schäffer, “Comparison of Atomic Force Microscopy and Scanning Ion Conductance Microscopy for Live Cell Imaging.,” *Langmuir*, vol. 31, no. 24, pp. 6807–13, Jun. 2015.

[307] S. Zhang, S.-J. Cho, K. Busuttil, C. Wang, F. Besenbacher, and M. Dong, “Scanning ion conductance microscopy studies of amyloid fibrils at nanoscale.,” *Nanoscale*, vol. 4, no. 10, pp. 3105–10, May 2012.

[308] A. Bhargava, X. Lin, P. Novak, K. Mehta, Y. Korchev, M. Delmar, and J. Gorelik, “Super-resolution scanning patch clamp reveals clustering of functional ion channels in adult ventricular myocyte.,” *Circ. Res.*, vol. 112, no. 8, pp. 1112–20, Apr. 2013.

[309] J. Rheinlaender and T. E. Schäffer, “Image formation, resolution, and height measurement in scanning ion conductance microscopy,” *J. Appl. Phys.*, vol. 105, no. 9, pp. 1–9, 2009.

[310] P. Happel, D. Thatenhorst, and I. D. Dietzel, “Scanning ion conductance microscopy for studying biological samples.,” *Sensors (Basel).*, vol. 12, no. 11, pp. 14983–5008, Jan. 2012.

[311] D. Sánchez, N. Johnson, C. Li, P. Novak, J. Rheinlaender, Y. Zhang, U. Anand, P. Anand, J. Gorelik, G. I. Frolenkov, C. Benham, M. Lab, V. P. Ostanin, T. E. Schäffer, D. Klenerman, and Y. E. Korchev, “Noncontact measurement of the local mechanical properties of living cells using pressure applied via a pipette.,” *Biophys. J.*, vol. 95, no. 6, pp. 3017–27, Sep. 2008.

[312] M. L. Manning, R. a. Foty, M. S. Steinberg, and E.-M. Schoetz, “Coaction of intercellular adhesion and cortical tension specifies tissue surface tension,” *Proc. Natl. Acad. Sci.*, vol. 107, no. 28, pp. 12517–12522, 2010.

[313] G. W. Brodland, J. H. Veldhuis, S. Kim, M. Perrone, D. Mashburn, and M. S. Hutson, “CellFIT: a cellular force-inference toolkit using curvilinear cell boundaries.,” *PLoS One*, vol. 9, no. 6, p. e99116, Jan. 2014.

[314] K. Bambardekar, R. Clément, O. Blanc, C. Chardès, and P.-F. Lenne, “Direct laser manipulation reveals the mechanics of cell contacts in vivo.,” *Proc. Natl. Acad. Sci. U. S. A.*, vol. 112, no. 5, pp. 1416–21, Feb. 2015.

[315] O. Campàs, T. Mammoto, S. Hasso, R. A. Sperling, D. O’Connell, A. G. Bischof, R. Maas, D. A. Weitz, L. Mahadevan, and D. E. Ingber, “Quantifying cell-generated mechanical forces within living embryonic tissues.,” *Nat. Methods*, vol. 11, no. 2, pp. 183–9, Feb. 2014.

[316] A. R. Harris, L. Peter, J. Bellis, B. Baum, A. J. Kabla, and G. T. Charras, “Characterizing the mechanics of cultured cell monolayers.,” *Proc. Natl. Acad. Sci. U. S. A.*, vol. 109, no. 41, pp. 16449–54, Oct. 2012.

[317] J. Maître, G. Salbreux, F. Jülicher, E. Paluch, and C. Heisenberg, “Adhesion Functions in Cell Sorting by of Adhering Cells,” vol. 253, 2012.

[318] V. Lulevich, H. Y. Yang, R. R. Isseroff, and G. Y. Liu, “Single cell mechanics of keratinocyte cells,” *Ultramicroscopy*, vol. 110, no. 12, pp. 1435–1442, 2010.

[319] J. G. Rheinwald and H. Green, “Serial cultivation of strains of human epidermal keratinocytes: the formation of keratinizing colonies from single cells.,” *Cell*, vol. 6, no. 3. pp. 331–343, 1975.

[320] M. Théry and M. Piel, “Adhesive micropatterns for cells: A microcontact printing protocol,” *Cold Spring Harb. Protoc.*, vol. 4, no. 7, pp. 1–12, 2009.

[321] D. Sánchez, N. Johnson, C. Li, P. Novak, J. Rheinlaender, Y. Zhang, U. Anand, P. Anand, J. Gorelik, G. I. Frolenkov, C. Benham, M. Lab, V. P. Ostanin, T. E. Schäffer, D. Klenerman, and Y. E. Korchev, “Noncontact measurement of the local mechanical properties of living cells using pressure applied via a pipette.,” *Biophys. J.*, vol. 95, no. 6, pp. 3017–3027, 2008.

[322] P. Novak, J. Gorelik, U. Vivekananda, A. I. Shevchuk, Y. S. Ermolyuk, R. J. Bailey, A. J. Bushby, G. W. J. Moss, D. A. Rusakov, D. Klenerman, D. M. Kullmann, K. E. Volynski, and Y. E. Korchev, “Nanoscale-Targeted Patch-Clamp Recordings of Functional Presynaptic Ion Channels,” *Neuron*, vol. 79, no. 6, pp. 1067–1077, 2013.

[323] L. Ying, A. Bruckbauer, A. M. Rothery, Y. E. Korchev, and D. Klenerman, “Programmable delivery of DNA through a nanopipet.,” *Anal. Chem.*, vol. 74, no. 6, pp. 1380–5, Mar. 2002.

[324] M. Plodinec, M. Loparic, C. A. Monnier, E. C. Obermann, R. Zanetti-Dallenbach, P. Oertle, J. T. Hyotyla, U. Aebi, M. Bentires-Alj, R. Y. H. Lim, and C.-A. Schoenenberger, “The nanomechanical signature of breast cancer.,” *Nat. Nanotechnol.*, vol. 7, no. 11, pp. 757–65, 2012.

[325] J. C. Martens and M. Radmacher, “Softening of the actin cytoskeleton by inhibition of myosin II,” *Pflügers Arch. - Eur. J. Physiol.*, vol. 456, no. 1, pp. 95–100, 2008.

[326] G. Salbreux, G. Charras, and E. Paluch, “Actin cortex mechanics and cellular morphogenesis.,” *Trends Cell Biol.*, vol. 22, no. 10, pp. 536–45, 2012.

[327] H. Haga, C. Irahara, R. Kobayashi, T. Nakagaki, and K. Kawabata, “Collective movement of epithelial cells on a collagen gel substrate.,” *Biophys. J.*, vol. 88, no. 3, pp. 2250–2256, 2005.

[328] S. Huang, C. P. Brangwynne, K. K. Parker, and D. E. Ingber, “Symmetry-breaking in mammalian cell cohort migration during tissue pattern formation: role of random-walk persistence.,” *Cell Motil. Cytoskeleton*, vol. 61, no. 4, pp. 201–13, Aug. 2005.

[329] T. Das, K. Safferling, S. Rausch, N. Grabe, H. Boehm, and J. P. Spatz, “A molecular mechanotransduction pathway regulates collective migration of epithelial cells,” *Nat Cell Biol*, vol. 17, no. 3, pp. 276–287, Mar. 2015.

[330] K. Doxzen, S. R. K. Vedula, M. C. Leong, H. Hirata, N. S. Gov, A. J. Kabla, B. Ladoux, and C. T. Lim, “Guidance of collective cell migration by substrate geometry,” *Integr. Biol.*, vol. 5, no. 8, p. 1026, 2013.

[331] M. R. Ng, A. Besser, G. Danuser, and J. S. Brugge, “Substrate stiffness regulates cadherin-dependent collective migration through myosin-II contractility,” *J. Cell Biol.*, vol. 199, no. 3, pp. 545–563, 2012.

[332] F. Peglion, F. Llense, and S. Etienne-Manneville, “Adherens junction treadmilling during collective migration,” *Nat. Cell Biol.*, vol. 16, no. 7, pp. 639–651, 2014.

[333] M. Melani, K. J. Simpson, J. S. Brugge, and D. Montell, “Regulation of cell adhesion and collective cell migration by hindsight and its human homolog RREB1.,” *Curr. Biol.*, vol. 18, no. 7, pp. 532–7, Apr. 2008.

[334] Y. Matsubayashi, W. Razzell, and P. Martin, “‘White wave’ analysis of epithelial scratch wound healing reveals how cells mobilise back from the leading edge in a myosin-II-dependent fashion.,” *J. Cell Sci.*, vol. 124, no. Pt 7, pp. 1017–21, Apr. 2011.

[335] M. Poujade, E. Grasland-Mongrain, A. Hertzog, J. Jouanneau, P. Chavrier, B. Ladoux, A. Buguin, and P. Silberzan, “Collective migration of an epithelial monolayer in response to a model wound.,” *Proc. Natl. Acad. Sci. U. S. A.*, vol. 104, no. 41, pp. 15988–93, Oct. 2007.

[336] P. Friedl and D. Gilmour, “Collective cell migration in morphogenesis, regeneration and cancer.,” *Nat. Rev. Mol. Cell Biol.*, vol. 10, no. 7, pp. 445–57, Jul. 2009.

[337] A. Wicki, F. Lehembre, N. Wick, B. Hantusch, D. Kerjaschki, and G. Christofori, “Tumor invasion in the absence of epithelial-mesenchymal transition: podoplanin-mediated remodeling of the actin cytoskeleton.,” *Cancer Cell*, vol. 9, no. 4, pp. 261–72, Apr. 2006.

[338] P. Friedl, J. Locker, E. Sahai, and J. E. Segall, “Classifying collective cancer cell invasion,” *Nat. Cell Biol.*, vol. 14, no. 8, pp. 777–783, 2012.

[339] Y. Kam, C. Guess, L. Estrada, B. Weidow, and V. Quaranta, “A novel circular invasion assay mimics in vivo invasive behavior of cancer cell lines and distinguishes single-cell motility in vitro.,” *BMC Cancer*, vol. 8, p. 198, Jan. 2008.

[340] W. Yu, A. Datta, P. Leroy, L. E. O’Brien, G. Mak, T.-S. Jou, K. S. Matlin, K. E. Mostov, and M. M. P. Zegers, “Beta1-integrin orients epithelial polarity via Rac1 and laminin.,” *Mol. Biol. Cell*, vol. 16, no. 2, pp. 433–45, Mar. 2005.

[341] S.-Y. Tee, J. Fu, C. S. Chen, and P. A. Janmey, “Cell Shape and Substrate Rigidity Both Regulate Cell Stiffness,” *Biophys. J.*, vol. 100, no. 5, pp. L25–L27, 2011.

[342] A. Rigato, F. Rico, F. Eghiaian, M. Piel, and S. Scheuring, “Atomic Force Microscopy Mechanical Mapping of Micropatterned Cells Shows Adhesion Geometry-Dependent Mechanical Response on Local and Global Scales.,” *ACS Nano*, no. Xx, pp. 5846–5856, 2015.

[343] J. Rheinlaender and T. E. Schäffer, “Lateral Resolution and Image Formation in Scanning Ion Conductance Microscopy.,” *Anal. Chem.*, vol. 87, no. 14, pp. 7117–24, Jul. 2015.

[344] S. Del Linz, E. Willman, M. Caldwell, D. Klenerman, A. Fernández, and G. Moss, “Contact-free scanning and imaging with the scanning ion conductance microscope.,” *Anal. Chem.*, vol. 86, no. 5, pp. 2353–60, Mar. 2014.

[345] B.-C. Liu, X.-Y. Lu, X. Song, K.-Y. Lei, A. A. Alli, H.-F. Bao, D. C. Eaton, and H.-P. Ma, “Scanning ion conductance microscopy: a nanotechnology for biological studies in live cells.,” *Front. Physiol.*, vol. 3, p. 483, Jan. 2012.

[346] A. E. Markaki, “alamarBlue® Assay for Assessment of Cell Proliferation using the FLUOstar OPTIMA.” [Online]. Available: http://www.bmglabtech.com/media/35216/1043818.pdf. [Accessed: 29-Sep-2015].

[347] Y. E. Korchev, J. Gorelik, M. J. Lab, E. V Sviderskaya, C. L. Johnston, C. R. Coombes, I. Vodyanoy, and C. R. Edwards, “Cell volume measurement using scanning ion conductance microscopy.,” *Biophys. J.*, vol. 78, no. 1, pp. 451–7, Jan. 2000.

[348] A. Das, “Extracellular Matrix Density Regulates Extracellular Proteolysis via Modulation of Cellular Contractility,” *J. Carcinog. Mutagen.*, vol. S13, 2013.

[349] Y. Barrandon and H. Green, “Cell size as a determinant of the clone-forming ability of human keratinocytes.,” *Proc. Natl. Acad. Sci. U. S. A.*, vol. 82, no. 16, pp. 5390–5394, 1985.

[350] C. Bottier, C. Gabella, B. Vianay, L. Buscemi, I. F. Sbalzarini, J.-J. Meister, and A. B. Verkhovsky, “Dynamic measurement of the height and volume of migrating cells by a novel fluorescence microscopy technique,” *Lab Chip*, vol. 11, no. 22, p. 3855, Oct. 2011.

[351] R. Kalaji, “Mechanisms regulating keratinocyte morphology,” *PhD Thesis, Imp. Coll. London*, no. September, 2008.

[352] F. M. Watt and H. Green, “Involucrin synthesis is correlated with cell size in human epidermal cultures.,” *J. Cell Biol.*, vol. 90, no. 3, pp. 738–42, 1981.

[353] J. H. Hoh and C. A. Schoenenberger, “Surface morphology and mechanical properties of MDCK monolayers by atomic force microscopy.,” *J. Cell Sci.*, vol. 107 (Pt 5, pp. 1105–14, May 1994.

[354] P. Rørth, “Fellow travellers: emergent properties of collective cell migration,” *EMBO Rep.*, vol. 13, no. 11, pp. 984–991, 2012.

[355] S. L. Haigo and D. Bilder, “Global Tissue Revolutions in a Morphogenetic Movement Controlling Elongation,” *Science (80-.).*, no. February, pp. 1071–1074, 2011.

[356] A. Bianco, M. Poukkula, A. Cliffe, J. Mathieu, C. M. Luque, T. a Fulga, and P. Rørth, “Two distinct modes of guidance signalling during collective migration of border cells.,” *Nature*, vol. 448, no. 7151, pp. 362–365, 2007.

[357] J. Gerhart, M. Danilchik, T. Doniach, S. Roberts, B. Rowning, and R. Stewart, “Cortical rotation of the Xenopus egg: consequences for the anteroposterior pattern of embryonic dorsal development,” *Development*, vol. 107 Suppl, pp. 37–51, 1989.

[358] T. J. Diefenbach, N. K. Koehncke, and J. I. Goldberg, “Characterization and development of rotational behavior inHelisoma embryos: Role of endogenous serotonin,” *J. Neurobiol.*, vol. 22, no. 9, pp. 922–934, Dec. 1991.

[359] K. Tanner, H. Mori, R. Mroue, A. Bruni-Cardoso, and M. J. Bissell, “Coherent angular motion in the establishment of multicellular architecture of glandular tissues,” *Proc. Natl. Acad. Sci.*, vol. 109, no. 6, pp. 1973–1978, 2012.

[360] H. Wang, S. Lacoche, L. Huang, B. Xue, and S. K. Muthuswamy, “Rotational motion during three-dimensional morphogenesis of mammary epithelial acini relates to laminin matrix assembly,” *Proc. Natl. Acad. Sci.*, vol. 110, no. 1, pp. 163–168, 2013.

[361] C. Brangwynne, S. Huang, K. K. Parker, D. E. Ingber, and E. Ostuni, “Symmetry breaking in cultured mammalian cells.,” *In Vitro Cell. Dev. Biol. Anim.*, vol. 36, no. 9, pp. 563–5, Oct. 2000.

[362] B. Li and S. X. Sun, “Coherent Motions in Confluent Cell Monolayer Sheets,” *Biophys. J.*, vol. 107, no. 7, pp. 1532–1541, Oct. 2014.

[363] F. Y. Leong, “Physical Explanation of Coupled Cell-Cell Rotational Behavior and Interfacial Morphology: A Particle Dynamics Model,” *Biophys. J.*, vol. 105, no. 10, pp. 2301–2311, Nov. 2013.

[364] A. B. Verkhovsky, T. M. Svitkina, and G. G. Borisy, “Self-polarization and directional motility of cytoplasm,” *Curr. Biol.*, vol. 9, no. 1, pp. 11–S1, Jan. 1999.

[365] T. E. Angelin, E. Hannezo, X. Trepat, J. J. Fredberg, and A. D. Weitz, “Cell Migration Driven by Cooperative Substrate Deformation Patterns,” vol. 18, no. 9, pp. 1199–1216, 2013.

[366] R. Tchao, “Novel Forms of epithelial cell motility on collagen and on glass surfaces,” *Cell Motil.*, vol. 2, no. 4, pp. 333–341, Feb. 1982.

[367] A. Kumar, A. Maitra, M. Sumit, S. Ramaswamy, and G. V. Shivashankar, “Actomyosin contractility rotates the cell nucleus,” *Sci. Rep.*, vol. 4, 2014.

[368] V. W. Victoria, W. Allen, and D. L. Kropf, “Nuclear rotation and lineage specification in Pelvetia embryos,” *Development*, vol. 115, no. 3, pp. 873–883, 1992.

[369] C. M. Pomerat, “Rotating nuclei in tissue cultures of adult human nasal mucosa,” *Exp. Cell Res.*, vol. 5, no. 1, pp. 191–196, Jan. 1953.

[370] J. Wu, K. C. Lee, R. B. Dickinson, and T. P. Lele, “How dynein and microtubules rotate the nucleus,” *J. Cell. Physiol.*, vol. 226, no. 10, pp. 2666–2674, 2011.

[371] J. R. Levy and E. L. F. Holzbaur, “Dynein drives nuclear rotation during forward progression of motile fibroblasts,” *J. Cell Sci.*, vol. 121, no. 19, pp. 3187–3195, 2008.

[372] A. J. Engler, F. Rehfeldt, S. Sen, and D. E. Discher, “Microtissue elasticity: measurements by atomic force microscopy and its influence on cell differentiation.,” *Methods Cell Biol.*, vol. 83, pp. 521–45, Jan. 2007.

[373] S. Nemir and J. L. West, “Synthetic Materials in the Study of Cell Response to Substrate Rigidity,” *Ann. Biomed. Eng.*, vol. 38, no. 1, pp. 2–20, 2010.

[374] J. H.-C. Wang and J.-S. Lin, “Cell traction force and measurement methods.,” *Biomech. Model. Mechanobiol.*, vol. 6, no. 6, pp. 361–71, Nov. 2007.

[375] V. Vogel and M. Sheetz, “Local force and geometry sensing regulate cell functions.,” *Nat. Rev. Mol. Cell Biol.*, vol. 7, no. 4, pp. 265–75, Apr. 2006.

[376] J. L. Tan, J. Tien, D. M. Pirone, D. S. Gray, K. Bhadriraju, and C. S. Chen, “Cells lying on a bed of microneedles: an approach to isolate mechanical force.,” *Proc. Natl. Acad. Sci. U. S. A.*, vol. 100, no. 4, pp. 1484–9, Feb. 2003.

[377] A. D. Rape, W.-H. Guo, and Y.-L. Wang, “The regulation of traction force in relation to cell shape and focal adhesions.,” *Biomaterials*, vol. 32, no. 8, pp. 2043–51, Mar. 2011.

[378] M. Mrksich, L. E. Dike, J. Tien, D. E. Ingber, and G. M. Whitesides, “Using microcontact printing to pattern the attachment of mammalian cells to self-assembled monolayers of alkanethiolates on transparent films of gold and silver.,” *Exp. Cell Res.*, vol. 235, no. 2, pp. 305–13, Sep. 1997.

[379] A. Brock, E. Chang, C.-C. Ho, P. LeDuc, X. Jiang, G. M. Whitesides, and D. E. Ingber, “Geometric Determinants of Directional Cell Motility Revealed Using Microcontact Printing †,” *Langmuir*, vol. 19, no. 5, pp. 1611–1617, Mar. 2003.

[380] J. James, E. D. Goluch, H. Hu, C. Liu, and M. Mrksich, “Subcellular curvature at the perimeter of micropatterned cells influences lamellipodial distribution and cell polarity.,” *Cell Motil. Cytoskeleton*, vol. 65, no. 11, pp. 841–52, Nov. 2008.

[381] N. Wang and D. E. Ingber, “Control of cytoskeletal mechanics by extracellular matrix, cell shape, and mechanical tension.,” *Biophys. J.*, vol. 66, no. 6, pp. 2181–9, Jun. 1994.

[382] O. M. Rossier, N. Gauthier, N. Biais, W. Vonnegut, M.-A. Fardin, P. Avigan, E. R. Heller, A. Mathur, S. Ghassemi, M. S. Koeckert, J. C. Hone, and M. P. Sheetz, “Force generated by actomyosin contraction builds bridges between adhesive contacts,” *EMBO J.*, vol. 29, no. 6, pp. 1055–1068, Feb. 2010.

[383] S. K. Wu and A. S. Yap, “Patterns in Space: Coordinating Adhesion and Actomyosin Contractility at E-cadherin Junctions,” *Cell Commun. Adhes.*, vol. 20, no. 6, pp. 201–212, 2013.

[384] N. Wang, J. D. Tytell, and D. E. Ingber, “Mechanotransduction at a distance: mechanically coupling the extracellular matrix with the nucleus.,” *Nat. Rev. Mol. Cell Biol.*, vol. 10, no. 1, pp. 75–82, Jan. 2009.

[385] M. Webster, K. L. Witkin, and O. Cohen-Fix, “Sizing up the nucleus: nuclear shape, size and nuclear-envelope assembly,” *J. Cell Sci.*, vol. 122, no. 10, pp. 1477–1486, May 2009.

[386] A. Buxboim, I. L. Ivanovska, and D. E. Discher, “Matrix elasticity, cytoskeletal forces and physics of the nucleus: how deeply do cells ‘feel’ outside and in?,” *J. Cell Sci.*, vol. 123, no. 3, pp. 297–308, Feb. 2010.

[387] R. M. Stewart, A. E. Zubek, K. A. Rosowski, S. M. Schreiner, V. Horsley, and M. C. King, “Nuclear-cytoskeletal linkages facilitate cross talk between the nucleus and intercellular adhesions.,” *J. Cell Biol.*, vol. 209, no. 3, pp. 403–18, May 2015.

[388] A. J. Streets, B. E. Wagner, P. C. Harris, C. J. Ward, and A. C. M. Ong, “Homophilic and heterophilic polycystin 1 interactions regulate E-cadherin recruitment and junction assembly in MDCK cells.,” *J. Cell Sci.*, vol. 122, no. Pt 9, pp. 1410–7, 2009.

[389] M. Versaevel, T. Grevesse, and S. Gabriele, “Spatial coordination between cell and nuclear shape within micropatterned endothelial cells,” *Nat. Commun.*, vol. 3, p. 671, 2012.

[390] J. R. Davis, A. Luchici, F. Mosis, J. Thackery, J. A. Salazar, Y. Mao, G. A. Dunn, T. Betz, M. Miodownik, and B. M. Stramer, “Inter-cellular forces orchestrate contact inhibition of locomotion.,” *Cell*, vol. 161, no. 2, pp. 361–73, Apr. 2015.

[391] N. Gerald, J. Dai, H. P. Ting-Beall, and A. De Lozanne, “A role for Dictyostelium racE in cortical tension and cleavage furrow progression.,” *J. Cell Biol.*, vol. 141, no. 2, pp. 483–92, Apr. 1998.

[392] G. S. Lakshmikanth, H. M. Warrick, and J. A. Spudich, “A mitotic kinesin-like protein required for normal karyokinesis, myosin localization to the furrow, and cytokinesis in Dictyostelium,” *Proc. Natl. Acad. Sci.*, vol. 101, no. 47, pp. 16519–16524, Nov. 2004.

[393] A. E. Rodríguez-Fraticelli, M. Auzan, M. A. Alonso, M. Bornens, and F. Martín-Belmonte, “Cell confinement controls centrosome positioning and lumen initiation during epithelial morphogenesis.,” *J. Cell Biol.*, vol. 198, no. 6, pp. 1011–23, Sep. 2012.

[394] F. Martín-Belmonte, W. Yu, A. E. Rodríguez-Fraticelli, A. J. Ewald, A. Ewald, Z. Werb, M. A. Alonso, and K. Mostov, “Cell-polarity dynamics controls the mechanism of lumen formation in epithelial morphogenesis.,” *Curr. Biol.*, vol. 18, no. 7, pp. 507–13, Apr. 2008.

[395] K. A. Kilian, B. Bugarija, B. T. Lahn, and M. Mrksich, “Geometric cues for directing the differentiation of mesenchymal stem cells.,” *Proc. Natl. Acad. Sci. U. S. A.*, vol. 107, no. 11, pp. 4872–7, Mar. 2010.

[396] J. Y. Sim, J. Moeller, K. C. Hart, D. Ramallo, V. Vogel, A. R. Dunn, W. J. Nelson, and B. L. Pruitt, “Spatial distribution of cell-cell and cell-ECM adhesions regulates force balance while maintaining E-cadherin molecular tension in cell pairs.,” *Mol. Biol. Cell*, vol. 26, no. 13, pp. 2456–65, Jul. 2015.

[397] T. Nishimura and M. Takeichi, “Remodeling of the adherens junctions during morphogenesis.,” *Curr. Top. Dev. Biol.*, vol. 89, pp. 33–54, Jan. 2009.

[398] N. Wang and Z. Suo, “Long-distance propagation of forces in a cell.,” *Biochem. Biophys. Res. Commun.*, vol. 328, no. 4, pp. 1133–8, Mar. 2005.

[399] R. Blumenfeld, “Isostaticity and controlled force transmission in the cytoskeleton: A model awaiting experimental evidence.,” *Biophys. J.*, vol. 91, no. 5, pp. 1970–83, Sep. 2006.

[400] D. E. Jaalouk and J. Lammerding, “Mechanotransduction gone awry,” *Nat. Rev. Mol. Cell Biol.*, vol. 10, no. 1, pp. 63–73, Jan. 2009.

[401] C. M. Nelson, D. M. Pirone, J. L. Tan, and C. S. Chen, “Vascular endothelial-cadherin regulates cytoskeletal tension, cell spreading, and focal adhesions by stimulating RhoA.,” *Mol. Biol. Cell*, vol. 15, no. 6, pp. 2943–53, Jun. 2004.

[402] K. Takaishi, T. Sasaki, H. Kotani, H. Nishioka, and Y. Takai, “Regulation of cell-cell adhesion by rac and rho small G proteins in MDCK cells.,” *J. Cell Biol.*, vol. 139, no. 4, pp. 1047–59, 1997.

[403] A. I. Ivanov, D. Hunt, M. Utech, A. Nusrat, and C. A. Parkos, “Differential roles for actin polymerization and a myosin II motor in assembly of the epithelial apical junctional complex.,” *Mol. Biol. Cell*, vol. 16, no. 6, pp. 2636–50, Jun. 2005.

[404] T. Lecuit and A. S. Yap, “E-cadherin junctions as active mechanical integrators in tissue dynamics,” *Nat. Cell Biol.*, vol. 17, no. 5, pp. 533–539, 2015.

[405] R. Fernandez-Gonzalez, S. D. M. Simoes, J.-C. Röper, S. Eaton, and J. a. Zallen, “Myosin II Dynamics Are Regulated by Tension in Intercalating Cells,” *Dev. Cell*, vol. 17, no. 5, pp. 736–743, 2009.

[406] T. Nishimura and M. Takeichi, “Shroom3-mediated recruitment of Rho kinases to the apical cell junctions regulates epithelial and neuroepithelial planar remodeling.,” *Development*, vol. 135, no. 8, pp. 1493–502, Apr. 2008.

[407] S. de M. Simões, A. Mainieri, and J. A. Zallen, “Rho GTPase and Shroom direct planar polarized actomyosin contractility during convergent extension.,” *J. Cell Biol.*, vol. 204, no. 4, pp. 575–89, Feb. 2014.

[408] J. D. Hildebrand, “Shroom regulates epithelial cell shape via the apical positioning of an actomyosin network.,” *J. Cell Sci.*, vol. 118, no. Pt 22, pp. 5191–203, 2005.

[409] K. Suffoletto, N. Ye, F. Meng, D. Verma, and S. Z. Hua, “Intracellular forces during guided cell growth on micropatterns using FRET measurement.,” *J. Biomech.*, vol. 48, no. 4, pp. 627–35, 2015.

[410] Y. Oda, T. Otani, J. Ikenouchi, and M. Furuse, “Tricellulin regulates junctional tension of epithelial cells at tricellular contacts via Cdc42,” *J. Cell Sci.*, vol. 127, no. 19, pp. 4201–4212, 2014.

[411] T. Hayashi and R. W. Carthew, “Surface mechanics mediate pattern formation in the developing retina.,” *Nature*, vol. 431, no. 7009, pp. 647–652, 2004.

[412] R. Farhadifar, J.-C. Röper, B. Aigouy, S. Eaton, and F. Jülicher, “The influence of cell mechanics, cell-cell interactions, and proliferation on epithelial packing.,” *Curr. Biol.*, vol. 17, no. 24, pp. 2095–104, Dec. 2007.

[413] J. Y. Sim, J. Moeller, K. C. Hart, D. Ramallo, V. Vogel, a. R. Dunn, W. J. Nelson, and B. L. Pruitt, “Spatial distribution of cell-cell and cell-ECM adhesions regulates force balance while main taining E-cadherin molecular tension in cell pairs,” *Mol. Biol. Cell*, vol. 26, no. 13, pp. 2456–2465, 2015.

[414] S. C. Stapleton, A. Chopra, and C. S. Chen, “Force Measurement Tools to Explore Cadherin Mechanotransduction,” *Cell Commun. Adhes.*, vol. 21, no. 3, pp. 193–205, 2014.

[415] N. O. Petersen, W. B. McConnaughey, and E. L. Elson, “Dependence of locally measured cellular deformability on position on the cell, temperature, and cytochalasin B.,” *Proc. Natl. Acad. Sci. U. S. A.*, vol. 79, no. 17, pp. 5327–5331, 1982.

[416] E. Bazellières, V. Conte, A. Elosegui-Artola, X. Serra-Picamal, M. Bintanel-Morcillo, P. Roca-Cusachs, J. J. Muñoz, M. Sales-Pardo, R. Guimerà, and X. Trepat, "Control of cell-cell forces and collective cell dynamics by the intercellular adhesome.," *Nat. Cell Biol.*, vol. 17, no. 4, pp. 409–420, 2015.

[417] K. K. H. Svoboda, P. Moessner, T. Field, and J. Acevedo, "ROCK inhibitor (Y27632) increases apoptosis and disrupts the actin cortical mat in embryonic avian corneal epithelium.," *Dev Dyn.*, vol. 229, no. 3, pp. 579–590, 2004.

[418] E. A. Reits and J. J. Neefjes, "From fixed to FRAP: measuring protein mobility and activity in living cells.," *Nat. Cell Biol.*, vol. 3, no. 6, pp. E145–E147, 2001.

[419] C.-Y. Zheng, R. S. Petralia, Y.-X. Wang, and B. Kachar, "Fluorescence recovery after photobleaching (FRAP) of fluorescence tagged proteins in dendritic spines of cultured hippocampal neurons.," *J. Vis. Exp.*, vol. 9, no. 50, pp. 9–11, 2011.

[420] J. a Theriot and T. J. Mitchison, "Actin microfilament dynamics in locomoting cells.," *Nature*, vol. 352, no. 6331. pp. 126–131, 1991.

[421] K. Murthy and P. Wadsworth, "Myosin-II-Dependent Localization and Dynamics of F-Actin during Cytokinesis," *Curr. Biol.*, vol. 15, no. 8, pp. 724–731, 2005.

[422] J. C. Burns and J. T. Corwin, "Responses to Cell Loss Become Restricted as the Supporting Cells in Mammalian Vestibular Organs Grow Thick Junctional Actin Bands That Develop High Stability," *J. Neurosci.*, vol. 34, no. 5, pp. 1998–2011, 2014.

Supplementary Material

S.1 Image Analysis - Macros in Fiji

S.1.1 Morphology Macro

The following macro has been described in the methods section (2.7.2 – page 50). The code below was saved as a '.ijm' file for use with Fiji.

Code in Fiji	Comments

//get info
input = getDirectory("Location of images");
output = getDirectory("Location for cropped images");
list = getFileList(input);
sr=getString("Name for results", "series");
	Cropped images containing the four channels are selected: Channel 1 (Nuclei), Channel 2 (E-cadherin, Channel 3 (F-actin) and Channel 4 (Phase contrast).

//open files from directory
for(i=0;i<list.length;i++){
full = input + list[i];
run("Bio-Formats Importer", "open=full autoscale color_mode=Composite view=Hyperstack stack_order=XYCZT");
fn=getInfo("image.filename");
getDimensions(width, height, channels, slices, frames);
w=width;
h=height;
c=channels;
z=slices;
f=frames;
roiManager("Reset");
setTool("freeline");
title = "Get info";
msg = "draw cuved line to split cells\n then select OK to continue";
waitForUser(title, msg);
roiManager("Add", "000000", 5);
rename("temp");
run("Split Channels");
	The channels are split and opened separately after being renamed. Channels are renamed so that they can be accurately called for by the program.

//measure nuclear distance
selectWindow("C1-temp");
setAutoThreshold("Default dark");
setOption("BlackBackground", false);
run("Convert to Mask");
run("Watershed");
rename(fn + " Nuclear Distance");
run("Analyze Particles...", " show=Outlines display");
out = output + fn + " Nuclear Distance drawing";
saveAs("Tiff",out);
	Channel 1 (Nuclei) is selected and thresholded (selected according to brightness). The centres of each of the nuclei in XY coordinates are calculated.

//measure channel 2
//straight line
selectWindow("C2-temp");
rename(fn + " Junctional StraightLine distance");
setLineWidth(5);
setTool("line");
title = "Get info";
msg = "draw straight line between cells\n then select OK to continue";
waitForUser(title, msg);
run("Measure");
	Channel 2 (E-cadherin) is selected and a straight line drawn along the junction covering end to end. The length of the straight line is calculated.

//curved line
rename(fn + " Curvedline signal Channel 2");
setTool("freeline");
run("Enhance Contrast", "saturated=0.35");
title = "Get info";
msg = "draw cuved line between cells\n then select OK to continue";
waitForUser(title, msg);
roiManager("Add", "000000", 5);
roiManager("Select", 1);
roiManager("Measure");
	The actual junction is then traced through the image (called the 'curved line') and the length calculated.

//measure edge to edge distance
selectWindow(fn + " Curvedline signal Channel 2");
rename(fn + " Edge to edge distance");
roiManager("Select", 0);
run("Measure");
	The actual junction is then extended to reach the edges of the shape (called the 'edge to edge distance') and the length calculated.

//split cells
selectWindow(fn + " Curvedline signal Channel 2");
rename(fn + " Cell size");
roiManager("Select", 0);
roiManager("Set Color", "black");
roiManager("Show All");
run("Flatten");
run("8-bit");
run("Threshold...");
title = "Get info";
msg = "set junctional threshold\n then select OK to continue";
waitForUser(title, msg);
rename(fn + " Cell Area");
run("Analyze Particles...", "size=25-Infinity show=Outlines display");
out = output + fn + " Cell Area drawing";
saveAs("Tiff",out);
run("Close All");
}
	The cells are split along the 'edge to edge distance' and the areas of both cells selected. Areas are then calculated for the two cells.

//save results file
out = output + sr + " measurements.csv";
saveAs("Results",out);
	Results saved in excel.

S.1.2 Intensity Macro

The following macro has been described in the methods section (2.7.2 – page 51). The first two sections described above for the Morphology Macro (//get info and //open files from directory) remain the same for this macro and will not be repeated here. The code below was the additional code used for the Intensity Macro and saved as a '.ijm' file for use with Fiji.

Code in Fiji	Comment

//close unnecessary channels
fn=getInfo("image.filename");
rename("temp");
run("Split Channels");
selectWindow("C1-temp");
run("Close");
selectWindow("C4-temp");
run("Close");
	Close channel 1 (Nuclei) and channel 4 (Phase contrast) as they wil not be used in this analysis.

//Threshold Junction in E-cad Channel
selectWindow("C2-temp");
run("Threshold...");
	The junctional region is selected using the E-cadherin channel and intensity and area of the junction measured.

title = "Get info";
msg = "set junctional threshold\n then select OK to continue";
waitForUser(title, msg);
run("Analyze Particles...", "size=5-Infinity show=Outlines add");
title = "Get info";
msg = "delete unecessary ROI's\n then select OK to continue";
waitForUser(title, msg);
selectWindow("C2-temp");
newname1=fn + " Cadherin";
rename(newname1);
roiManager("Show all");
roiManager("Measure");
n=roiManager("count");
if(n==0){
exit("No ROI's")
};
for (j=0;j<=n-1;j++){
roiManager("select", j);
run("Clear", "slice");
}
	The outline of the junctional region is then overlaid in the actin channel and the intensity and area of junctional actin measured.

//Threshold non-junctional region in Actin channel
roiManager("Show all");
run("Threshold...");
title = "Get info";
msg = "set non junctional threshold for Cadherin\n then select OK to continue";
waitForUser(title, msg);
run("Analyze Particles...", "size=5-Infinity display");
selectWindow("C3-temp");
newname2=fn + " Actin";
rename(newname2);
roiManager("Show all");
roiManager("Measure");
n=roiManager("count");
if(n==0){
exit("No ROI's")
};
for (k=0;k<=n-1;k++){
roiManager("select", k);
run("Clear", "slice");
}
run("Clear", "slice");
roiManager("Show all");
run("Threshold...");
title = "Get info";
msg = "set non-junctional threshold for Actin\n then select OK to continue";
waitForUser(title, msg);
run("Analyze Particles...", "size=5-Infinity display");
run("Close All");
}
	The non-junctional region or the rest of the cell is selected by expanding the selection to reach the edges of the shape covered by the cell pair. The actin channel is used here since the periphery is clearly labelled with actin making the edges of the cell better visible.
	
	The outline of the rest of the cells is then overlaid on the E-cadherin channel and the intensity and area measured.

//Save data
out = output + sr + " measurements.csv";
saveAs("Results",out);
	Results saved in Excel.

S.2 Mean height and volume of cell pairs

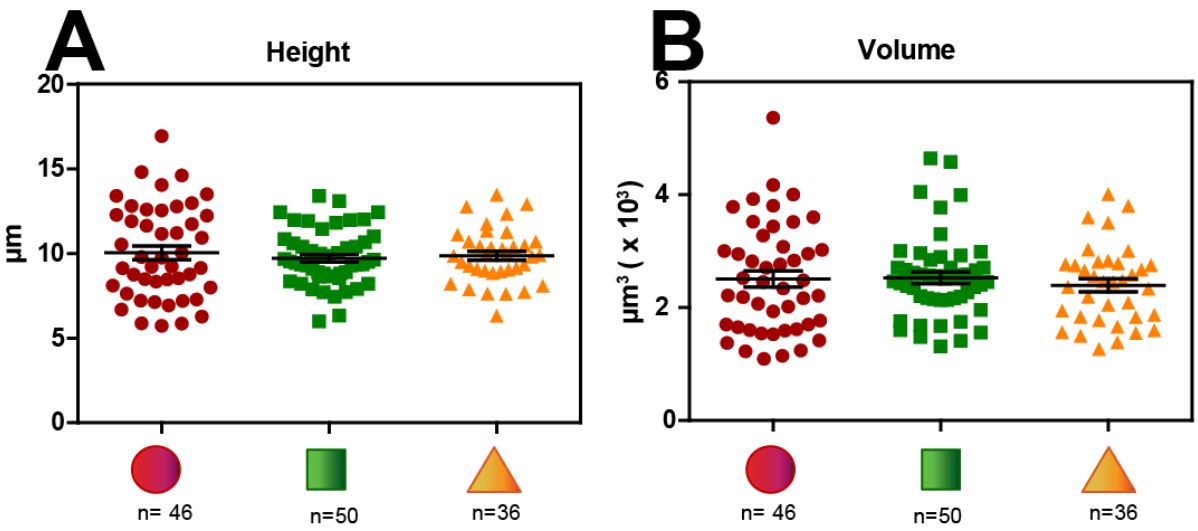

Figure S.1: Cell heights and volumes do not differ between geometries. Cell height and volume were calculated using SICMImageViewer software. Average cell heights (A) and volumes (B). Graphs represent values per cell. Error bars represent SEM. Data were analysed statistically by one-way ANOVA followed by Tukey post-hoc test. N numbers for individual cells are shown below each of the shapes. Data are representative of 4 independent experiments. Dr. Sanchez-Alonso contributed to analysis of data.

S.3 Junction positioning of cells (not normalised to probability)

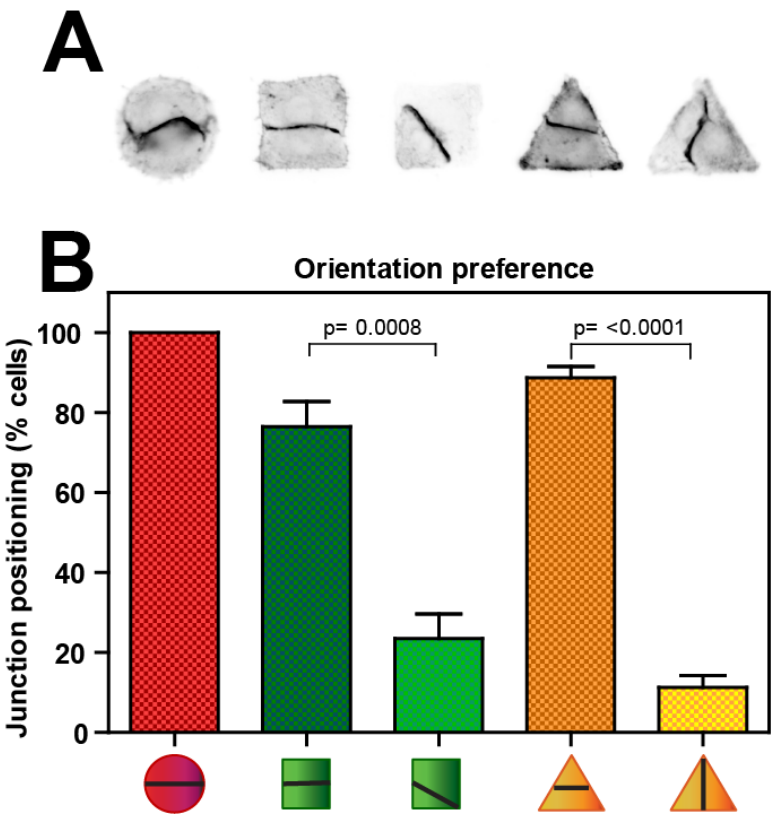

Figure S.2: Junction positioning of cell pairs grown on micropatterns. (A) Inverted immunofluorescence images of E-cadherin staining depicting different orientations of junctions for cells pairs on the three different shapes. (B) Quantification of percentage of cells in a given orientation of junctions. Error bars show SEM. Data were analysed statistically using t-tests for the two different orientations within a single shape (square or triangle). Data are representative of 4 independent experiments.